

**THE MODELLING, DESIGN AND THE
OPERATION OF AN ELECTROMAGNETIC
TORQUE CONVERTER**

Thesis Submitted for the degree of

Doctor of Philosophy

at the University of Leicester

by

Eljaroshi Mohamed E. Diryak

Department of Engineering

University of Leicester

2014

To my mother

The Modelling, Design and the Operation of an Electromagnetic Torque Converter

Eljaroshi Diryak

ABSTRACT

The current hydraulic torque converter has many drawbacks. It requires a significant amount of oil to drive the impeller, and the turbine, which may cause a loss of energy. In addition, the direct contact of the mechanical parts of the conventional hydraulic torque converter increases the possibility of parts failure and mechanical noise.

This thesis proposes a new and novel Electromagnetic Torque Converter (EMTC) system, which replaces the conventional hydraulic torque converter. The new EMTC system comprises of two parts, a Differential Machine (DM) part, which is a double rotor single stator machine, and a Variable Frequency Rotary Transformer (VFRT) part, which is responsible for transferring the slip power from between the DM rotors to the DM stator. One of the purposes the VFRT is to eliminate the use of slip rings. In addition, an electronic power converter is used in the EMTC system to convert the frequency of the slip power for re-injection into the DM. Finite Element Modelling (FEM) simulations were primarily used to define the design specifications of an experimental prototype EMTC system. These specifications include the minimum cogging torque, the ripple torque, and the high electromagnetic torque of the DM. FEM simulations were also used to select the stator slot configuration and for predicting the dynamic behaviour of each part of the EMTC system, and a mathematical model was developed. Each part of the EMTC system was characterised experimentally. The complete EMTC system was then tested in both open and closed loop configurations. The FEM simulations and the mathematical model showed good agreement with the experimental results.

The new EMTC system resolves many of the drawbacks of the conventional hydraulic torque converter. The outcome of this thesis is expected to provide a step change in electromagnetic converter technology.

ACKNOWLEDGMENTS

I would like to express my sincere thanks and profound appreciation to my supervisor Dr. Paul Lefley for his invaluable assistance and encouragement. In addition, I would like to express my gratitude to Luigi Alessandro, Alan Rice, Alan Wale and, Mohammed Arakate for all their help and assistance.

Thanks to all my colleagues in the power research group for their help during the measurements phase. The Libyan Cultural Affairs is gratefully acknowledged for sponsoring this project. My thanks go also to Dr. Amar Alaswad, the academic supervisor at the Libyan embassy in London for his continuous support.

Finally, I am most grateful to my father Mr. Mohammed Eljaroshi, my brothers and my wife Fatima Eljaroshi. They gave me great support, which helped me to go further in this road. In addition, I would like to thank my children practically my dearest daughters Fathia and Marwa for being patient.

CONTENTS

ABSTRACT	i
ACKNOWLEDGMENTS	ii
CONTENTS	iii
LIST OF SYMBOLS	ix
LIST OF ABBREVIATIONS	xi
1 INTRODUCTION	1
1.1 Introduction	1
1.1.1 The Manual Transmission System	1
1.1.2 The Automatic Transmission System	2
1.2 State-of-the art.....	2
1.3 Motivations and Research Objectives	3
1.4 Contributions to the Field.....	5
1.5 Thesis Overview.....	6
1.6 Thesis Outline	8
2 Background and Literature Review	10
2.1 The Hydraulic Torque Converter	10
2.1.1 The Torque Converter Model	11
2.1.2 The Gearbox Model	12
2.2 Development of the Torque Converter.....	13
2.2.1 The Magnetic Torque Converter.....	13
2.2.2 The Electromechanical Torque Converter	14
2.2.3 The Electrical Torque Converter.....	15
2.2.4 The Electromagnetic Torque Converter.....	17
2.2.4.1 The Integrated Energy Transducer.....	19
2.3 Double Rotor Machine Topologies	20
2.4 Background of the Brushless Permanent Magnet Machine	24
2.4.1 Brushless AC Machine (BLACM) Modelling	26
2.4.2 Brushless DC Machine (BLDCM) Modelling	29
2.5 Summary	34

3	Research Methodology	35
3.1	Introduction	35
3.1.1	The Philosophy of the EMTC system	35
3.1.2	Strategy of the EMTC Design	35
3.1.3	Data Collection and Analysis Methods	37
3.1.4	The Validity of the EMTC system	39
3.2	Summary	40
4	The Electromagnetic Torque Converter Concept	41
4.1	Introduction	41
4.2	The EMTC System Description	41
4.3	DM Principle of Operation	44
4.4	EMTC System Operating Range	45
4.4.1	Stalling Operating Range	45
4.4.2	Synchronization Operating Range	46
4.5	Summary	47
5	Design and Optimization of the EMTC System	48
5.1	Introduction	48
5.2	Design Criteria of the Proposed EMTC System	48
5.2.1	Cogging Torque	49
5.2.2	Electromagnetic Torque	50
5.2.3	Torque Ripple	51
5.3	Preliminarily Differential Machine Design	51
5.4	Development of the EMTC system by Re-design	53
5.4.1	Design limitations	54
5.4.2	EMTC System Frame Design Specification	54
5.4.3	Design and Configuration of the Differential Machine (DM)	55
5.4.3.1	Electrical Design	55
5.4.3.2	Mechanical Design of the BLDCM	58
5.4.3.3	Mechanical Design of the PMIM	60
5.4.4	Design and Configuration of the VFRT Machine	63
5.5	Design Optimization of the Differential Machine	64
5.5.1	Optimization Design Methodology	64
5.5.1.1	Machine Specification	65
5.5.1.2	Selection of Pole-Slot Combination	66

5.5.2	Design Flowchart	67
5.5.2.1	Slot Design optimization	69
5.5.2.2	Number of Turns per Slot per Coil Selection	71
5.6	Summary	73
6	Finite Element Modelling of the EMTC System.....	74
6.1	Introduction	74
6.2	Over view of FEM.....	74
6.3	EFM Modelling Methodology	75
6.3.1	Pre-Processing	75
6.3.2	Processing	75
6.3.3	Post Processing	75
6.4	FEM Set-Up	75
6.4.1	Differential Machine Modelling Set-Up	76
6.5	FEM Simulation Results	76
6.5.1	Influence of the Combination of Pole and Slot Numbers	77
6.5.2	FEM Simulation of the Cogging Torque Using Iteration Technique	78
6.5.2.1	The Fully Pitched Models.....	78
6.5.2.2	The Gapped Magnets Models	80
6.5.3	Summary of Using the Iteration Method	82
6.5.4	FEM Simulation Based on the Optimal Magnet Arc Length Calculations	82
6.5.4.1	Integrated DM Simulations of the Cogging Torque	87
6.5.5	FEM Simulation of the Electromagnetic Torque and Ripple Torque	89
6.6	Models Selection of the Differential Machine	90
6.6.1	Winding Distribution of the Differential Machine.....	94
6.7	Integrated Differential Machine Modelling Methodology	95
6.7.1	FEM Simulation of the Back-Electromagnetic Force	98
6.7.2	Integrated DM Simulation of the Flux Distribution	101
6.7.3	Generating Mode Simulation of the Differential Machine	102
6.7.3.1	The Slip Speed Simulation at no-Load Condition	103
6.7.3.2	The Slip Speed Simulation at Load Condition.....	103
6.7.3.3	Slip Speed Simulation with of an External Resistance Connected	105
6.7.3.4	Generating Mode with outer rotor free running.....	106
6.8	VFRT Modelling Set-Up.....	109
6.8.1	Winding Distribution of the VFRT Machine	110
6.8.1.1	The Flux Distribution Analysis in the VFRT.....	111
6.9	Summary	113

7	Mathematical Modeling of the EMTC System	114
7.1	Introduction	114
7.1.1	Modelling Assumptions	114
7.1.2	Modelling of the Differential Machine	114
7.1.2.1	The Outer Part of the DM (BLDCM) Modelling.....	115
7.1.2.2	The Inner Part of the DM (Double Rotor Machine) Modelling.....	115
7.1.2.3	The Complete Differential Machine Modelling.....	116
7.1.3	Modelling of the VFRT	118
7.2	Determination of the EMTC System Parameters	119
7.2.1	Back-EMF Constant of the Differential Machine	119
7.2.2	Electromagnetic Torque of the Differential Machine	120
7.2.3	Self and Mutual Inductances of the Differential Machine Windings.....	121
7.2.4	Phase Resistance of the Differential Machine Windings	122
7.3	MATLAB Simulation	123
7.3.1	Simulation results	124
7.4	Summary	126
8	Construction of the EMTC System and the Experimental Set-Up	127
8.1	Introduction	127
8.1.1	The EMTC System Main Components	127
8.1.1.1	Twin stators	129
8.1.1.2	Differential Machine Inner rotor.....	129
8.1.1.3	Permanent Magnet Outer Rotor.....	131
8.1.1.4	Slip-Rings and Brush Holders	132
8.1.1.5	Optical Sensors	133
8.1.1.6	Rotor of the VFRT.....	133
8.1.1.7	Power Electronic Converter.....	134
8.2	Experimental Set-Up	139
8.2.1	BLDC Machine Preparation	148
9	Experimental Results and Validation.....	155
9.1	Introduction	155
9.2	Differential Machine (DM) Testing	156
9.2.1	The BLDCM, No-load Test with the Inner Rotor Free Running	156
9.2.2	The BLDCM, Load Test with the Inner Rotor Free Running	158
9.2.3	The PMIM, Test with the Outer Rotor Locked.....	160
9.2.4	PMIM Test with the Outer Rotor Free Running	161
9.2.5	PMIM Test with Locked Inner rotor.....	166

9.2.5.1	Discussion of the PMIM (Generating Mode) Test.....	169
9.2.6	Complete Differential Machine Test on no Load Condition.....	170
9.2.6.1	Discussion on the Complete DM Test	172
9.3	VFRT Testing.....	173
9.3.1	Rotor Windings Fed by an External Power Supply and Non-Rotating.....	173
9.3.2	Saturation Test	176
9.3.3	VFRT Rotor and DM Inner Rotor Connection	178
9.3.4	VFRT Testing with the Outer Rotor Locked	184
9.3.4.1	Discussion of the VFRT Testing.....	186
9.4	Complete EMTC System Testing	186
9.4.1	Open Machine Loop Test.....	186
9.4.2	Closed Machine Loop	190
9.4.2.1	Boundary Condition for Torque Amplification	190
9.4.3	Torque Amplification.....	193
9.5	Summary	194
10	Conclusion and future work.....	195
10.1	A Summary of the Key Research Output in the Modelling, Design and Operation of the EMTC System.....	196
10.2	Experimental Validation of the FEM Modelling	197
10.2.1	The BLDCM and PMIM Characterisation Test	197
10.2.2	The VFRT Machine Test	198
10.2.3	Open Machine Loop Test.....	198
10.2.4	Closed Machine Loop Test	198
10.3	Future work	199
	References.....	200
	APPENDICES	207
	Appendix A.....	207
	A1. Differential Machine Design.....	207
	A.1.1 Design of the BLDCM.....	207
	A.1.2 Design of the PMIM.....	210
	A2. MATLAB Simulink	211
	Appendix B	217
	B1. MagNet Software Package	217
	B2. MotorSolve software package details.....	220

Appendix C	221
C1: The FEM simulation results of the cogging torque	221
C2: The air gap flux at the inner and outer parts of the differential	227
C3: Closed Differential Machine Loop Simulation	228
C4: The data sheet parameters of the used devices in the EMTC system measurements	232
Appendix D	237
D1: Stator Windings Fed by an External Power Supply	237
Appendix E	240
Appendix F.....	244
F1: Faults on the system during the research	244
F1.1: The Inner Rotor Fault	244

LIST OF SYMBOLS

A_s	Slot area (mm ²)
B_g	Air gap flux density (T)
B_m	Maximum value of air gap flux (T)
B_{scm}	Maximum stator core flux density (T)
B_{stm}	Maximum stator tooth flux density (T)
b_{r1}	Lower inner rotor slot width (mm)
b_{r2}	Upper inner rotor slot width (mm)
b_{s1}	Lower stator slot width (mm)
b_{s2}	Upper stator slot width (mm)
D	Outer rotor diameter (mm)
D_{is}	Inner stator diameter (mm)
D_o	Stator lamination stack outside diameter (mm)
D_{os}	Outer stator diameter (mm)
D_r	Inner rotor Outer diameter (mm)
D_{ri}	Inner rotor diameter (mm)
d_{c1}	Shank length (mm)
d_r	Inner rotor slot depth (mm)
E_{on}	Energy losses at on state (Joule)
E_{off}	Energy losses at off state (Joule)
f	Frequency (Hz)
h_{ry}	Inner rotor Back iron depth (mm)
h_s	Core thickness (mm)
h_{sy}	Back iron depth (mm)
k_{ds}	Distribution factor
k_{ps}	Pitch factor
I_L	Line current (A)
L_{ls}	Stator leakage inductance (H)
L_m	Mutual inductance between the inner rotor and the stator windings (H)
L_{ms}	Stator inductance varying with rotation (H)
L_o	Static inductance (H)
l_{mo}	Outer magnet thickness (mm)
l_s	Stack length (mm)
M_{ai}	Inner rotor magnet thickness (mm)
N_m	Number of poles
N_{ph}	Number of phases
N	Number of turns per coil
P_{in}	Input power (W)
P_{out}	Output power (W)
P_{cond}	Conduction losses (W)
P_T	Total power losses (W)
Q_s	Number of slots
q	Slots per pole per phase
R_r	Rotor resistance (ohm)
R_s	Stator resistance (ohm)

s_o	Tooth gap width (mm)
SF	Stacking factor
T_{in}	Input shaft torque (Nm)
T_{out}	Output shaft torque (Nm)
T_{tdr}	Inner rotor tooth tang depth (mm)
T_{tds}	Stator tooth tang depth (mm)
T_{wr}	Inner rotor tooth width (mm)
T_{ws}	Stator tooth width (mm)
V_{ph}	Phase voltage (V)
W'	Co-energy (Joule)

Greek Symbols

α	Angle of short pole pitch (deg.)
γ	Angle of slot pitch (deg.)
δ_i	Inner air gap length (mm)
δ_o	Air gap length (mm)
λ_{so}	Stator slot pitch length (mm)
λ_{si}	Inner rotor slot pitch length (mm)
ρ_s	Angle of short pitch (deg.)
ω_{in}	Inner rotor angular speed (rpm)
ω_{out}	Outer rotor angular speed (rpm)
ω_r	Angular speed of the inner rotor (rpm)
ϕ_g	Air gap flux (Wb)
\mathcal{R}	Air gap reluctance (ampere per weber)
η	Efficiency
μ_o	Permeability of space
μ_r	Relative permeability of the lamination material
ω	Angular speed of the outer rotor (rpm)
Ψ	Flux linkage (weber-turn)
θ	Rotor angular position (degrees)

LIST OF ABBREVIATIONS

<i>AC</i>	Alternating current
<i>BLAC</i>	Brushless Alternating Current
<i>BLDC</i>	Brushless Direct Current
<i>CT</i>	Cogging torque
<i>DC</i>	Direct current
<i>EMTC</i>	Electromagnetic torque converter
<i>FEM</i>	Finite Element Modelling
<i>IGBT</i>	Insulated Gate Bipolar Transistor
<i>PWM</i>	Pulse Width Modulation
<i>RMS</i>	Root-mean- square
<i>TC</i>	Torque converter
<i>VFRT</i>	Variable frequency rotary transformer
V_{L-L}	Line-to-line voltage

1 INTRODUCTION

1.1 Introduction

Since the focus of this thesis is on the modelling and design of an Electromagnetic Torque Converter (EMTC) system, this chapter will give an overview on two types of automotive transmission systems: manual and automatic transmission systems. The torque converter is part of the automatic transmission system, as will be explained in detail in chapter two.

The development of a Torque Converter requires some knowledge of vehicle transmission systems. The most popular systems are manual and automatic transmission systems.

1.1.1 The Manual Transmission System

Figure 1.1 shows a typical manual transmission system. As the name suggests, the driver has to change manually between one gear ratio and another, as the vehicle requires, when using this type of transmission system. There are many advantages to the manual transmission system. For example, it is relatively cheap to produce and it has a lighter weight in comparison to the automatic transmission system. Additionally, it is simpler from a mechanical point of view, which makes it easier to repair [1]. Besides these advantages, there are some disadvantages, such as using the clutch for changing gears, which can be tiring, especially in heavy traffic.

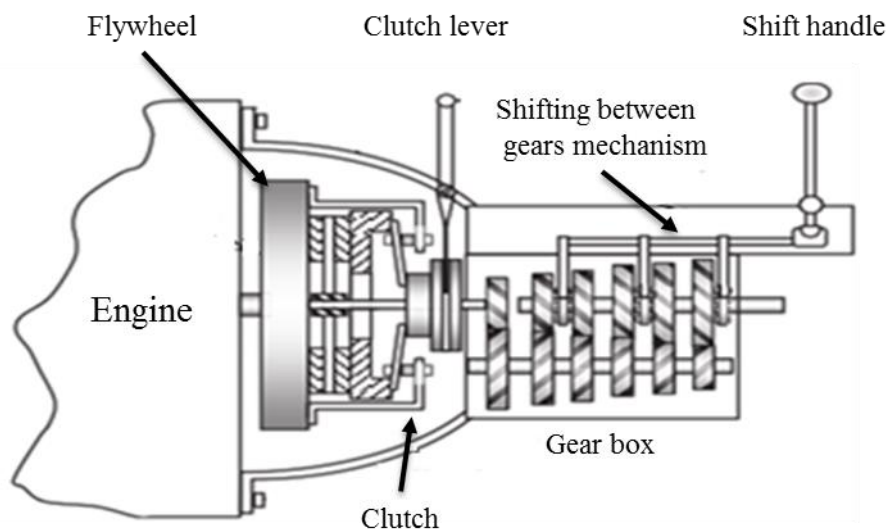


Figure 1.1: Manual transmission system [1]

1.1.2 The Automatic Transmission System

Using this type of transmission system allows the vehicle to alter the gear ratio automatically as the vehicle moves. The main difference between a manual and an automatic transmission system is that the latter utilises a fluid torque converter, whereas a clutch is used in the manual transmission system. Figure 1.2 shows an example of the automatic transmission system employing a conventional torque converter [2]. The main benefit in terms of ease of operation in an automated system is that it makes a better selection of gear ratios compared to the manual type, and this will offer more convenience to the driver, and higher reliability. The main components of the automatic transmission system are the gearbox and the torque converter.

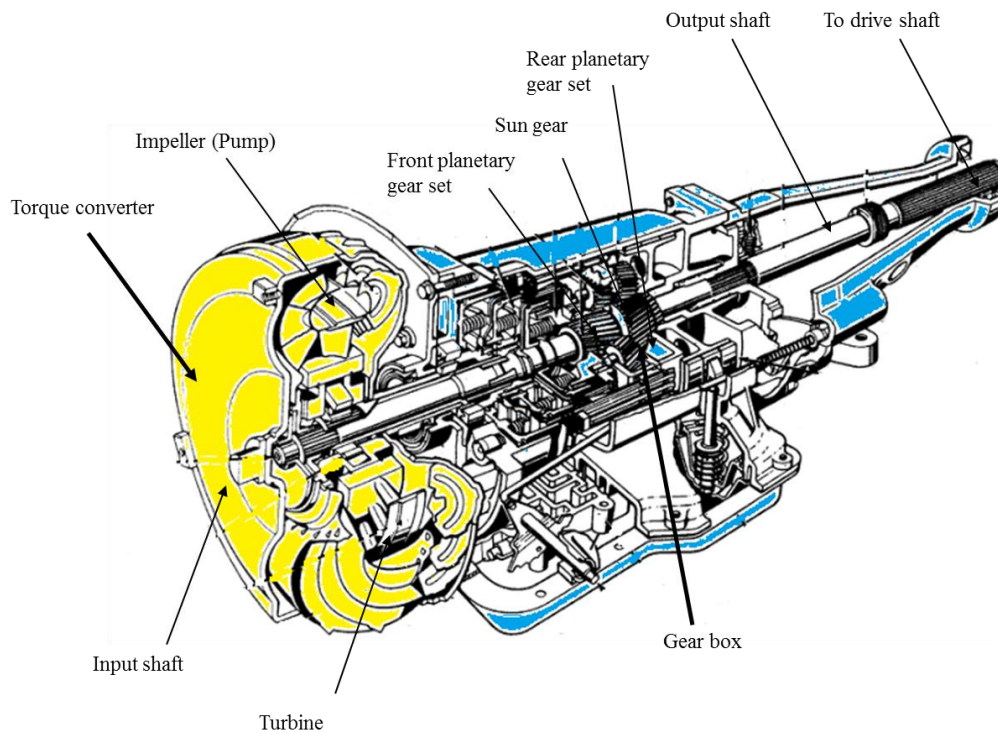


Figure 1.2: Example of an automatic transmission [2]

1.2 State-of-the art

The hydraulic torque converter has been utilised as a coupling component between the engine and the gearbox in automatic transmission systems since 1940 [3]. Although the automatic transmission systems have continuously improved, the torque converter design has not been considerably changed until 1970 when the lock up clutch was introduced. In order to minimize the disadvantages of the lock up clutch and to improve the torque converter performance, the Luk-Torn Con system was introduced in 1994.

Then in 1997 the Luk-Tore Con type has been produced for Allison's World Transmission Series [4]. Since that time, the hydraulic torque converter system has not been replaced by another system. However, there are several attempts to introduce alternative systems such as the magnetic torque converter, the electromechanical torque converter, the electrical torque converter and the electromagnetic torque converter. However, these designs have not been applied because they need an external power source to excite their windings. These techniques are explained in the next chapter.

1.3 Motivations and Research Objectives

Hydraulic torque converters are extensively used in automatic transmission systems. However, the use of a fluid as a medium to convert the input torque to output torque needs to be improved. The improvement of the hydraulic torque converters may include the design. This is because the hydraulic torque converters depend on the oil viscosity and the fluid flow, which make it an unreliable system. Additionally, they run at low efficiency both at stalled output speed and when both the input and output speeds are equal [5].

A novel technique is introduced in this research that replaces the hydraulic torque converter by an electromagnetic torque converter that retains the function of the conventional torque converter at the stalling, acceleration and high-speed condition of automobiles.

The aim of this research was to develop a novel Electromagnetic Torque Converter (EMTC) system, which can be used in the automatic transmission systems. The novel EMTC does not only employ the inherent advantages of Permanent Magnet Machines (PMMs) but also utilises the advantages of slip energy recovery to increase the output torque compared with the input torque. Therefore, the objectives of the research are:

- 1) To Design and Analyse the Novel EMTC System.*

The new EMTC system comprises of two parts, the differential machine (DM) and the variable frequency rotary transformer (VFRT).

The design of the DM is based on three designing criteria (1) the minimum cogging torque (2) the minimum ripple torque, and (3) a high electromagnetic torque. These

design criteria are satisfied by selecting the winding type, the magnet pole arc-length, the stator slot configuration, and the pole slot combination.

The design of the VFRT is based on its function to extract the slip power from the inner rotor of the DM and to re-inject this power back to the stator of the DM. Therefore, the rotor windings were selected for this function. In order to ease dismantling the rotors of both the DM and VFRT, the stator of the VFRT design should be identical to the stator of the DM.

2) To Design the Power Electronics (Power Converter) Circuit.

In order to achieve a self-excited model, the power converter circuit in the new EMTC system is designed. The slip power extracted from the DM rotors has a different frequency with the stator of the DM. Therefore, DC link converter is used with the input frequency being the frequency of the slip speed and the output frequency is synchronously locked to the frequency of the output shaft. The design of the DC-link power converter circuit includes the selection of the three-phase unidirectional full wave rectification circuit, the snubber capacitor and the three-phase, six semiconductor switches along with its control circuit. Once the power converter circuit is provided, the slip voltage from the inner rotor of DM can be stepped up with the aid of the VFRT and re-injected back to the DM stator.

3) To Model the Novel EMTC System Using Finite Element Modelling (FEM).

FEM is used to speed up the design process and predict the performance of the EMTC system. This includes selecting the pole-slot combination, the winding type and the slotted elements such as the stators and the rotors slot configuration. This can be achieved by investigating the cogging torque, the electromagnetic torque, and the flux distribution. These investigations were carried out for both, the DM and VFRT using FEM to model each part separately.

4) To Develop a Mathematical Model of the Novel EMTC System.

The purpose of the mathematical model of the EMTC system was to develop a suitable control system. After the novel EMTC system was mathematically modelled, then the

Matlab/ Simulink simulation can be carried out to predict the system performance. The Matlab simulation parameters were defined by the FEM modelling.

5) To Implement the New EMTC Prototype System.

The prototype EMTC system design is to be fabricated and assembled to perform the required verification experiments. The measurement results are compared then with the FEM and Matlab/Simulink simulations.

1.4 Contributions to the Field

The key concept in the development of the EMTC system is to utilise the slip energy when there is speed difference between the inner and outer rotors. The speed differences increase once the output load is increased. Thus, the main contributions that have been made to the subject of the torque converter of road vehicles include:

1- Innovative Design of the Electromagnetic Torque Converter (EMTC) system.

The design of the EMTC system was successfully achieved and optimised by using the following: (1) the concentrated, fractional slot winding. With this type of winding, the cogging torque is minimized, reducing the copper losses and hence increasing the efficiency of the system. (2) The slot configuration was optimized using the aid of FEM modelling. (3) Iterative and analytical methods were used to investigate the sixty-eight pole slot combinations in order to select the optimal model. The optimal pole-slot combination has a minimum cogging torque; a high electromagnetic torque and a low ripple torque.

2- Effective Elimination of the Slip Rings for Extracting the Slip Power.

The second contribution to the field was to eliminate the slip rings; the slip rings make the system less reliable, *i.e.* frequent maintenance of the carbon brushes. In addition, the carbon brushes may produce a flammable material, which makes the system classified as a hazard area. Solving these drawbacks of not using slip rings in the EMTC system makes it more applicable for use in automobiles.

3- Conceptual Development a Variable Frequency Rotary Transformer.

The use of the variable frequency rotary transformer (VFRT) is to step up the slip voltage and to eliminate the slip rings. The three-phase windings of its rotor can be connected in either star or delta. The different connection can be wired in the rotating terminal strip mounted on the input shaft.

4- Development of an Efficient Cascaded Connection between the two Wound Rotors.

The two cascaded rotors contribute an external resistance needed to develop a starting torque. These rotor windings can be disconnected, which allows each machine to run separately in case of maintenance.

5- Design of a Novel Torque Converter System for Several Applications.

The new torque converter not only converts low torque to a high torque but it can also work in an opposite way. This can be achieved by supplying power to the outer rotor side and tracking it from the inner rotor side. This feature will add another application to the EMTC system.

1.5 Thesis Overview

This section presents a brief summary of the overall methodology that was followed during this research. The methods and tools used in this research focus on producing an optimal design of the new EMTC system by satisfying three design criteria including a minimum cogging torque, a high electromagnetic torque and a low ripple torque.

The research was accomplished using the following methods and tools:

- **The Methods**

- (a) An iterative method: This method was used to select the optimal configuration of the DM. 68 pole-slot combinations were investigated to select the optimum pole-slot configuration for each machine of the DM.
- (b) An optimal arc length method: This method was used to validate the iteration method. Several magnet arc lengths, starting from the full arc length, can contribute to produce a minimum cogging torque in the PM machines. The first

two iterations of the arc lengths were used to satisfy the second design criteria, the high electromagnetic torque.

- **The Tools**

- (a) The Finite Element Method (FEM): Two packages of the FEM were used, the MotorSolve and the MagNet (Infolytica, Canada). The MotorSolve software was used to select the optimum configuration out of the 68 pole-slot configurations of the PM machines based on the predicted cogging torque, the electromagnetic torque and the ripple torque. The MagNet software was then used to model the selected pole-slot combinations of the DM, the VFRT and the complete EMTC system at both the open loop and the closed loop conditions.
- (b) The Matlab/Simulink platform: The Matlab/Simulink, SimPowerSystems toolbox was used to model the new EMTC system mathematically. The direct-quadrature-zero (dq0) representation was applied to model the EMTC system. The simulation was carried out using the machine parameters obtained by the FEM simulation.
- (c) The physical implementation of the new EMTC system: Experimental results were obtained using the physical implementation of the EMTC system. Several experiments were conducted to validate the EMTC system operation.

- **Research Process**

A brief overview of the research process is summarised as follows:

The comprehensive literature review was conducted at the beginning of this research to define the research aim and objectives. A primary design of the EMTC system was established. This design was then optimised based on the simulation results of the FEM modelling of the EMTC system. The optimisation including the selection of an optimum pole-slot configuration which was investigated utilising a range of poles, 8, 10 and 12 with the relevant number of slots, 9, 12, 15, 18, 24, 27, and 33 as indicated in table 1.1. This resulted in 17 pole-slot combinations. Because there are two machines of the DM, the number of pole-slot combinations were 34. These pole-slot combinations were for a fully pitched (FP) magnet. In addition to these investigations, the Gape Magnet (GM) were modelled as well. The gap between the magnets was selected based on the FEM results of the pole-slot combinations which

have the minimum cogging torque in the FP models. The FEM results showed that the optimum gap was $1/3$ of the FP magnet. Therefore, another 34 pole-slot combinations were investigated at GM models. The mathematical modelling of the EMTC system was then carried out and followed by the establishment of the physical implementation and the experimental evaluation of the EMTC system. Several tests were conducted to validate the operation of the EMTC system.

Poles	No. of Slots							
	9	12	18	21	24	27	30	33
8								
10								
12								

Table 1.1: Pole- slot combinations

1.6 Thesis Outline

The novel EMTC system has many features such as a high electromagnetic torque density, low ripple torque with minimum cogging torque. There are ten chapters in this thesis, dedicated to the design aspects and features of the EMTC system.

Chapter 1 describes the background of automotive transmission systems, the state of the art. In addition, the main objectives and contributions of the research subject are presented.

Different techniques for the torque converter have been adopted in order to upgrade the hydraulic torque converter, as described in chapter 2 with their advantages and drawbacks. In addition, the background of the conventional permanent magnet machines along with their mathematical modelling are also presented.

Chapter 3 describes the research methodology. There are several stages explaining very clearly how the findings were achieved and analysed.

In chapter 4, the novel EMTC system concept, its principle of operation and the possible operating ranges of the system are presented.

In chapter 5, the design procedure for the EMTC system is described. It is based on three design criteria, the minimum cogging torque, the high electromagnetic torque and the low ripple torque. Therefore, an optimization procedure is introduced.

In chapter 6, there are sixty-eight pole-slot combinations, which were investigated using FEM for achieving a low of cogging torque. Then the results obtained were further investigated for other design criteria. The FEM simulations allow the selection of the optimum pole-slot combinations. Indeed, the complete EMTC system in both the open and closed loop conditions was simulated with the FEM.

In chapter 7, the development of the mathematical modelling of the proposed EMTC system is presented. The mathematical modelling is achieved based on the conventional PM machines modelling such as permanent magnet synchronous machine and the permanent magnet induction machine.

Chapter 8 presents the verification, the validity and shows the merits of the new torque converter technique. The construction of the prototype EMTC system is described.

Moreover, FEM and Matlab/Simulink simulations are compared with the practical experimental results in chapter 9.

Finally, conclusions from this thesis are made in Chapter 10, and future work is also included.

2 Background and Literature Review

2.1 The Hydraulic Torque Converter

Many decades ago, the Torque Converter (TC) was invented as a solution to the clutch problem with the automatic transmission system. The TC is a key component that links the engine and the gearbox in an automatic transmission system. It has two main functions. Firstly, the torque converter, as the name denotes, transfers multiplied engine torque to the gearbox [6, 7]. The second function of the torque converter is to improve the vehicle's performance, rather than using the clutch to disconnect the engine from the gearbox. The improvement of vehicle performance in the US was obtained from 1940. In contrast, Engines in European manufactured cars are smaller, so transmission losses in automatic cars are higher than in manual gearbox models. Recently, the torque converter features a lock-up facility in top gear, whereby it drives directly, with no slip losses. This feature made the torque converter more efficient even in small cars [8]. However, the currently available torque converter has a number of drawbacks such as it needs oil to drive the impeller, the gearbox, and the hydraulic pump. In addition, the mechanical parts in the hydraulic torque converter being subject to faults due to direct contact with each other at the coupling stage. The most common causes of torque converter failures are due to excessive heat. This can happen after a long period of time by slipping, since it would not be able to dissipate the heat fast enough. Moreover, it is subject to energy loss, especially at low speed, as it is not highly efficient in the use of its turbine.

In 1994, Luk-Tor Con invented the first reported TC with a lock-up feature for an automatic transmission system, as shown in figure 2.1 [4]. The Luk-Tor Con system still utilises the advantages of the torque converter but minimises the disadvantages by using a speedy lock up clutch. The hydraulic torque converter has three modes of operation, namely stall, acceleration, and coupling. These three modes are explained below.

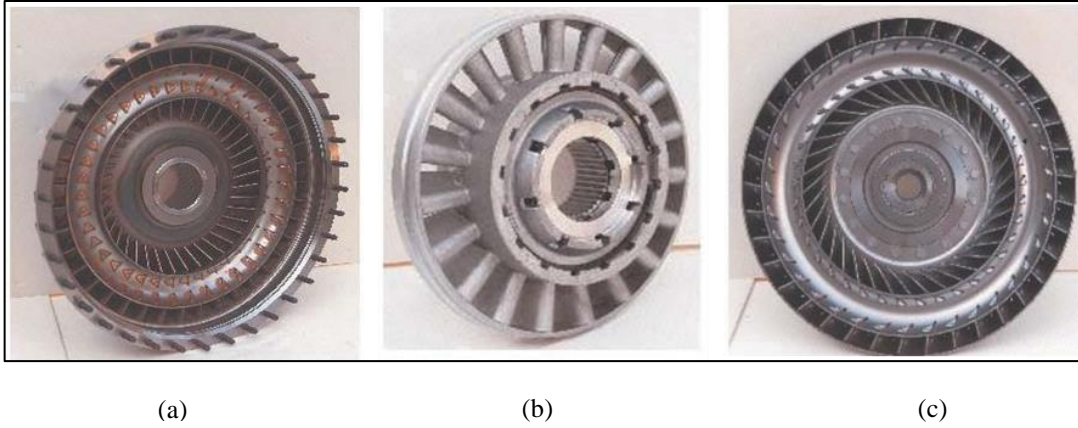


Figure 2.1: Hydraulic torque converter components: a) Pump, b) Stator and c) Turbine [4]

In the first mode, stall, the prime mover is providing power to the impeller, while the turbine cannot rotate because of the vehicle's brakes. In this mode, the torque converter produces maximum torque multiplication. However, this state may cause damage to the torque converter if it is in a stall condition for a long time. This is due to the huge difference between the pump and the turbine speeds. The second mode is acceleration, where the transmission is accelerating gradually. In this mode, the TC produces less torque multiplication than in the stall mode. The third mode is coupling and in this mode the turbine can reach nearly 90% of the impeller speed [9]. In this case, the torque converter is behaving as a simple fluid coupling and the TC efficiency is better than modes one and two.

The hydraulic torque converter was improved by Kawashima [10] by using a magnetic viscous fluid as a circulating working fluid between the pump and the turbine. The magnetic circuit is created by providing a coil connected to the oil in the turbine. The advantage of the magnetic viscous medium is to help the lock up feature of the torque converter to eliminate the slip between the pump and the turbine.

2.1.1 The Torque Converter Model

The turbine torque (T_T) to the impeller torque (T_I) is defined as the torque ratio (T_R). Similarly, the ratio of turbine speed (ω_T) to the impeller speed (ω_I) is defined as the speed ratio (ω_R). These two ratios are separate, as defined in [1, 7].

$$T_R = \frac{T_T}{T_I} \quad (2.1)$$

$$\omega_R = \frac{\omega_T}{\omega_I} \quad (2.2)$$

Where

$$T_T = \rho Q (\omega_t r_{tx}^2 - \omega_p r_{px}^2) \quad (2.3)$$

$$T_P = \rho Q (\omega_p r_{px}^2 - \omega_t r_{tx}^2) \quad (2.4)$$

Where,

ρ : Transmission fluid density

Q: Volume flow rate through the converter

ω_p, ω_t : Pump and turbine angular speed

r_{px}, r_{tx} : Radius from the centre axis to pump and turbine, respectively

ω_p : Pump input speed

ω_t : Turbine input speed

2.1.2 The Gearbox Model

The main function of the gearbox is to change the input speed into a different output speed. The change of gear enables the smooth motion transmission of two shafts at a fixed ratio. The gearbox therefore is used to vary the speed of the vehicle. Figure 2.2 illustrates the typical planetary gear set that is used for an automatic transmission system. The main function of the planetary or epicyclic gear set is its responsibility for gear ratios. It consists of three main components, namely sun gear (S), ring gear (R) and planet gear (P). The three components are rotated on a common planet carrier (C) [1].

The sun gear and the planets have external teeth, while the ring gear has internal teeth. The rotation speed of the sun, ring and carrier are denoted as ω_S, ω_R and ω_C which are related to the planet gear speed.

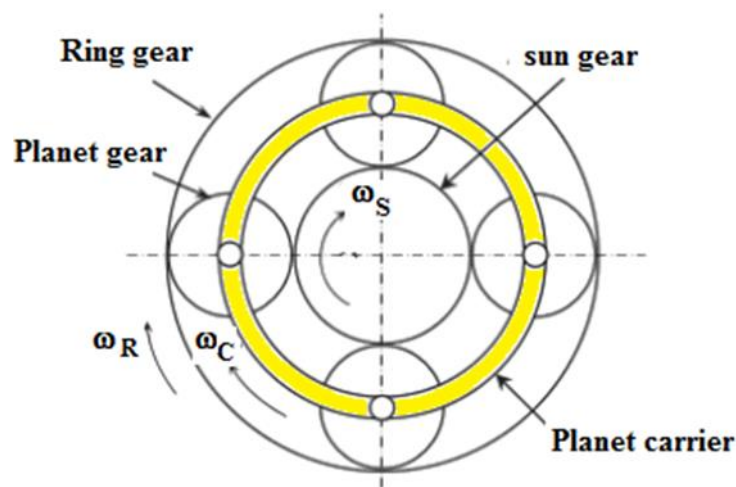


Figure 2.2: A typical schematic diagram of the planetary gear [1]

The transmission gearbox is modelled as a simple input-output torque with variable gear ratios G_r accompanied by the efficiency η of each gear [9]. The input torque T_{in} , and the output torque T_{out} to the wheels is determined by the torque ratio. Moreover, the gear ratios are altered based on the vehicle's velocity and the engine's rotational speed. The variables ω_{in} and ω_{out} represent the input and output angular speed, respectively.

$$\frac{T_{out}}{\omega_{in}} = \frac{T_{in}}{\omega_{out}} \quad (2.5)$$

$$T_{out}(t) = T_{in}(t) \cdot G_r \cdot \eta \quad (2.6)$$

$$\omega_{out}(t) = \omega_{in}(t) \cdot G_r \quad (2.7)$$

T_{in} represents the output torque from the pump of the TC. Similarly, the input speed ω_{in} is the same as the torque converter output shaft speed.

There is a clear difference between a torque converter and a gearbox, even though both convert power between torque and speed. The latter has a fixed gearing and there is an inversely proportional relationship between the torque and the speed, as stated in (2.5). On the other hand, the torque converter has a continuous variable speed and torque ratios. The output torque and speed do not have a direct or fixed inversely proportional relationship, as stated in (2.1 and 2.2). In addition, the torque converter was based on the mechanical properties of the fluid such as the fluid density and flow rate volume.

2.2 Development of the Torque Converter

The development of the hydraulic torque converter did not reach an optimum solution until 1940. Since that time, there have been many attempts to develop the performance of the torque converter to improve reliability and provide greater efficiency. The background of the torque converter currently available is given below.

2.2.1 The Magnetic Torque Converter

In 1978 Donald A. Kelly [12] presented his invention of the magnetic torque converter. The torque converter consists of two components; a non-magnetic flat large disk containing permanent magnets arranged in an array, and a small rotor containing permanent magnets as well. The two rotors are located at a perpendicular angle to each other as shown in figure 2.3. The main disadvantage of this invention is the use of a

large number of magnets, which leads to an increase in the cost of the machine. In addition, at high speed the repulsion and attraction of the magnets may lead to a decrease in the system's reliability. However, it can be argued that this technique represents a gearing rather than torque converter because both the input speed and torque to the output speed and torque have a linear relationship.

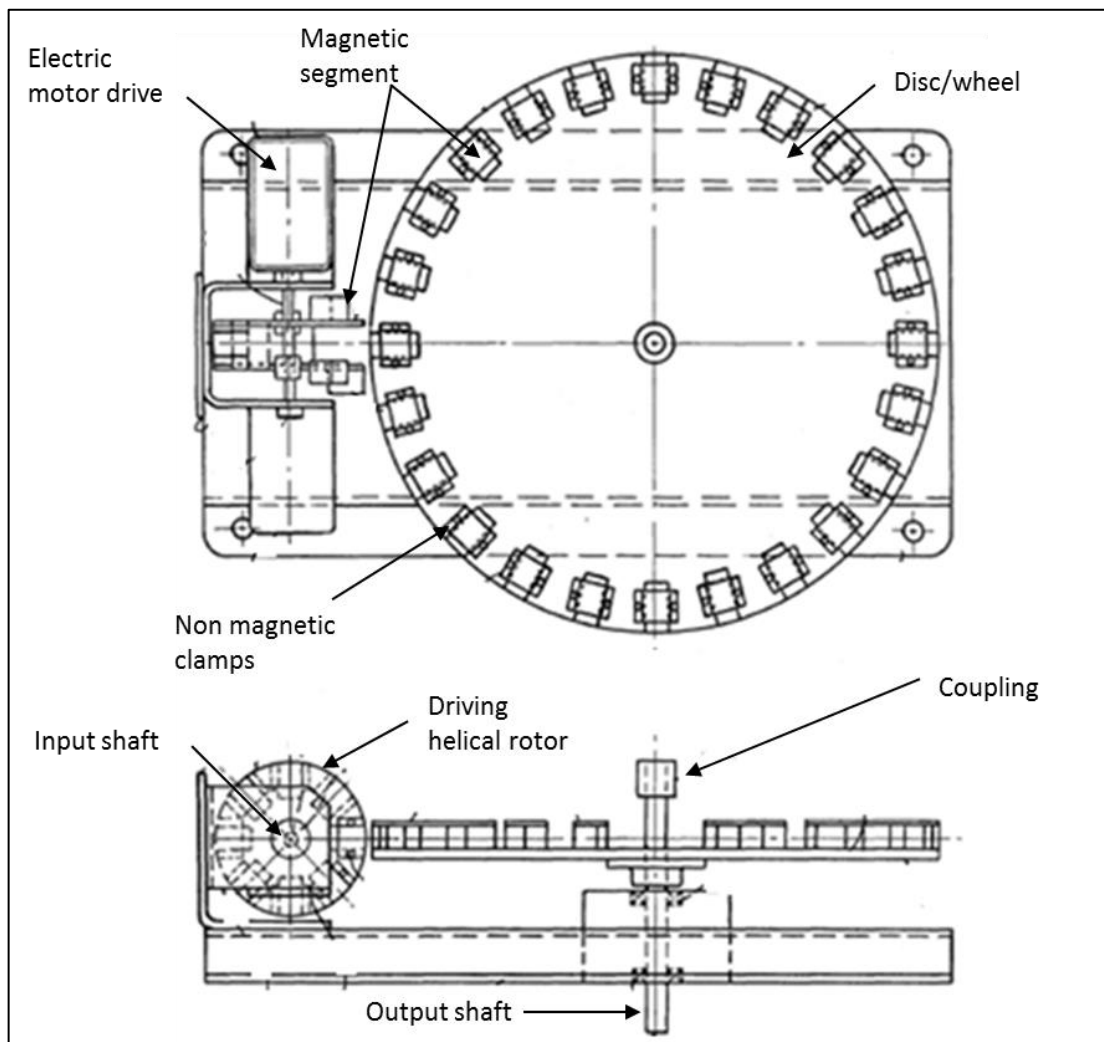


Figure 2.3: Magnetic torque converter [12]

2.2.2 The Electromechanical Torque Converter

In 1949, E. Charles and N. Mahwah [13] invented a torque converter machine to convert mechanical motion at a fixed speed into variable speed. They presented their invention by using the magnetic bars at the inner rotor and the stator with an interposed cylindrical driven member, as shown in figure 2.4. The outer rotor is a non-magnetic armature such as copper or aluminium. The stator is divided axially into two parts

separated by the field coil. The function of the field coil is to create a steady magnetic field through the stator and the inner rotor. The principle of operation of this type of torque converter can be summarised by the interaction of the magnetic forces at the inner rotor and the stator, which makes the outer rotor rotate. The speed of the outer rotor is dependent upon to the load torque. Hence, they proposed the idea of using an induction machine for torque conversion. The main drawback of the invention is the use of a squirrel cage type in the inner rotor that makes the use of slip energy recovery impossible. In addition, the use of field coils between the stator bars has another disadvantage; these coils need an external DC source to create the circulating magnetic flux.

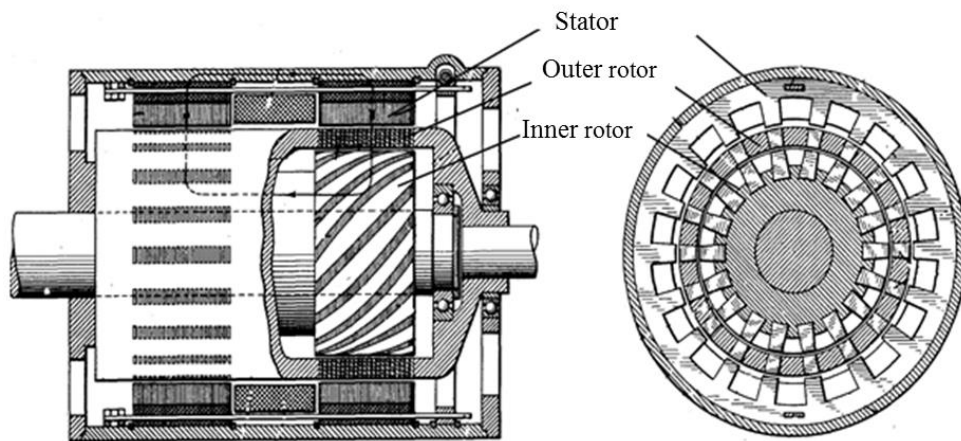


Figure 2.4:Electromechanical torque converter [13]

2.2.3 The Electrical Torque Converter

In 1953 and updated in 1957 Lev A. Trofimov [14, 15] invented an electrical torque converter that is similar to the electromechanical torque converter except the slip rings are added. A slip ring was used in this machine to energise the magnetic poles at the inner rotor with a direct current. Figure 2.5 shows the configuration of the electrical torque converter. It can be seen that the inner (primary) rotor has magnetic field poles that are connected mechanically to the engine. The outer (secondary) rotor is rotating as an induction motor with the slip speed between the rotating field and the outer rotor. The main drawbacks of this invention lie in the use of a conventional induction machine as a torque converter, as the power factor remains very low.

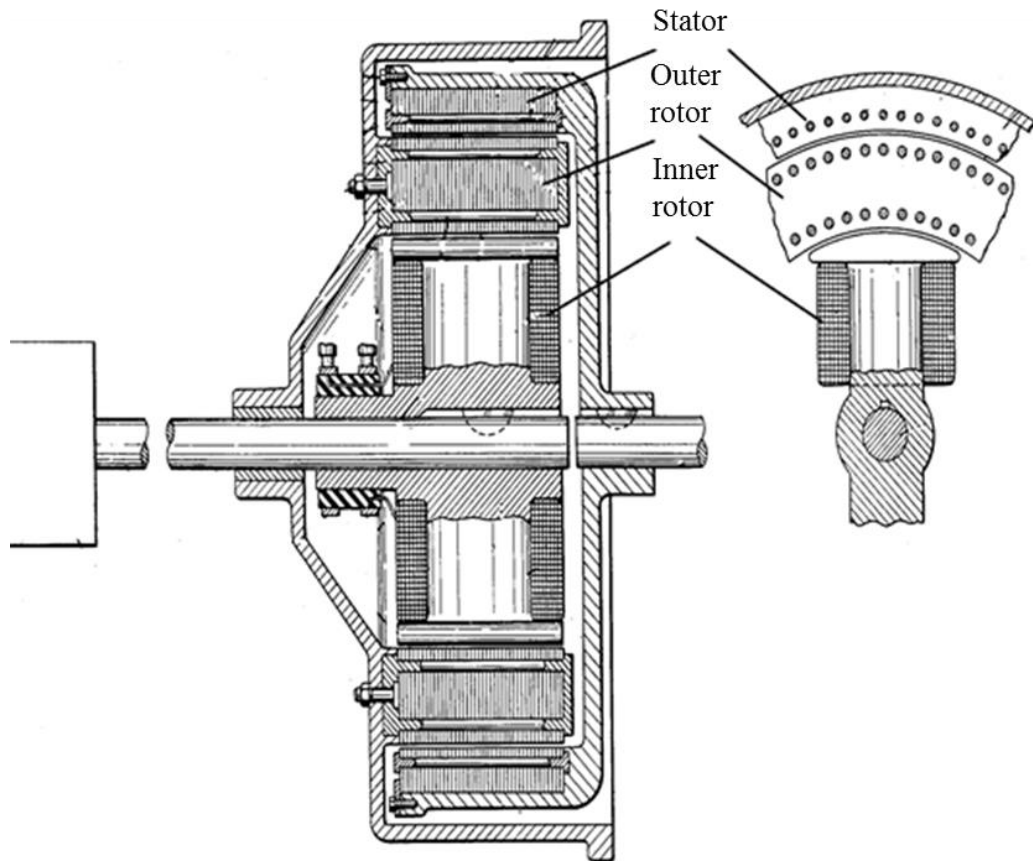


Figure 2.5: Electrical torque converter [15]

A different design of electrical torque converter used in an automatic transmission and especially for a hybrid vehicle, is described in the patent by Masato *et al.* patent [16]. Figure 2.6 shows a simplified skeleton diagram of the system. It can be seen from the figure 2.6 that it is a very complicated system. Furthermore, it is equipped with a motor/generator machine to circulate the oil between the impeller and the turbine. Using the electric machine in a closed frame, its maintenance becomes very difficult. Moreover, this machine will be exposed to a high temperature, leading to a reduction in its efficiency.

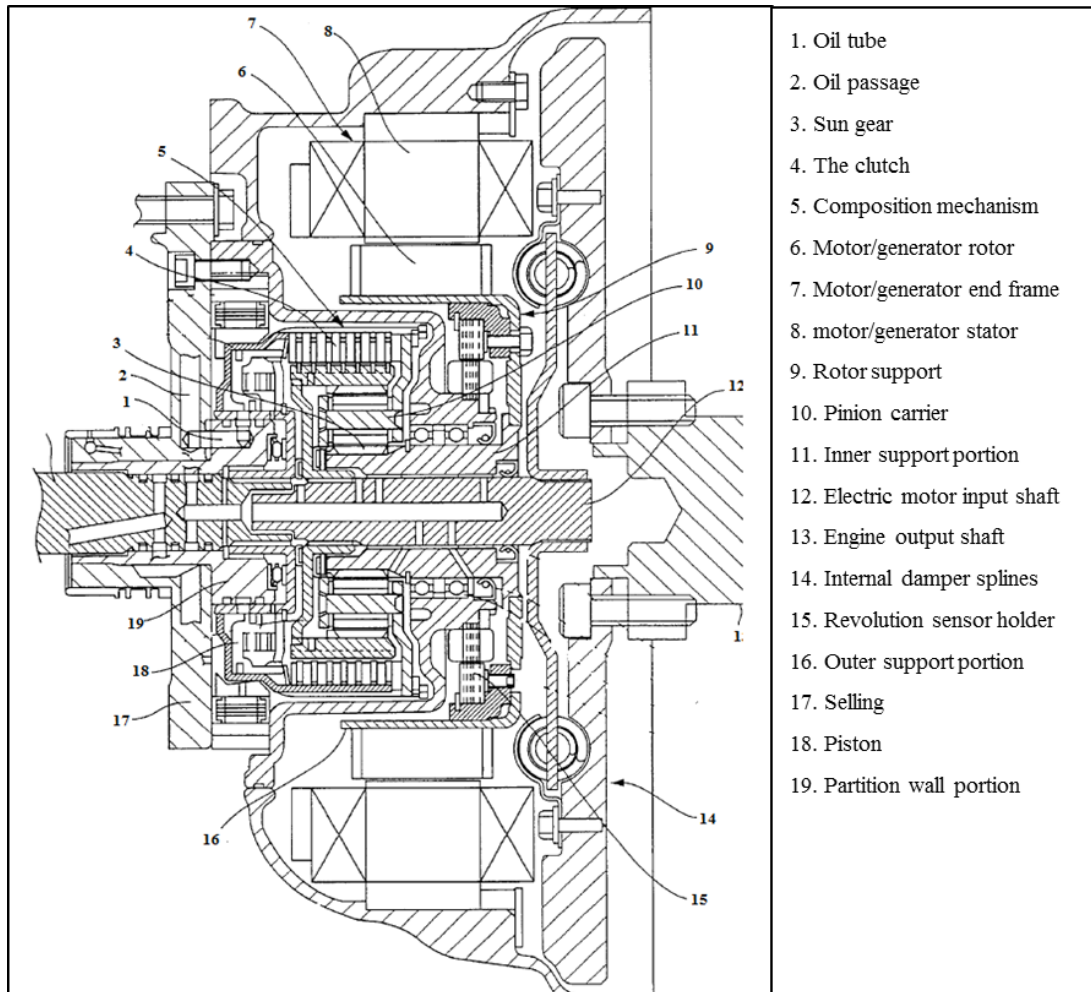


Figure 2.6: Electrical torque converter [16]

2.2.4 The Electromagnetic Torque Converter

In 1959 both D. Bishop and G. Brosan presented a patent described in [17], for an electromagnetic variable ratio torque converter. They used two high permeability-rotating cylinders and a stator with a very small gap between these rotors and the stator, as shown in Figure 2.7. Each cylinder was connected to a separate shaft, and they operate in a way similar to the squirrel-cage rotor induction machine. The machine housed double excitation coils for the purpose of establishing a magnetic flux.

The torque is converted from one cylinder to the other using an electromagnetic coupling. The disadvantage of this system was the use of mercury to help the flow of current through the air gap as the viscosity of the mercury increased mechanical losses.

The other disadvantage of the system was the use of an external power supply to energise the coils on the stator.

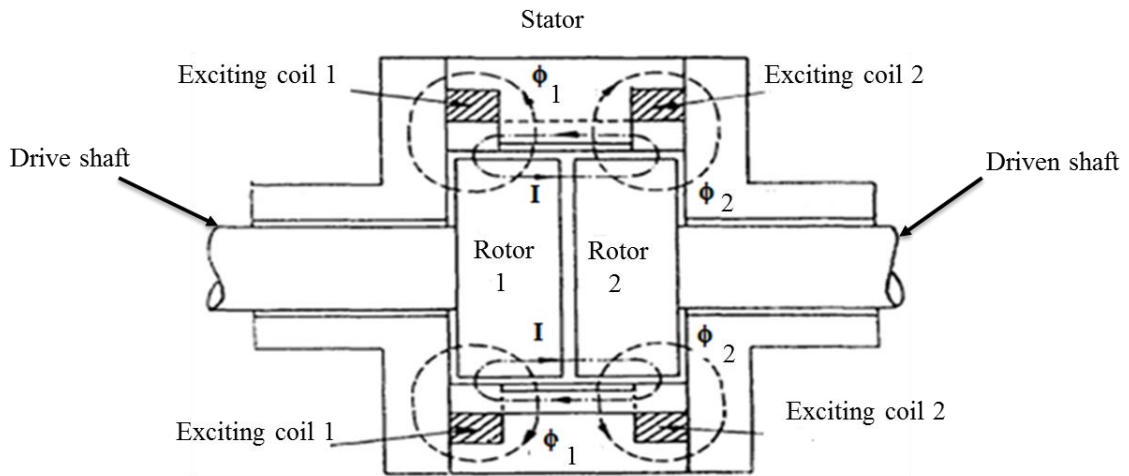


Figure 2.7: Axial rotors electromagnetic torque converter [17]

In 1987 Christopher D. Smith [18] invented an electromagnetic torque converter as shown in figure 2.8. However, the invention is similar to the Charles and Mahwah invention in that it has two air gaps (3) and (4). The main difference between these two designs was that in the latter, the load shaft (5) is connected to the wound inner rotor (7), and the wound outer rotor (8) is connected to an input drive, via drive shaft (1) and excited by the field coils (2), which were used instead of squirrel cage bars in the previous design. This change led it to the utilisation of the secondary armature current at low speed, to be supplied into the primary armature, while at high speed the primary armature acts as a generator and supplies direct current to the secondary armature. The output to input torque ratio is determined by the direction and magnitude of this current via the commutator (6). Adjusting the main and auxiliary windings resistance can be achieved. In addition, the controller (11) is located between the two sides of the brushes (10) to adjust the voltage between the input and the output rotational velocities. The main disadvantage of the design is the use of an external field current instead of permanent magnets. The external current source will increase the machine's cost and decrease its reliability and efficiency [19].

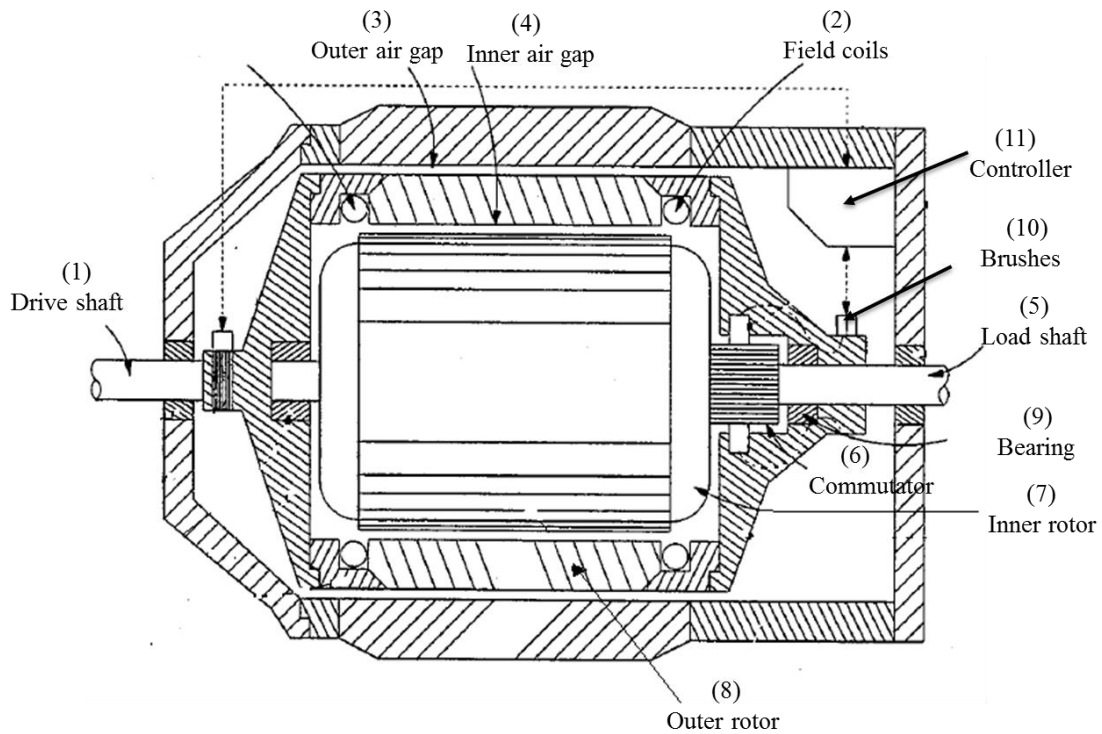


Figure 2.8: Wound rotors electromagnetic torque converter [18]

2.2.4.1 The Integrated Energy Transducer

The Integrated Energy Transducer (IET) system [20], can be considered a torque converter. It can be seen in figure 2.9 that the Internal Combustion Engine (ICE) is mechanically connected to the inner rotor of a double rotor machine (DRM) which is fed electrically from a power converter via slip rings, and the outer rotor has permanent magnets fixed to the inside surface. The machine is intermediate between the mechanical gearbox and the engine. This system has some disadvantages, one of them being that it is an unreliable system because an external power source is required to feed the three phase windings in the DRM to increase the outer rotor speed. Since the machine is a permanent magnet synchronous generator, the Back Electromotive Force (back EMF) is induced in the inner rotor windings and increases as the inner rotor speed increases. This will add another disadvantage to the system because the voltage supply (from a battery) needed to be higher than the induced back EMF in the inner rotor windings.

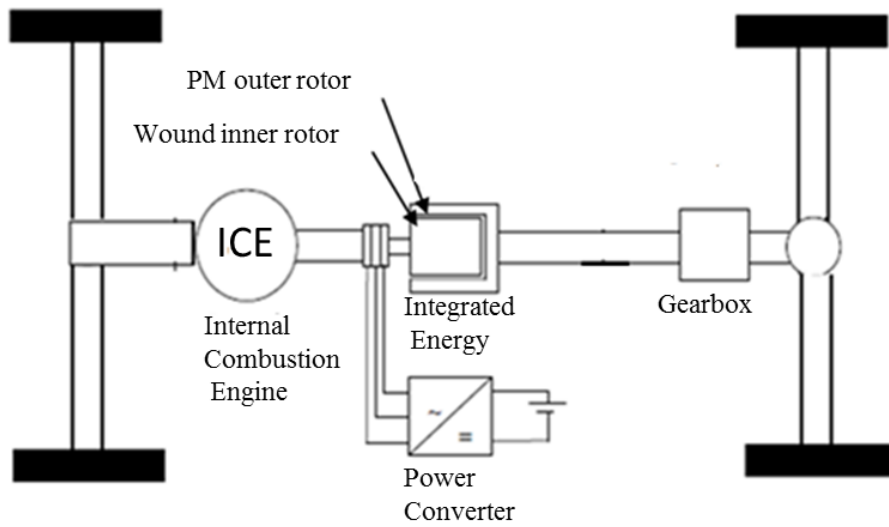


Figure 2.9: Integrated energy transducer system [20]

2.3 Double Rotor Machine Topologies

Since the electromagnetic torque converter is composed of two rotors, the double rotor machine is the most related topic. Various types of double rotor machines have been designed for many applications. These machines are operated as induction machines and permanent magnet machines.

In 1969, Kelly proposed an induction machine with a double rotor radial flux as shown in figure 2.10 [21]. The machine has an inner rotor with a cup outer rotor. The inner rotor carries current and it is magnetically coupled to both the outer rotor and the stator. Therefore, the inner rotor speed affects the machine's characteristics.

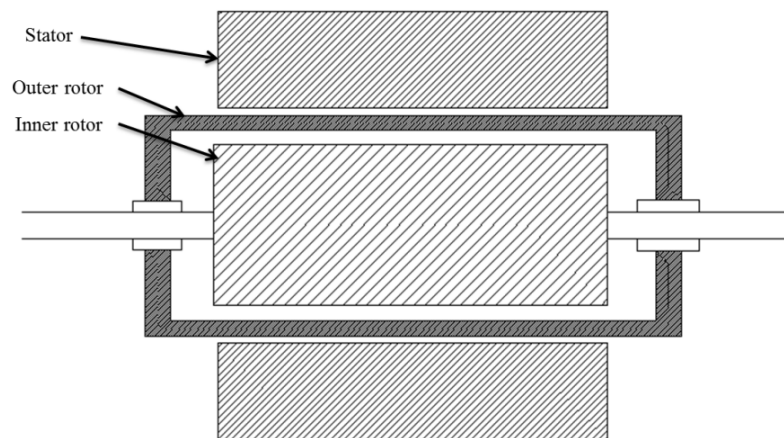


Figure 2.10: Double-rotor induction machine construction [21]

The double rotor machine shown in figure 2.10 is designed with low core losses in the inner rotor, and it can provide a high torque density [21]. The major disadvantages of this machine are using the squirrel cage rotors. With the squirrel cage inner and outer rotors, the slip power cannot be extracted and utilised.

A new topology of the double-rotor induction machine was introduced in 2004 by Zhang [22] as shown in figure 2.11. Different from the squirrel cage rotors mentioned above, the stator is slotted and placed in between the inner and outer rotors of this machine. The inner and outer surfaces of the stator are slotted as well. The principle of operation of this machine can be summarized as follows: When the windings in the stator are energized by three phase currents, the rotating magnet field is coupled with the flux in the inner and outer rotors. Hence, both rotors can produce electromagnetic torque and rotate. Although the machine has two rotors, the principle of operation is likely to be the same as the conventional induction machine. In addition, the slip speed between neither the stator and the inner rotor nor the outer rotor is utilised.

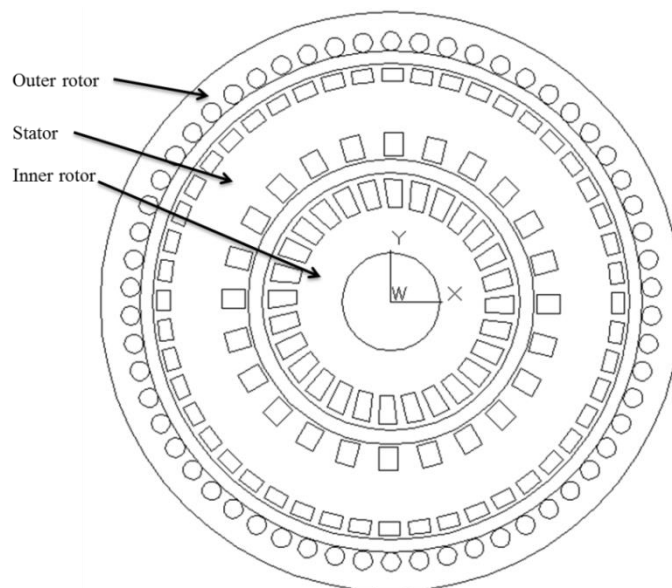


Figure 2.11: Schematic structure diagram of double rotor induction machine [22]

In 2006 [23], a double-rotor radial flux structure was improved by using distributed windings instead of concentrated windings in the stator. Moreover, in this machine, Permanent Magnets (PM) are used to get a higher torque density as shown in figure 2.12. The PMs are mounted on the surfaces of both rotors. The principle of operation of this machine is based on stator windings and the PM arrangements. Different speeds of

the inner and outer rotors can be achieved in this type of machine, since both rotors, having a permanent magnet structure, rotate at the synchronous speeds on each side of the stator. However, the slip power is impossible to be utilised with this type of machine.

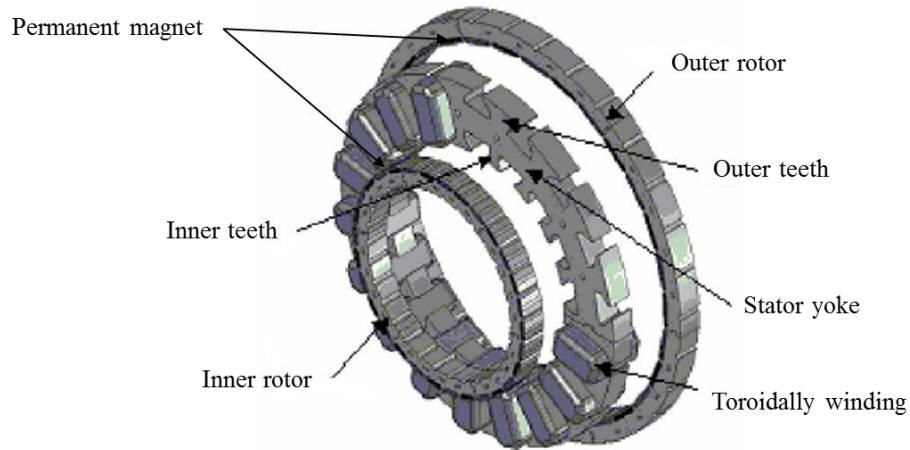


Figure 2.12: Double rotor and toroidally wound structure [23]

A switched reluctance double rotor machine applicable to hybrid electric vehicles was proposed and analysed in 2008 by Cui [24]. It has two rotors and one stator as shown in Figure 2.13. The proposed machine was divided into two motors; the outer motor is composed of the stator and the outer rotor while the inner motor is formed from the inner rotor and the outer rotor. This machine retains the switched reluctance machine characteristic, hence it is difficult to be utilised as a torque converter because it needs a double-side external excitation.

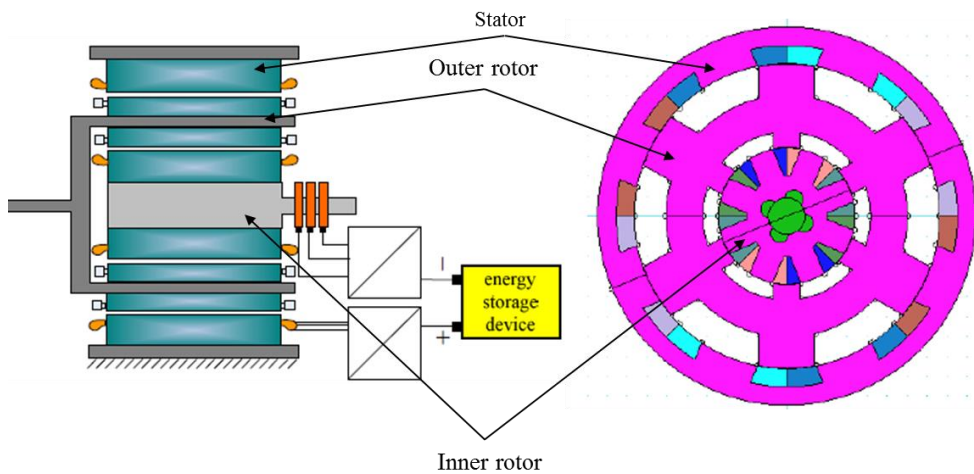


Figure 2.13: Switched reluctance double-rotor system [24]

A new topology of double-stator machine was proposed in 2010 by Peter Pišek, *et al* [25]. A single stator and two rotors are involved in this machine, as shown in Figure 2.14. The inner rotor is a wound rotor and the outer rotor is a permanent magnet structure. In the machine the back EMF from the inner rotor windings is always less than in the stator windings, hence a battery is necessary. However, the method of feeding the battery by two sources is undesirable, because they may damage the battery. In addition, the current flow between the two sources may damage the inverters as well. The alternative is to use two bi-directional inverters and two batteries. However, the system will be costly and unreliable. The other disadvantage of the system is that the inner rotor winding is fed through slip rings, leading to concerns about the reliability for automotive applications.

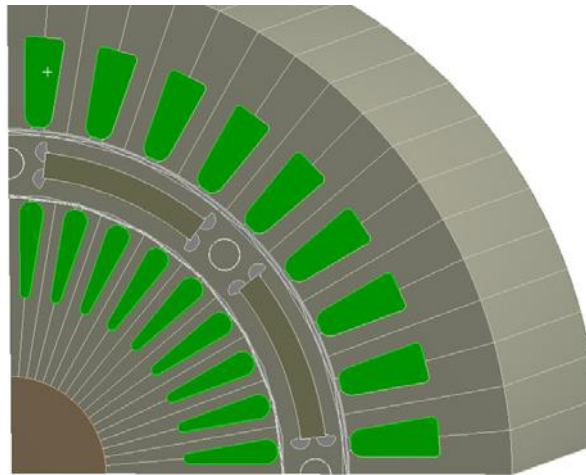


Figure 2.14: View of double rotor machine [25]

In 2014 [26], a claw-pole double-rotor machine was proposed for power-split hybrid electric vehicles as shown in figure 2.15. The machine was studied with the following configuration; a permanent-magnet rotor. Although, the claw-pole double rotor machine removes brushes and slip rings, the cogging torque of the machine is higher than conventional PM machines even after the design optimisation, due to the slots between claw poles.

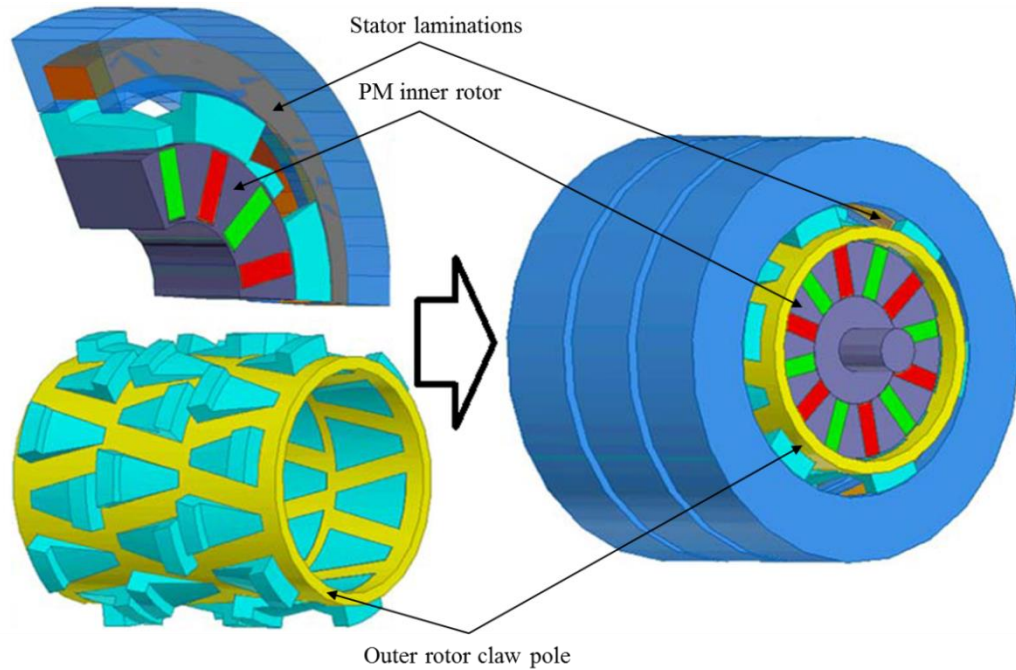


Figure 2.15: claw-pole double-rotor machine configuration [26]

Different electric machines have been used to convert the mechanical power into electrical power. Induction machines are the most commonly used due to its simplicity to manufacture and robustness in control. However, in the induction machines, there are some drawbacks such as they have low power factor and the slip rings are essential in the wound type. On the other hand, in the squirrel cage type, the slip power is difficult to be utilised. In contrast, brushless permanent magnet machines can offer higher efficiency and higher torque than the induction machines with the same volume, due to its permanent magnet excitation. The subsection below gives the background of the brushless permanent magnet machines.

2.4 Background of the Brushless Permanent Magnet Machine

The Brushless Permanent Magnet Machine (BLPMM) is composed of a stator with three phase windings and with a permanent magnet rotor as shown in figure 2.16. The permanent magnets provide the field flux instead of an external supply to excite the rotor field. The absence of an external field source gives the BLPMM an advantage in occupying less space, less weight as well as lower power losses. As a consequence, this

type of machine has a higher power density and torque to inertia ratio compared with a wound rotor type such as the induction machine [27].

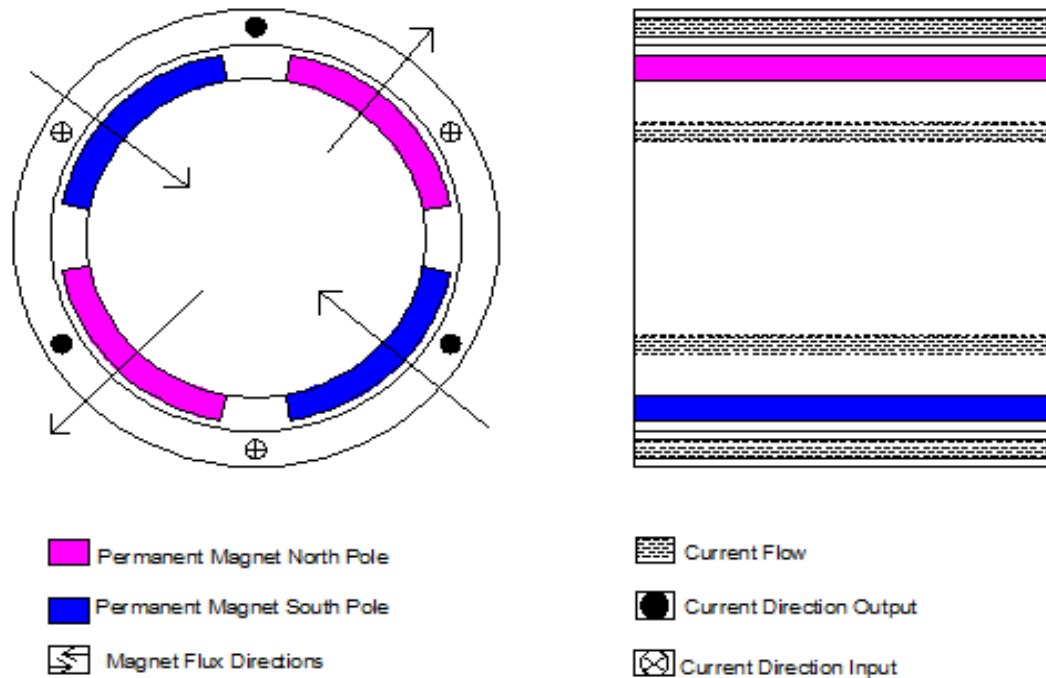


Figure 2.16: The permanent magnet machine construction

There are two types of the BLPM machines in general, namely, the Brushless AC Permanent Magnet Machine (BLACM) and the Brushless DC Permanent Magnet Machine (BLDCM). Although both are synchronous machines, the shape of the supplying voltage waveforms are different, the BLACM is fed by three-phase sinusoidal voltages, while the BLDCM is fed by switched voltages from an inverter and has a trapezoidal back EMF waveform.

Many rotor geometries for BLPM machines have been designed. They can be classified into two types, radially and axially orientated to the field magnetization [27]. In a radial-flux oriented type, the rotor magnets' field is in a radial direction while the current flows in an axial plane, whereas in the axial- flux oriented type, the flux flows axially, while the current flows in a radial plane, as shown in Figure 2.16.

The radial-flux machine type is classified into three configurations, depending on the location of the magnets on the rotor, namely the surface mounted, the buried, and the inset types [28]. The machine with the surface mounted magnet type is the most

commonly used configuration due to its simplicity by comparison with other configurations [28]. The following subsections present the mathematical modelling of the permanent magnet machine using the dq0 reference frame of the Brushless AC Machine and using the ABC reference frame of the Brushless DC machine.

2.4.1 Brushless AC Machine (BLACM) Modelling

The BLACM is a three phase synchronous machine with permanent magnets fixed to the rotor, instead of a wound field rotor [29]. The permanent magnet synchronous machine was analysed using the dq0 rotating reference frame. The Park transformation matrix was used to transform the three phase variables from the ABC reference frame into two-phase variables in the dq0 reference frame. These quantities are represented by f_a , f_b and f_c in the ABC frame, whereas in the dq0 frame the same quantities are represented by f_d and f_q and the third component is equal to zero in a balanced three phase system. Prior to having a rotating dq0 reference frame, there is usually a stationary reference frame called α - β in which the α axis is aligned with the phase a axis [30]. The machine voltage equations are expressed in the (abc) quantities as:

$$V_{abc} = R_s i_{abc} + p \lambda_{abc}$$

$$V_{abc} = \begin{pmatrix} v_{as} \\ v_{bs} \\ v_{cs} \end{pmatrix}, \quad R_s = \begin{pmatrix} R_s & 0 & 0 \\ 0 & R_s & 0 \\ 0 & 0 & R_s \end{pmatrix} \text{ and } i_{abc} = \begin{pmatrix} i_{as} \\ i_{bs} \\ i_{cs} \end{pmatrix} \quad (2.8)$$

$$\lambda_{abc} = \lambda_{abc}(s) + \lambda_{abc}(r)$$

Where p is the differential operator, v_{as} , v_{bs} and v_{cs} and i_{as} , i_{bs} and i_{cs} are the machine phase voltages and currents respectively. The phase resistances are represented by R_s and the stator inductances are represented by L in the following equation.

$$\lambda_{abc}(s) = \begin{pmatrix} L_{aas} & L_{abs} & L_{acs} \\ L_{bas} & L_{bbs} & L_{bcs} \\ L_{cas} & L_{cbs} & L_{ccs} \end{pmatrix} \begin{pmatrix} i_{as} \\ i_{bs} \\ i_{cs} \end{pmatrix} \quad (2.9)$$

Where all the elements of the main diagonal are the self-inductances of their index phases for example, L_{aas} is the phase a self-inductance. L_{abs} , L_{acs} and L_{bcs} are the mutual inductances between phase a, phase b, and phase c, respectively. The same definition is given for the other mutual inductance symbols. In addition, the permanent

magnet flux linkage $\lambda_{abc}(r)$ of the rotor side is equivalent to the produced magnetic flux by the cosine of the angular rotor position.

$$\lambda_{abcs}(r) = \lambda_m \begin{pmatrix} \cos(\theta) \\ \cos\left(\theta - \frac{2\pi}{3}\right) \\ \cos\left(\theta + \frac{2\pi}{3}\right) \end{pmatrix} \quad (2.10)$$

$$L_{aas} = L_{ls} + L_{ms} \cos(2\theta) \quad (2.11)$$

$$L_{bbs} = L_{ls} + L_{ms} \cos\left(2\theta + \frac{2\pi}{3}\right) \quad (2.12)$$

$$L_{ccs} = L_{ls} + L_{ms} \cos\left(2\theta - \frac{2\pi}{3}\right) \quad (2.13)$$

$$L_{abs} = L_{bas} = -M_s - L_{ms} \cos\left(2\left(\theta + \frac{\pi}{6}\right)\right) \quad (2.14)$$

$$L_{bcs} = L_{cbs} = -M_s - L_{ms} \cos\left(2\left(\theta + \frac{\pi}{6} - \frac{2\pi}{3}\right)\right) \quad (2.15)$$

$$L_{acs} = L_{cas} = -M_s - L_{ms} \cos\left(2\left(\theta + \frac{\pi}{6} + \frac{2\pi}{3}\right)\right) \quad (2.16)$$

Where, L_{ls} is the stator leakage inductance, M_s is the average mutual inductance between the stator windings, and L_{ms} is a maximum inductance value that determines its variation. The nature of the inductance variations is determined as a function of the rotor position θ .

The original Park's transformation matrix T_{dq0} is a matrix that can convert a three-phase system into a two-phase system [31].

$$\begin{bmatrix} f_d \\ f_q \\ f_0 \end{bmatrix} = [T_{dq0}] \begin{bmatrix} f_a \\ f_b \\ f_c \end{bmatrix} \quad (2.17)$$

Where the transformation matrix T_{dq0} is:

$$T_{dq0}(\theta) = \frac{2}{3} \begin{bmatrix} \cos \theta & \cos\left(\theta - \frac{2\pi}{3}\right) & \cos\left(\theta + \frac{2\pi}{3}\right) \\ -\sin \theta & -\sin\left(\theta - \frac{2\pi}{3}\right) & -\sin\left(\theta + \frac{2\pi}{3}\right) \\ 0.5 & 0.5 & 0.5 \end{bmatrix} \quad (2.18)$$

Figure 2.17 shows the q-axis leads the d-axis by 90° while the angle θ is changed according to the rotor position. Therefore, the d-axis is considered as a reference for

measuring the rotor position that is aligned to the phase a-axis as a stationary reference frame.

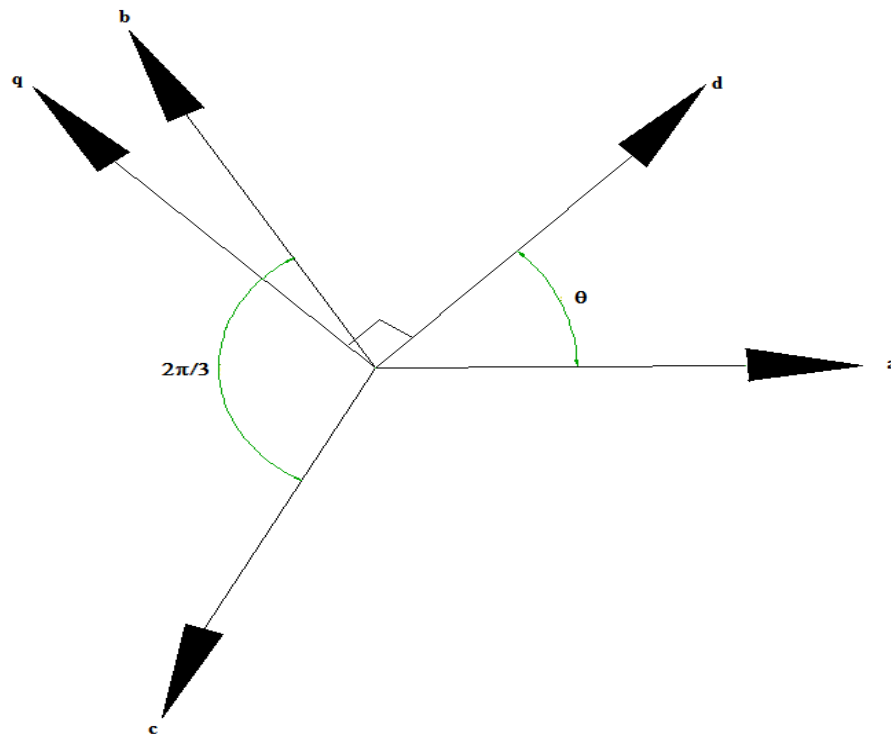


Figure 2.17: The a-b-c and d-q system frames relationship [32]

For the synchronous permanent magnet machine, the dq0 rotor reference frame is used to analyse the machine equivalent circuit [30] as shown in figure 2.18. Usually zero sequence is neglected, assuming the system is balanced.

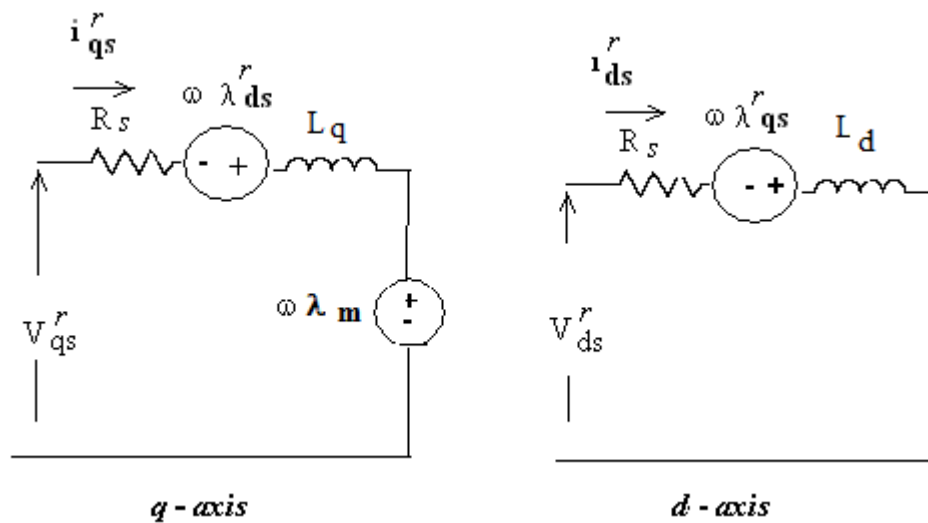


Figure 2.18: The circuit diagram of the dq0 representation

The voltages and the flux linkages in dq0 of the PM synchronous machine are

$$\begin{aligned} v_{ds}^r &= R_s i_{ds}^r + \frac{d}{dt} \lambda_{ds}^r - \omega \lambda_{qs}^r \\ v_{qs}^r &= R_s i_{qs}^r + \frac{d}{dt} \lambda_{qs}^r + \omega \lambda_{ds}^r \end{aligned} \quad (2.19)$$

Where the flux linkages are defined as

$$\begin{aligned} \lambda_{ds}^r &= L_d i_{ds}^r + \lambda_m \\ \lambda_{qs}^r &= L_q i_{qs}^r \end{aligned} \quad (2.20)$$

The electromagnetic torque is given as

$$T_{em} = \frac{3P}{2} (\lambda_m i_{qs} - (L_d - L_q) i_{ds} i_{qs}) Nm \quad (2.21)$$

Where L_d and L_q are the direct and quadrature axes inductances. The machine dynamics is stated as

$$T_{em} = J(d\omega/dt) + T_{load} + T_{fr} \quad (2.22)$$

Where J is the moment of inertia, T_{load} and T_{fr} are the load torque and the friction torque respectively.

2.4.2 Brushless DC Machine (BLDCM) Modelling

The Brushless DC (BLDC) machines are generally designed with either a single or three-phase windings in its stator. With a certain configuration of the permanent magnets on the rotor, a trapezoidal back-EMF shape is obtained in the stator windings. As the BLDC machines operate with an electronic drive instead of mechanical commutators and brushes, they have the same configuration with the field on the rotor and the armature on the stator. In order to achieve a constant torque production, square wave currents are applied to the stator windings.

In a three-phase type BLDC machine, two phases can be energized in each instant by electronic switching in a sequence and synchronized with the rotor position. There are three main techniques to find the rotor position. The first one is by using an optical position sensor, which consists of a rotating slotted disc called an interrupter, a light source and a photo sensor. The rotating disc rotates with the shaft and the detected interrupted light generates digital signals. There are two types of optical position sensors, incremental and absolute encoders. Although the second type can provide a

higher position resolution than the first one, it is more costlier than the incremental one [27]. The second technique is the Hall-effect position sensor. It is usually used for the BLDC motors with a trapezoidal back-EMF due to its simplicity. With the three-phase BLDC motor, there are three Hall switches displaced by 60° (or 120° electrical). These switches open and close depends on their position in the magnetic field that higher than a certain threshold value. Therefore, based on the hall-effect, the generation of an EMF is proportional to the flux density when these switches are energised [27].

Since the brushless AC machines have a sinusoidal back-EMF, the Park's transformation is used to model that kind of machine. On the other hand, the brushless DC machines produce non-sinusoidal back EMF. Therefore, these kinds of machines are modelled by using the a-b-c reference frame.

Figure 2.19, shows a single-phase equivalent circuit of a permanent magnet BLDC machine that consists of phase windings supplied by a bus DC voltage V and a current i flows in the phase inductance L and the phase resistance R . The back EMF (e) is generated owing to the movement of permanent magnet/armature windings in the magnet field. The voltage induced is proportional to the machine speed and it is in opposition to the applied terminal voltage [27].

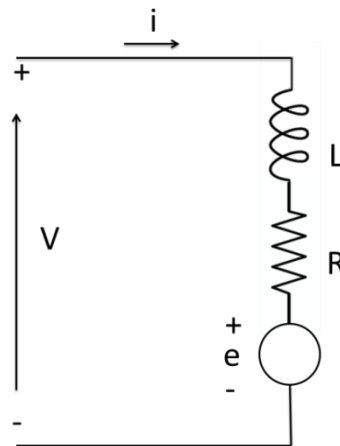


Figure 2.19: Circuit diagram of the single-phase BLDC machine

From the equivalent circuit shown in figure 2.19, the voltage equation per phase is defined as:

$$V = e + R i + L \frac{di}{dt} \quad (2.23)$$

The rotor angular speed ω_m is directly proportional to the back-EMF (e) as stated in [27]:

$$e(t) = k_m \omega_m(t) \quad (2.24)$$

Where ω_m (rad/s) is the angular velocity, k_m is the back-EMF constant (V.s/rad). In the brushless DC machine the EMF constant k_m can be used instead of torque constant k_T . The three-phase with six solid state switches (at 120° commutation drive, star connected windings), each two-phase windings are connected in series in each instance, for example, phase a and phase b are conducting, with a balanced system $R_a = R_b$ and $L_a = L_b$. Hence, the line voltage equation is

$$V_{ab} = e_{ab} + 2R_a i_a + 2L_a \frac{di_a}{dt} \quad (2.25)$$

Where e_{ab} is the line-to-line back EMF and it is equal to $e_a - e_b$.

The phase voltage equations for a three-phase system are given by:

$$\begin{bmatrix} V_a \\ V_b \\ V_c \end{bmatrix} = \begin{bmatrix} R_a & 0 & 0 \\ 0 & R_b & 0 \\ 0 & 0 & R_c \end{bmatrix} \begin{bmatrix} i_a \\ i_b \\ i_c \end{bmatrix} + \frac{d}{dt} \left[\begin{bmatrix} L_{aa} & L_{ba} & L_{ca} \\ L_{ab} & L_{bb} & L_{cb} \\ L_{ca} & L_{cb} & L_{cc} \end{bmatrix} \begin{bmatrix} i_a \\ i_b \\ i_c \end{bmatrix} \right] + \begin{bmatrix} e_a \\ e_b \\ e_c \end{bmatrix} \quad (2.26)$$

Where, R_i is the equivalent resistance per phase, L_{ii} , L_{ij} are the self and mutual inductances. Where i and j represent a, b or c phases.

In the balanced system, all self-inductances are equal and can be represented by L . Similarly, the mutual inductances between each two windings are the same and can be denoted by M . Three resistances have the same values under a balanced three-phase system, hence substituting the equivalent resistance and the inductances, the matrices of equation (2.26) can be written as:

$$\begin{bmatrix} V_a \\ V_b \\ V_c \end{bmatrix} = \begin{bmatrix} R_s & 0 & 0 \\ 0 & R_s & 0 \\ 0 & 0 & R_s \end{bmatrix} \begin{bmatrix} i_a \\ i_b \\ i_c \end{bmatrix} + \begin{bmatrix} L & M & M \\ M & L & M \\ M & M & L \end{bmatrix} \frac{d}{dt} \begin{bmatrix} i_a \\ i_b \\ i_c \end{bmatrix} + \begin{bmatrix} e_a \\ e_b \\ e_c \end{bmatrix} \quad (2.27)$$

With symmetrical three-phase systems, the sum of the three currents must be zero. Under this assumption, the three-phase BLDCM mathematical modelling can be represented as

$$i_a + i_b + i_c = 0 \quad (3 \text{ switches conducting}) \implies i_a + i_b = -i_c \quad (2.28)$$

$$\begin{bmatrix} V_a \\ V_b \\ V_c \end{bmatrix} = \begin{bmatrix} R_s & 0 & 0 \\ 0 & R_s & 0 \\ 0 & 0 & R_s \end{bmatrix} \begin{bmatrix} i_a \\ i_b \\ i_c \end{bmatrix} + \begin{bmatrix} L_t & 0 & 0 \\ 0 & L_t & 0 \\ 0 & 0 & L_t \end{bmatrix} P \begin{bmatrix} i_a \\ i_b \\ i_c \end{bmatrix} + \begin{bmatrix} e_a \\ e_b \\ e_c \end{bmatrix} \quad (2.29)$$

Where $L_t = L - M$

In the three- phase system, the electromagnetic torque and the voltage in the time domain are

$$T_{em} = (e_a i_a + e_b i_b + e_c i_c) / \omega_m \quad (2.30)$$

$$v_a(t) = R_s i_a(t) + L_a \frac{d}{dt} i_a(t) + k_e \omega_m(t) \quad (2.31)$$

By the transformation of equation (2.31) into a Laplace equation, the current for phase a is given by:

$$I_a(s) = \frac{V_a(s) - k_e \omega_m(s)}{R_a + sL_a} \quad (2.32)$$

The electromechanical torque can be stated as:

$$T_{em}(t) = T_L(t) + JP\omega_m(t) + B\omega_m(t) \quad (2.33)$$

By substituting equation (2.33) in the electromagnetic torque $T_{em} = k_T I$, the electromagnetic torque in the Laplace transformation of the BLDC machine is given by:

$$T_{em} = \frac{k_T(V_a(s) - k_e \omega_m)}{R_a + sL_a} \quad (2.34)$$

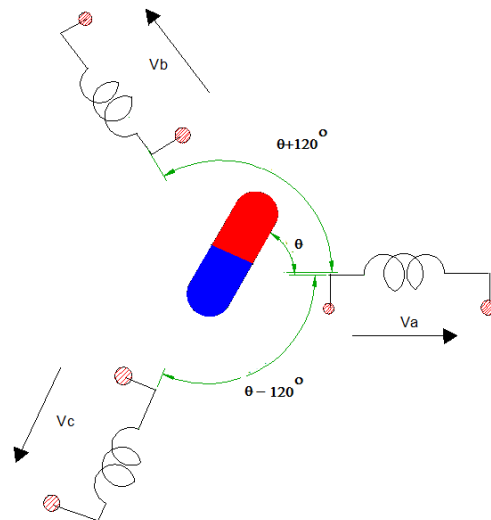


Figure 2.20: Rotor position with respect to the phase a- axis

where θ as the rotor angle with respect to the phase a- axis, shown in figure 2.20. At any given time, the rotating EMF can be written as follows:

$$e = \frac{K_e}{P} \left[\begin{matrix} \sin \theta \\ \sin (\theta - 120^\circ) \\ \sin (\theta + 120^\circ) \end{matrix} \right] \frac{d\theta}{dt} \quad (2.35)$$

The six switches T_1 – T_6 , as shown in figure 2.21, are used to supply and control the power of the stator phase terminals, two phases conduct in each instance in the BLDCM 120° conduction angle mode. Table 2.1 shows the example of the relationship between the input signals (S_0 – S_2) and the six- switches [27]. The electromagnetic power and the torque are always positive due to the product of the negative current by the negative EMF, which gives a positive power and a torque as shown in figure 2.22 for phase a. Figure 2.22 illustrates the peak values of the back EMF and the current of phase a. According to [34], the BLDCM is able to supply 15% more power and torque than the BLACM from the same size with an equal core losses.

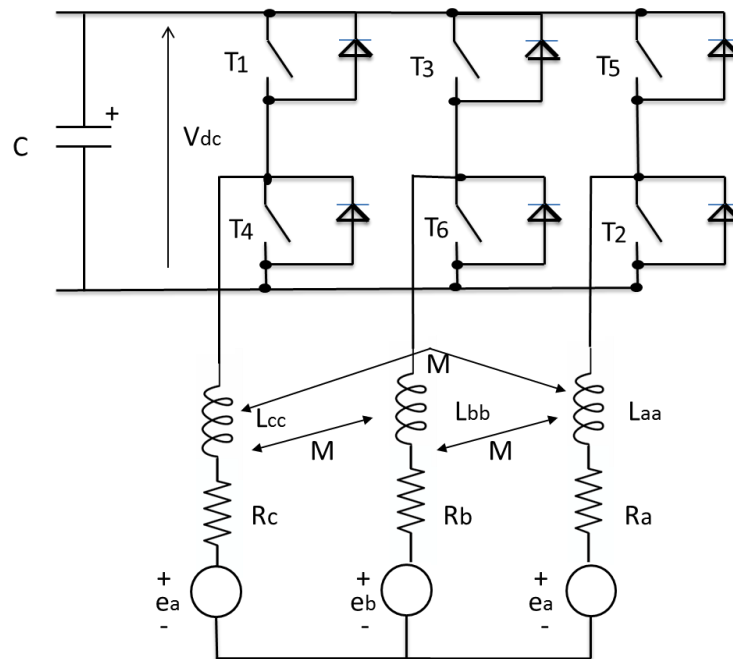


Figure 2.21: The BLDCM equivalent circuit

S0	S1	S2	T1	T4	T3	T6	T5	T2
0	1	0	1	0	0	0	0	1
1	1	0	1	0	0	1	0	0
1	0	0	0	0	0	1	1	0
1	0	1	0	1	0	0	1	0
0	0	1	0	1	1	0	0	0
0	1	1	0	0	1	0	0	1

Table 2.1: The BLDCM 120° Conduction angle mode

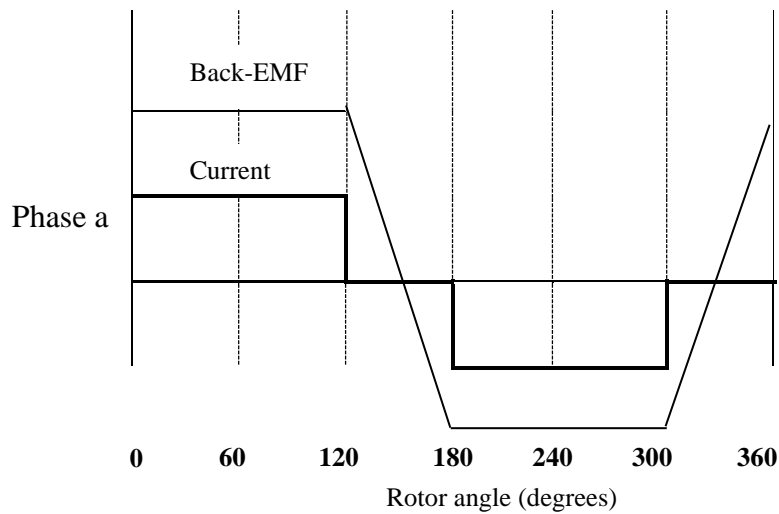


Figure 2.22: Two-pole BLDC machine excitation current and back-EMF waveforms of phase a

2.5 Summary

The torque converters in their varied forms and techniques have been proposed and studied over the years. At the same time, many drawbacks have been discovered, leading to further investigations into alternative techniques. The electromechanical torque converter and the IET can solve some of the conventional type of problems, but they are not the optimum solution. They have some disadvantages, as they are not a reliable systems since they need an external power source. Furthermore, slip energy cannot be recovered.

3 Research Methodology

3.1 Introduction

This chapter presents and explains the methodology in this research study. The research study includes theoretical and practical phases. Seven stages were adopted to achieve the research aim. This chapter consist of three categories namely, the strategy of the EMTC design, the data collection and analysis methods, along with the validation and the limitations.

3.1.1 The Philosophy of the EMTC system

The main function of the current hydraulic torque converter is to couple the engine with the gearbox at all times using the fluid medium. Therefore, the philosophy behind the EMTC system is to perform this coupling electromagnetically rather than by employing a fluid. The use of an electric machine instead of hydraulics is desirable due to the high efficiency of electric machines, especially the permanent magnet machines. In addition, the speed response of electric machines is faster than the fluid coupling when the load changes.

3.1.2 Strategy of the EMTC Design

In this subsection, the starting point of the research is presented. Stages, I and II explain the beginning of the research and how the design was begun as shown in figure 3.1. However, due to high cogging torque of the preliminary design, it was redesigned and optimized. A high cogging torque is not just a noise source but it makes the machine hard to work. In addition, a machine with a high cogging torque absorbs a high current when it starts and it may damage the power electronic switches.

Stage I (starting the research)

At this stage, the up to date techniques in developing torque converters were surveyed. The survey showed that the electromagnetic technique using permanent magnets has not been studied for a torque converter. Exploring the idea to use the electromagnetic torque converter to replace the hydraulic torque converter came from the Integrated Energy Transducer (IET). In the IET, the permanent magnet induction machine was used to convert the input torque to the output torque. However, in the IET technique, slip rings

were used to extract the slip power when the speeds of the inner and outer rotors were different. In addition, the slip power is utilised to energize the external battery in the IET. Therefore, in the IET technique the external power source such as the battery is needed. In contrast, the slip power is re-injected back into the system in the new EMTC. The other advantage of the EMTC system is that it eliminates the slip rings.

The EMTC system was divided into two parts, the differential machine (DM) and the Variable Frequency Rotary Transformer (VFRT). A preliminary design of the DM was developed at this stage using two simple permanent magnet machines with a common permanent magnet rotor

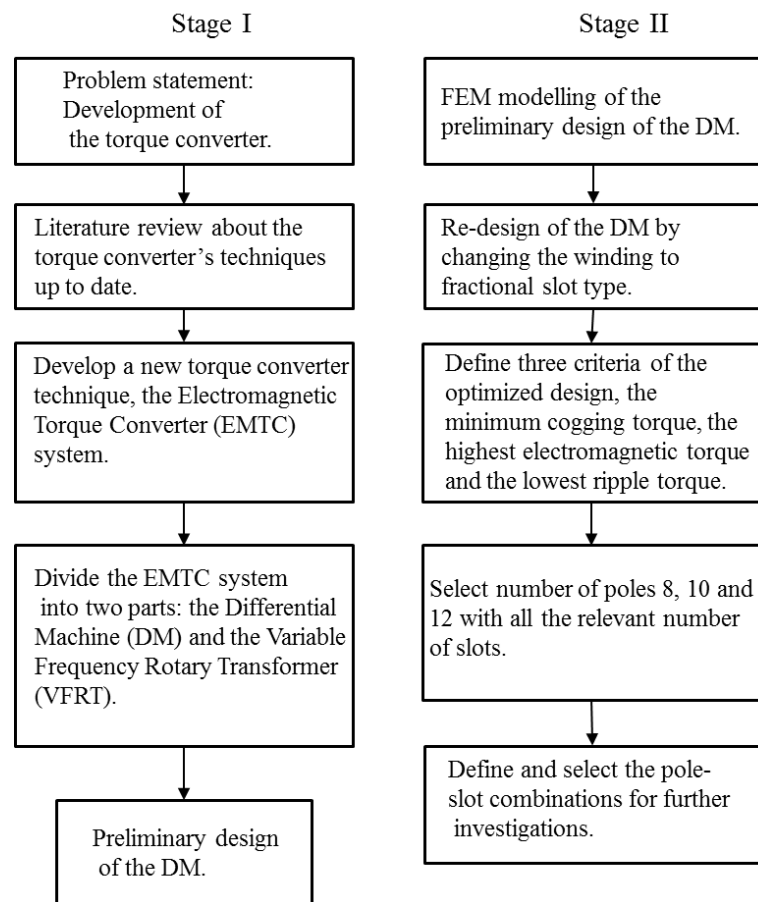


Figure 3.1: Flow charts of the strategy of the EMTC design stages

Stage II (Defining the pole-slot combinations of the DM)

At the stage shown in figure 3.1, the Finite Element Method (FEM) was used to model the designed DM. It was divided into two permanent magnet machines, external and internal surface mounted permanent magnet machines. The FEM modelling indicated that the concept of the EMTC system can be achieved. However, it revealed that the

cogging torque was very high in both machines. The reason for that was the use of the integral winding type. Hence, the DM was re-designed by changing the winding type to the fractional winding type. The FEM results showed that the cogging torque using the fractional winding was significantly reduced.

In order to design a permanent magnet machine in a proper way, the number of poles and slots needs to be defined correctly. To design an electric machine with a high electromagnetic torque, a high number of poles should be selected. However, with a high number of poles, the fundamental frequency will increase, which will increase the iron losses. On the other hand, with a low number of poles, the yoke thickness will be increased to withstand the flux. As the yoke thickness increases, the slot area will decrease and the produced torque will also decrease. Therefore, the 8, 10 and 12 poles with a relevant number of slots were chosen. There were 17 pole-slot combinations for each machine in the DM which were investigated accordingly.

3.1.3 Data Collection and Analysis Methods

This subsection as stated in stages III to V, shown in figure 3.2, explains how the pole-slot combinations of the DM machines, the Brushless DC Machine (BLDCM) and the Permanent Magnet Induction Machine (PMIM) were selected. The FEM was used to simulate 68 models. The simulations included the cogging torque, electromagnetic torque and the ripple torque. The optimal design was then achieved for the DM.

Stage III (FEM modelling of the 68 models)

After dividing, the DM into two machines namely, the BLDCM and the PMIM, each machine was investigated individually with 17 pole-slot combinations. The total pole-slot combinations of both machines were 34 models. However, these models were Fully Pitched (FP) magnet arc length. The ratio between the pole-arc to the fully pitched-arc length was investigated to define the optimal Gapped Magnet (GM) arc length by using the FEM. The investigated models for the GM were selected from those that have the lowest cogging torque in FP models. Therefore, the models that were investigated using FEM for both machines, the BLDCM and the PMIM were 68 models (34 FP and 34 GM models).

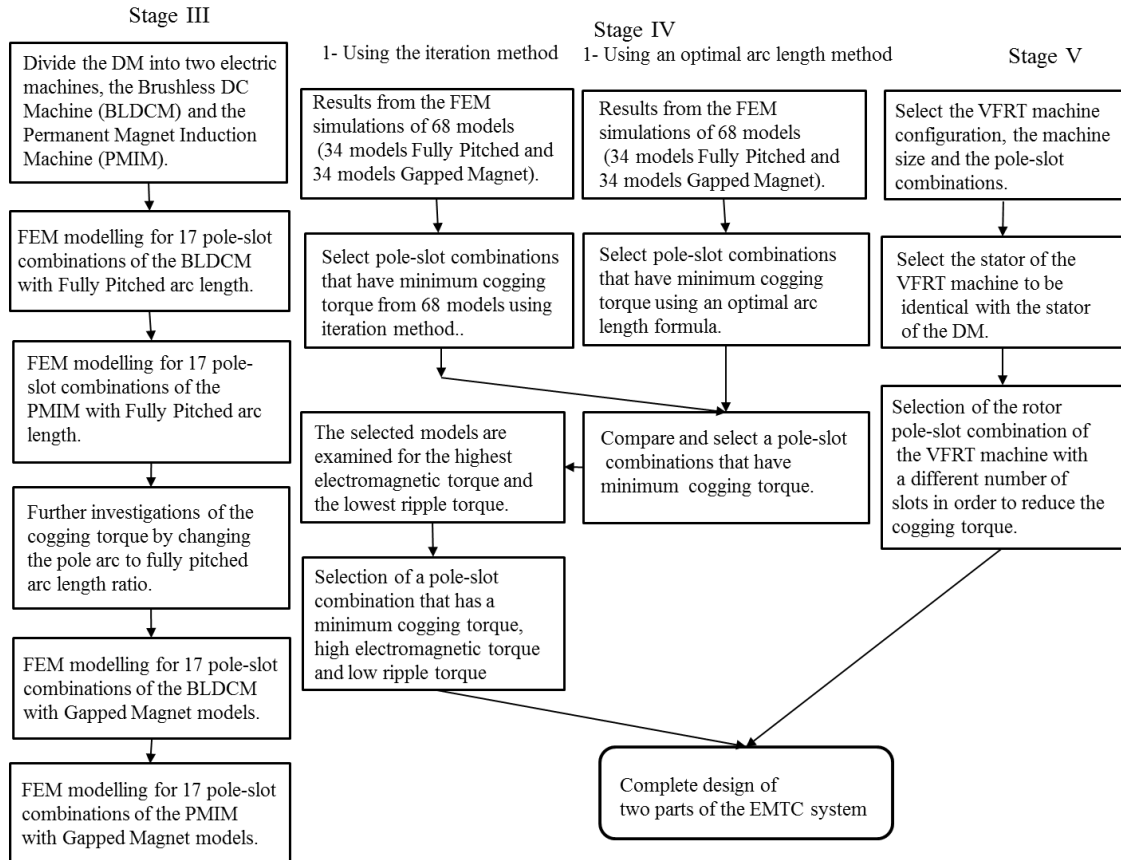


Figure 3.2: Flow charts of data collection and analysis methods stages

Stage IV (Select the optimal pole-slot combinations for each machine in the DM)

The selecting of the pole-slot combinations based on the design criteria was started by the modelling of 34 models for each machine in the DM. The results of the minimum cogging torque models were selected by using two methods, the iteration method and the optimal arc length method. Where, the FEM was used in both methods. Then, each machine in the DM had a number of pole-slot combinations that have a very low cogging torque. These models were investigated further to satisfy the second and third design criteria, the high electromagnetic torque and the lowest ripple torque. Finally, the optimal pole-slot combination of each machine in the DM was defined.

Stage V (Select the pole-slot combination of the VFRT)

As the DM machines were configured, the pole-slot combinations of the rotor and the stator of the VFRT were defined. The stator configuration was chosen to be identical to the stator of the DM. The reason for that is to ease dismantling the rotors in case of

maintenance. On the other hand, in order to reduce the cogging torque in the VFRT machine, the number of slots must be different (± 3) between its stator and rotor.

3.1.4 The Validity of the EMTC system

The validity of the EMTC system stages are shown in figure 3.3. It consists of FEM and the mathematical modelling of the integrated DM and the VFRT machines.

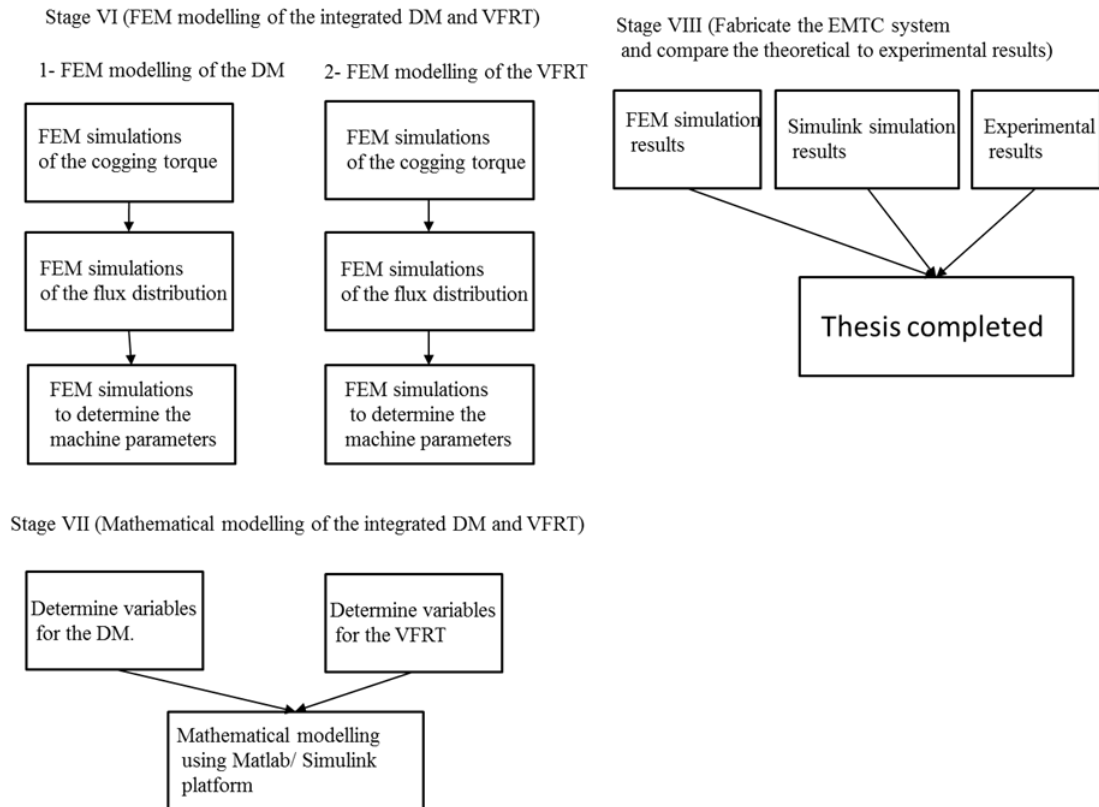


Figure 3.3: Flow chart of the validity of the EMTC system

Stage VI (FEM modelling of the integrated DM and VFRT)

Once each part of the EMTC system was configured, the FEM modelling was carried out for each part individually. The FEM modelling included the flux distribution and cogging torque of the integrated machine. The investigations of the cogging torque on the DM were performed at several slip speeds between the inner and outer rotor. On the other hand, the FEM modelling of the VFRT machine was carried out when its rotor windings were fed by an external power source. In addition, the FEM was used to define the parameters of the DM and the VFRT machines in order to be used for the mathematical model simulation.

Stage VII (Mathematical modelling of the EMTC system)

In order to implement a control system, a mathematical model is needed. Therefore, the mathematical model of the EMTC based on the IET mathematical model, the permanent magnet synchronous machine and the three-phase transformer was derived. The derivation of the mathematical model of the EMTC system was achieved using dq0 representation. Once, the nonlinear differential equations were derived for the system, the circuit diagram of each machine and the complete system was configured and modelled using the Matlab/ Simulink platform. The parameters of the system such as resistances, self and mutual inductances were defined with the aid of FEM. Finally, the simulations of the complete system were performed to predict the system performance.

The study of the EMTC system research was limited of using the system to convert a low torque into a higher (multiple) torque. This is because the proposed application is for automobile transmission system. However, the system can be used for other applications, which will be presented in the next chapter.

3.2 Summary

This chapter has introduced and discussed the design, modelling and operation of the new torque converter technique and methodology for a research study. The selection of the pole-slot combinations that have been investigated are inherently related to the design of the novel system, the Electromagnetic Torque Converter (EMTC) system.

A Finite Element Method (FEM) has been used to provide data regarding the design of the EMTC system. The FEM was validated by many research publications in which it is a powerful tool to simulate the electrical machine. From the results of the FEM modelling, the design of both parts of the EMTC system, the Differential machine (DM) and the Variable Frequency Rotary Transformer (VFRT) were achieved. The FEM modelling of the DM and VFRT was carried out to investigate the performance of these parts. Along with the FEM modelling, a mathematical model was developed for the EMTC system. The methodology of the research was followed to achieve the practical implementation of the EMTC system.

4 The Electromagnetic Torque Converter Concept

4.1 Introduction

A description of the proposed Electromagnetic Torque Converter (EMTC) system is presented in this section. The proposed EMTC system is a combination of three machines as shown in the figure 4.1. Two of them are permanent magnet machines. These two machines were labelled as the Differential Machine (DM), whereas the third machine was named as the Variable Frequency Rotary Transformer (VFRT).

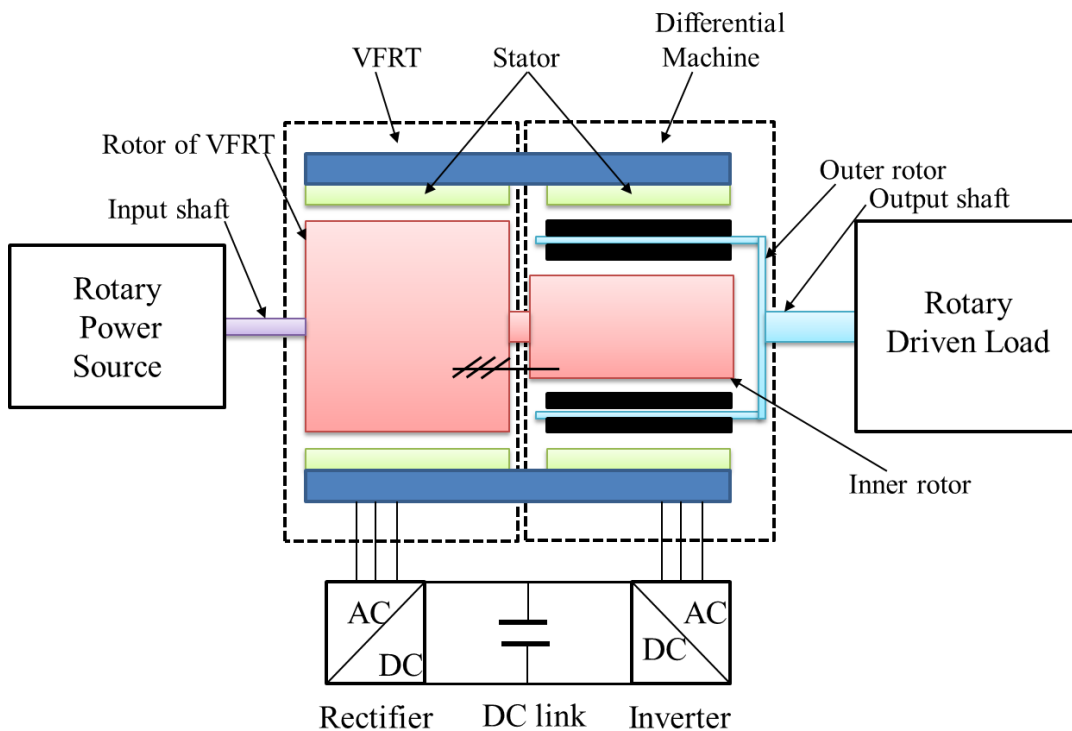


Figure 4.1: Configuration of the EMTC system

4.2 The EMTC System Description

The EMTC system has two parts, the DM and the VFRT machines. The DM is composed of two machines, the Brushless DC Machine (BLDCM) and the Permanent Magnet Induction machine (PMIM) as shown in figure 4.2. These two machines are composed of three cylindrical elements concentric about a common axis. The outer element stationary with three-phase stator windings, the inner element is rotating with three-phase windings driven by the input shaft (prime mover), and the intermediate element is a freely rotating drum with permanent magnets, fixed to the output shaft in

order to connect to the driven load. There are two air gaps between the intermediate element and the outer and inner elements.

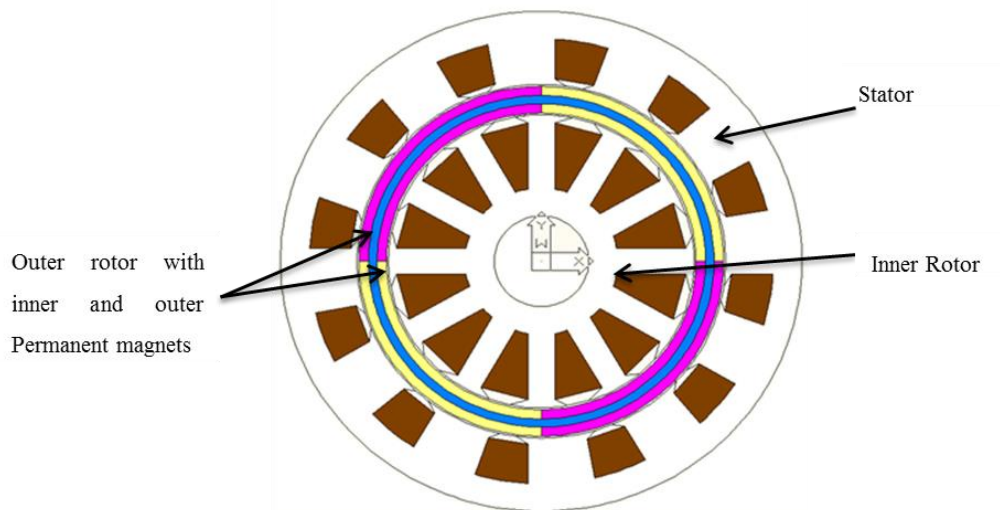


Figure 4.2: Cross section of the differential machine

On the other hand, the VFRT machine has three phase primary windings connected electrically with the inner rotor of the DM and mounted on the input shaft, and a stationary element also having three phase (secondary) windings as shown in figure 4.3. There are two functions of the VFRT. It transmits the slip power from the PMIM to the BLDCM without the use of slip rings and to step- up the slip voltage.

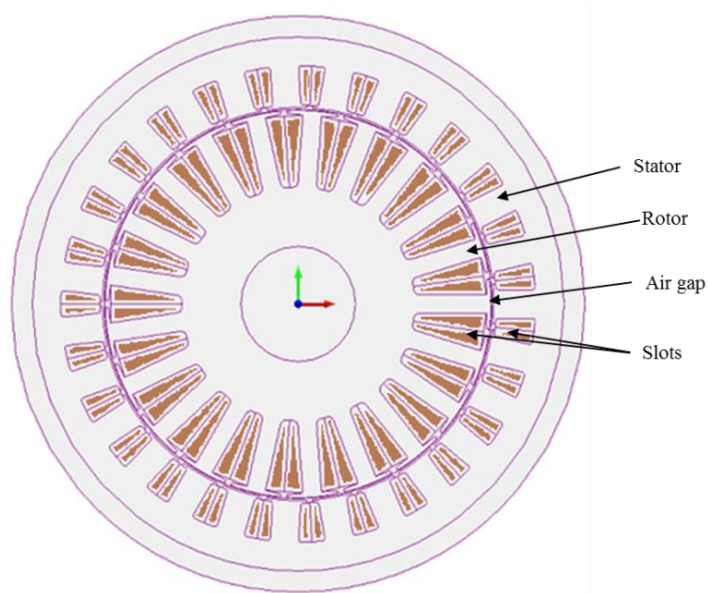


Figure 4.3: Variable frequency rotary transformer cross section

The schematic diagram of the EMTC system is shown in figure 4.4. It shows the inner rotor windings that are connected to the rotor of the VFRT windings via the rotating slip rings. The rotating slip rings allow connecting the inner rotor of the DM with the rotor of the VFRT windings, and either in delta or in star connection. The diagram also illustrates how the stator windings of both the DM and the VFRT machines are connected via the power converter. The power converter has unidirectional power flow. It consists of a rectification circuit, a DC link and an inverter circuit. The rectification circuit consists of a three-phase uncontrolled full wave rectifier. On the other hand, the inverter circuit is composed of six semiconductor-switching elements of Insulated Gate Bipolar Transistors (IGBTs). Between the rectification and inverter circuits, there is a DC link. There is a snubber circuit including a capacitor with a high voltage rating. The main advantage of using the snubber circuit is to reduce the switching losses of the IGBTs at turn off. The extracted power from the stator of the VFRT supplies power to the stator of the DM. Due to the system having two shafts; there are four bearings, the inner bearing and the outer bearing separated by an enough space to run both shafts separately. The input shaft is driven from a prime mover through the machine enclosure. The output shaft supplies mechanical power to the load.

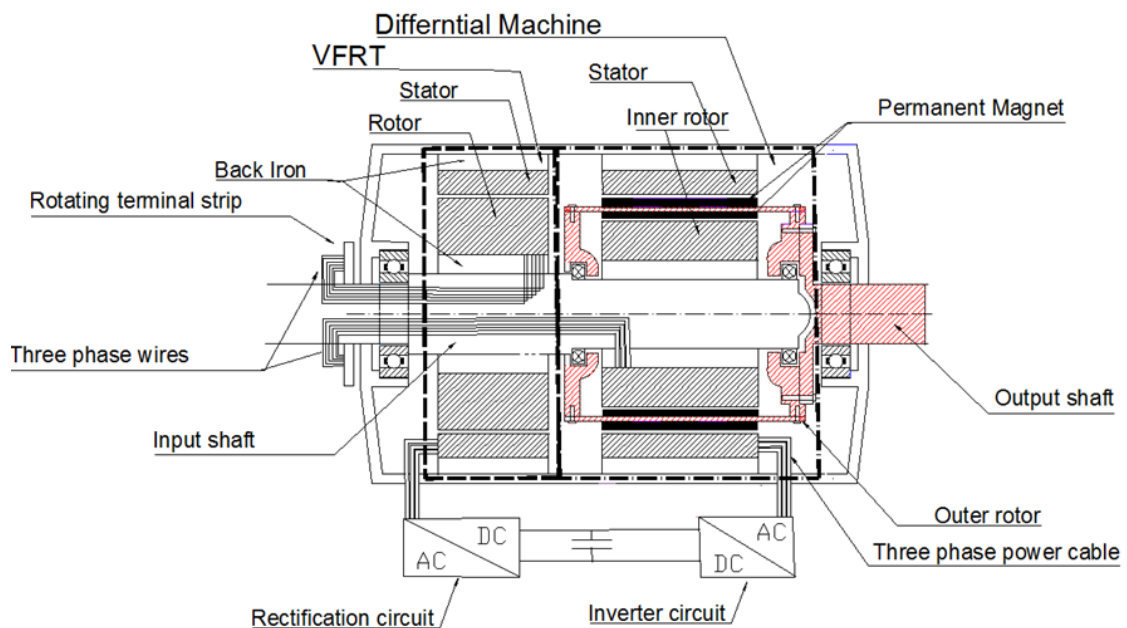


Figure 4.4: The proposed EMTC system

4.3 DM Principle of Operation

Figure 4.5 shows the angular speed for each element in the DM denoted by ω . The stator has a rotating magnetic field rotates at (ω_1), the inner rotor element has an angular slip speed (ω_3) that depends on the drive machine, whereas the intermediate element has an angular speed (ω_2) that depends on the driven load. The difference between the inner and the outer rotor speeds is called slip speed. Increase of the slip speed leads to an increase in the generated back EMF. The stator is supplied by the generated back EMF. Therefore, more load torque leads to more slip speed and then more back EMF.

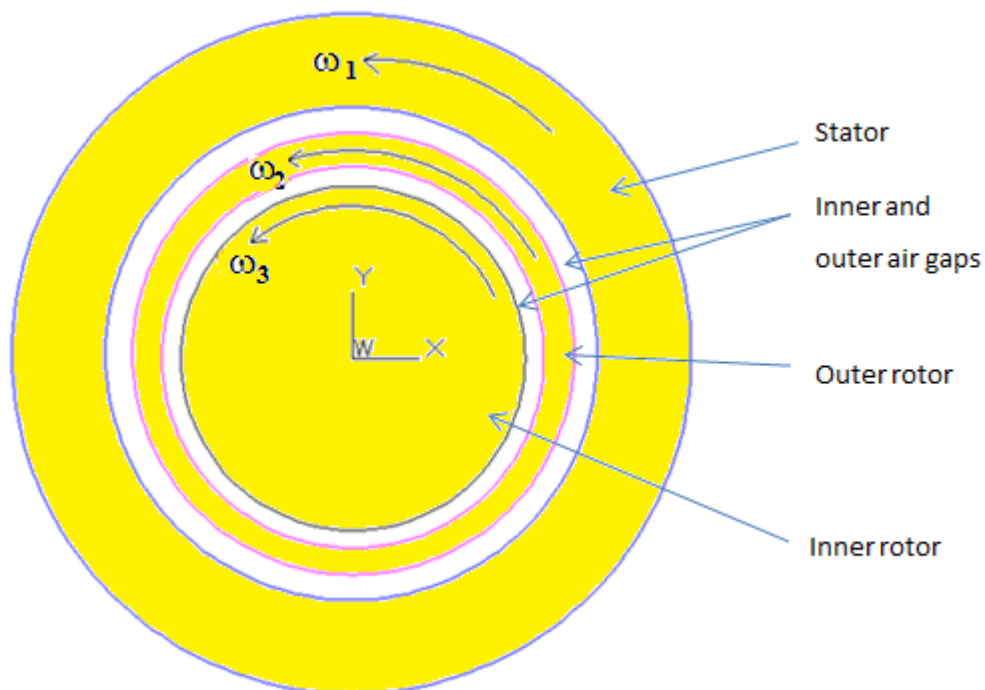


Figure 4.5 : Differential Machine operating principle

When the engine operates, the input shaft rotates at speed (ω_{in}), and with the input torque (T_{in}) produces the input power (P_{in}) to the inner rotor of the DM and to the rotor of the VFRT. At no-load torque, the outer rotor rotates synchronously with the inner rotor, which means no slip power is produced. At no slip power, there is no power delivered to the power converter. The inverter circuit shown in figure 4.4 is effectively an open circuit in this case since the applied voltage is less than the back EMF from the stator of BLDCM windings. This analogy is like when the vehicle is running at a high-speed downhill, with a very small load torque. As the load torque increases, the outer

rotor decelerates which means slip power is produced. The slip power is transformed through the VFRT to the AC/ AC power converter. Then, the power converter delivers this power to the stator of the BLDCM. The outer rotor then rotates to drive the load.

The basic mathematical equations for the EMTC system can be written as follows:

$$P_{in} = \omega_{in}T_{in} \quad (4.1)$$

$$P_{out} = \omega_{out}T_{out} \quad (4.2)$$

Where P_{out} is the output power, ω_{out} and T_{out} are the outer rotor speed and the output mechanical torque respectively. The stator windings of the BLDCM are supplied by the slip power:

$$P_{stator} = 3 E_s I_s \quad (4.3)$$

E_s and I_s are the phase voltage and the current feeding the BLDCM, respectively.

4.4 EMTC System Operating Range

The EMTC system can operate from the stalling condition (zero speed output) to the synchronisation operating condition, and theoretically beyond synchronism.

4.4.1 Stalling Operating Range

In this operating range, shown in Figure 4.6, the drive machine (prime mover) is supplying an input mechanical torque (T_{in}) to the inner rotor of the DM and the rotor of VFRT. When the outer rotor is locked ($T_{out} = \text{Maximum}$), the slip power P_{slip} is transferred to the stator of the DM from the stator of the VFRT. This condition occurs when the vehicle is stopped while the engine is running. Hence, the torque converter produces a maximum torque multiplication. Like in the conventional torque converter, the stall operating condition lasts for only a short period when the slip speed between the inner rotor and the outer rotor is very large.

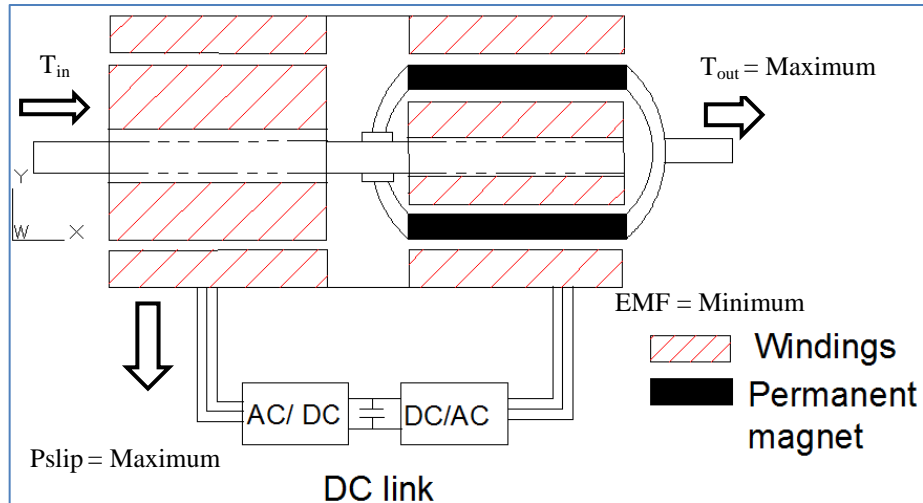


Figure 4.6: Stalling operating range

4.4.2 Synchronization Operating Range

This range, as shown in Figure 4.7, is the most frequent condition in the conventional mechanical torque converter, the speed of the engine and the output shaft are consistent. However, with the EMTC system, the inner rotor speed and the outer rotor speed may not be exactly the same due to the impedance of the inner rotor windings, which leads to create a small slip speed. In this operating condition, nearly zero power slip is obtained from the VFRT, but the outer rotor rotates with high slip speed makes the stator of the BLDCM produce a maximum Back Electromotive Force (Back EMF).

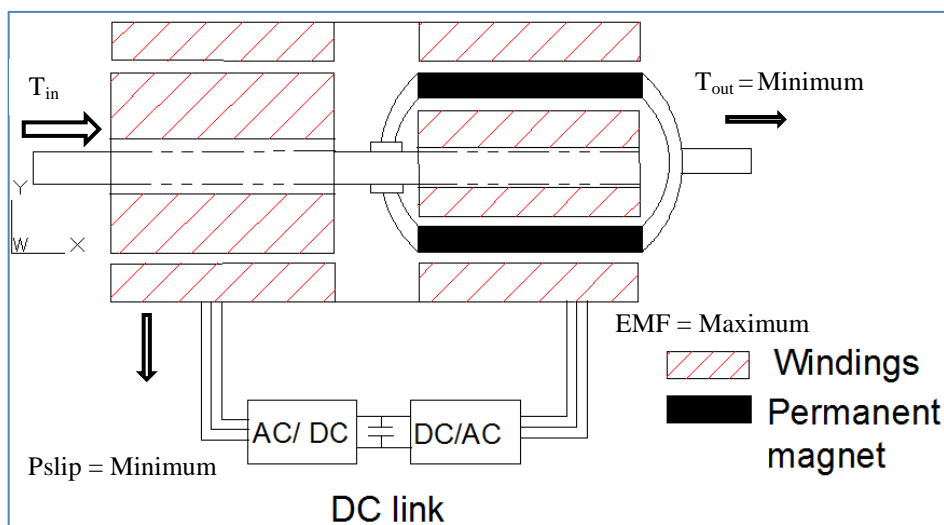


Figure 4.7: synchronization range

4.5 Summary

An overview of the proposed system was described in this chapter. The description includes two parts of the proposed EMTC system along with their principle of operation. The two parts of the EMTC system were introduced and defined. The first part consists of two permanent magnet machines namely the BLDCM and the PMIM. The second part was composed of a VFRT. The interaction between these two parts was defined as well. The next chapter describes the method to design these two parts of the EMTC system.

5 Design and Optimization of the EMTC System

5.1 Introduction

The design and optimization of the proposed Electromagnetic Torque Converter system (EMTC) is presented in this chapter. As mentioned earlier in chapter two, the EMTC system is a combination of two parts, the Differential Machine (DM) and the Variable Frequency Rotary Transformer (VFRT) machine. The design of the DM is different from the conventional or a Single Stator Single Rotor (SSSR) permanent magnet machine in terms of flux distribution. In the DM, which is a Single Stator Double Rotor (SSDR) permanent magnet machine, in order to simplify the design, the DM is split into two permanent magnet machines, namely, the brushless DC machine (BLDCM) and the Permanent Magnet Induction Machine (PMIM). While the VFRT machine is designed as an ordinary AC machine. The aim of this chapter is to present the design of both parts of the EMTC system.

5.2 Design Criteria of the Proposed EMTC System

The first design criterion of the proposed EMTC system is based on the selection of the pole-slot combination that has the minimum cogging torque. In an optimal design, the cogging torque should be less than 2.5% of the rated electromagnetic torque [35]. Another design requirement is the attainment of an output electromagnetic torque that is high enough to operate the load and that the torque ripple within the limit specified by Hendershot [27]. Therefore, the EMTC system design should meet the following criteria:

- Minimum cogging torque
- High electromagnetic torque
- Low torque ripple

5.2.1 Cogging Torque

The cogging torque is produced due to the interaction between the rotor magnets and the stator slots and is independent of the stator current [36]. The cogging torque T_{cog} can be expressed mathematically by using the following equation [37].

$$T_{cog} = -\frac{1}{2}\phi_g^2 \frac{d\mathcal{R}}{d\theta} \quad (5.1)$$

Where ϕ_g is the magnetic flux per pole, \mathcal{R} is the air gap reluctance and θ is the rotor angular position. The negative sign means the cogging torque tends to oppose the rotation direction of the rotor. From (5.1), it is clear that the cogging torque can be eliminated by either eliminating magnetic flux or keeping the reluctance in the air gap constant. Eliminating the magnetic flux is not realistic since it is needed for rotating the machine. On the other hand, keeping the reluctance at the air gap constant is very difficult since the slot opening produces a rate of change of the reluctance at the air gap. Therefore, the cogging torque can only be reduced [37]. Many techniques have been published for reducing the cogging torque in the permanent magnet machines including these mentioned below.

a) Skewing Stator Slots or Rotor Magnets

The skewing of the stator slots or rotor magnets is discussed in [27, 28, 38, 39]. Although skewing of rotor magnet or the stator slots can reduce the cogging torque, it makes the design more expensive because it requires special tools to manufacture. In addition to the high cost of the machine production, the torque ripple is increased by using the method of the magnet skewing. This is because if the skew angle is non-ideal due to manufacturing impreciseness, the torque can be affected by the second order harmonics [40].

b) Stator Slots Shaping

Zhu and Howe [41] discussed the minimization of the cogging torque in permanent magnet (PM) machines by adjusting the stator slot opening. Although the cogging torque decreases with opening slot width, there is a limitation on its width to allow the coils to be inserted.

c) Rotor Magnets Shaping

The magnet edges are tapered in this technique [27]. The main disadvantage of this technique is increasing the machine production cost.

d) Pole and Slot Combinations

The influence of the pole and the slot combinations on the cogging torque in permanent magnet machines has been investigated by Zho and Howe [41]. The least common multiple LCM between the slot number Q_s and the pole number N_m is one of the significant factors influencing the cogging torque. An increase of this number often leads to the decrease of the cogging torque [42]. However, the study of Zho and Howe [41] and Hwang [42] were limited to magnets occupying the full pole-pitch.

5.2.2 Electromagnetic Torque

In both types of the brushless machines, AC and DC, the electromagnetic torque T_{em} can be expressed by the following formula [43, 44] :

$$T_{em} = \left[\frac{\partial W'}{\partial \theta} \right]_{I=constant} \quad (5.2)$$

Where I is the excitation current, θ is the rotor position and W' is the co-energy. In the brushless machines, the co-energy can be replaced by the product of the flux linkage Ψ and the excitation current I due to the small amount of stored field energy compared with the product of ΨI .

As the rotor rotates and the current remains constant, the co-energy will change accordingly. This relationship will give the electromagnetic torque:

$$T = I \frac{d\Psi}{d\theta} \quad (5.3)$$

The electromagnetic torque of the permanent magnet brushless machine was assessed using the Finite Element Analysis by and Dan Ionel [45]. The effect of the fluctuations of the magnetic field distribution was discussed. The main cause of the torque pulsation is the cogging torque, which was discussed before, from the permanent magnet and the stator teeth interaction. There are three other causes of the torque pulsation: the non-sinusoidal current waveform, the difference between the back-EMF and current shapes, and the power converter state at the commutation time, which results the higher order

harmonics. Most of the presented techniques are discussed in [46]. However, some of the techniques discussed are not always utilised because they increase the complexity of the machine manufacturing.

5.2.3 Torque Ripple

The torque ripple in all electrical machines is usually undesirable, since it may cause a high electrical noise. High torque ripple may require changing the machine geometry to reduce the machine noise. There are many factors that cause the torque ripple. However, the two main ones are the cogging torque and the distortion of the magnetic flux density in the air gap [28]. The torque ripple T_r is defined as:

$$T_r = \frac{T_{max} - T_{min}}{T_{av}} \quad (5.4)$$

Where T_{max} is the maximum peak amplitude of the electromagnetic torque, T_{min} is the minimum electromagnetic torque amplitude and the T_{av} is the average amplitude of the torque.

The torque ripple was assessed in a BLDCM and discussed by H. Zeroug [47]. According to [47], the only types of torque ripple are the cogging torque, reluctance torque and commutation ripple. However, the machine design and the distortion of the flux density in the air gap are also sources of the ripple [48]. It is shown in [49] that the ripple torque in permanent magnet motors can be reduced by shifting one of the pole pair by half a slot pitch. However, this technique may reduce the electromagnetic torque and increase the complexity of motor construction.

5.3 Preliminarily Differential Machine Design

In order to achieve the required criteria as discussed above, several assumptions were made to define the initial design of the DM. Some of these assumptions were identified from the conventional design techniques of the permanent magnet machines as most permanent magnet machines have magnets mounted on their rotor surface [28]. The 12-slot /6-pole for both wound components of the DM were initially selected as a starting design point. The time-stepping finite element method was then used to evaluate the performance of the DM. The physical design specifications are listed in table 5.1.

Inner rotor inner diameter	44.4mm
Inner rotor outer diameter	116mm
Air gap lengths	0.7mm
Outer rotor ring sheet	3 mm
Permanent magnet thickness	6 mm
Outer stator diameter	204 mm
Pole number	6
Stator slot number	12
Inner rotor slot number	12
Stack length	153 mm
Rated power	5Kw
Line- Line Voltage (RMS)	250 V
Inner rotor speed	3000 rpm
Outer rotor speed	1000 rpm
Current density (peak)	10 A/mm ²
Phases	3
winding layers	single
Inner and outer airgap lengths	1 mm
Rated torque of the PMIM	15Nm
Rated torque of the BLDCM	47Nm
Desired cogging torque (Nm)	< 1% of the rated torque

Table 5.1: Preliminary design specification of the DM machine

The inner rotor was designed to operate with 3000 rpm maximum speed level, and the outer rotor was designed with 1000 rpm maximum speed level. The corresponding front view cross-section of the initial proposed machine is shown in figure 5.1. The cogging torque predicted using a Finite Element Modelling (FEM) is shown in figure 5.2 (a, b). Figure 5.2a shows the cogging torque versus the rotor position of the PMIM, and the BLDCM is shown in figure 5.2b, of the primarily design. Due to the integral winding in both the stator and the inner rotor structures, their cogging torque is higher than the desired values.

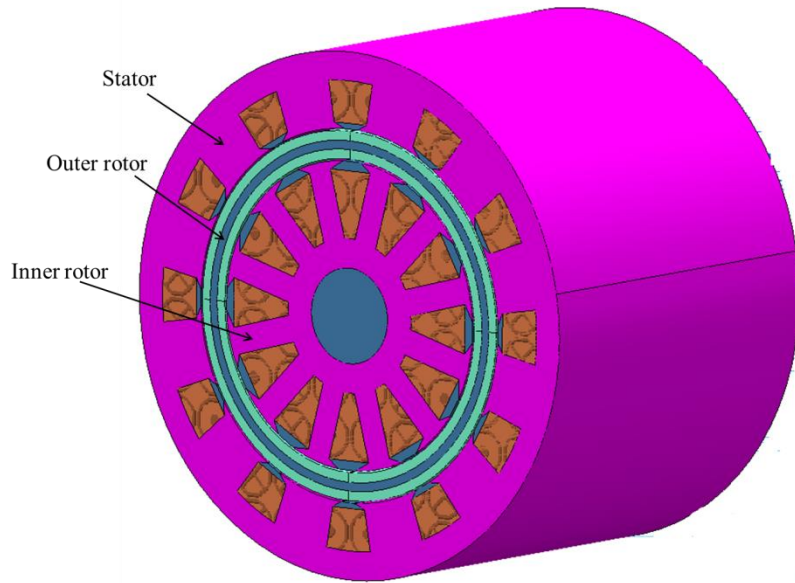


Figure 5.1: Cross section of the preliminary proposed DM

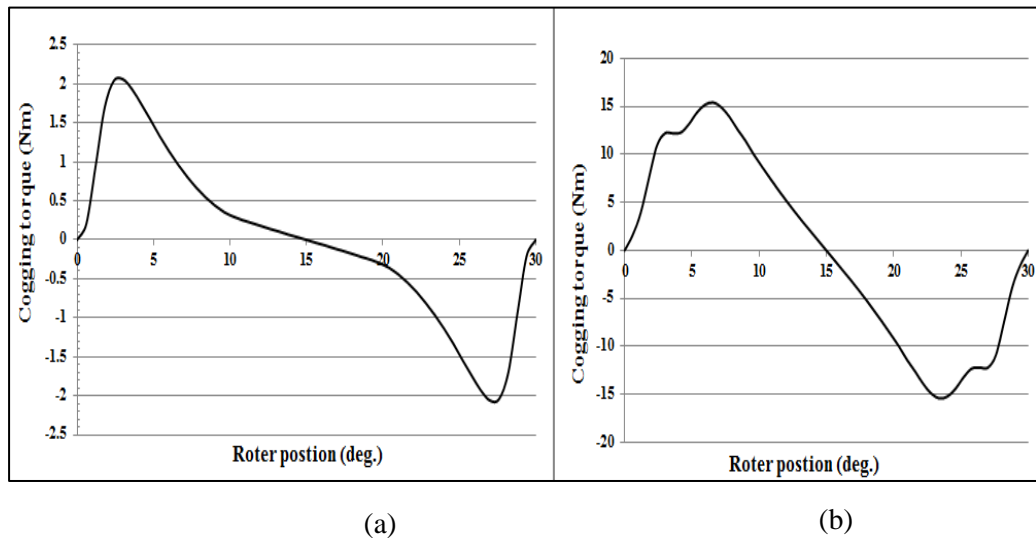


Figure 5.2: The predicted cogging torque of the preliminary proposed design of the DM (a) The (inner) PMIM machine and (b) The (outer) BLDCPM machine

5.4 Development of the EMTC system by Re-design

The main purpose of re-designing the EMTC system was to overcome the high cogging torque of the preliminary design achieving the first design criteria (see section 5.2).

5.4.1 Design limitations

For the purpose of developing a research test bed, the EMTC system was designed to be operated between two electrical machines; one as a motor and the other as a load. The power rating and speed of these machines are listed in table 5.2. The EMTC system design specifications were chosen according to these ratings.

Rotary Power Source specification		Load Driven specification	
Power	7.5 kW	Power	3 kW
Speed	5300 rpm	Speed	2000/3000 rpm

Table 5.2: The power source and the load driven specification

5.4.2 EMTC System Frame Design Specification

The guidelines for classification and rating of the electrical machines can be presented by using the International Electro-technical Commission (IEC) standards. The IEC standards maintain an international sizing for all electrical machines [50]. Figure 5.3 shows the basic frame dimensions according to IEC. The specific values of these dimensions are illustrated in table 5.3. The machine frame used in this thesis is designed based on the 132S- type of the IEC standards.

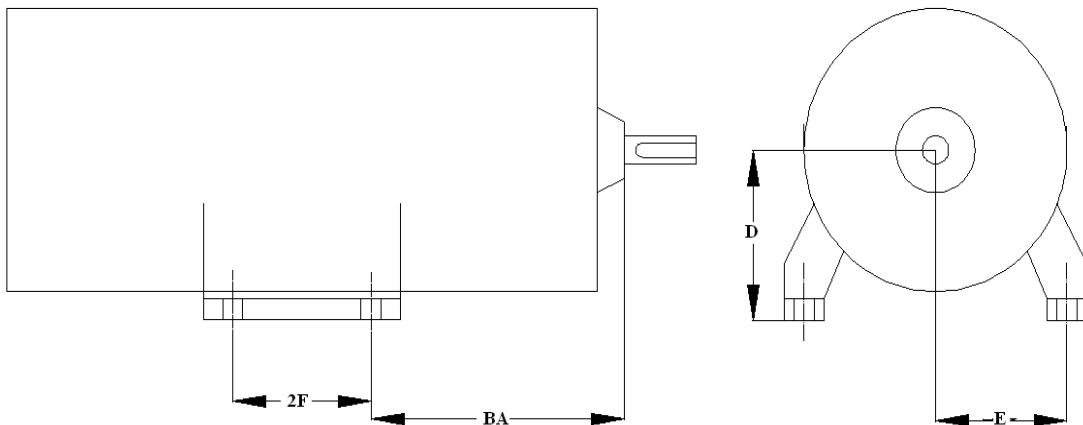


Figure 5.3: The basic IEC frame dimensions

Frame type	D (mm)	2E (mm)	2F(mm)	BA (mm)
90S	90	140	100	56
90L	90	140	125	56
112S	112	190	114	70
112M	112	190	140	70
132S	132	216	140	89
132M	132	216	178	89
The existing machine Frame	132	204	140	90

Table 5.3: IEC frame dimensions for various electric machine types

5.4.3 Design and Configuration of the Differential Machine (DM)

The design and configuration of both parts of the differential machine are presented in this section. The electrical and the mechanical designs are stated in the following subsections.

5.4.3.1 Electrical Design

The electrical design including the selection of the slot layer, the coil and the winding configurations are presented in this section.

a) Number of Layers Selection

There are two types of windings, either the single-layer windings or the double-layer windings. In single-layer windings, the coil is wound between two full slots. In contrast, in double-layer windings, a coil is wound to occupy one-half of the slot and a different coil occupies the second half. Table 5.4 shows the comparison between the single and the double-layer windings. EL-Refaie [51] discussed thoroughly these two types, their influence on the winding factor of the electro-motive force (EMF) and the machine performance. Salminen in [52] proposed the double layer windings type to minimise the torque ripple. The losses minimisation is another advantage of using a fractional slot double-layer concentrated winding [53, 54].

Electrical Machine performance	Single layer	Double layers
The AC losses	high	low
Machine efficiency	Low	high
Power density	Low	high

Table 5.4: The comparison between single and double layers concentrated windings

b) Winding Type Selection

There are two main configurations of the coils used in the electrical machines, full-pitched and short pitched winding. In full-pitched winding, coils will have a span mathematically equal to one pole-pitch. While, in the short-pitched winding the span is less than one pole-pitch.

The coil-span factor K_c is defined as [55]:

$$k_c = \frac{\text{vector sum of the induced e.m.f per coil}}{\text{arithmetic sum of the induced e.m.f per coil}} \quad (5.5)$$

Equation (5.5) results in less than unity for the fractional winding type because the vectorial sum of induced Electro-Motive Force (EMF) per coil is less than the arithmetic sum of the same induced EMF per coil.

In industrial applications, the most popular winding type is the distributed winding. By using this type of winding a sinusoidal Magneto-Motive Force (MMF) can be achieved. Another type of winding is the integral winding. This type is directly proportional to the machine pole number and the number of slots. However, in this type, each coil crosses the other coil, which leads to the production of a high cogging torque [56, 57]. Other winding type is called a concentrated winding. In this type, the produced sinusoidal EMF is less than the distributed type. Even though, the construction complexity of distributed type leads to choosing the concentrated winding type in the permanent magnet (PM) machine design.

There are many advantages for using concentrated windings, such as minimizing the cogging torque and maximizing the high machine performance [56]. These advantages include short end turn especially used with fractional slot concentrated winding type [58-60]. Fractional slot winding could be either an overlapping or a non-overlapping of the phases with concentrated winding which are studied thoroughly in [52, 53, 61]. Usually the slot per-pole-per-phase is chosen between 0.25- 0.5 in the three phase permanent magnet machines [35].

c) Conductors per Slot Selection

With the phase voltage V_{ph} (V), stator outer diameter D_{os} (mm), stack length l_s (mm), the air gap flux density B_g (T) and the frequency f (Hz), the number of conductors per each single stator slot N_s can be determined as:

$$N_s = \frac{V_{ph}}{\sqrt{2} \pi l_s f D_{os} B_g} \quad (5.6)$$

In each phase, coils are distributed in a number of slots and displaced from each other by a certain angle. The induced EMF in each phase differs by the same displacement angle. With the number of slots S , the number of phases N_{ph} and the number of poles

N_m , the slots-per-pole-per-phase q can be calculated by:

$$q = \frac{S}{N_{ph} N_m} \quad (5.7)$$

The pitch factor k_{ps} and the distribution factor k_{ds} can be calculated with two-layer winding type as defined in [63] as:

$$k_{ps} = \cos(\rho_s/2) \quad (5.8)$$

$$k_{ds} = \frac{\sin(q\gamma_1/2)}{q \sin(\gamma_1/2)} = \frac{1}{2q \sin\left(\frac{\pi}{6q}\right)} \quad (5.9)$$

Where ρ_s is the short pitch angle, and γ_1 is the slot pitch angle

$$\gamma_1 = \frac{\pi}{3q} \quad (5.10)$$

Thus, the winding factor can be expressed as:

$$k_w = k_{ps} k_{ds} \quad (5.11)$$

d) Phase Current Loading

The full load phase current is determined by using the following formula [63] :

$$I_L = \frac{P}{\sqrt{3} * V_{L-L} \eta} \quad (5.12)$$

Where, P is the active power, V_{L-L} is the line-to-line RMS voltage and η is the machine efficiency.

5.4.3.2 Mechanical Design of the BLDCM

Figure 5.4 illustrates the geometrical dimensions of the BLDCM. These dimensions are stated in equations (5.13) to (5.20) describing the machine structure.

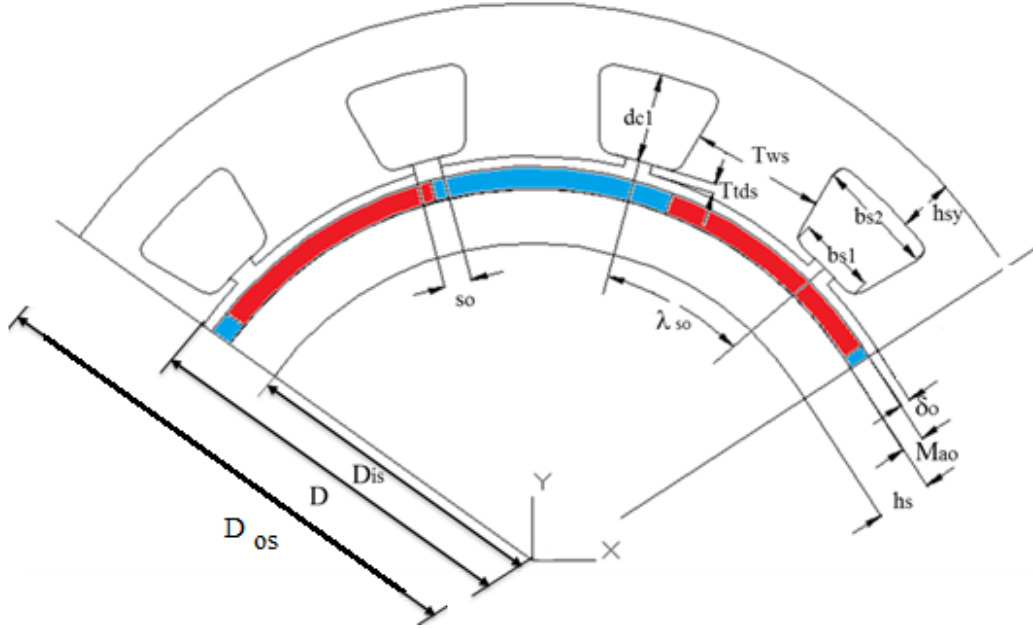


Figure 5.4: The geometrical dimensions for the BLDCM

$$D = D_{is} + 2h_s + 2M_{ao} + 2\delta_o \quad (5.13)$$

$$\lambda_{so} = \pi \frac{D}{Q_s} \quad (5.14)$$

$$b_{s1} = \pi \frac{(D + T_{tds})}{Q_s} - T_{ws} \quad (5.15)$$

$$h_{sy} = (D_{os} - D - 2d_{c1})/2 \quad (5.16)$$

$$b_{s2} = \pi \frac{(D + 2d_{c1})}{Q_s} - T_{ws} \quad (5.17)$$

The stator slot area A_s which is trapezium shaped can be calculated by eq. (5.18).

$$A_s = \frac{1}{2} (b_{s1} + b_{s2})(d_{c1}) \quad (5.18)$$

$$A_s = \frac{F_C}{k_f} \quad (5.19)$$

Where k_f is the winding space factor and F_C is the copper area per slot [64].

$$k_f = 0.3 \text{ to } 0.45, \text{ for round wires [64]}$$

$$d_{c1} = (2 \text{ to } 5)((b_{s1} + b_{s2})/2) \quad (5.20)$$

From equations (5.18), (5.19) and (5.20), the average slot width $h_s = (b_{s1} + b_{s2})/2$ and the shank length d_{c1} can be calculated. The configuration parameters and their definitions are illustrated in table 5.5.

Parameter	definition	Parameter	definition
D	Outer rotor diameter (mm)	b_{s2}	Upper slot width (mm)
d_{c1}	Shank length (mm)	h_{sy}	Back iron depth (mm)
s_o	Tooth gap width (mm)	M_{ao}	Outer magnet thickness (mm)
D_{is}	Inner stator diameter (mm)	δ_o	Outer air gap length (mm)
h_s	Sheet thickness (mm)	T_{tds}	Stator tooth tang depth (mm)
b_{s1}	Lower slot width (mm)	T_{ws}	Stator tooth width (mm)
D_{os}	Outer stator diameter (mm)	A_s	Slot area (mm ²)
λ_{so}	Slot pitch length (mm)	Q_s	Number of slots

Table 5.5: Parameters and definitions of the BLDCM configuration

a) Permanent Magnets Configuration

The configuration of the permanent magnet is shown in Figure 5.5. The permanent magnet dimensions have an effect on the air-gap flux. In addition, the permanent magnet plays a major role in producing a high torque density. The magnet thickness can be calculated using the air gap flux density B_g as stated in [65]:

$$B_g = \frac{M_a}{h_m + g} \cdot B_r \quad (5.21)$$

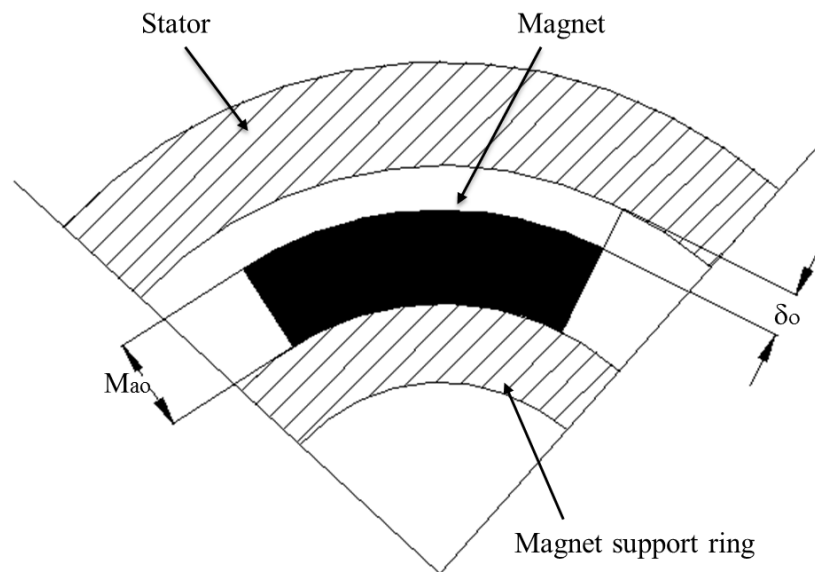


Figure 5.5: Permanent magnet thickness of the outer part (BLDCM)

With a permanent magnet type *NdFeB* (40 H), its remenant flux density $B_r = 1 T$, (see Appendix C4.1), the estimated air gap flux density $B_g = 0.85 T$ (see appendix C2.1) and the air gap length $\delta_o = 1 \text{ mm}$, has been calculated by using the MATLAB programme, see appendix A. The outer magnet thickness can be calculated as:

$$M_{ao} = \delta_o \frac{\frac{B_g}{B_r}}{1 - \left(\frac{B_g}{B_r}\right)} \quad (5.22)$$

Equation (5. 22) gives the outer magnet thickness $M_{ao} \cong 6 \text{ mm}$.

b) Flux Density in the Stator of BLDCM

The flux density checks are needed before starting to design the inner rotor. This is because the inner rotor tooth width is thinner than the stator tooth, which makes the flux density in its tooth higher. If the flux density in the stator tooth is high, corrective action is possible by reconsideration of the stator slot dimensions. The maximum stator tooth flux density B_{stm} and stator core flux density B_{scm} are calculated as defined in [63]:

$$B_{stm} = \frac{\frac{\pi}{2} B_m}{\frac{S_1}{p} T_{ws} l_s (SF)} \quad (5.23)$$

$$B_{scm} = \frac{\frac{B_m}{2}}{\left(\frac{D_o - D}{2} - d_s\right) l_s SF} \quad (5.24)$$

Where B_m is the maximum value of air gap flux, T_{ws} is the tooth width, l_s is the stack length, D_o is the stator lamination stack outside diameter, D is the stator bore diameter, d_{c1} is the slot depth as shown in figure 5.4 and SF is a stacking factor with the range $0.94 \leq SF \leq 0.97$ [63].

5.4.3.3 Mechanical Design of the PMIM

Designing of the PMIM can be determined by its geometrical structure as follows:

a) Configuration of the Inner Permanent Magnets

Figure 5.6 shows a cross section of the PMIM with the inner permanent magnet and the magnet support ring. The magnet support-ring is designed to have a 3mm thickness in order to withstand the high centrifugal force and not to be heavy during operation.

The inner permanent magnet thickness M_{ai} is calculated by using similar approach as the outer permanent magnet thickness designed in section 5.4.3.2. In this calculation the air gap length $\delta_i = 1\text{mm}$, $B_r = 1\text{ T}$, as stated in the data sheet of the permanent magnet (see appendix C4.1), and the estimated air gap flux density $B_g = 0.8\text{ T}$ (see appendix C2.2). Using these parameters in equation (5.22) results in an inner magnet thickness is equal to 4mm.

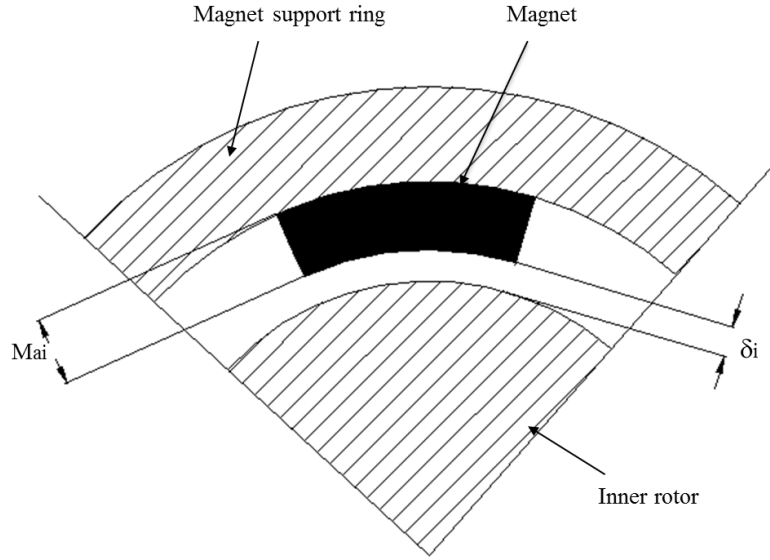


Figure 5.6: Permanent magnet thickness of the PMIM

Figure 5.7 shows the PMIM geometric structure. The following equations were used for the PMIM machine configuration.

$$D_{ri} = D_{ro} - 2M_{ai} - 2\delta_i \quad (5.25)$$

$$b_{r1} = \pi \frac{D_r - 2T_{tdr}}{Q_s} - T_{wr} \quad (5.26)$$

$$b_{r2} = \pi \frac{D_r - 2d_r}{Q_s} - T_{wr} \quad (5.27)$$

$$h_{ry} = \frac{1}{2}(D_r - 2d_r) \quad (5.28)$$

The configuration parameters and their definitions can be illustrated in table 5.6.

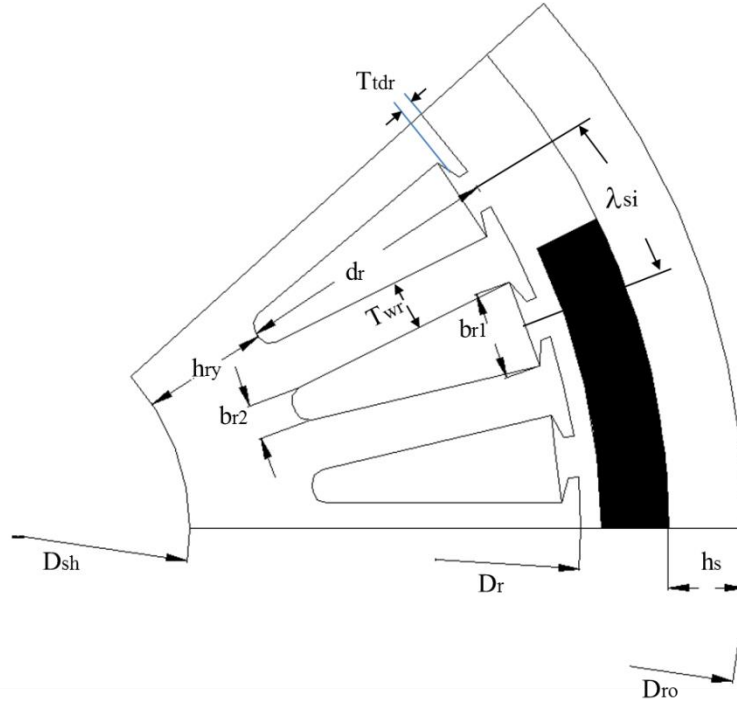


Figure 5.7: The geometrical dimensions of the PMIM machine

D_{ri}	Inner rotor diameter (mm)	d_r	Inner rotor slot depth (mm)
M_{ai}	Inner rotor magnet thickness (mm)	h_{ry}	Inner rotor Back iron depth (mm)
δ_i	Inner air gap length (mm)	T_{tdr}	Inner rotor tooth tang depth (mm)
b_{r1}	Lower slot width (mm)	T_{wr}	Inner rotor tooth width (mm)
D_r	Inner rotor outer diameter (mm)	b_{r2}	Upper slot width (mm)
λ_{si}	Inner rotor slot pitch (mm)		

Table 5.6: The configuration parameters of the PMIM

b) Inner Rotor Diameter Design

Since the stator was designed and both the conductor's current density and flux density were determined, the inner rotor can then be designed. The value of the air gap is fixed to be $l_a = 1$ mm with the chosen metal sheet thickness of the ring $b_{so} = 3$ mm and outer magnet thickness is to be $M_{ao} = 6$ mm, and the inner magnet thickness is to be $M_{ai} = 4$ mm. The inner rotor diameter D_{r1} can be found by:

$$D_{r1} = D_{os} - 2(M_{ao} + M_{ai} + h_s + \delta_i + \delta_o + h_{sy} + d_{c1} + T_{tds}) \quad (5.29)$$

c) Flux Density in the Inner Rotor Checks

The flux density checks are needed before starting to design the inner rotor. The maximum inner rotor tooth flux density B_{rtm} and the inner rotor core flux density B_{rcm} can be calculated as [63]:

$$B_{rtm} = \frac{\frac{\pi}{2} \phi_m}{\frac{S_1}{P} T_{wr} l_s(SF)} \quad (5.30)$$

$$B_{rcm} = \frac{\frac{\phi_m}{2}}{(D_r - 2d_r) l_s SF} \quad (5.31)$$

Where T_{wr} is the inner rotor tooth width, D_r is the inner rotor bore diameter as shown in figure 5.7.

5.4.4 Design and Configuration of the VFRT Machine

The following sections discuss the procedure of designing the VFRT machine, which is the second part of the EMTC system. The goal is to design a machine that can transmit power through its stator to eliminate the slip rings and to step up the inner rotor voltage.

a) Secondary Side Configuration

The mechanical design of the VFRT is carried out after designing the DM. The stator (secondary side) of the VFRT was chosen with the same stator configuration of the BLDCM stator. This leads to the stator bore of DM having the same dimensions as the stator bore of VFRT for ease of dismantling and air circulation.

b) Primary Side Configuration

According to Jimmie [63], in order to reduce the cogging torque, the number of rotor slots should be different to the number of stator slots according to the equation below:

$$S_1 - S_2 = \mp 3, \mp 5 \quad (5.32)$$

Where S_1 and S_2 are the stator and the rotor slots, respectively.

c) **Air Gap Sizing**

The significant portion of the effective reluctance in the machine is the air gap. The selection of this dominant factor can affect the determination of the required magnetization current required. Thus, the length of the air gap should be as short as realistically possible. However, in this machine, taking in the consideration the four bearings, the air gap is fixed to be 0.5 mm.

5.5 Design Optimization of the Differential Machine

The geometry of the two machines has been presented in the previous sections and the parameters explained in full in section 5.4.3. In order to optimize the design parameters, the machine geometry optimization is carried out along with an additional technique where the cogging torque can be minimized by using optimal magnet arc length formulas [66]. On the other hand, the pole-slot combination issue also influences the cogging torque [27]. Therefore, in this thesis the best pole-slot combination model is selected to minimize the cogging torque.

Studies in the literature that have focused on the minimization of the cogging torque and the ripple torque along with the investigation of the electromagnetic torque together are rare or non-existent. Most of the studies discussed in section 5.2.1 were limited to the study each of these subjects individually. However, in order to design an optimized system, it is not only the minimization of cogging torque that is the ultimate goal, but also the electromagnetic and ripple torques are considered as well. In this section, these three components are considered when designing the differential machine.

5.5.1 Optimization Design Methodology

The optimized design is implemented for the permanent magnet machines of the Differential Machine (DM). The simulation for both machines is performed by a 2-D FEM platform. The final design is obtained by using the following steps:

- Initialising the motor design specification.
- Selecting the pole-slot combination to be implemented in the EMTC system.
- Applying the related equations to choose the slot dimensions for both the interior and the exterior permanent magnet machines.
- Choosing the magnet arc length to produce a low cogging torque.

- Performing the FEM of each model to evaluate the machines' parameters and performance.
- Creating a lookup table and saving all the results that have been obtained.
- Selecting the models that match the first design criteria.
- Investigation to be carried out for the selected models in which the remained criteria are applied.

The 17 pole-slot models in each PM machines are investigated from Table 5.9. Then, a stator slot dimension is optimized in each model. The winding current density is calculated in order to avoid any saturation in the iron core or/and stator teeth. Once the FEM analyses have been pre-processed, the processing of the selected models according to the design criteria and their data are saved in a lookup table. Each single model is investigated for the minimum Cogging Torque CT , the higher Electromagnetic Torque T_{em} and lower Torque Ripple T_r .

5.5.1.1 Machine Specification

The investigated machines in this thesis are of the surface mounted magnets type, interior or exterior, see figure 5.8. In each machine type, the investigated models have the same external dimension; the difference between them is the slot-pole numbers and relevant stator configurations. Table 5.7 and 5.8 show the main design parameters of the BLDCM and the PMIM of the differential machine.

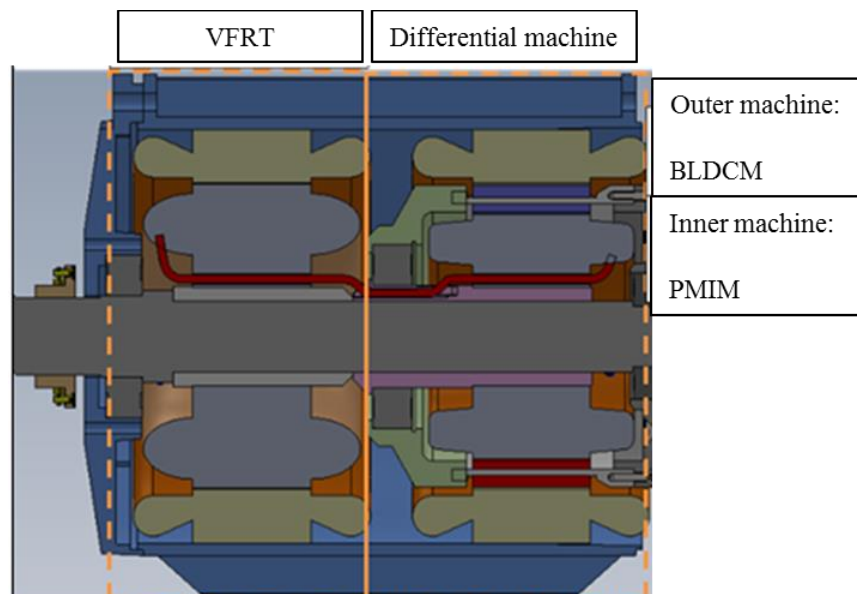


Figure 5.8: Cross-section of the EMTC system showing, the inner and outer machines of the differential machine and VFRT

Supply voltage: 250 V	PM rotor inner dia.: 136 mm	Core material: Losil 400
Rated speed: 1000 rpm	PM rotor outer dia.: 148 mm	Coil material: Copper
Air-gap thickness: 1 mm	Magnet thickness: 6 mm	Magnet Material: NdFeB
Magnet location: Interior	Stator inner dia.: 150 mm	Number of turns:50 turns
Stack length: 59 mm	Stator outer dia.: 204 mm	Cogging torque limit: ≤ 0.1 Nm
Tooth tang depth: 1.0 mm		Tooth gap width: 2.22 mm

Table 5.7: Specifications of the (BLDCM)

Rated rotor speed: 3000 rpm	Inner rotor inner dia.: 44 mm	Magnet thickness: 4 mm
Air-gap thickness: 1 mm	Inner rotor outer dia.: 120 mm	Magnet Material: NdFeB
Coil material: Copper	PM rotor inner dia.: 122 mm	Core material: Losil 400
Stack length: 59 mm	PM rotor outer dia.: 148 mm	Number of turns:50 turns
Slot depth: 25.9 mm	Magnet location: Exterior	Cogging torque: ≤ 0.1 Nm
Tooth tang depth: 1.0 mm	Shank length: 25 mm	Tooth gap width: 2.22 mm

Table 5.8: Specifications of the (PMIM)

5.5.1.2 Selection of Pole-Slot Combination

The number of poles for each machine part is from 8, 10 and 12 poles. The reason for choosing a large pole number is to provide a higher torque at a lower speed, to reduce the volume of the back iron, and to avoid increasing the size of end winding which leads to higher copper losses and leakage inductance. However, a large pole number will increase the fundamental frequency for a given speed, which may also increase the iron losses. The correspondence number of slots can be shown in Table 5.9 [27].

Slots	3	6	9	12	15	18	21	24	27	30	33	36	39	42	45	48
Poles	2	2	2	2	2	2	2	2	2	2	2	2	2	2	2	2
	4	4	4	4	4	4	4	4	4	4	4	4	4	4	4	4
			6	8	10	6	8	8	6	8	8	6	8	8	6	8
			8	10		8	14	10	8	10	10	8	10	10	8	10
			12	18		12	16	16	10	20	14	10	14	14	10	14
						14		20	12	22	20	12	16	16	12	16
						16			18	26	22	14	26	26	14	20
									20		26	16	28	28	16	32
									22		28	22	32	32	20	34
									24			24	34	34	28	38
												26			30	40
												28			32	
												30			34	
												32				

Table 5.9: Pole-slot combinations per each machine in the DM (The investigated pole-slot combinations are highlighted in red)

According to Hendershot [27], the more popular pole-slot combinations in manufacturing than others are listed in Table 5.9. On the other hand, some other pole-slot combinations such as 8 poles-15 slots, 10 poles-18 slots and 10 poles-21 slots are not listed because they do not have an identical Back EMF per phase neither in amplitude nor in phase.

The expression of an objective function to either minimize or maximize of the design variables is needed to achieve the optimization approach. The possible objective function is minimising the cogging torque, at keeping the electromagnetic torque high and the ripple torque low. These objectives are functionalised by the following.

- The permanent magnet configuration, contributing significantly to the motor performance.
- The use of a fractional slot motor configuration, minimizing copper losses.
- The slot dimensions, being essential for the field distribution and saturation.

The machine weight is mostly a function of these variables. Considering more challenges to achieve the motor performance and smooth run requirements than to attain a low motor weight where the bore sizing is kept fixed in all simulations. A high motor performance is more important than a low motor weight particularly in the torque converter purpose comparing to the overall vehicle's weight. On the other hand, the outer rotor needs to be able to run at a high load torque, and therefore its weight is not convenient as objective function.

5.5.2 Design Flowchart

Figure 5.9 shows the flowchart of the machine design procedure, according to the design specifications listed in tables 5.7 and 5.8. The design starts by determining the optimum pole-slot combination choices in both the minimum cogging torque and the high electromagnetic torque. The chosen models are then preceded to the next step for sizing their stator slot. The slot dimensions must withstand the current density. On the other hand, the teeth should be able to overcome any flux saturation. This flow chart is applied for both parts, the BLDCM and the PMIM, of the Differential Machine.

Figure 5.10 shows the final designing stage of the Differential Machine. It can be seen that it consists of two subroutines, one for the BLDCM and the other for the PMIM. The

program will terminate after examining the specified electromagnetic torque and the ripple values of the selected models that have the minimum cogging torque.

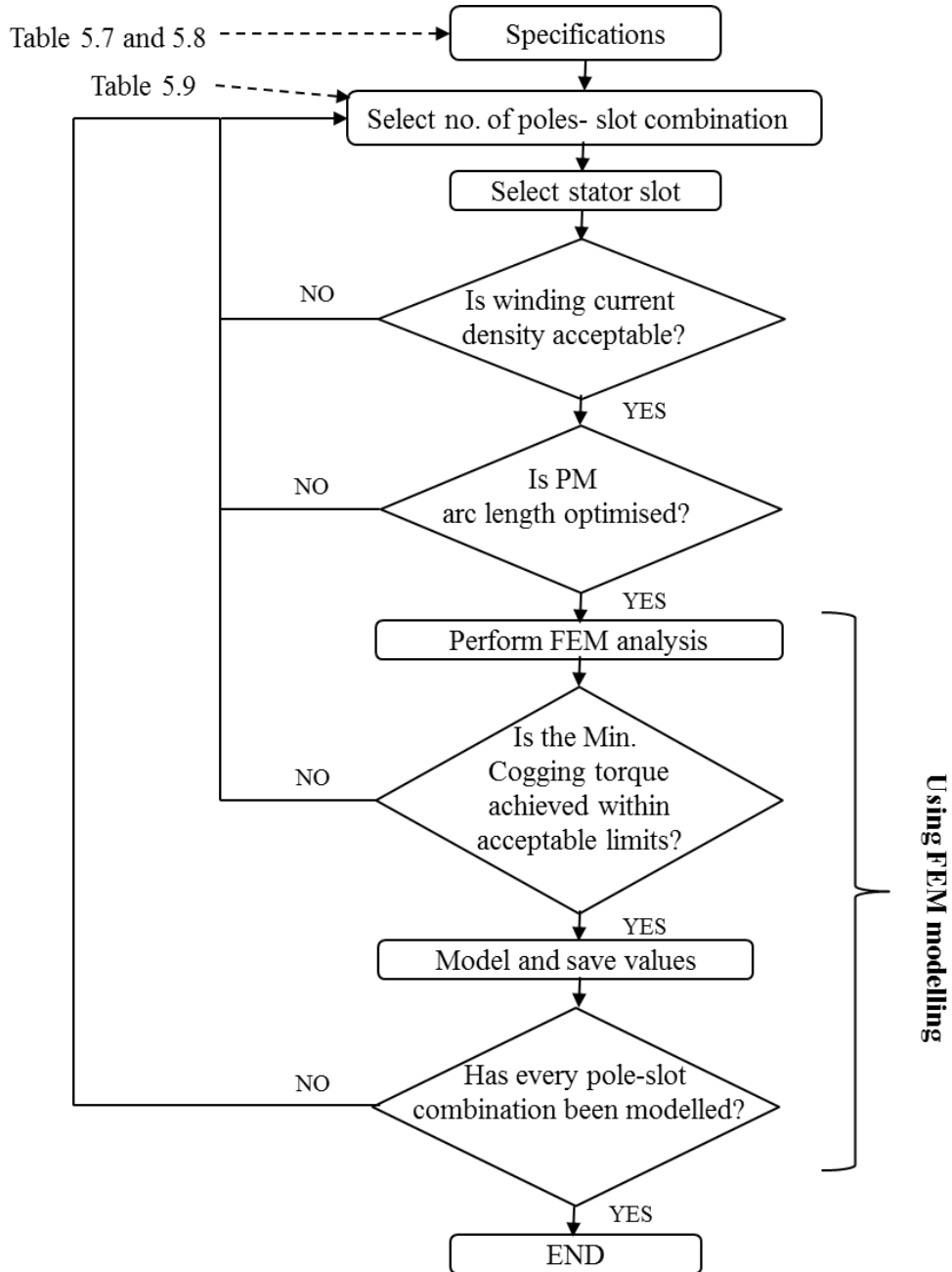


Figure 5.9: Flow chart of differential machine design procedure

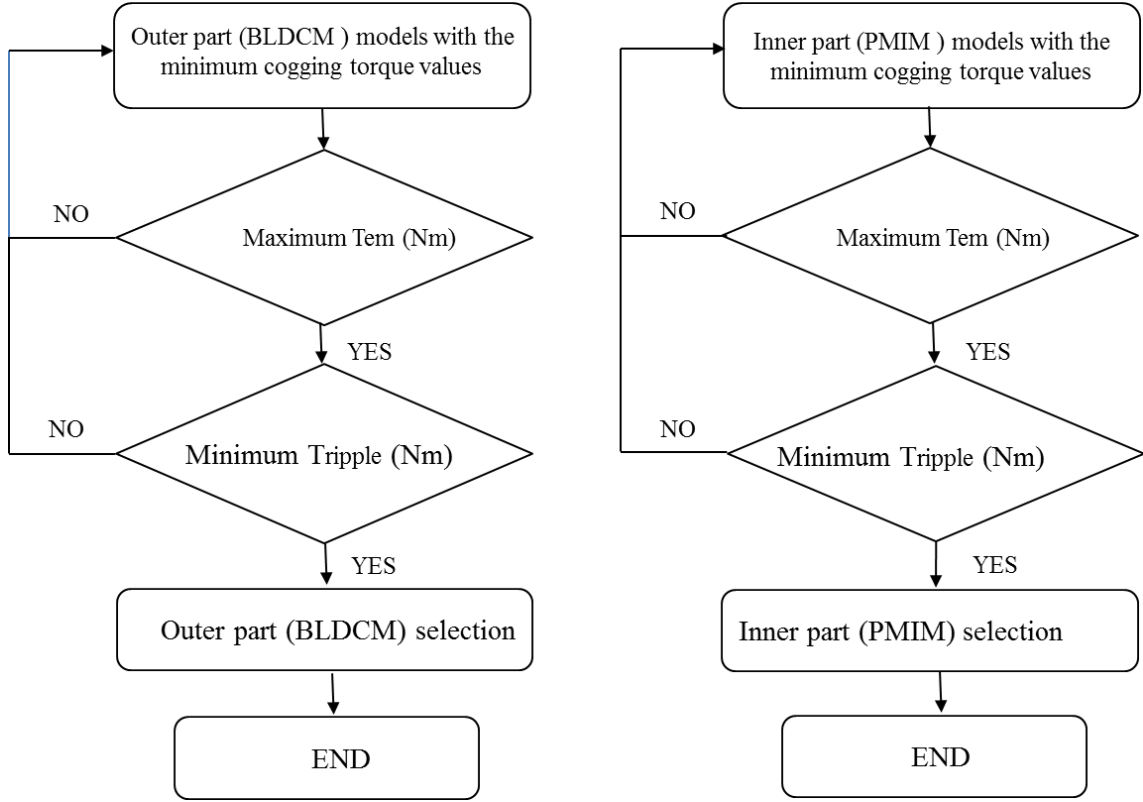


Figure 5.10: Complete chart of Differential Machine design method

5.5.2.1 Slot Design Optimization

The slot design is liable to depend on the geometrical variables which are limited by the lower and the upper band ranges [67]. Choosing the design variables x_1 to x_3 of the stator slot can be characterized. The x_1 is applied for the slot's upper dimension (bs_2), x_2 for the lower dimension (bs_1) and x_3 for its height (dc_1), x_{s-mid} is the middle width of the stator slot respectively, while the output variable is chosen to be y_1 for the overall slot area.

$$x_{s-mid} = \frac{x_1 + x_2}{2} \quad (5.33)$$

$$y_1 = f(x) = f(x_1, x_2, x_3) = 0.5 (x_1 + x_2)x_3 \quad (5.34)$$

$$0.6\lambda_1 \geq x_{s-mid} \geq 0.5\lambda_1 \quad (5.35)$$

$$4 \lambda_1 \geq x_3 \geq 2\lambda_1 \quad (5.36)$$

In the inner rotor slot as shown in figure 5.7, the input design variables are x_4 (b_{r2}), x_5 (b_{r1}) and x_6 (d_r) while the output variable is y_2 . Considering the slot is an approximate trapezoidal shape, the polynomial function can be stated as:

$$x_{r-mid} = \frac{x_1 + x_2}{2} \quad (5.37)$$

$$y_2 = f(x) = f(x_4, x_5, x_6) \cong 0.5 * (x_4 + x_5) * x_6 \quad (5.38)$$

$$0.4 d_{c2} > x_{r-mid} > 0.2 d_{c2} \quad (5.39)$$

$$0.7 x_{r-mid} > x_6 > 0.5 d_{s1} \quad (5.40)$$

Where x_4 is the bottom width, x_5 is the outer width of the slot, x_{r-mid} is the middle width of the inner rotor slot width respectively, and x_6 is the slot height.

The ranges of each parameter have been applied to have the proper slot area. The proper slot area means to limit the used space and hence improve the machine performance. Table 5.10 and table 5.12 illustrate the initial slot parameters; Table 5.11 and Table 5.13 give the final dimensions of the slot area.

Bore perimeter (mm)	λ_{s0} (mm)	Q_s	dc_1 (mm)	S_0 (mm)	T_{tds} (mm)
451.0	52.3	9.0	16.3	2.22	1.0
444.4	39.3	12.0	16.0	2.22	1.0
431.0	26.2	18.0	15.7	2.22	1.0
424.4	22.4	21.0	15.6	2.22	1.0
417.7	19.6	24.0	15.6	2.22	1.0
411.1	17.4	27.0	15.6	2.22	1.0
404.4	15.7	30.0	15.5	2.22	1.0
397.7	14.3	33.0	15.5	2.22	1.0

Table 5.10: Initial values of stator slot dimensions

Q_s	λ_{s0} (mm)	x_{s-mid} (mm)	Slot area (mm ²)	d_{c1} (mm)
9.0	52.3	25.2	320	11.6
12.0	39.3	19.0	237	11.5
15.0	31.4	13.7	168	10.2
18.0	26.2	12.7	156	11.3
21.0	22.4	11.0	133	11.3
24.0	19.6	9.6	116	11.3
27.0	17.4	8.5	104	11.3
30.0	15.7	7.7	93	11.2
33.0	14.3	7.0	84	11.2

Table 5.11: Final values of stator slot dimensions

D (mm)	λ_{si} (mm)	Q_s	d_r (mm)	br2 (mm)	T_{tdr} (mm)	x_{r-mid} (mm)	Slot Area (mm ²)
356.82	41.87	9	25.5	2.22	1.0	15.4	392
350.16	31.4	12	25.3	2.22	1.0	10.2	259
343.5	25.12	15	25.1	2.22	1.0	8.6	216
336.84	20.93	18	25.0	2.22	1.0	8.3	207
330.18	17.94	21	22.5	2.22	1.0	8.1	182
323.52	15.7	24	24.9	2.22	1.0	6.3	158
316.86	13.95	27	24.8	2.22	1.0	5.7	141
310.2	12.56	30	24.8	2.22	1.0	5.3	131
303.54	11.42	33	24.7	2.22	1.0	4.7	116

Table 5.12: Initial values of the inner rotor slot dimensions

Q_s	λ_{si} (mm)	x_{r-mid} (mm)	Slot area (mm ²)	d_r
9.0	41.87	25.1	446	26.3
12.0	31.4	18.8	332	26.0
15.0	25.12	15.1	264	25.9
18.0	20.93	12.6	219	25.8
21.0	17.94	10.8	170	23.3
24.0	15.7	9.4	163	25.7
27.0	13.95	8.4	145	25.6
30.0	12.56	7.5	130	25.6
33.0	11.42	6.9	118	25.5

Table 5.13: Final values of the inner rotor slot dimensions

5.5.2.2 Number of Turns per Slot per Coil Selection

During the comparison between 34 machine models, the number of turns of each coil is fixed by using the minimum slot area. According to tables 5.11 and 5.13, the minimum slot is 84 mm². Therefore, the number of turns to fill 80% of the selected slot is 50 turns, assuming the cross sectional area of the conductor is 1 mm².

- **Slot Tang Depth and Gap Width**

There are essential factors that affect the cogging torque such as the tang depth and the gap width. Investigations were performed by changing both the slot width or the opening W_o and the tooth tang depth T_d separately (see figure 5.11). The value of T_d was investigated first to find the best depth that gives a minimum cogging torque. Simulation results of the relationship between T_d and the cogging torque are shown in

figure 5.12. Obviously, the thinner the tang depth, the lower the cogging torque, but laser cutting or stamping the lamination needs to be considered. Therefore, a T_d of 1 mm was chosen and kept constant. With a fixed T_d , W_o was then varied by incremental values starting from 2 mm. Figure 5.13 shows the predicted cogging torque as the slot opening changes. However, the particular conductor gauge should be considered i.e. the minimum slot opening of 3mm could be chosen in practice.

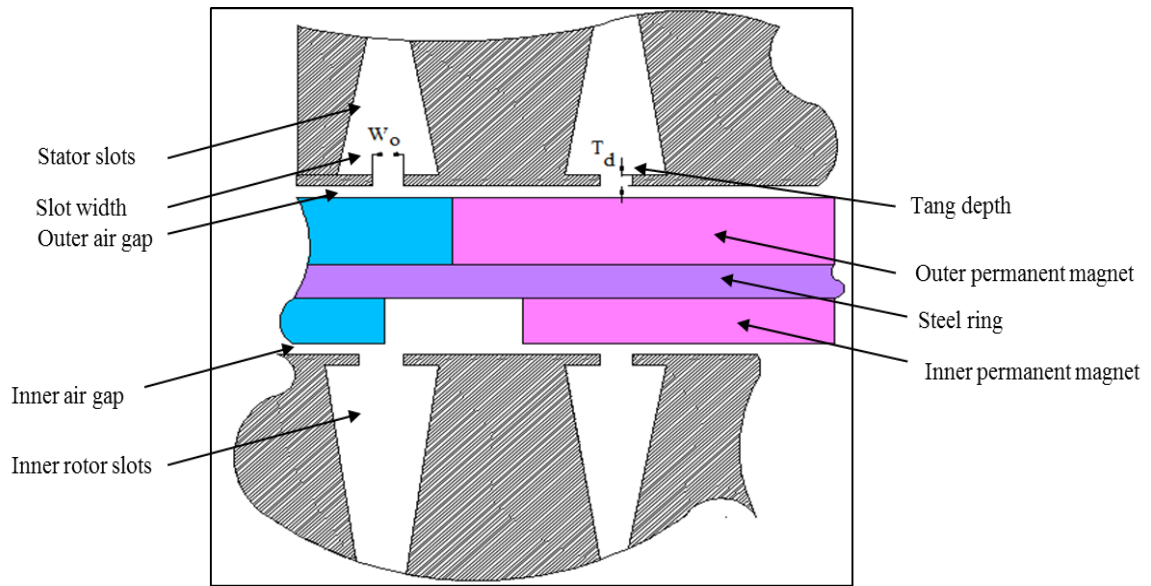


Figure 5.11: The tang depth and the gap width of the inner rotor and stator slots

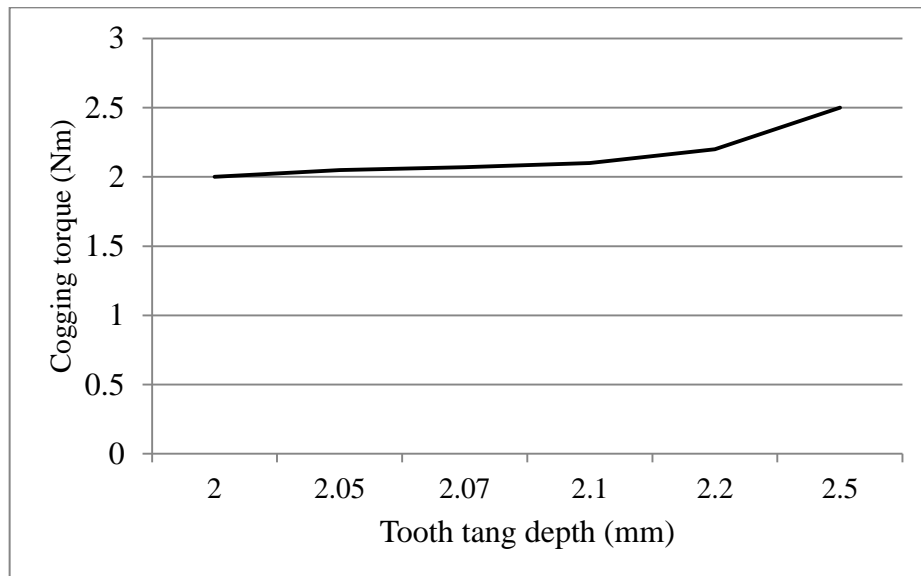


Figure 5.12: Relationship between the tooth tang depth and cogging torque

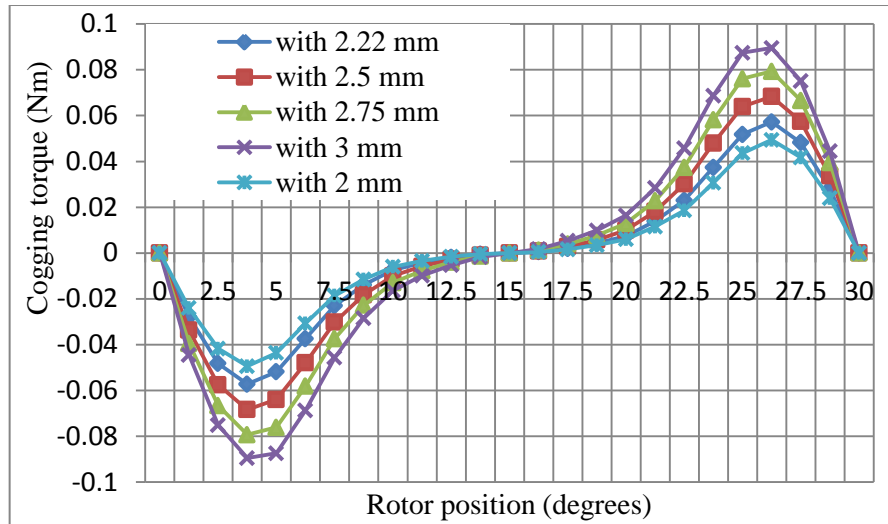


Figure 5.13: Relationship between the slot opening and cogging torque

The machines' slot dimensions were the subject of optimization. As the Differential Machine has two rotors, the heat that produced from both windings may cause power losses. Furthermore, the permanent magnet rotation produces heat, which may damage the machine. Therefore, the minimization of the slot dimension needs a cooling system that can withstand this temperature. On the other hand, an overly large slot dimension will lead to a high saturation in the inner rotor and the stator teeth.

5.6 Summary

The designed EMTC system consists of two parts, the differential machine (DM) and the variable frequency rotary transformer (VFRT). The DM part comprises of two permanent magnet machines, namely the Brushless DC machine (BLDCM) and the Permanent Magnet Induction Machine (PMIM). The DM consists of permanent magnet materials that interact with the stator slots of the BLDCM and the inner rotor of the PMIM. As a result a cogging torque is produced, which generates a noise in the machine and prevents the machine from rotating smoothly. Therefore, the cogging torque minimisation was the first goal in the system design. To do that, a double layer winding is selected, and the slot dimension of both the stator of the BLDC and the inner rotor of the PMIM was computed with respect to the machine performance. Then, the proper combination of pole and slot numbers was determined. The optimisation procedure of the design was introduced in order to select the optimum pole-slot combination in both machines of the DM. In the next chapter, Finite Element Method (FEM) is used to analyse both parts of the EMTC system.

6 Finite Element Modelling of the EMTC System

6.1 Introduction

In this chapter, the results of the investigation into the cogging, ripple and the electromagnetic torque for sixty-eight pole-slot combinations, 34 combinations for the Brushless DC Machine (BLDCM) and 34 combinations for the Permanent Magnet Induction Machine (PMIM) are presented. For each pole-slot combination, the number of slots per pole per phase (q) is calculated using equation (5.7) in chapter five and varied between 0.25 and 1.375. It can be shown by utilising Finite Element Modelling (FEM) how the machine design criteria that have already been specified in chapter 5 can be achieved and modelled.

6.2 Over view of FEM

MagNet and MotorSolve software packages, from the Infolytica Corporation (Montréal, Canada), were used to solve the electromagnetic problems in the electric machines in many publications such as [68-71]. The principle of this technique is to use a numerical approach to solve the differential equations in a continuous domain. The first application of FEM on electrical machines was made by Silvester and Chan [72]. They used nonlinear equations to formulate the field distribution inside the electrical motors. Their FEM methods are still being used in analysing the flux distribution and in the prediction of the electrical motor performance [73]. There are two kinds of electromagnetic problems including:

- Magneto static problem
- Magneto dynamic problem

The MagNet software provides the analysis of the machine structure as designed and drawn by users. This feature was applied to import conventional as well as non-conventional machines that can be drawn using the Computer Aided Design (CAD) software. The meshing element size and the processing data are then defined to achieve the solution. The finer the mesh the more accurate the results achieved but will take more time to solve the Maxwell's equations. The cogging, ripple and the electromagnetic torque were stringently analysed using both software analyses.

6.3 EFM Modelling Methodology

There are three stages to model a machine in the MagNet software listed below:

1. Pre-processing.
2. Processing.
3. Post processing.

6.3.1 Pre-Processing

At the beginning of modelling in FEM, this part is very essential. It has two tasks, material definition and mesh generation. The cross section for different machines can be divided in different regions such as stator lamination, air, and magnets. The mesh generation feature divides each region into small triangular elements after all the used materials are defined.

In this stage, all the requested input data are provided such as the current in the stator windings and all material characteristics of the machine (permanent magnet, copper wire and B-H magnetising curve).

6.3.2 Processing

The simulation of the electric machine according to the input data is calculated in this stage to solve the nonlinear differential equations. The input data can be used for estimating the flux in different elements. This stage is influenced by the meshing element size selection.

6.3.3 Post Processing

The extraction and the presentation of the FEM analysis results such as the flux distribution and the flux density from the problem solution is defined as post processing. The graphical facility gives important information from which the flux and flux density can be displayed based on the model solutions. Further details about the MagNet and MotorSolve software are in the Appendix B.

6.4 FEM Set-Up

The analysis of each machine of the electromagnetic torque converter (EMTC) system was undertaken individually. This is because the available FEM MotorSolve software platform, can analyse only the conventional machines which have one rotor and one

stator [74]. Then, as each machine's design is selected according to the proposed criteria, the integrated machine can be modelled in the FEM MagNet software.

6.4.1 Differential Machine Modelling Set-Up

The design specification of the BLDCM and the PMIM models were listed in tables 5.7 and 5.8. After the optimization process, the model of each machine will be defined. The following subsections present the Differential Machine (DM) components as shown in figure 6.1 (a, b) followed by the integrated model.

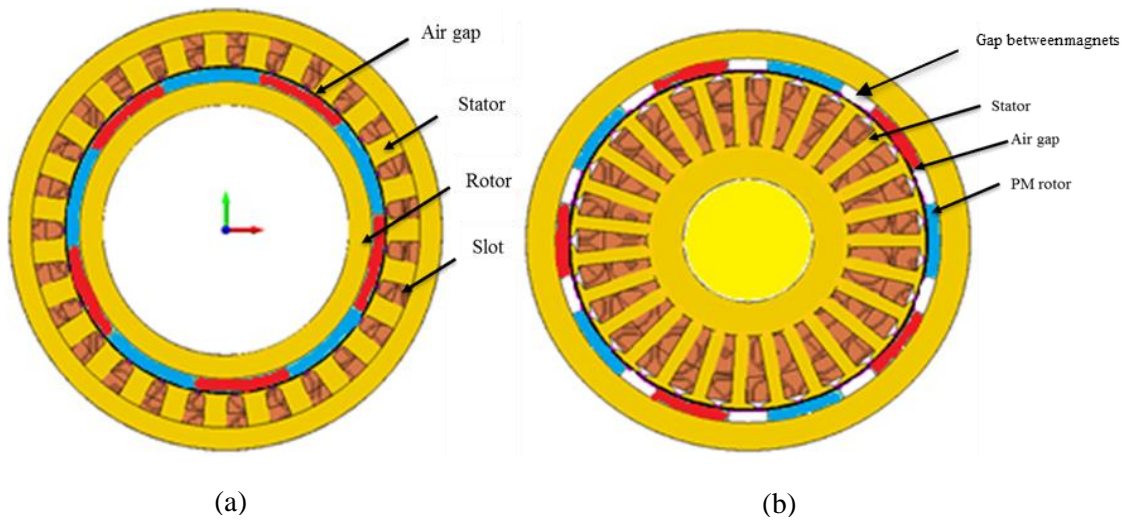


Figure 6.1: The DM components, a) BLDCM and b) PMIM machines

6.5 FEM Simulation Results

The presented results in this section are computed by using the software packages defined in section 6.2. Prior to simulation of the models shown in figure 6.1 (a, b), the MagNet software FEM meshing is generated over the cross section of each model. The FEM mesh of the selected models is illustrated in Figure 6.2 (a, b).

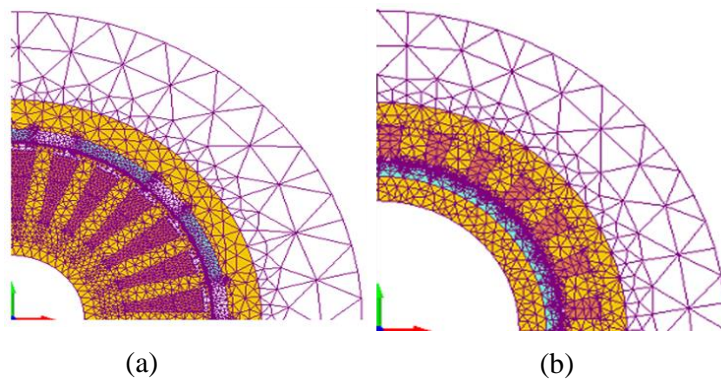


Figure 6.2: Finite element mesh of the a) BLDCM and b) PMIM models

6.5.1 Influence of the Combination of Pole and Slot Numbers

Low amplitude of the cogging torque is obtained by choosing slot and pole number that has a large LCM between them as shown in figure 6.3. On the other hand, the cogging torque frequency increases as the LCM decreases, as shown in table 6.1. The relationship between the amplitude and the frequency of the cogging torque can be stated as:

$$R_{cc} = \frac{N_m}{2} \frac{2\pi}{LCM} \quad (6.1)$$

Where, R_{cc} (deg.) is the complete cycle of the cogging torque profile, and N_m is the pole pair of the machine.

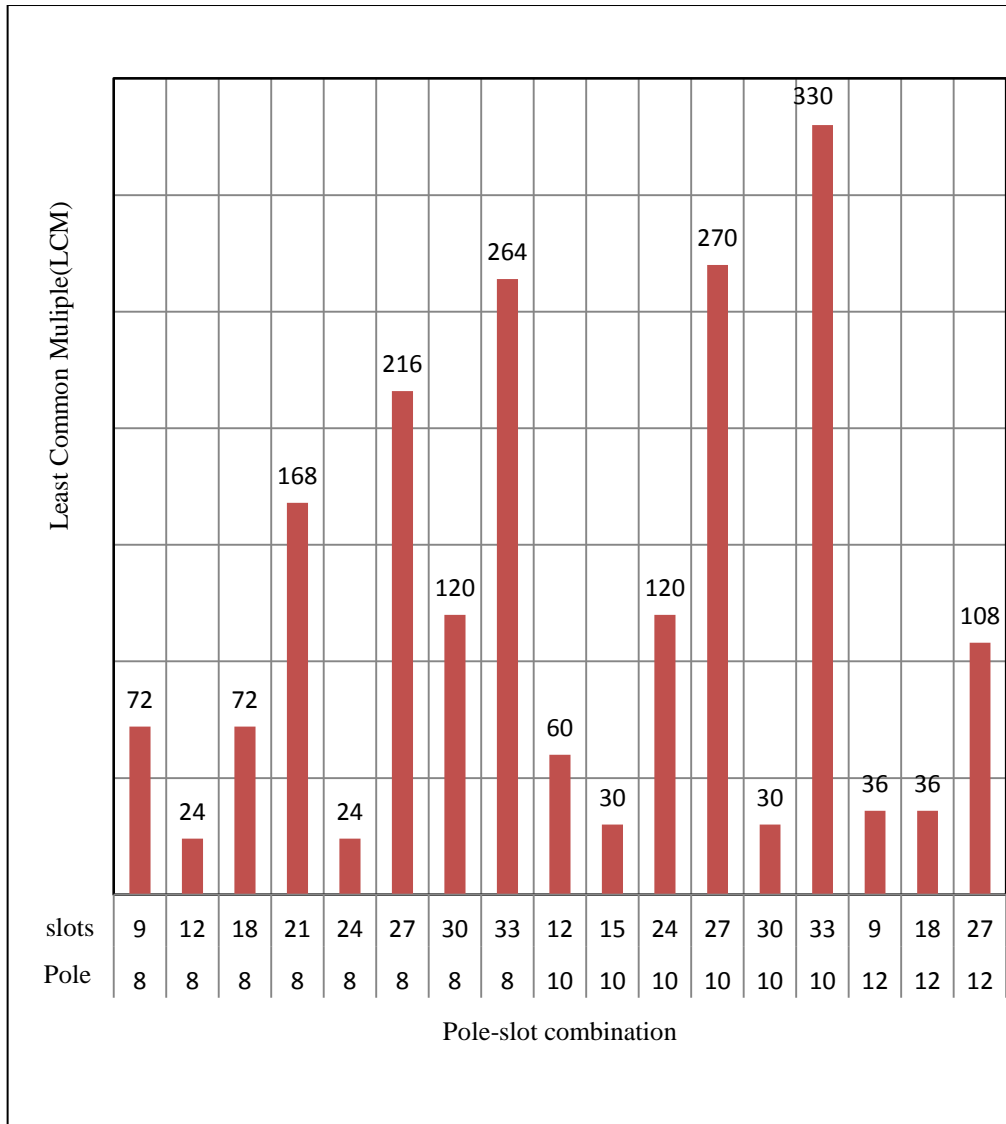


Figure 6.3: Least common multiple number chart of different pole-slot combinations.

Least Common Multiple (LCM)	Complete cogging torque cycle (deg.)
24	60
30	60
36	60
60	30
72	20
120	15
108	20
168	8.57
216	6.67
264	5.45
270	6.67
330	5.45

Table 6.1: The relation between the rotor position and the least common multiple

6.5.2 FEM Simulation of the Cogging Torque Using Iteration Technique

This sub-section presents investigations to the cogging torque in the Permanent Magnet (PM) models, how it was carried out, and how the minimum cogging torque was determined. The first stage was to investigate the influence of the pole-slot combination on the cogging torque. Tables 6.2 and 6.3 list the fully pitched magnet arc length of the inner (PMIM) and the outer (BLDCM) part respectively. To compare between the investigated models, they have the same slot opening, magnet thickness and air gap size. The least common multiple (LCM) between the number of poles and the number of slots in each of the PM machines is provided to show the influence of the LCM on the cogging torque [42]. The following investigations were carried out for both the Fully Pitched (FP) at first and then the Gapped Magnet (GM) models.

6.5.2.1 The Fully Pitched Models

There are 17 pole-slot combinations for each (inner) PMIM and (outer) BLDCM that have been investigated. The investigated pole-slot combinations are mixed, the fractional and the integral slot winding types. Tables 6.2 and 6.3 summarize the Cogging Torque (CT) simulations for 17 models of each machine. Table 6.2 shows the peak cogging torque as a function of a pole-slot combination of the PMIM. The FEM computed peak cogging torque varied over wide range from 0.013 Nm to 3.5 Nm with respect to pole-slot combination. It had a minimum peak value of 0.013 at a pole/slot combination of 10 pole-27 slots. The other pole-slot combinations that have a minimum

cogging torque in this table are 8 poles-27 slots, 8 poles-33 slot. On the other hand, for the BLDCM models, table 6.3 shows the minimum cogging torque of the following pole-slot combinations 8 poles-27 slots, 8 poles-33 slots, 10 poles-12 slots, 10 poles-27 slots and 10 poles-33 slots. The models that have the minimum cogging torque from tables 6.2 and 6.3 were then selected for the electromagnetic and the ripple torques comparison.

Pole- slot combination	q	LCM	CT (Nm)
8 poles- 9 slots	0.296	72	1.3
8 poles- 12 slots	0.222	24	1
8 poles- 18 slots	0.148	72	0.38
8 poles- 21 slots	0.126	168	0.1
8 poles- 24 slots	0.111	24	3.5
8 poles- 27 slots	0.098	216	0.062
8 poles- 30 slots	0.088	120	0.62
8 poles- 33 slots	0.08	264	0.054
10 poles- 12 slots	0.277	60	0.81
10 poles- 15 slots	0.222	30	1
10 poles- 24 slots	0.138	120	0.025
10 poles- 27 slots	0.123	270	0.013
10 poles- 30 slots	0.111	30	2
10 poles- 33 slots	0.10	330	0.03
12 poles- 9 slots	0.444	36	1.25
12 poles- 18 slots	0.222	36	0.6
12 poles- 27 slots	0.148	108	0.17

Table 6.2: FP models of the PMIM

Pole- slot combination	q	LCM	CT (Nm)
8 poles-9 slots	0.296	72	0.5
8 poles-12 slots	0.222	24	6
8 poles- 18 slots	0.148	72	1.3
8 poles-21 slots	0.126	168	0.18
8 poles- 24 slots	0.111	24	10.2
8 poles- 27 slots	0.098	216	0.08
8 poles- 30 slots	0.088	120	0.35
8 poles- 33 slots	0.08	264	0.054
10 poles- 12 slots	0.277	60	0.08
10 poles- 15 slots	0.222	30	0.33
10 poles- 24 slots	0.138	120	0.58
10 poles- 27 slots	0.123	270	0.021
10 poles- 30 slots	0.111	30	0.2
10 poles- 33 slots	0.10	330	0.07
12 poles- 9 slots	0.444	36	0.45
12 poles- 18 slots	0.222	36	0.35
12 poles- 27 slots	0.148	108	0.1

Table 6.3: FP models of the BLDCM

6.5.2.2 The Gapped Magnets Models

The investigation of the Gapped Magnet (GM) models is presented in this subsection. Prior to start investigation, there are two conditions: the gap between the magnets is identified as 5° incremental step avoiding fractions on a number (to be realistic for manufacturing) and the simulated models are among on those that have the minimum cogging torque on the FP models. Therefore, 27 slots with 8, 10 and 12 poles were selected for the further investigations. Although 8, 10 poles -33 slots produce a low cogging torque, they were excluded because it is very complicated to manufacture them. Hence, the gap space between the magnets was determined between 20 and 40 degrees in 8-pole machines in steps of 5 degrees. While in a 10-pole machine, the gap is selected between 15 and 30 degrees, and in the 12-pole machines, the gap is selected between 15 and 25 degrees incremented by 5 degrees at a step. Even though less than 20 degrees arc length of the magnet will not produce the required torque density, the investigations include them. The relevant results can be seen in table (6.4, 6.5 and 6.6).

Pole Arc Angle (degrees)	Cogging Torque (N. m)
40	0.058
35	0.055
30	0.042
25	0.045
20	0.043

Table 6.4: Cogging torque Vs spaces between magnets in (8 poles 27 slots GM)

Pole Arc Angle (degrees)	Cogging Torque (N. m)
30	0.015
24	0.004
20	0.017
15	0.011

Table 6.5: Cogging torque Vs spaces between magnets in (10 poles 27 slots GM)

Pole Arc Angle (degrees)	Cogging Torque (N. m)
5	0.4
15	0.45
20	0.05
25	0.38

Table 6.6: Cogging torque Vs spaces between magnets of (12 poles 27 slots GM)

It can be seen from tables 6.4, 6.5 and 6.6 that the minimum cogging torque is produced with 30°, 24° and 20° spaces between the magnets for 27 slots/ 8, 10 and 12 poles,

respectively. In other words, two thirds of the fully pitched arc length gives the minimum cogging torque at the investigated models, i.e. using 30° out of 45°, 24° out of 36° and 20° out of 30° degrees. The selection of the magnet pole and number of slots has been carried out by modelling the BLDCM using FEM. The models provided low cogging torque are 8 poles 18 slots, 8 poles 27 slots, 10 poles 27 slots, 10 poles 33 slots, 12 poles 9 slots and 12 poles 27 slots, see table 6.7. Since the minimum cogging torque obtained from 10 poles 27 slots, this configuration was selected in the design. Similarly, table 6.8 shows the PMIM selection of magnet pole and slot number respectively. There are five models provide low cogging torque, the 8 poles 21 slots, 8 poles 27 slots, 8 poles 33 slots, and 10 poles 33 slots, and the minimum cogging torque is 10 poles 27 slots. Therefore, the 10 poles 27 slots configuration was selected in the PMIM design.

In tables 6.7 and 6.8, it is clear that the LCM cannot always predict the cogging torque as stated in [37, 75, 76]. An example for both the FP and GM machines, the 10 poles-27 slots configuration has a low LCM and low cogging torque in comparison with the 10 poles-33slots configuration with higher LCM and cogging torque. This is because the machine design parameters also have influence on the cogging torque as discussed in [42, 75].

Pole- slot combination	q	LCM	CT (Nm)
8 poles- 9 slots	0.296	72	0.81
8 poles- 12 slots	0.222	24	1.8
8 poles- 18 slots	0.148	72	0.06
8 poles- 21 slots	0.126	168	0.03
8 poles- 24 slots	0.111	24	0.17
8 poles- 27 slots	0.098	216	0.042
8 poles- 30 slots	0.088	120	0.35
8 poles- 33 slots	0.08	264	0.018
10 poles- 12 slots	0.277	60	0.13
10 poles-15 slots	0.222	30	0.38
10 poles- 24 slots	0.138	120	0.5
10 poles- 27 slots	0.123	270	0.004
10 poles- 30 slots	0.111	30	3
10 poles- 33 slots	0.10	330	0.032
12 poles- 9 slots	0.444	36	0.021
12 poles- 18 slots	0.222	36	0.35
12 poles- 27 slots	0.148	108	0.05

Table 6.7: GM models of the BLDC machine

Pole- slot combination	q	LCM	CT (Nm)
8 poles- 9 slots	0.296	72	0.5
8 poles- 12 slots	0.222	24	3.5
8 poles- 18 slots	0.148	72	0.12
8 poles- 21 slots	0.126	168	0.058
8 poles- 24 slots	0.111	24	3.5
8 poles- 27 slots	0.098	216	0.018
8 poles- 30 slots	0.088	120	0.43
8 poles- 33 slots	0.08	264	0.026
10 poles- 12 slots	0.277	60	0.28
10 poles- 15 slots	0.222	30	3.9
10 poles- 24 slots	0.138	120	0.2
10 poles- 27 slots	0.123	270	0.0075
10 poles- 30 slots	0.111	30	7
10 poles- 33 slots	0.10	330	0.02
12 poles- 9 slots	0.444	36	1.2
12 poles- 18 slots	0.222	36	4
12 poles- 27 slots	0.148	108	0.15

Table 6.8: GM models of the PMIM

6.5.3 Summary of Using the Iteration Method

The iteration method has been used to investigate cogging torque of both the BLDCM and the PMIM with fully pitched and gapped magnet. The results of the minimum cogging torque that have been obtained can be summarized as follows:

The cogging torque is influenced by the pole-slot combination which is increased as the LCM decreased and vice versa. In addition, the winding type is another factor to determine the cogging torque, i.e. with the fractional slot winding type; the cogging torque is less than the integral slot winding type.

6.5.4 FEM Simulation Based on the Optimal Magnet Arc Length Calculations

The magnet pole arc length has a significant effect on the cogging torque amplitude [66]. The optimization of the magnet arc length α_p as shown in figure 6.4 and the equation (6. 2) is used to validate the FEM modelling and for the analysis of the 68 models in the two permanent magnet machines.

$$\alpha_p = \frac{N - k_i}{N}, \quad k_i = 0, 1, 2, \dots, N \quad (6. 2)$$

$$N = \frac{N_{sc}}{2N_m} \quad (6. 3)$$

The smallest common multiple N_{SC} between the slot numbers Q_s and the pole number N_m is a technique that is aimed at predicting the cogging torque amplitude. In order to avoid fringing at the magnet ends, a small factor is added to the equation 6. 2:

$$\alpha_p = \frac{N - k_i}{N} + k_f, \quad k_i = 0,1,2, \dots, N \quad (6. 4)$$

Where k_f basically has a small value from 0.01 to 0.03 mm [66]. This value is directly proportional to the air gap length.

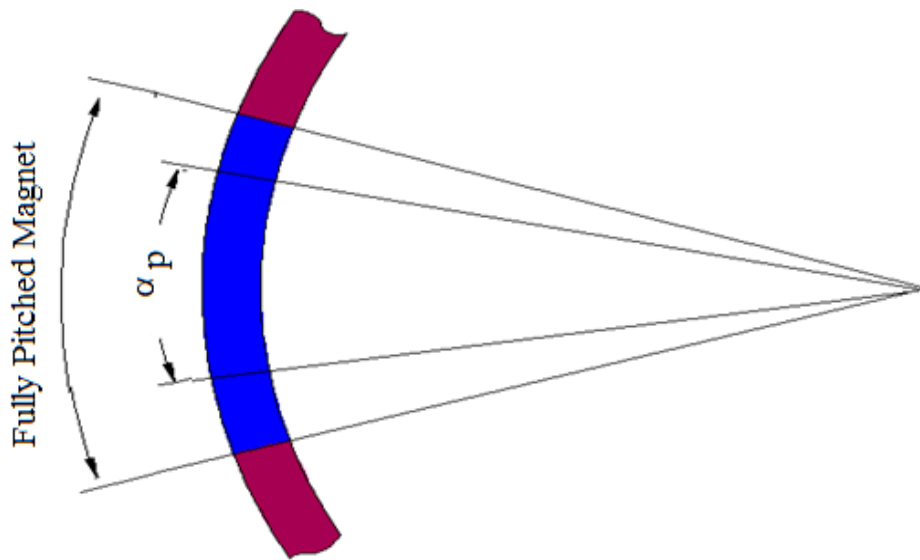


Figure 6.4: Magnet pole pitch

Further to the previous FEM iteration technique, equation (6. 2) can be applied to predict an optimal arc length in order to obtain the lowest cogging torque. The results that have been found by using iteration technique have been compared to the optimal arc length technique. It was started by calculating the Optimal Arc Length (OAL) in all the selected pole-slot combinations as shown in table 6.9. Then the first calculated arc length was selected because their arc lengths are the largest, which means that they can produce the highest electromagnetic torque.

p	Qs	Nc	N	Full magnet arc length	α at k=1	OAL	α at k=2	OAL
8	9	72	9	45	0.89	40.00	0.78	35.00
8	12	24	3	45	0.67	30.00	0.33	15.00
8	18	72	9	45	0.89	40.00	0.78	35.00
8	21	168	21	45	0.95	42.86	0.90	40.71
8	24	24	3	45	0.67	30.00	0.33	15.00
8	27	216	27	45	0.96	43.33	0.93	41.67
8	30	120	15	45	0.93	42.00	0.87	39.00
8	33	264	33	45	0.97	43.64	0.94	42.27
10	12	60	6	36	0.83	30.00	0.67	24.00
10	15	30	3	36	0.67	24.00	0.33	12.00
10	24	120	12	36	0.92	33.00	0.83	30.00
10	27	270	27	36	0.96	34.67	0.93	33.33
10	30	30	3	36	0.67	24.00	0.33	12.00
10	33	330	33	36	0.97	34.91	0.94	33.82
12	9	36	3	30	0.67	20.00	0.33	10.00
12	18	36	3	30	0.67	20.00	0.33	10.00
12	27	108	9	30	0.89	26.67	0.78	23.33

Table 6.9: An optimal arc length with respect to the full pole pitch

Based on the OAL for each single pole-slot combination that has been investigated for the BLDCM shown in table 6.10, the lowest cogging torque of investigated models was selected. From table 6.10, it can be seen that the 10 pole-27 slot produces the lowest cogging torque at 0.0056 Nm peak, followed by the 8 pole-33 slot combinations and 10 pole-33-slots at 0.0214 and 0.013 Nm peak, respectively.

p	Qs	OAL	CT
8	9	40	0.655
8	12	30	1.79
8	18	40	0.619
8	21	42.86	0.121
8	24	30	1.66
8	27	43.33	0.055
8	30	42	0.12
8	33	43.64	0.0214
10	12	30	0.114
10	15	24	0.38
10	24	33	0.283
10	27	34.67	0.0056
10	30	24	2.22
10	33	34.91	0.013
12	9	20	0.0633
12	18	20	0.341
12	27	26.67	0.094

Table 6.10: BLDC machine cogging torque with the OAL technique

Since the BLDC machine was configured and chosen to be 10 poles-27 slots, then the PMIM was also chosen to be from the 10 pole as well. Table 6.11 shows the cogging torque produced using the OAL of the first iteration of the 10 pole models. According to this table, the lowest cogging torque was produced by using 10 poles-27 slots [77, 78].

p	Qs	OAL	CT
10	12	30	0.266
10	15	24	4.06
10	24	33	0.436
10	27	34.67	0.0112
10	30	24	5.3
10	33	34.91	0.032

Table 6.11: PMIM cogging torque at OAL technique in 10 poles configuration

Both parts of the differential machine should give the same pattern of the back-EMF waveform i.e. both are trapezoidal type waveforms. Since the BLDCM gives a trapezoidal back-EMF waveform, the PMIM was adjusted by changing the permanent magnet configuration in order to give a trapezoidal waveform shape. Therefore, the iterations from table 6.9 were simulated to provide a trapezoidal waveform shape. This was achieved by using an arc length from either, 33.33, 32, 30.67 or 29.33 degrees. The cogging torque was simulated for these models to choose the lowest cogging torque, shown in Figure 6.5.

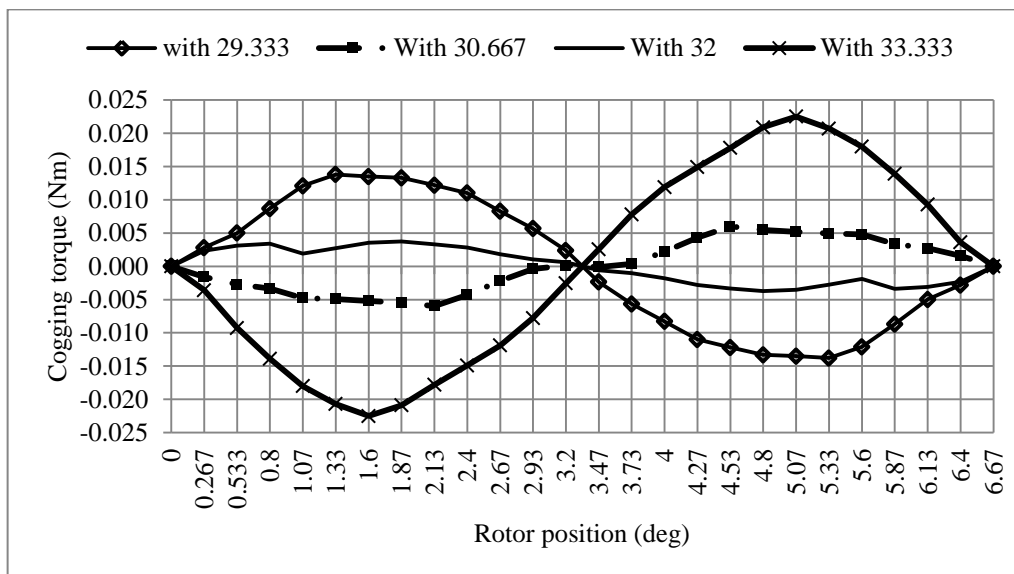


Figure 6.5: cogging torque for the PMIM 10 poles-27 slots machine

Figures 6.6 and 6.7 show the cogging torque comparison results between the actual mounted magnet arc length and the optimal arc length computed using the optimal technique for the BLDCM and the PMIM respectively. It can be seen in figure 6.6 that the actual inner magnet arc length of the PMIM is 30° , whereas the computed optimal arc length is 29.33° . This is because it is difficult to manufacture the computed optimal arc length. The same minor difference applies for the outer magnet arc length of the BLDCM as shown in figure 6.7. The arc length of 35° was used instead of 36° (full pitched magnet). Using 36° arc length is not practical because they have tolerances, which may be impossible to fit them in.

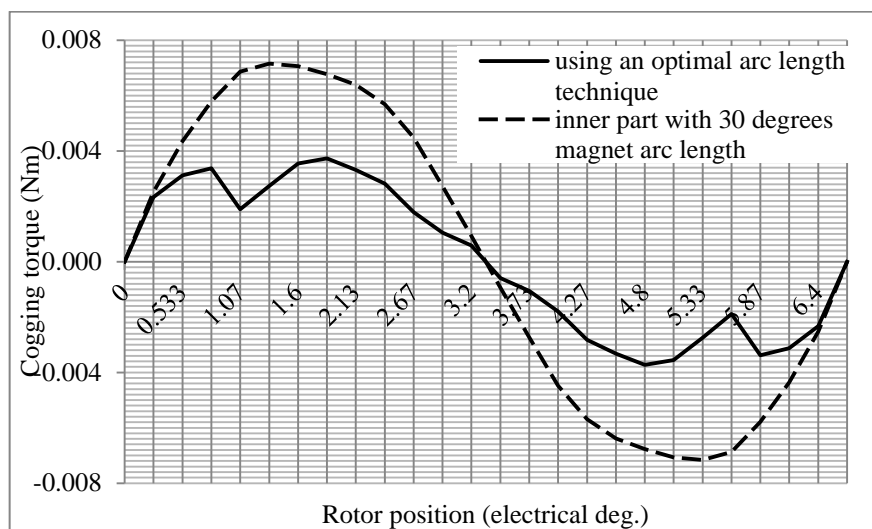


Figure 6.6: The inner part (PMIM) cogging torque

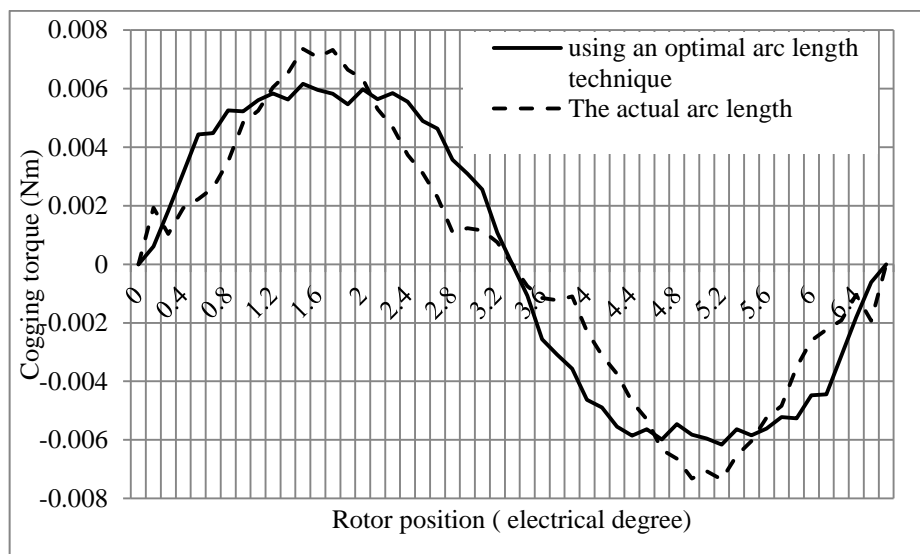


Figure 6.7: The outer part (BLDC) cogging torque

6.5.4.1 Integrated DM Simulations of the Cogging Torque

These simulations include several speed ratios between the inner and the outer rotor. The aim of these simulations is to predict the dynamic behaviour of the integrated machine under the following conditions. At the speed ratio between the outer and the inner rotor is 1000: 0 rpm, 0: 2000 rpm and 1000: 3000 rpm the computed cogging torque of these speed ratios are investigated as shown in figures 6.8-6.10, respectively. Figure 6.8 shows the computed cogging torque when the outer rotor is rotating at the maximum designed speed of 1000 rpm while the inner rotor is kept fixed. The simulation at the inner rotor rotates at the maximum designed slip speed can be shown in figure 6.9, while figure 6.10 illustrates the computed cogging torque waveform at the maximum speed designed of both the inner rotor and the outer rotor. The computed amplitude of the cogging torque at these speed ratios are listed in the Table 6.12. In general, the cogging is very low compared to the rated torque at all the simulated conditions. The low cogging torque may result in smoothed EMF waveforms in the stator and the inner rotor windings.

Speed ratio (outer rotor: inner rotor)	Cogging torque (Upper peak)	Cogging torque (lower peak)	Cogging torque (peak- peak)
1000: 0 rpm	0.031 Nm	-0.131 Nm	0.16Nm
0: 2000 rpm	0.036 Nm	-0.0078 Nm	0.04 Nm
1000: 3000 rpm	0.087 Nm	-0.084 Nm	0.17 Nm

Table 6.12: The relationship between the speed ratio and open circuit torque of the DM

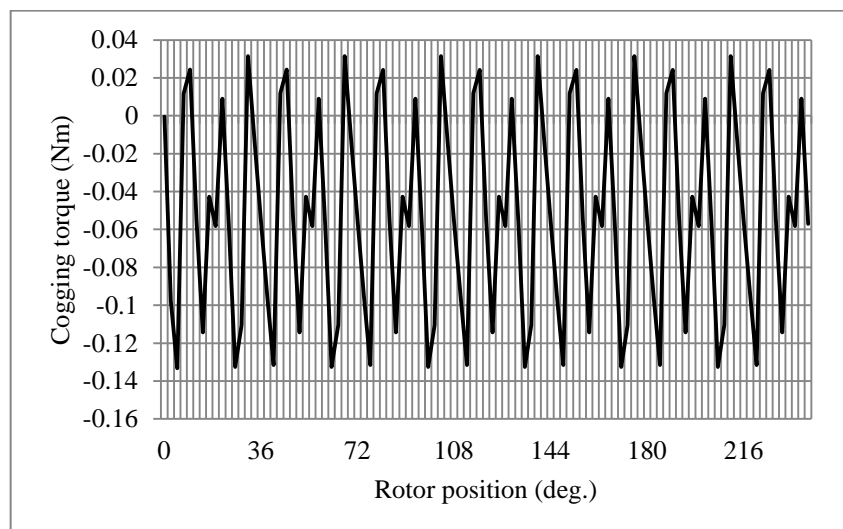


Figure 6.8: Cogging torque of the DM at 1000 rpm outer rotor rotates only

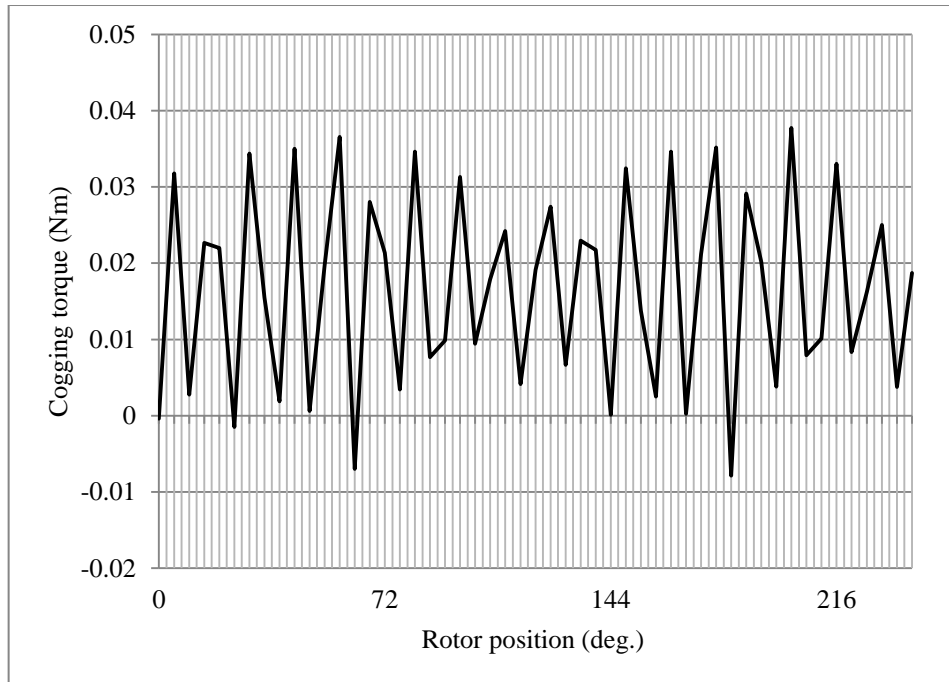


Figure 6.9: Cogging torque of the DM at inner rotor rotates 2000 rpm

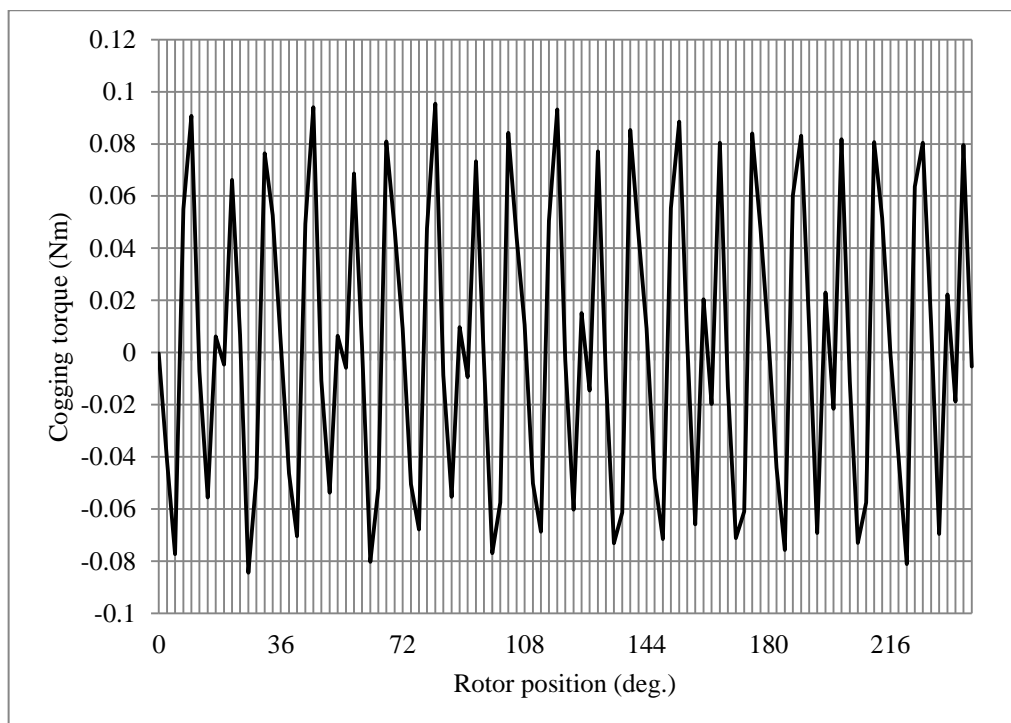


Figure 6.10: Cogging torque of the DM at 1000 (outer rotor) 3000 rpm (inner rotor)

6.5.5 FEM Simulation of the Electromagnetic Torque and Ripple Torque

Comparison of the two PM machines inside the Differential Machine in terms of the electromagnetic torque was carried out to select the most appropriate models. The number of turns per coil is kept constant, 50 turns for all simulations (as discussed in subsection 5.5.2.2), while the coil number was dependent on each single machine configuration. Since the current is proportionally related to the output torque, the rated current is chosen as an independent variable. By maintaining the ampere-turns AT for the investigated models constant, the T_{em} can be compared. The AT is defined in [28]:

$$AT = \frac{C_s N_s}{\pi D} I \quad (6.5)$$

Where, C_s is the number of coils per phase. The stator bore circumference πD is the same in each part model (inner and outer parts). Table 6.13 shows the models that have a minimum cogging torque, which were obtained from the flow chart presented in figures (5.9 and 5.10) in chapter 5.

Pole- slot combinations	Cs	Ns	Line Current (rms) for 2 phases	Line Current (rms) for 3 phases	Cs x Ns x I
8 poles- 18 slots GM	6	50	15.00	12.99	3896
8 poles- 21 slots FP	7	50	12.86	11.13	3896
8 poles- 21 slots GM	7	50	12.86	11.13	3896
8 poles- 27 slots FP	9	50	10.00	8.66	3896
8 poles- 27 slots GM	9	50	10.00	8.66	3896
8 poles- 33 slots FP	11	50	8.18	7.09	3896
8 poles- 33 slots GM	11	50	8.18	7.09	3896
10 poles- 12 slots FP	4	50	22.50	19.49	3896
10 poles- 27 slots FP	9	50	10.00	8.66	3896
10 poles- 27 slots GM	9	50	10.00	8.66	3896
10 poles- 33 slots FP	11	50	8.18	7.09	3896
10 poles- 33 slots GM	11	50	8.18	7.09	3896
12 poles- 9 slots GM	3	50	30.00	25.98	3896
12 poles- 27 slots GM	9	50	10.00	8.66	3896

Table 6.13: The excitation current for the BLDCM models

As can be seen from table 6.13 there are only 15 from 34 pole-slot combinations for the BLDCM that were selected. On the other hand, table 6.14 shows the pole-slot combinations, which are also obtained from flow charts in figures 5.9 and 5.10 for the PMIM. These combinations have the lowest cogging torques among the 34 models.

Pole- slot Combinations	Cs	Ns	Line Current (RMS) for 2 phases	Line Current (RMS) for 3 phases	I_x N_s x C_s
8 pole-21 slots GM	7	50	12.86	11.13	3896
8 poles- 24 slots FP	8	50	11.25	9.74	3896
8 poles- 27 slots GM	9	50	10.00	8.66	3896
8 poles- 27 slots FP	9	50	10.00	8.66	3896
8 poles- 33 slots GM	11	50	8.18	7.09	3896
8 poles- 33 slots FP	11	50	8.18	7.09	3896
10 poles- 24 slots FP	8	50	11.25	9.74	3896
10 poles- 27 slots FP	9	50	10.00	8.66	3896
10 poles-27slots GM	9	50	10.00	8.66	3896
10 poles- 33 slots FP	11	50	8.18	7.09	3896
10poles-33 slots GM	11	50	8.18	7.09	3896

Table 6.14: The excitation current for the PMIM models

6.6 Models Selection of the Differential Machine

The models selection of the DM was achieved according to the minimum cogging torque and high electromagnetic torque with low ripple torque. Figures 6.11 and 6.12 illustrate the simulated cogging torque of the 34 models at each part. The electromagnetic and the ripple torque of both parts are shown in figure 6.13 and 6.14. Hence, the selected PMIM and BLDCM pole- slot combinations are 10 pole-27 slots at each machine. Figure 6.15 shows the predicted electromagnetic torque that can be produced in each machine, BLDCM and PMIM.

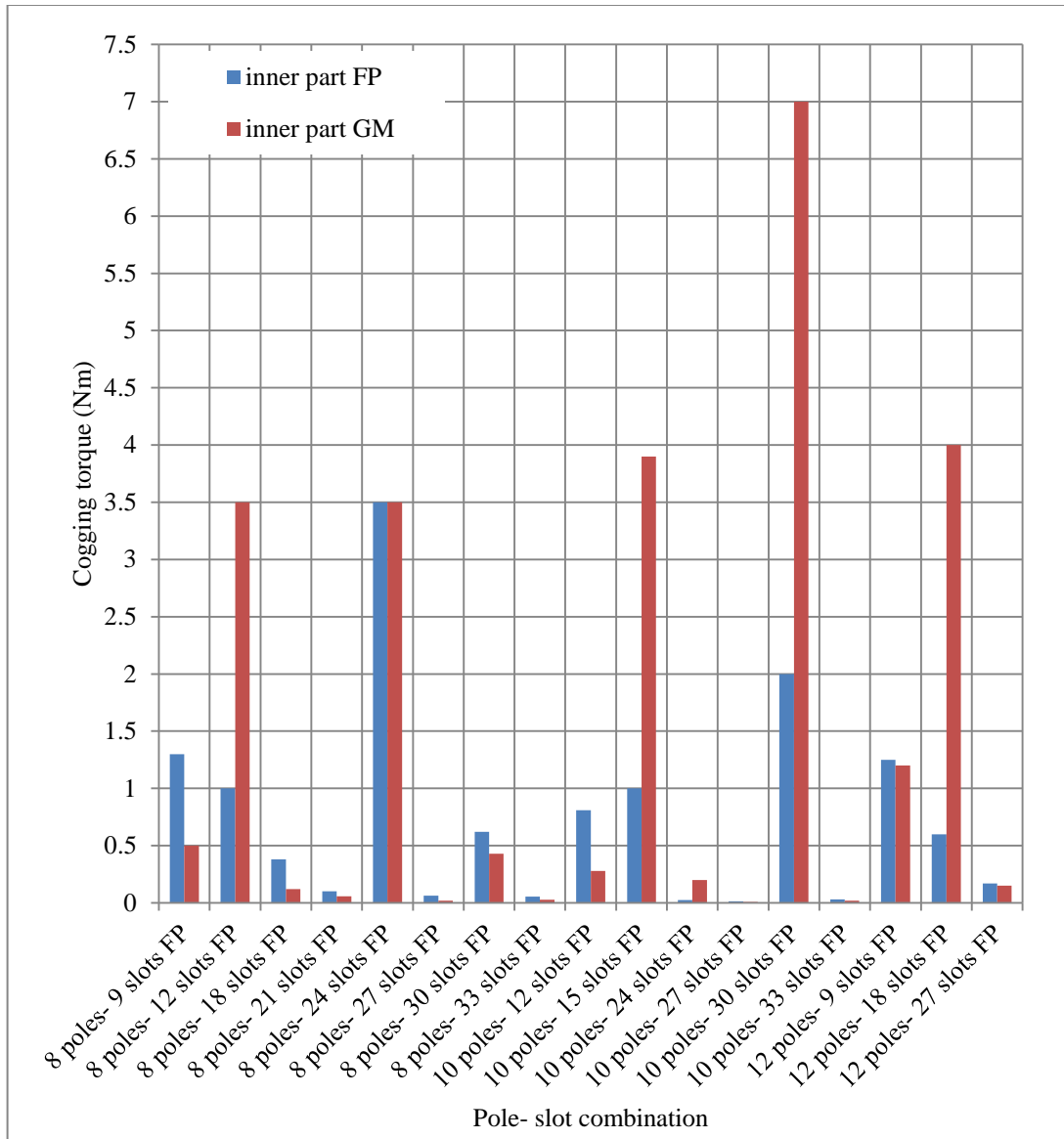


Figure 6.11: Cogging torque of 34 pole- slot combinations of the PMIM

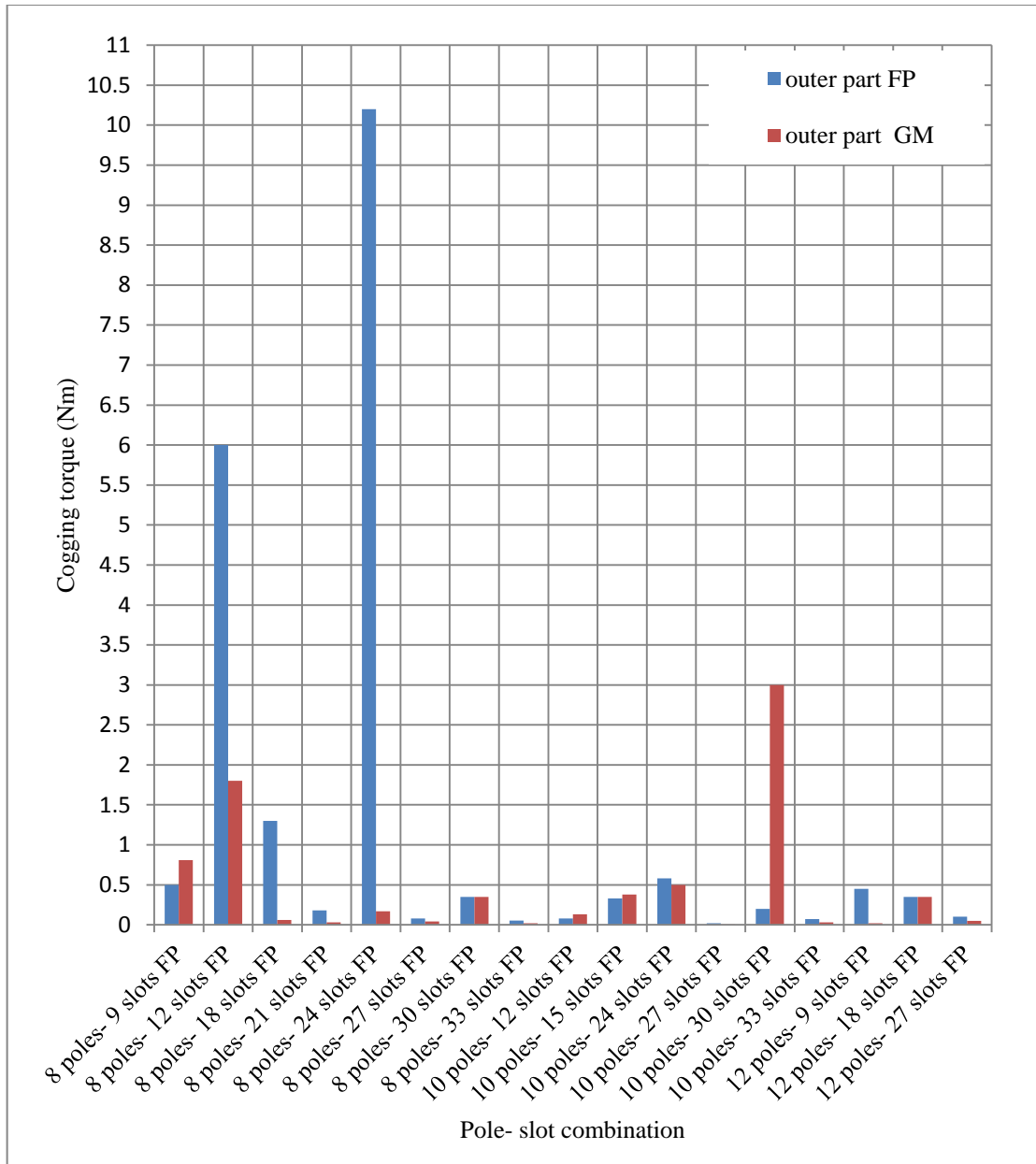


Figure 6.12: Cogging torque of 34 pole- slot combinations of the BLDCM

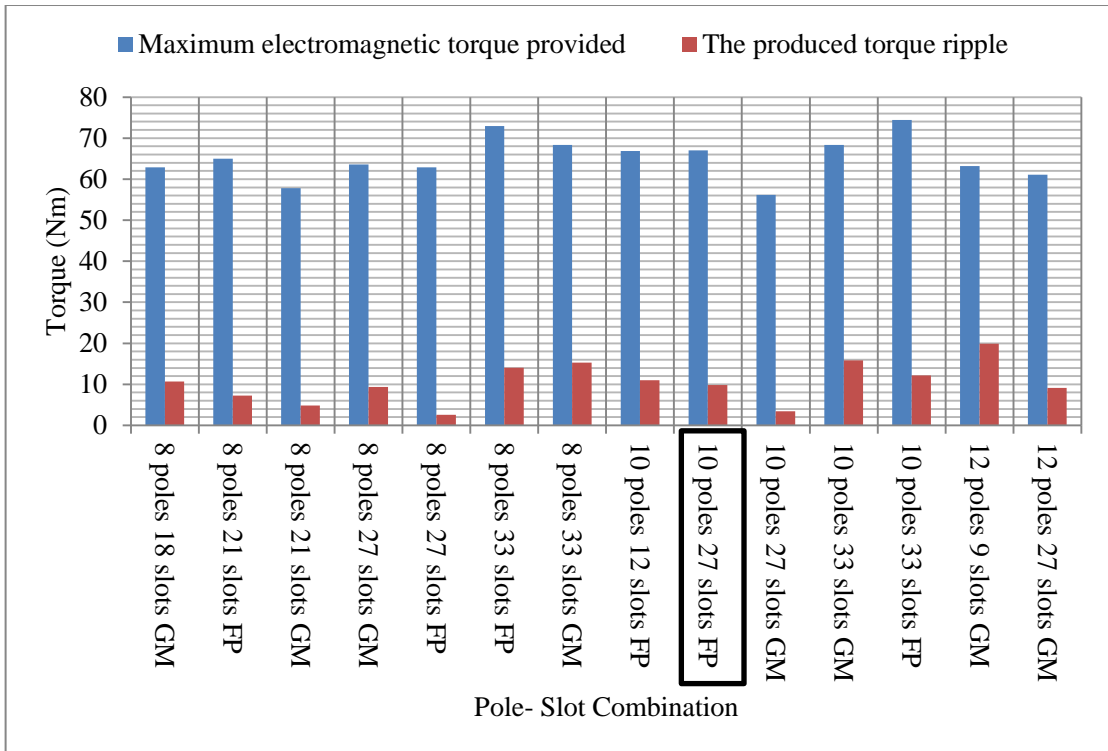


Figure 6.13: Electromagnetic torque and ripple torque of the minimum cogging torque models of the BLDCM, the black box defines the selected model

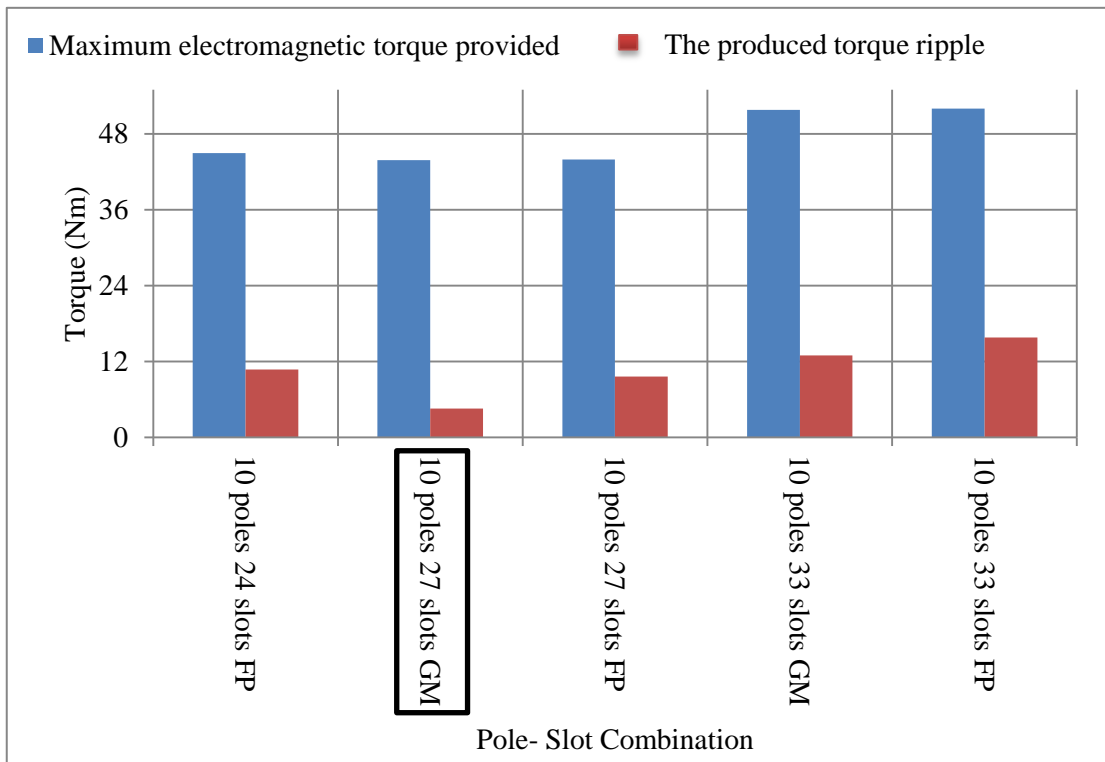


Figure 6.14: Electromagnetic torque and ripple torque of the selected 10 poles models that have minimum cogging torque of the PMIM, the black box defines the selected model

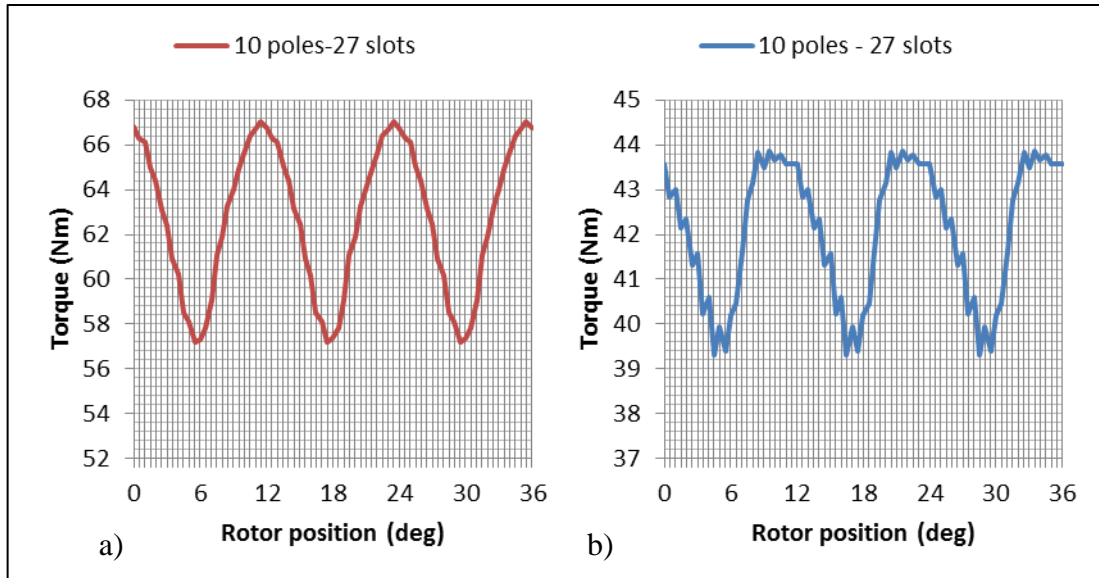


Figure 6.15: Electromagnetic torque of the a) BLDC Machine and b) PMI Machine

6.6.1 Winding Distribution of the Differential Machine

The winding distribution of the inner rotor is shown in Figure 6.16. The input and output of each coil in the three phase windings are illustrated in Table 6.15. The fractional slot winding type is used in the stator and inner rotor of DM. The reason for using this type of winding is to decrease the copper losses. In addition, this type of winding is easily wound on each teeth, which will reduce the production cost [79]. Moreover, the concentrated fractional slot winding (FSCW) reduces the torque ripple, cogging torque, high efficiency, short end turns [80] and increase the torque density [81]. However, there are some drawbacks for using this type of winding. Firstly, the pole-slot combination needs to be selected carefully otherwise, the winding factor will be very low [82]. Secondly, the non-overlapping windings have a higher iron losses [83, 84]. The former disadvantage was solved by selecting a pole-slot combination that has a minimum cogging torque. The later drawback was solved by using very thin laminations (0.5 mm) in order to reduce the eddy current and the iron losses.

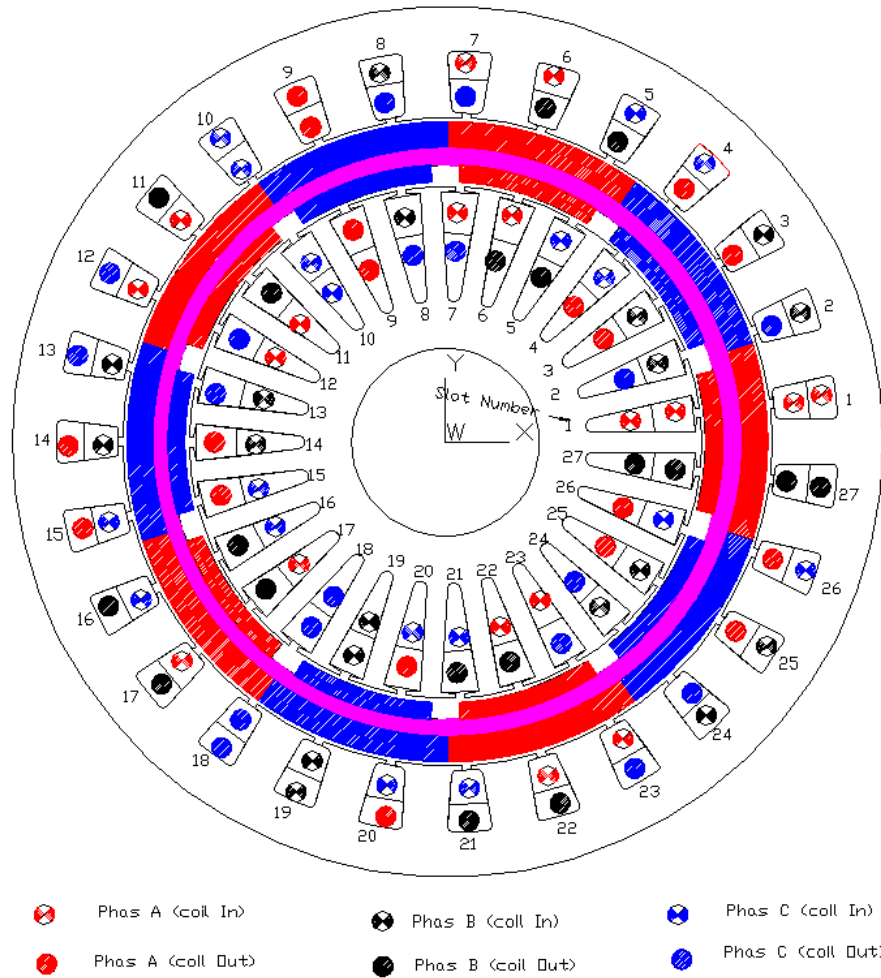


Figure 6.16: The winding distribution of the DM

Number of coils	Phase A		Phase B		Phase C	
	In	Out	In	Out	In	Out
1	1	3	19	21	10	12
2	6	4	24	22	15	13
3	7	9	25	27	16	18
4	11	9	2	27	20	18
5	12	14	3	5	21	23
6	17	15	8	6	26	24
7	22	20	13	11	4	2
8	23	25	14	16	5	7
9	1	26	19	17	10	8

Table 6.15: The coils distribution for each phase

6.7 Integrated Differential Machine Modelling Methodology

Since the DM has a complex geometry, a geometric modeller is required. However, the FEM (MagNet software), provides modelling support to model drawn by the user [85]. Hence, the DM model was drawn in the AutoCAD® software program (Autodesk Inc.,

San Rafael, CA) and then modelled in FEM as structured in the flowchart shown in figure 6.17. The method starts form stage-I, in which the PMIM geometry was exported from the AutoCAD to the FEM workspace Magnet in a Drawing Exchange File (DXF) format. All the materials throughout the model were then selected including the permanent magnets, stator yoke, rotor yoke, air gap and the support ring. To complete the modelling of the DM (see stage II), the coils were then inserted in the slots. The static solver was applied to define the pole numbers and then an open circuit was simulated to evaluate the back EMF waveform results. The drawing of the DM shown in Figure 6.18 and its specifications are listed in Table 6.16.

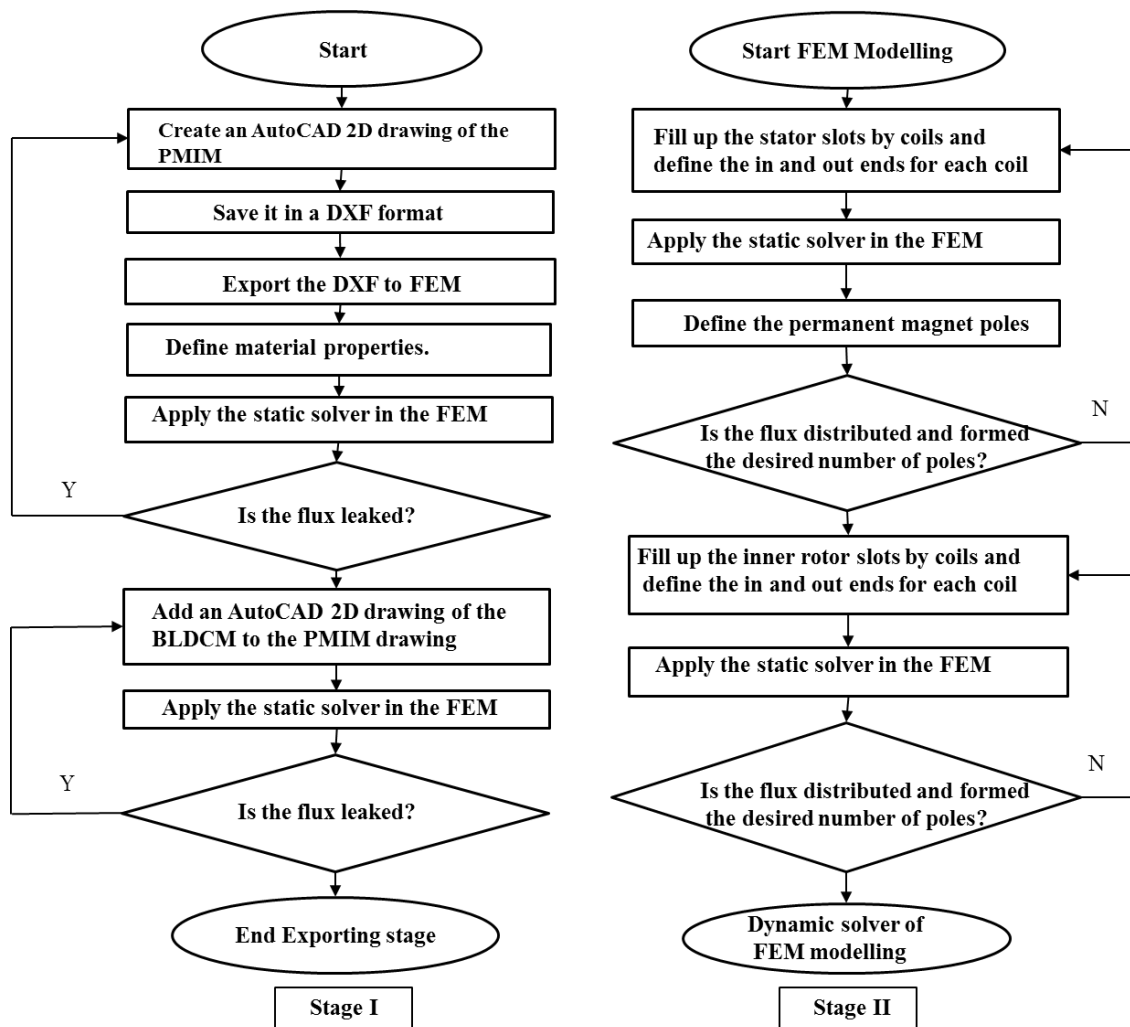


Figure 6.17: Flow chart for FEM modelling of the EMTC system

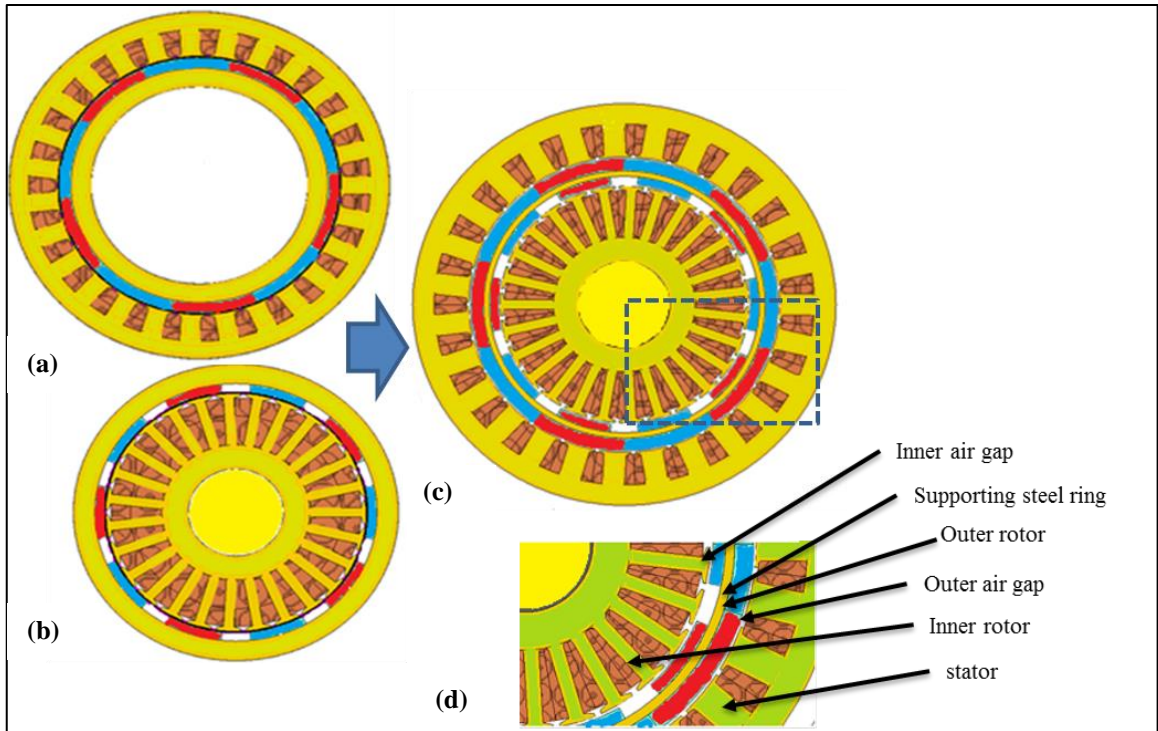


Figure 6.18: The cross section of the (a) PMI Machine, (b) BLDC Machine, (c) the integrated machine and (d) part of the integrated machine

Stator inner diameter	150 mm
Stator outer diameter	204 mm
Inner rotor inner diameter	44 mm
Inner rotor outer diameter	120 mm
Outer rotor inner diameter	122 mm
Outer rotor outer diameter	148 mm
Stack Length	59 mm
Permanent magnet material	Neodymium (NdFeB)
Coil material	Copper
Inner air-gap thickness	1 mm
Outer air-gap thickness	1 mm
Outer set magnet thickness	6 mm
Inner set magnet thickness	4 mm
Core material	Losil 400
Coil configuration	Concentrated fractional slot type
Layer type	double

Table 6.16: The Parameters and design Specification of the EMTC Differential Machine

6.7.1 FEM Simulation of the Back-Electromagnetic Force

The back EMF waveforms for both parts of the differential machine were simulated using the MagNet software package. As stated earlier, the PMIM and the BLDCM were selected as 10 poles-27 slots, with 30° and 35° arc length respectively. The number of turns in both machines was 50 turns per coil as stated in chapter three. The wound rotor of the PMIM was simulated with a rated speed of 3000 rpm while the BLDCM rotor rated speed was set at 1000 rpm. Figure 6.19 and figure 6.20 show the back EMF waveform produced by the PMIM and BLDCM that have a trapezoidal waveform shape. The simulation results have been taken as each machine is analysed separately. It can clearly be seen that the voltage in the BLDCM windings at open circuit is 370 V and at the PMIM is 692 V. Moreover, the back-EMF analyses were investigated at the integrated Differential Machine at several conditions. The aim of the simulation is to predict the induced back-EMF at both parts of the integrated machine in order to give an indication whether the inner rotor voltage is able to overcome the BLDCM back-EMF at different slip speeds.

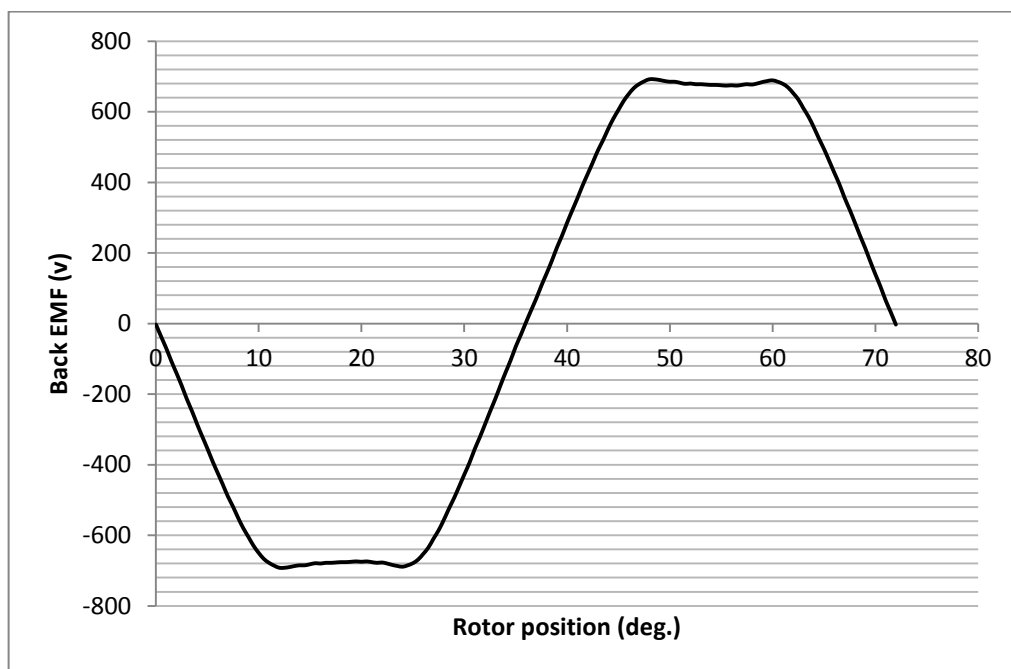


Figure 6.19: The back EMF in the inner rotor windings of the PMIM

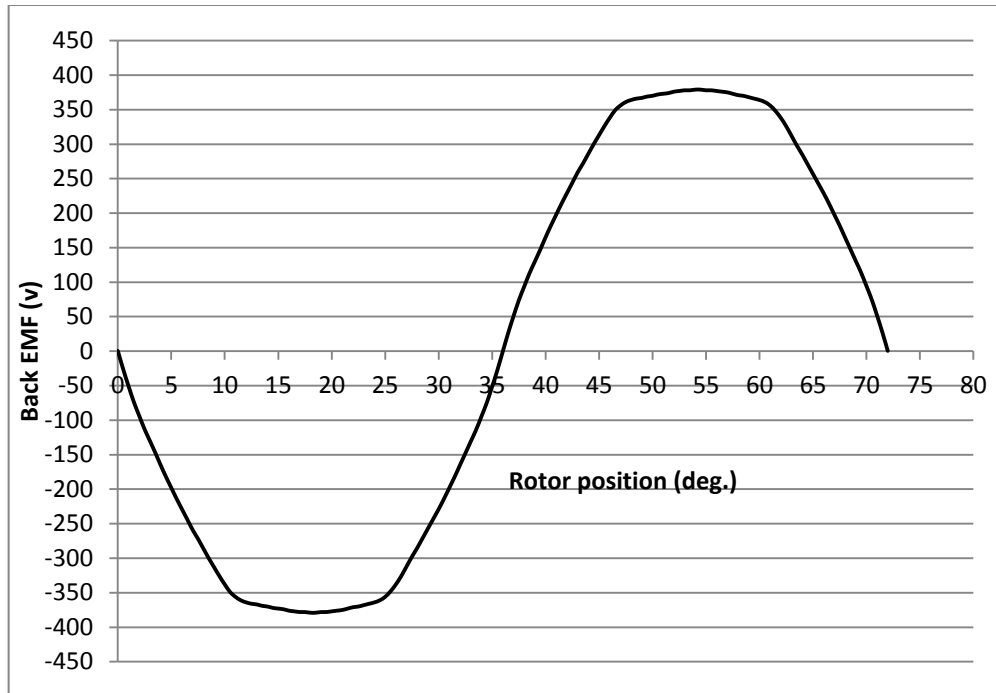


Figure 6.20: The back EMF in the stator windings of the BLDCM

The integrated DM model was simulated using the FEM MagNet software when both the stator of the BLDCM and the inner rotor windings of the PMIM were kept open circuited. With open circuit windings and the permanent magnet rotor rotates, the back EMF in both windings are induced according to the Faraday's law. The investigation was carried out under two conditions. First, when the outer and the inner rotors rotate in the same direction at 1000 and 3000 rpm, respectively. Secondly, when the outer rotor only rotates at 1000 rpm and the inner rotor was kept locked. The simulation results of these conditions are shown in figure 6.21 (a, b) and figure 6.22 (a, b). Figure 6.21a shows the back EMF in the inner rotor windings. It has 440 V amplitude which is decreased by 252 V compared to the back EMF when the PMIM was simulated individually. On the other hand, the back EMF in the stator windings when two machines are integrated together is the same when the BLDCM was simulated individually as shown in 6.21 b. The FEM modelling results of the back EMF in both the inner rotor and stator windings when the outer rotor only rotates at 1000 rpm are shown in figure 6.22 (a, b). The results shown in figure 6.22 (a, b) of the back EMF in the stator and the inner rotor windings were less than the induced back EMF when each machine simulated individually. This is because the flux produced by the magnets is distributed over both windings.

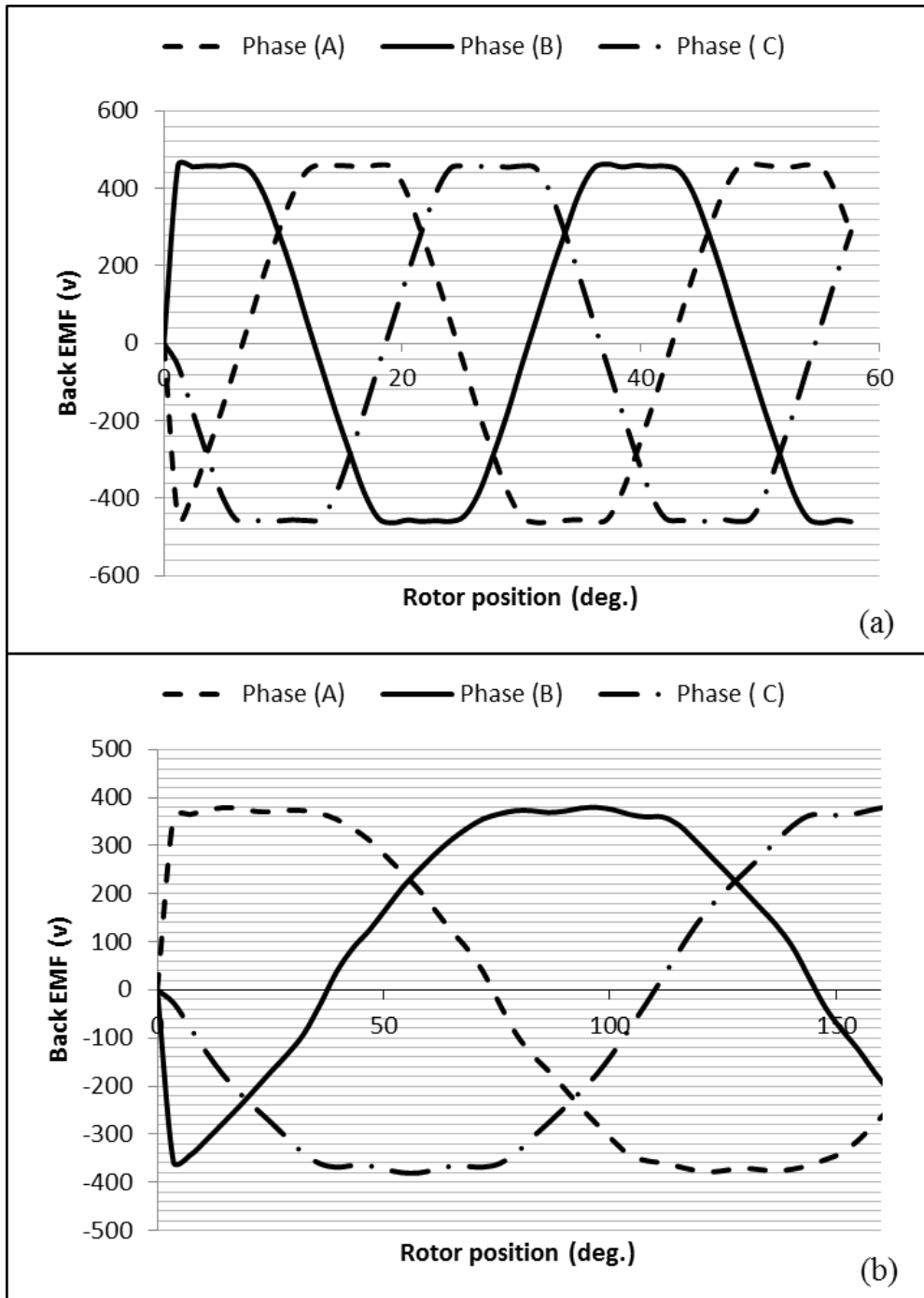


Figure 6.21: Back-EMFs as both rotors rotate (inner rotor: outer rotor) at 3000 and 1000 rpm (a) the inner rotor windings and (b) the stator windings

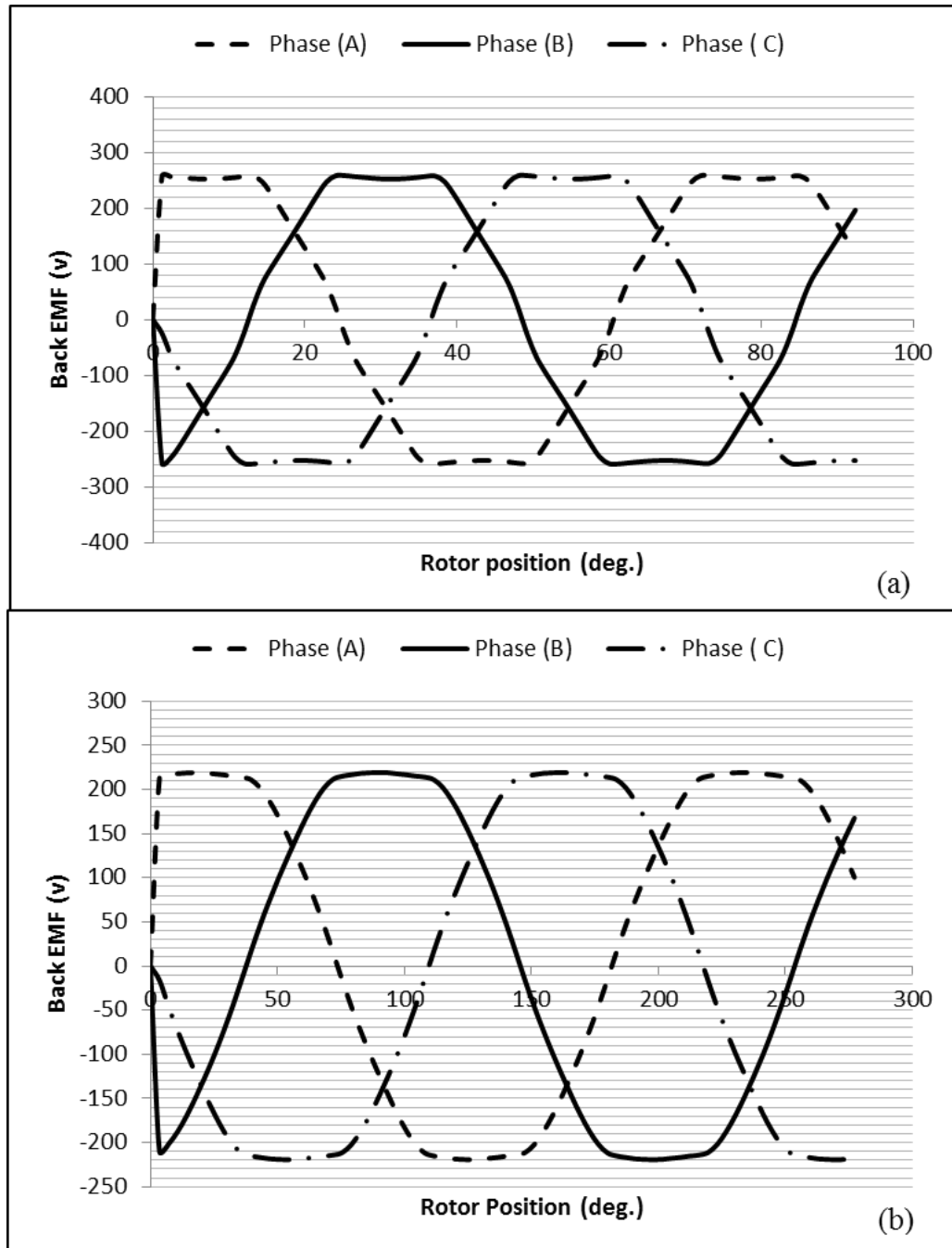


Figure 6.22: Back-EMFs in the (a) inner rotor windings and (b) stator windings, at the outer rotor only rotates at 1000 rpm

6.7.2 Integrated DM Simulation of the Flux Distribution

Figure 6.23 (a, b, and c) illustrates the flux distribution density (H) in the BLDCM, the PMIM separately, and the differential machine (DM). It is clear from Figure 6.23 (a, b) that the flux at the back iron and the teeth of the BLDCM and PMIM are higher than that in the integrated DM as shown in figure 6.23 (c). This is because the flux tends to

find the lowest reluctance in the magnetic circuit model, similar to the current in an electrical circuit flowing at the lowest resistance. Therefore, less saturation is occurred at the integrated DM. Figure 6.23 (b) shows that the flux is concentrated in some teeth less than others in the PMIM due to the gap between the magnets.

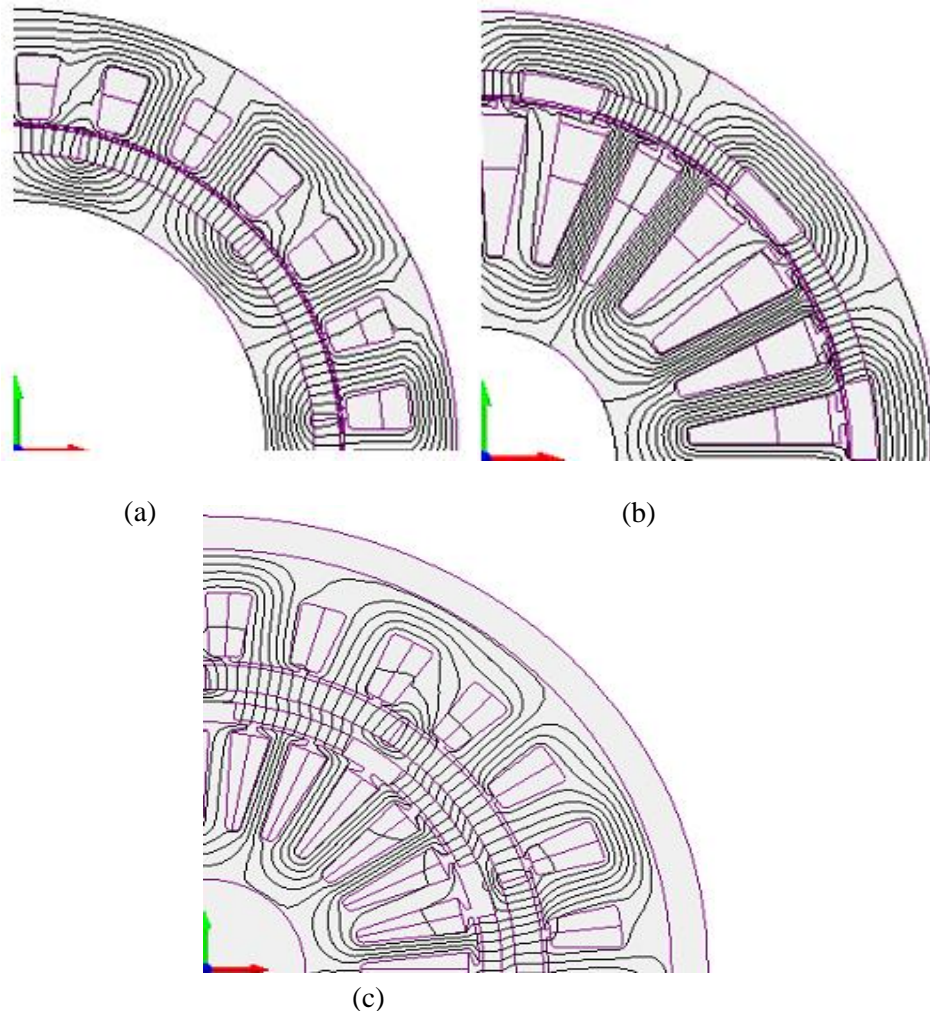


Figure 6.23: The flux distribution in the (a) BLDCM, (b) PMIM and (c) Integrated DM

6.7.3 Generating Mode Simulation of the Differential Machine

This FEM simulation aims to investigate the generating mode of the DM at no-load and load conditions. The speed ratio between the outer and the inner rotor will indicate the needed inner speed to produce the required voltage to overcome the back EMF in the stator windings. This simulation is very important because if the induced voltage in the inner rotor windings are less than or equal to the voltage in the stator windings, the BLDCM will not work.

6.7.3.1 The Slip Speed Simulation at no-Load Condition

In order to recover the slip power from the PMIM and return it to the stator of the BLDCM, the PMIM back EMF must be equal to or greater than the back EMF of the BLDCM. There will be a minimum slip speed between the two rotors for this condition. For example, in the case of no-load condition, both the inner rotor and the stator windings were kept open circuited. The simulation is carried out by choosing the speed of the inner rotor of 200, 250, 300 and 400 rpm while the outer rotor speed was kept fixed at 100 rpm. The reason for selecting these different speeds is to determine the predicted speed ratio between the outer and the inner rotor of the differential machine. Figure 6.24 shows different inner rotor speeds with respect to the outer rotor speed.

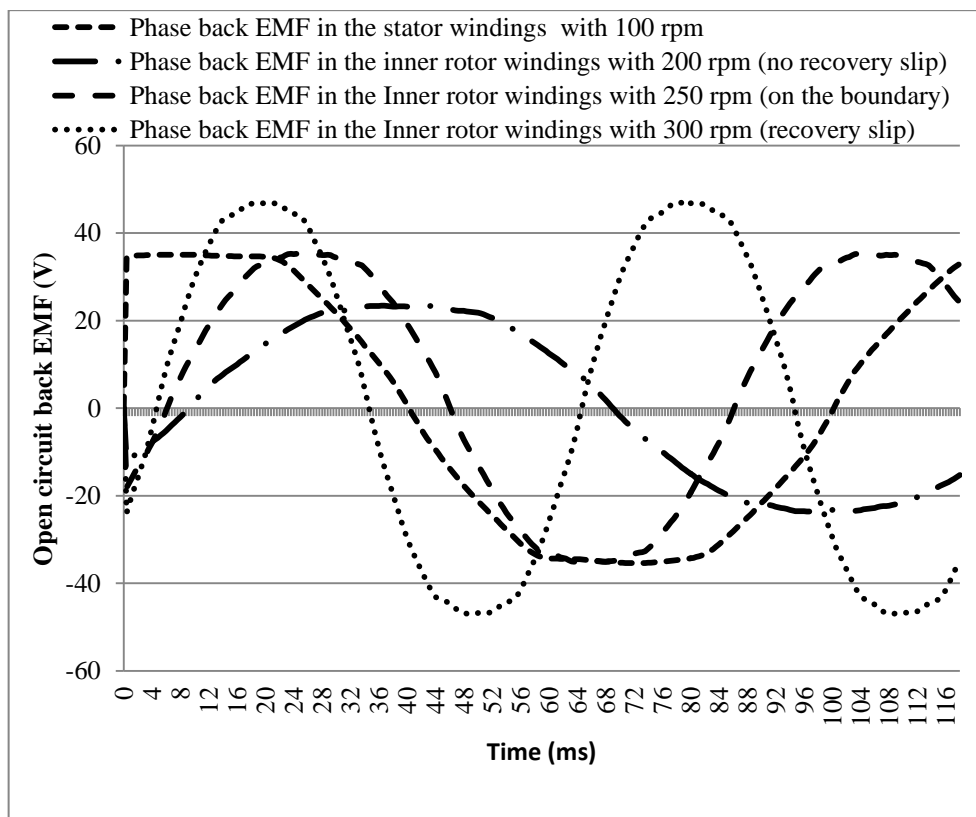


Figure 6.24: The inner rotor rotates with different speed; the outer rotor rotates at constant speed

6.7.3.2 The Slip Speed Simulation at Load Condition

As the FEM simulation can emulate the real situation ignoring the small losses, the EMTC machine is simulated at load condition and both the inner and outer rotors were accelerated. The back EMFs at both the stator and the inner rotor windings are shown in

figures 6.25 and 6.26, respectively. It can be seen from figure 6.25 that as the load decreased the voltage across the stator of the DM windings increased. On the other hand, the voltage across the inner rotor of the DM decreased gradually as shown in figures 6.26. In contrast, when the load on the outer rotor increases, the back EMF on the inner rotor windings of the DM will increase as shown in figure 6.27. The frequency of the induced voltage is increased or decreased proportionally to the load condition.

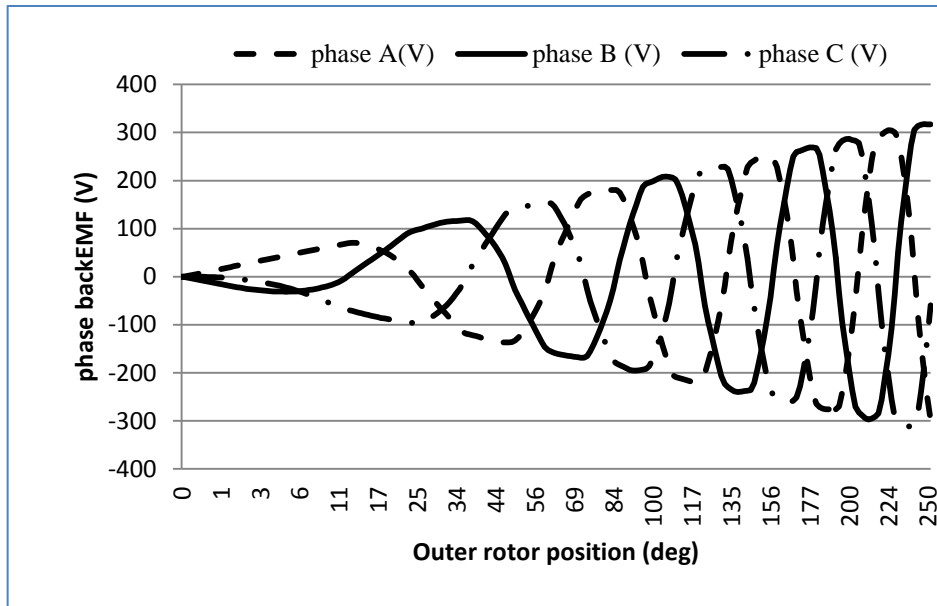


Figure 6.25: The back EMF in the stator windings

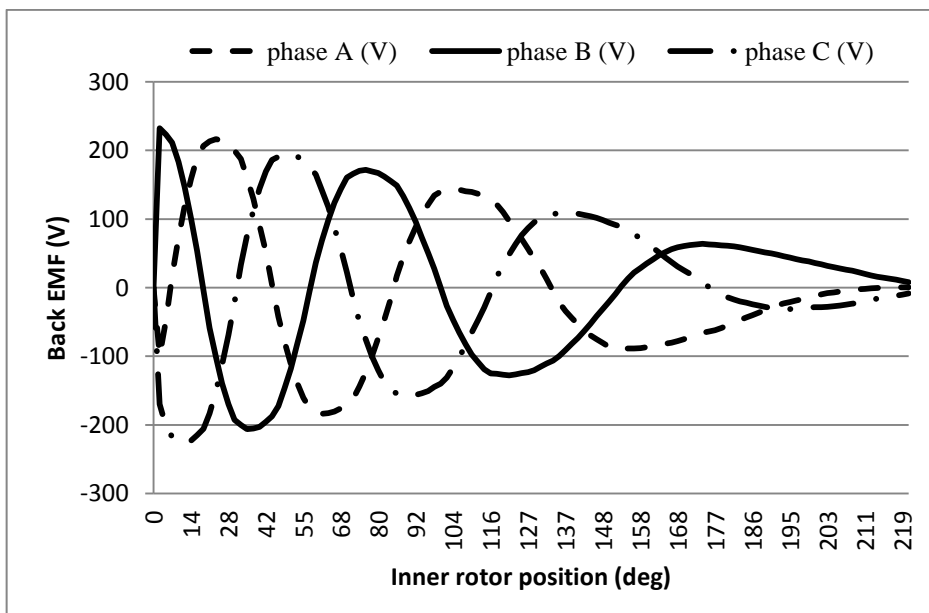


Figure 6.26: The back EMF in the inner rotor windings

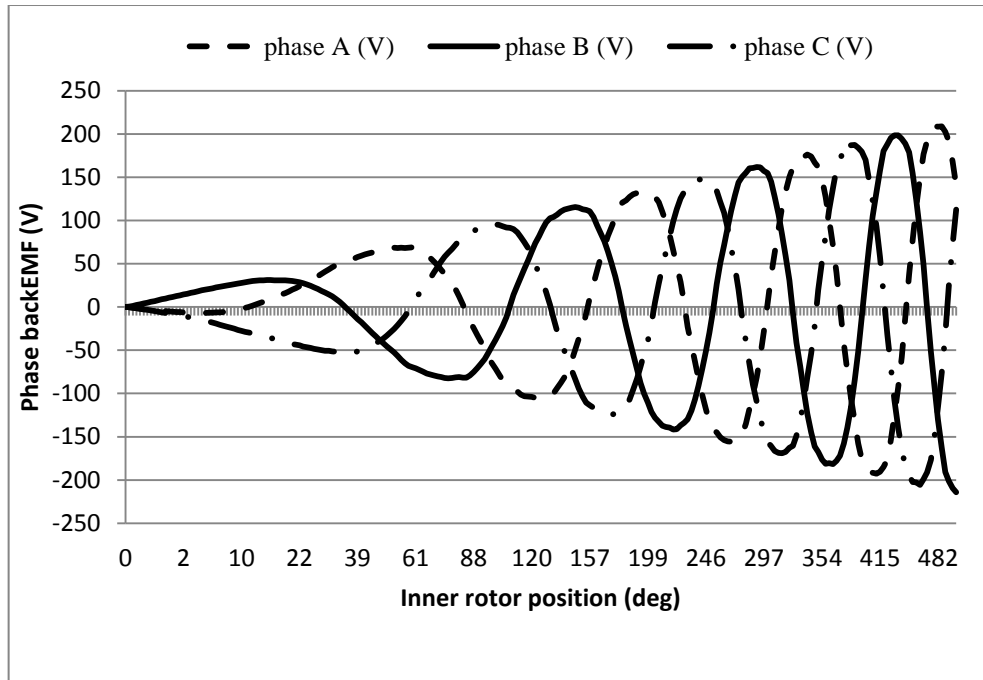


Figure 6.27: Back EMF across the inner rotor windings as load increases on the outer rotor

6.7.3.3 Slip Speed Simulation with of an External Resistance Connected

The aim of this simulation is to investigate the DM dynamic behaviour when the external resistance is connected at the inner rotor windings and driven by the prime mover at a speed of 2000 rpm. Figure 6.28 shows the inner and outer rotor speeds with a 12-ohm resistor connected. Figure 6.29 shows the simulated result of the DM when the external resistance was 6 ohms and the inner rotor speed was 1000 rpm. These results show that the slip speed is increased when the external resistance is decreased. Large external resistance leads to increase the slip power. In contrast, when the slip power is decreased, the outer rotor speed increased.

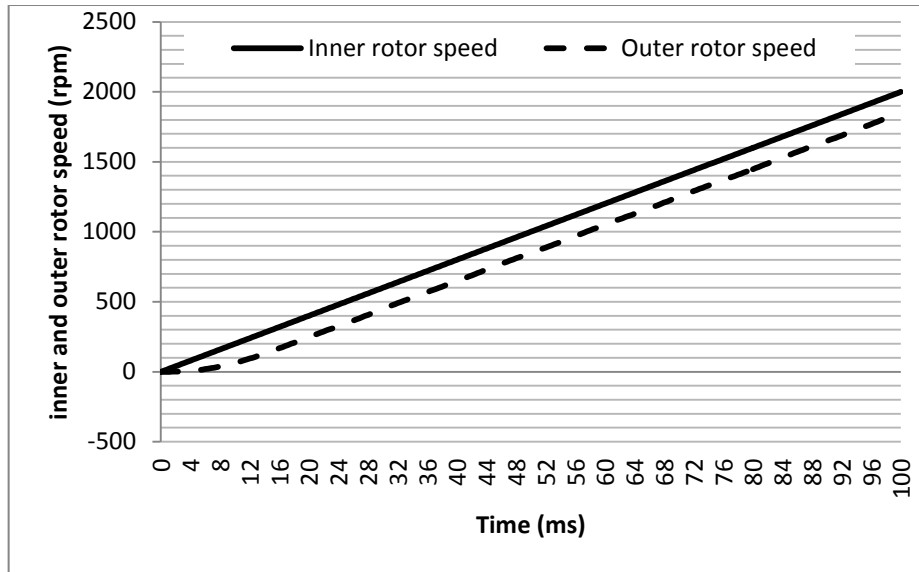


Figure 6.28: Slip speed between the outer and inner rotor at 12 ohm resistor

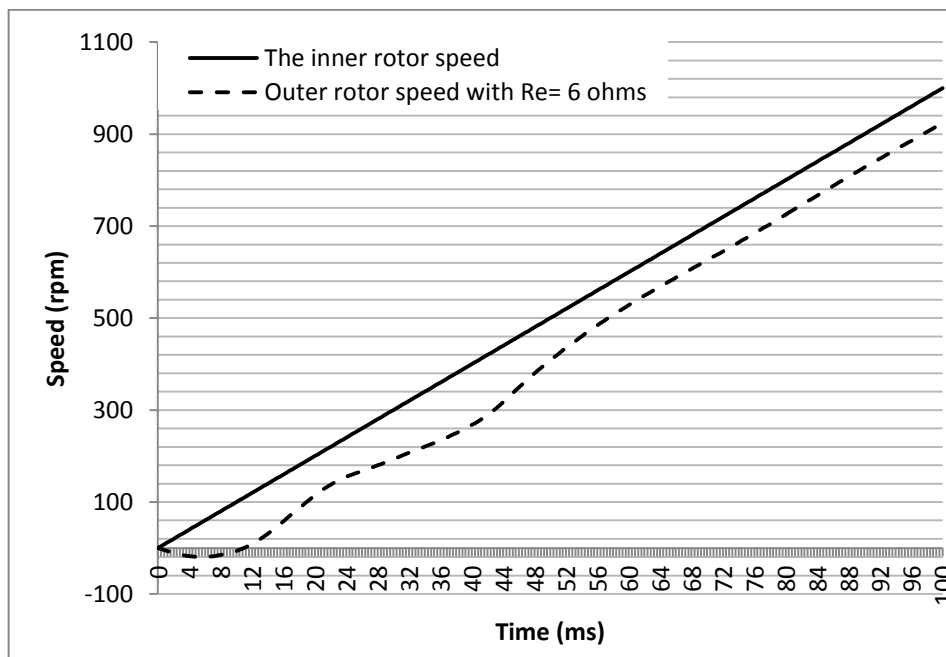


Figure 6.29: Slip speed between the outer and inner rotor at 6 ohms of external resistance

6.7.3.4 *Generating Mode with Outer Rotor Free Running*

During this simulation, the inner rotor was externally driven and the outer rotor was kept free running. The inner rotor windings were connected in star at one end and the other end of each phase was connected to a small resistance of 2.5 ohms, which

represent the actual resistance of each phase. The outer rotor was running with small slip speed compared to the inner rotor speed as shown in figure 6.30.

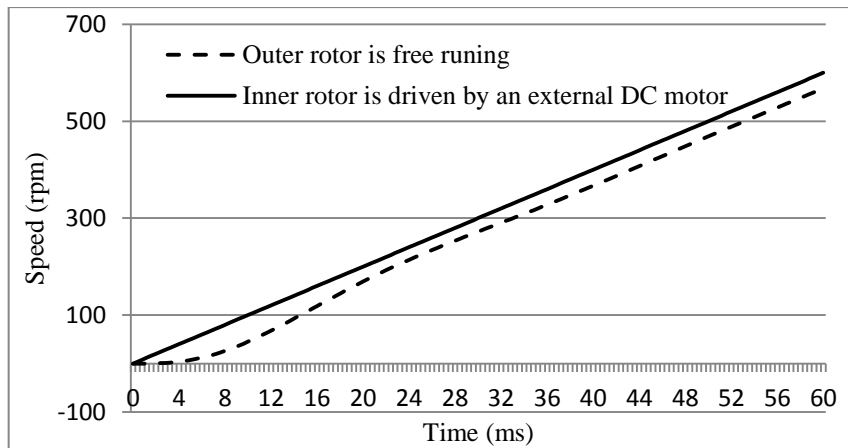


Figure 6.30: Inner and outer rotor speed when the outer rotor free running

a) Closed Differential Machine Loop Simulation

In this simulation, the closed loop of the DM was simulated as shown in the schematic diagram of Figure 6.31.

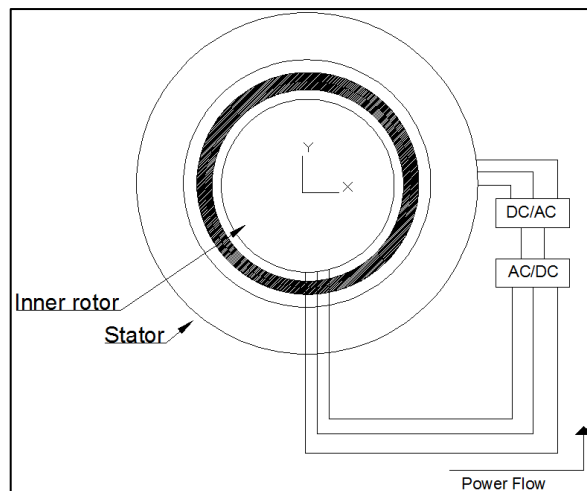


Figure 6.31: Schematic diagram of the DM simulation in closed loop

Figure 6.32 shows the circuit diagram of the DM. The inner rotor windings are connected to the full wave rectification circuit, which supplies the three-phase inverter circuit. The stator windings are then fed by this three-phase inverter circuit. The inner rotor of the DM is rotated at speed of 1000 rpm, then stepped up to 2000 rpm and back to 1000 rpm. The voltage waveforms in the stator windings are shown in figure 6.33. It can be seen that the voltage waveforms in the stator windings are symmetrical and

tracks the inner rotor speed, the steps of this simulation are given in the appendix C3. The predicted results of the closed differential machine loop indicate that the concept of the EMTC system can be practically achieved.

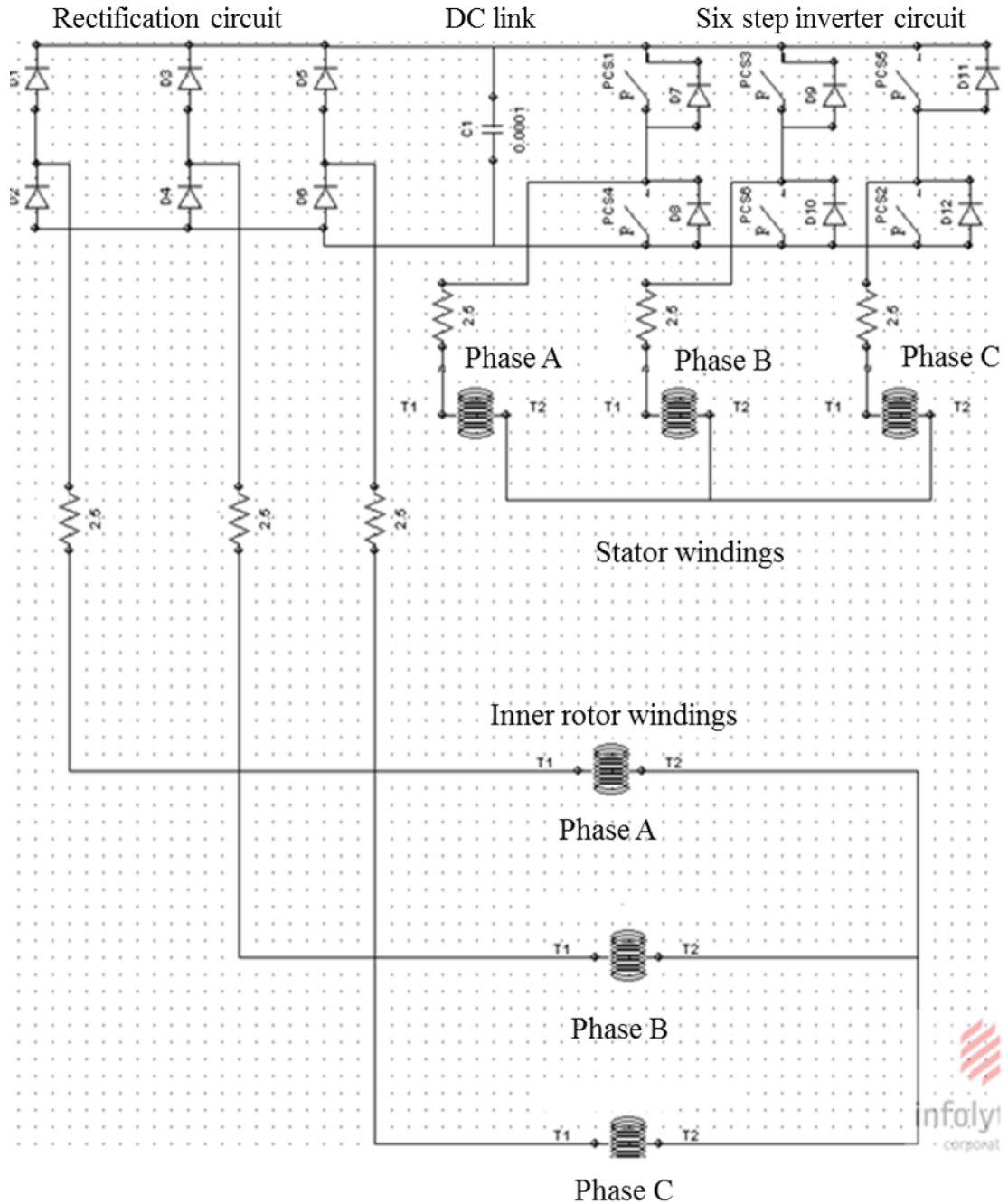


Figure 6.32: Circuit diagram of the DM connection

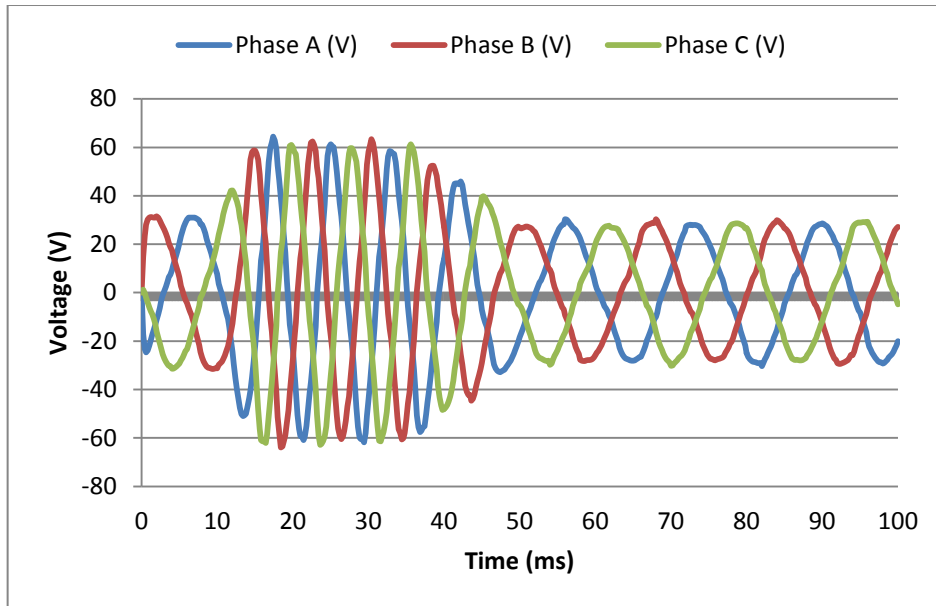


Figure 6.33: The voltage induced in the BLDCM windings

6.8 VFRT Modelling Set-Up

Figure 6.34 illustrates the typical configuration of the VFRT machine. The pole-slot combination of the primary (rotor) and the secondary (stator) parts is selected upon the configuration of the Differential Machine. Table 6.17 shows the design specification of the VFRT machine. The designed rated slip speed is 2000 rpm.

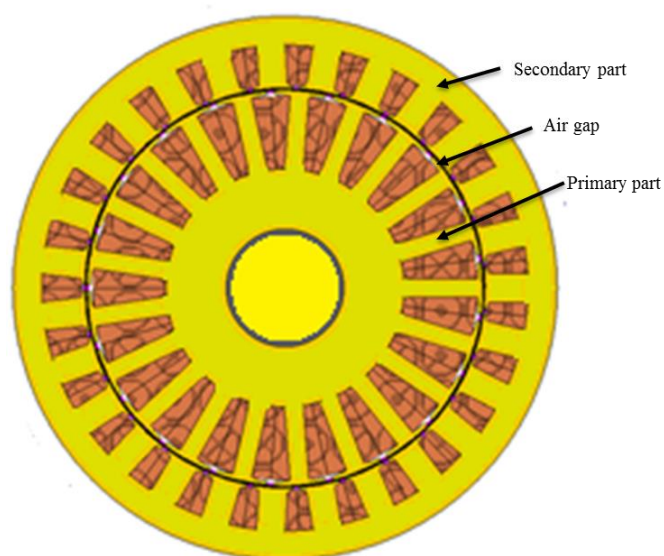


Figure 6.34 : VFRT machine configuration

Parameter	Value
Rated speed (rpm)	3000
Rated supply voltage into the rotor (V)	250
Axial length (mm)	59
Air gap length (mm)	0.5
Secondary (stator) outer diameter (mm)	204
Secondary (stator) inner diameter (mm)	150
Primary (rotor) outer diameter (mm)	149
Primary (rotor) inner diameter (mm)	44
Number of slots	24
Number of poles	10
Number of coils per phase	8
Number of turns per coil	50
Number of phases	3

Table 6.17: VFRT machine design specification

6.8.1 Winding Distribution of the VFRT Machine

The VFRT was designed with two elements, the primary side (rotor) and the secondary side (stator). The construction of the stator was designed to be identical to the stator of the BLDCM shown in figure 6.16 (section 6.6.1). Therefore, in this section, only the rotor construction is shown. The winding distribution of the VFRT rotor is shown in Figure 6.35 and the winding labels are listed in table 6.18. Since the number of slots was selected to be 24, the fractional winding type is obtained with 10 poles. With this type of winding, the concentrated winding was distributed in the rotor of the VFRT.

Table 6.18 illustrates the winding distribution of each phase. There are 8 coils connected in series gives the input and output ends, where each two ends make either a south or north pole. The total number of poles is 10 poles per phase. However, some of these poles are stronger than others due to use of the fractional slot winding type.

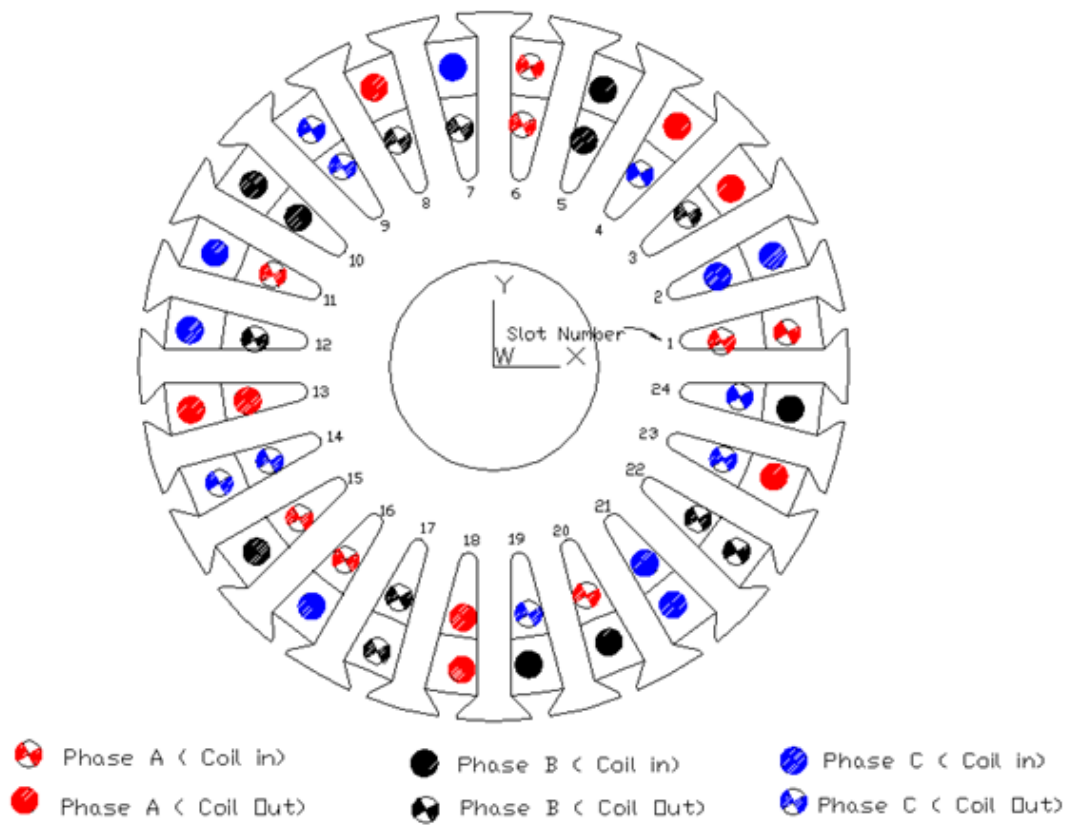


Figure 6.35: The winding distribution of the VFRT rotor

Number of coils	Phase A		Phase B		Phase C	
	In	Out	In	Out	In	Out
1	1	3	17	19	9	11
2	6	4	22	20	14	12
3	6	8	22	24	14	16
4	11	13	3	5	19	21
5	15	13	7	5	23	21
6	16	18	8	10	24	2
7	20	18	12	10	4	2
8	1	23	17	15	9	7

Table 6.18: The configuration and coils distribution of VFRT

6.8.1.1 The Flux Distribution Analysis in the VFRT

The VFRT was analysed in the dynamic mode only due to the absence of the permanent magnets in this machine. In order to investigate the VFRT dynamic behaviour, the simulations were carried out as the rotor rotates at 3000 rpm and its stator winding is connected to a resistance equivalent to the stator windings resistance of 0.6 ohms in order to produce an interaction between the stator and the rotor fields. The rotor

windings are fed by an external voltage waveform (which is produced from the PMIM at this speed). The flux distributions at several rotor positions are shown in Figure 6.36. At the rest position, there was no flux interaction, while at the DM model even at rest, the flux is produced by the magnets and flow through the stator and inner rotor laminations.

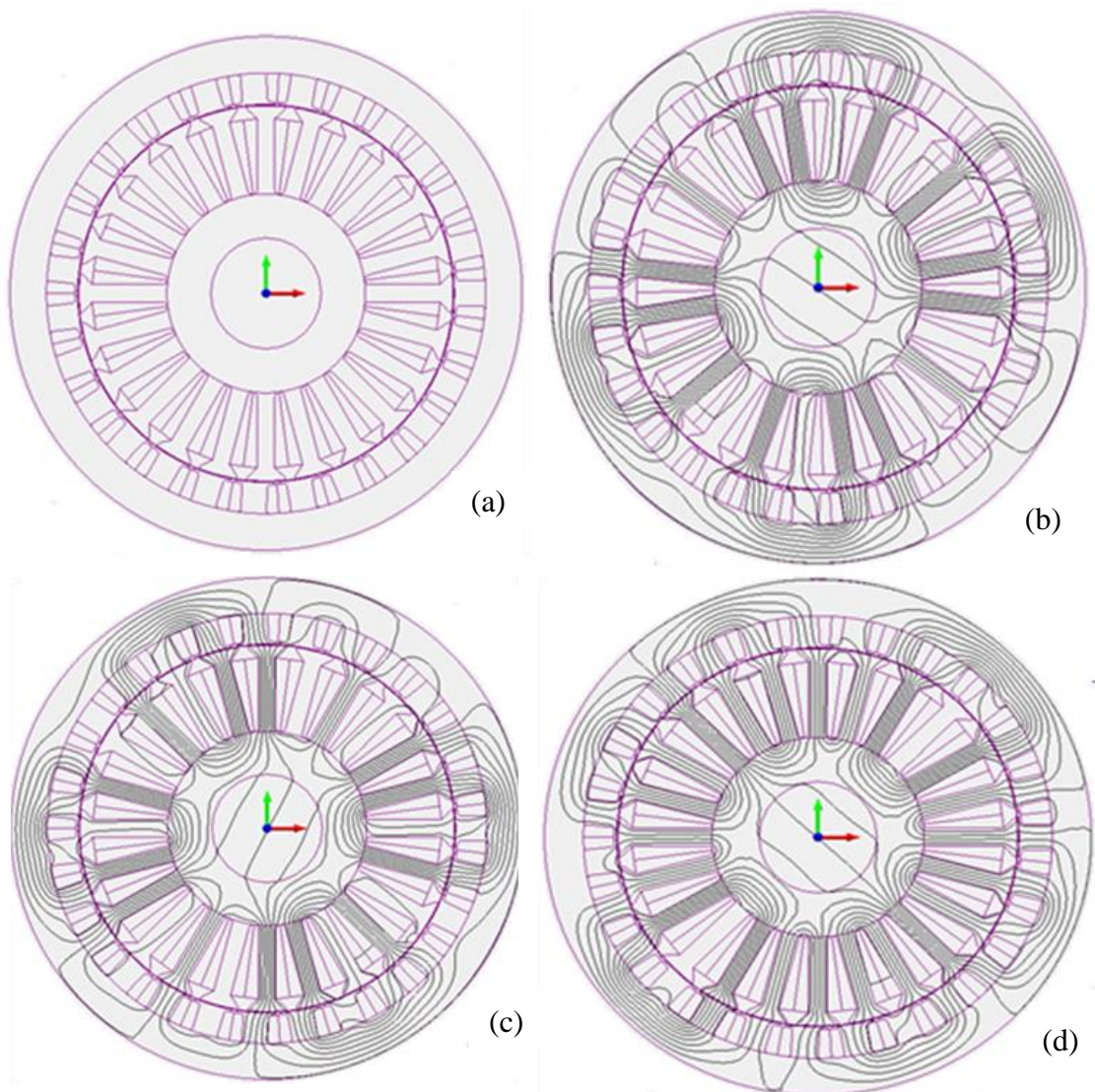


Figure 6.36: Flux distribution at several rotor positions (a) 0 deg., (b) 9 deg., (c) 45 deg., and (d) 90 deg.

6.9 Summary

Two methods were used to select the optimal pole-slot combination model. The iteration method and the optimal magnet-arc length method were performed in this chapter using FEM. The comparison conducted included the analysis of the cogging torque, the electromagnetic torque and the ripple torque. Initially, the minimum cogging torque among 34 pole-slot models at each machine of the Differential Machine, the BLDCM and the PMIM, was taken. Then, based on further investigations, the minimum torque ripple and high electromagnetic torque pole-slot combination model were selected for both machines of the DM. Furthermore, the complete EMTC system, including both the DM and VFRT machines, was presented. The EMTC system was analysed for both the steady state and the dynamic performances. The simulations for the induced back EMF in several cases also presented in this chapter.

After many investigations, the pole-slot combination of the DM was selected. The selected DM is the optimum selection of such machine configuration. Due to the lack of the FEM dealing with the complete EMTC system configuration, each part of the EMTC system was simulated individually. The next chapter will focus on the mathematical modelling of the proposed EMTC system.

7 Mathematical Modeling of the EMTC System

7.1 Introduction

In this chapter, the mathematical modelling of the new Electromagnetic Torque Converter (EMTC) system is presented. The first section deals with the modelling assumptions. Then, the Differential machine (DM) and the Variable Frequency Rotary Transformer (VFRT) are modelled mathematically.

7.1.1 Modelling Assumptions

Before starting the modelling process, it is essential to define the level of precision of the desired model. Thus, the following assumptions were made.

- The air gap was assumed to be uniform.
- The core losses were neglected, so the only considered power losses were the phase resistances.
- The effect of magnetic saturation is neglected.
- The three phases of the stator windings are identical, and are uniformly distributed, having the same parameters.
- The three-phase windings are star connected.

The DM of the EMTC system has two rotors, the permanent magnet as an outer rotor and the wound inner rotor. The outer rotor rotates synchronously with the stator rotating magnet field. Hence, the outer rotor is modelled as a BLDCM modelling part referring to the brushless AC machine (BLACM) mathematical modelling discussed in section (2.3.2). The inner wound rotor is rotating at the same speed of the drive machine. Therefore, it was considered as a permanent magnet induction machine. However, the outer rotor is also a function of the inner rotor and vice versa. The dq0 representation was used for the developed mathematical model. On the other hand, the VFRT is modelled according to [86].

7.1.2 Modelling of the Differential Machine

Since the Differential Machine is composed of two parts, its outer part represents a conventional PM machine (BLDCM), while the inner part represents a Double Rotor Machine (DRM). The DRM modelling was proposed by Backstrom [20]. Then both

models can be combined together to represent the differential machine. The mutual inductance between the inner rotor and the stator windings is added in the differential machine model.

7.1.2.1 The Outer Part of the DM (BLDCM) Modelling

The equivalent circuit of the outer part of the DM (BLDCM) was presented in section 2.3.2. Its voltage and torque equations are rewritten in this section as a part of the DM in case the sinusoidal current is used to drive the BLDCM [31].

- **Voltage equations**

$$v_{ds}^r = R_s i_{ds}^r + \frac{d}{dt} \lambda_{ds}^r - \omega \lambda_{qs}^r$$

$$v_{qs}^r = R_s i_{qs}^r + \frac{d}{dt} \lambda_{qs}^r + \omega \lambda_{ds}^r$$
(7.1)

Where the flux linkages are defined as

$$\lambda_{ds}^r = L_d i_{ds}^r + \lambda_m$$

$$\lambda_{qs}^r = L_q i_{qs}^r$$

The electromagnetic torque is given

$$T_{em} = \frac{3P}{2} (\lambda_m i_{qs} - (L_d - L_q) i_{ds} i_{qs}) Nm$$
(7.2)

7.1.2.2 The Inner Part of the DM (PMIM) Modelling

The inner part machine (PMIM) of the DM consists of double rotor machine. The equivalent circuit diagram of this machine is shown in figure 7.1. The PMIM consists of two rotors, the inner wound rotor and the outer permanent magnet rotor. Both rotors can rotate in both directions. When they rotate in the same direction, the slip speed is equal to the difference between both speeds. In contrast, when these rotors rotate in opposite direction, the slip speed is equal to the sum of both speeds.

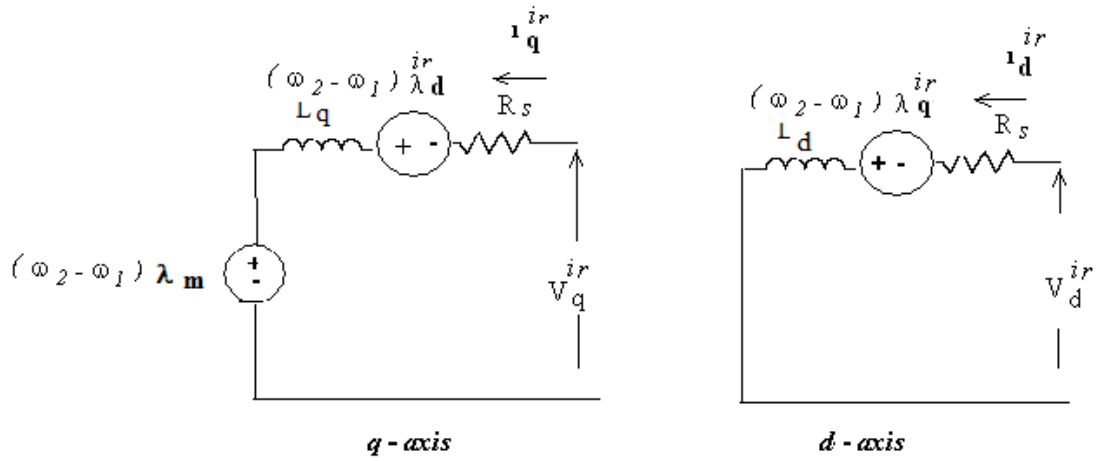


Figure 7.1: The circuit diagram of the PMIM in dq0 representation

Voltage equations

$$v_d^{ir} = R_s i_d^{ir} + \frac{d}{dt} \lambda_d^{ir} - (\omega_2 - \omega_1) \lambda_q^{ir} \quad (7.3)$$

$$v_q^{ir} = R_s i_q^{ir} + \frac{d}{dt} \lambda_q^{ir} + (\omega_2 - \omega_1) \lambda_d^{ir} \quad (7.4)$$

$$\lambda_d^{ir} = L_d i_d^{ir} + \lambda_m \quad (7.5)$$

$$\lambda_q^{ir} = L_q i_q^{ir}$$

Torque equations

$$T_{em} = \frac{3P}{2} (\lambda_m i_q^{ir} - (L_{dir} - L_{qir}) i_d^{ir} i_q^{ir}) Nm \quad (7.6)$$

7.1.2.3 The Complete Differential Machine Modelling

The equivalent circuit diagram of the DM can be seen in Figure 7.2. In this model, the outer rotor is a permanent magnet that rotates synchronously with the rotating magnetic field in the stator windings. Hence, they have the same angular speed. On the other hand, the inner rotor rotates with the same prime mover speed. Therefore, there is a slip speed between the outer and the inner rotor speed $(\omega_2 - \omega_1)$.

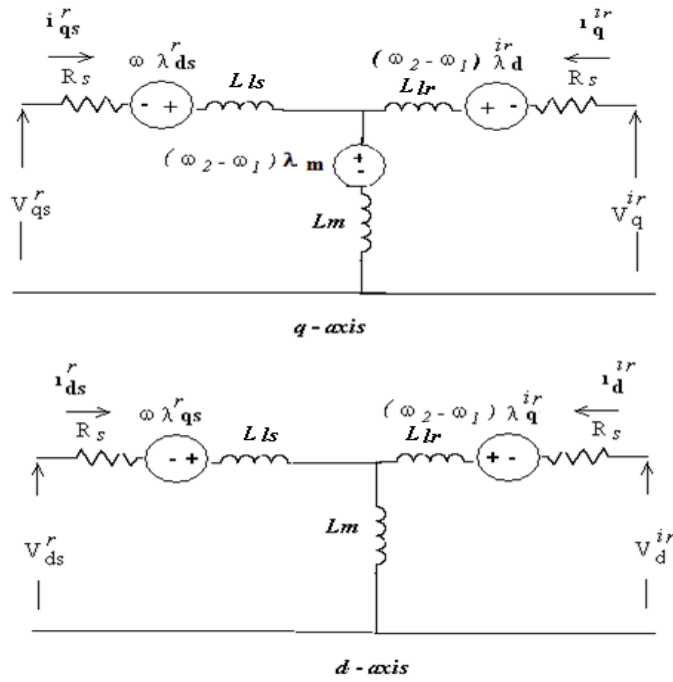


Figure 7.2: The differential machine equivalent circuits in d-q representation

- **Voltage Equations**

$$v_{ds}^r = R_s i_{ds}^r + \frac{d}{dt} \lambda_{ds}^r - \omega \lambda_{qs}^r \quad (7.7)$$

$$v_{qs}^r = R_s i_{qs}^r + \frac{d}{dt} \lambda_{qs}^r + \omega \lambda_{ds}^r$$

$$v_d^{ir} = R_{ir} i_d^{ir} + \frac{d}{dt} \lambda_d^{ir} - (\omega_2 - \omega_1) \lambda_q^{ir} \quad (7.8)$$

$$v_q^{ir} = R_{ir} i_q^{ir} + \frac{d}{dt} \lambda_q^{ir} + (\omega_2 - \omega_1) \lambda_d^{ir} \quad (7.9)$$

Where the flux linkages can be defined as:

$$\lambda_{ds}^r = (L_{ls} + L_m) i_{ds}^r + L_m i_d^{ir} + \lambda_m$$

$$\lambda_d^{ir} = (L_{lr} + L_m) i_d^{ir} + L_m i_{ds}^r + \lambda_m \quad (7.10)$$

$$\lambda_{qs}^r = (L_{ls} + L_m) i_{qs}^r + L_m i_q^{ir}$$

$$\lambda_q^{ir} = (L_{lr} + L_m) i_q^{ir} + L_m i_{qs}^r$$

- **Torque Equations**

$$T_{em} = \frac{3P}{2} ((\lambda_q^{ir} i_d^{ir} - \lambda_d^{ir} i_q^{ir})) Nm \quad (7.11)$$

7.1.3 Modelling of the VFRT

The VFRT machine is unlike the conventional transformer, where its frequency in the primary and the secondary windings are the same. The VFRT is a cascaded doubly fed permanent magnet induction machine. So far, no studies have been published on this kind of machine. However, the conventional cascaded doubly fed induction machine are modelled in [86, 87]. In the VFRT, the frequency in the primary and the secondary windings are different because its rotor (primary) windings are supplied by a variable frequency came from the inner rotor of DM. The secondary windings (stator) frequency is not the same as the frequency in the primary windings. The stator frequency can be expressed as:

$$f_s = s f_r \quad (7.12)$$

$$f_s = \frac{(n_s - n_m)}{n_s} f_r \quad (7.13)$$

Where f_s and f_r are the stator and the rotor frequencies and s is the slip speed between synchronous and the mechanical speeds. Equation 7.13 shows that the frequency in the stator winding is proportional to the difference of the synchronous and the mechanical rotational frequencies. i.e., either it is equal to double of the rotor frequency or to zero frequency. This theoretical result is proven experimentally by changing the inter connection between the rotors of the DM and the VFRT machines. Since the VFRT machine behaves like a transformer, the Ampere's law around the closed contour at the mean path of the magnetic flux as shown in figure 7.3, yields [62]:

$$N_s I_s - N_r I_r = 0 \quad (7.14)$$

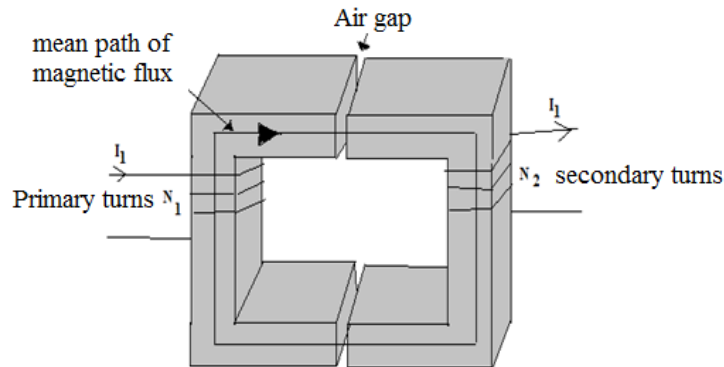


Figure 7.3: The mean path of magnetic flux in the VFRT

It can be seen from the schematic diagram of the VFRT in figure 7.3 that both the stator and the rotor windings link the same magnetic flux while their frequencies differ, therefore, their voltages will also differ by the same ratio [62]:

$$v_s = 4.44 N_s f_s \psi_s \quad (7.15)$$

$$v_r = 4.44 N_r f_r \psi_r \quad (7.16)$$

$$\psi_s = \psi_r = \psi_m \quad (7.17)$$

$$v_r/N_r = v_s/N_s \times f_r/f_s \quad (7.18)$$

Where,

f_s = frequency of voltage on stator winding (Hz),

f_r = frequency of voltage on rotor winding (Hz), and

ψ_m = mutual flux.

The nature of the machine in steady state, the rotor rotational speed f_{rm} is the difference between the frequency (electrical) on the stator and the rotor windings,

$$f_{rm} = f_s - f_r \quad (7.19)$$

$$n_{rm} = \left(120/N_m\right) f_{rm} \quad \text{rpm} \quad (7.20)$$

Where n_{rm} is the primary side (rotor) rotational speed.

7.2 Determination of the EMTC System Parameters

In order to model the real motor in the simulations in the MATLAB platform, the following parameters should be measured:

- Resistance R_s and phase inductance L_{ph} .
- Back-EMF constant K_E .

The voltages, resistances, inductances and torques determination are presented in the following subsections. The analytical calculations can be seen in the Appendix E2.

7.2.1 Back-EMF Constant of the Differential Machine

The back EMF of the DM parts, which includes the PMIM and the BLDCM, was simulated using the FEM Method. The simulation results are shown in Figure 6.19 and Figure 6.20 (in chapter 6). The K_E for both parts are calculated as defined in [27, 88] :

$$K_E = \frac{e_{L-L}}{\omega_m} \text{ Vs/rad} \quad (7.21)$$

Where e_{L-L} is a line-to-line back EMF and ω_m is the mechanical rotor angular speed. With the wye-connected BLDCM, two phases are connected at each commutation time, where

$$e_{L-L} = 2 e_{ph} \text{ and } \omega_m = 2\pi/60 \cdot$$

The back EMF in the inner rotor and the stator windings is an important factor that affects the operating principle of the EMTC system. The comparison between the back EMF obtained from the FEM simulations and the analytically calculated back EMF is shown in table 7.1 and 7.2.

1- Each Machine Separately

Separate simulation of the PMIM at 3000 rpm and the PMSM with 1000 rpm

Back EMF per phase (V)	Simulated by FEM	Analytically
PMIM	692 V (see Fig. 6.19)	814 V
BLDCM	370 V (see Fig. 6.20)	378 V

Table 7.1: Calculated and simulated back EMF per phase of the PMIM and BLDCM

2- Both Machines are Integrated

Both machines the BLDCM and the PMIM were simulated as an integrated machine with two different speeds. The ratio of the inner rotor speed: the outer rotor speed is 3000: 1000 rpm

Back- EMF per phase (V)	Simulated by FEM (see Fig. 6.21)
PMIM	440 v
BLDCM	370 v

Table 7.2: Simulated back EMF per phase of the PMIM and BLDCM

7.2.2 Electromagnetic Torque of the Differential Machine

The calculated parameters of the BLDC and the PMI machines compared to those acquired by FEM are presented in table 7.3.

Maximum Torque	Simulated by FEM	Analytically	
		Maximum Torque	Maximum Mechanical Power
BLDCM	66 Nm (see Fig. 6.15a)	62.4 Nm	6.5 kW@ 1000 rpm
		40 Nm	12.5 kW@ 3000 rpm
PMIM	46 Nm (see Fig. 6.15b)	40 Nm	12.5 kW@ 3000 rpm

Table 7.3: Calculated and simulated back EMF per phase of the PMIM and BLDCM

7.2.3 Self and Mutual Inductances of the Differential Machine Windings

The self and mutual inductances of the windings of the BLDCM and the PMIM are stated in table 7.4. It can be seen that the stator windings have almost the same inductances as in the inner rotor windings. The direct (L_d) and the quadrature (L_q) inductances are listed in Table 7.5. These parameters were needed for the Simulink/MATLAB modelling and simulation. The FEM solver used the following assumptions:

- 1- The windings in all three phases for both the stator and inner rotor are similar in terms of number of turns, wire type and cross-section.
- 2- The current used to excite any phase windings has 10 Amp (peak).
- 3- The outer rotor is rotating at rated speed of 1000 rpm.
- 4- The magnets on the surfaces of the outer rotor are disabled during the simulations, i.e. they have had their flux sources turned off.

Stator windings	Inner windings
Self-inductance 0.015 H per phase	Self-inductance 0.018 H per phase
Mutual inductance 0.005 H per phase	Mutual inductance 0.0065 H per phase

Table 7.4 Inductances of the inner rotor and stator windings of the DM in ABC reference frame

Stator windings			Inner windings		
RMS current (A)	Inductance (mH)		RMS current (A)	Inductance (mH)	
	Ld	Lq		Ld	Lq
4.33	19.7	18.7	4.78	7.77	14.8
8.66	18.7	18.9	9.74	11.4	19.7
13	19.3	19	14.6	15.2	20.7
17.3	19.7	18.9	19.5	17.4	20.9

Table 7.5: Inductances of the inner rotor and stator windings of the DM in the direct and quadrature reference frame

The Self-inductance at rated current (10 A) of phase A, B and C is 0.015 mH. Where, the mutual inductances between phases A, B and C is $L_M = 0.005$ mH. Therefore, the phase inductance can be evaluated as:

$$L_{ph} = L_S + L_M \quad (7.22)$$

Equation (7.22) gives the phase inductance per each phase A, B and C as 0.02 mH.

7.2.4 Phase Resistance of the Differential Machine Windings

- **Stator Phase Resistance**

The stator winding phase resistance is calculated with the aid of the selected number of coils and turns along with the following formula:

$$R = \frac{\rho L}{A} \quad (7.23)$$

Where ρ is the wire resistivity, L is the wire length and the A is the cross section.

The length was calculated from Figure 7.4. The length of the wire was calculated using the equation below:

$$L = (2 \times (l_{ss} + l_d)) \times Nt \times Nc \quad (7.24)$$

Where l_{ss} is the wire length between two midway slots and l_d is slot depth with $l_{ss} = 41.8$ mm, $\rho_{cu} = 1.95 \times 10^{-8}$ ohm-m, $l_d = 5.48$ mm and $A = 1$ mm², the phase copper wire length was 31.8 m. Hence the phase resistance was found to be 0.6 ohms per $Nt = 50$ turns and $Nc = 9$ coils.

- **Inner Rotor Phase Resistance**

The inner rotor winding phase resistance is calculated similarly as the stator winding resistance from the Figure 7.4. The main difference is the number of coils per phase, which are eight instead of nine in the stator windings

$$L = (2 \times (l_{ss} + l_d)) \times Nt \times Nc \quad (7.25)$$

Using equation (7.25) with $l_{ss} = 23.74$ mm, hence L is equal to 16.2 m. The phase resistance was found to be 0.32 ohms per $Nt = 50$ turns and $Nc = 9$ coils.

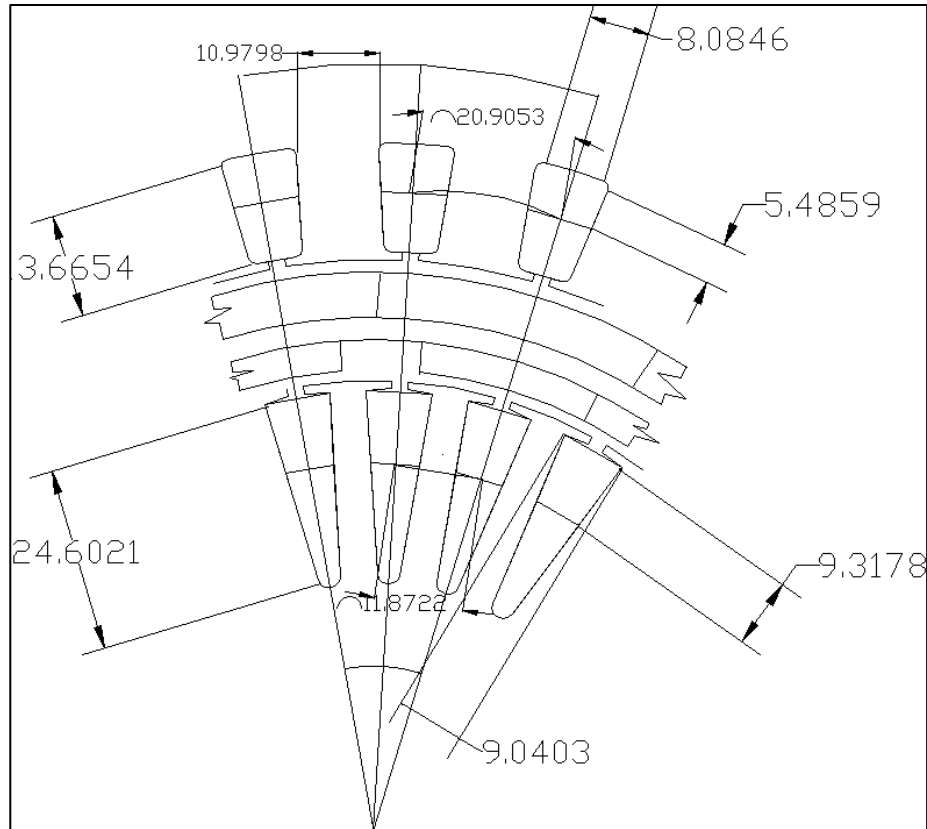


Figure 7.4: The differential machine view for resistance determination

7.3 MATLAB Simulation

All previously determined parameters were applied to the system simulation modelling using the software of MATLAB/Simulink version 2013a (Math works, MA, USA). The parameter specification used in the simulation is listed in table 7.6. The block diagrams are in the appendix A2. Tables 7.6 listed the obtained parameters of the DM of the EMTC system either from the FEM simulation or from the analytical calculations. The FEM simulations were carried out for an inductance by exciting the stator phase windings and rotate the rotors. This will produce a flux linkage between the excited windings and the inner rotor windings. By dividing the obtained flux linkage over the current flow value, the inductance can be obtained [89].

Parameter	value
Inner rotor resistance R_r	0.32 ohm
PMSM stator resistance R_s	0.6 ohm
Self-inductance of the inner rotor L_{sr}	0.015 H
Self-inductance of the BLDCM stator L_{ss}	0.018 H
Mutual inductance of the PMIM windings M_r	0.0065 H
Mutual inductance of the BLDCM stator M_s	0.005 H
Inner rotor of the PMIM L_d	0.0114 H
Inner rotor of the PMIM L_q	0.0197 H
stator of the BLDCM L_d	0.0187 H
stator of the BLDCM L_q	0.0189 H
Inertia J (BLDCM)	0.01 kg.m ²
Inertia J (PMIM)	0.009 kg.m ²
Load torque T_L	0.1 Nm
Number of poles	10

Table 7.6: Parameter specification of the DM

7.3.1 Simulation Results

The new EMTC system behaviour was predicted before prototype construction begins using Matlab/Simulink software simulation. Since the DM and VFRT models have been simulated using the FEM to define their parameters, the Matlab simulation can be performed. By varying the external resistance, the speed of the outer rotor with respect to the inner rotor speed was varied. Drive speed of the inner rotor was selected to be the same of the desired rated speed which is equal to 3000 rpm. The inner rotor speed is chosen to be gradually accelerated to 300 rpm/s. the outer rotor tracks the inner rotor speed. Figures 7.5 – 7.7 show the simulation results when the external resistance is changed. Figure 7.5 illustrates the relationship between the inner and the outer rotor speeds when the inner rotor windings were shorted. Although, the inner rotor short circuited, there is a slip speed. This is because the inner rotor windings have a small resistance. In figures 7.6 and 7.7, the EMTC system was simulated with an external resistance of 6 and 58 ohms. The reason for choosing these values is to be compared with the experimental results.

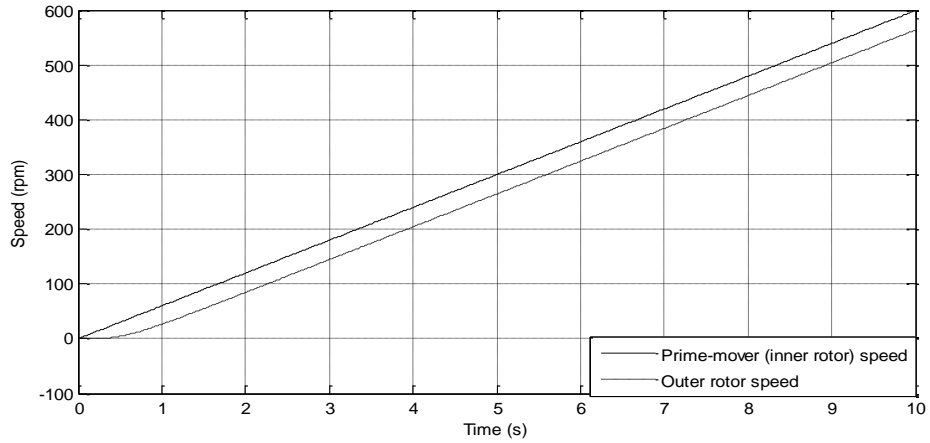


Figure 7.5: Matlab simulation result for the outer and the inner rotor speed when the inner rotor windings were short-circuited

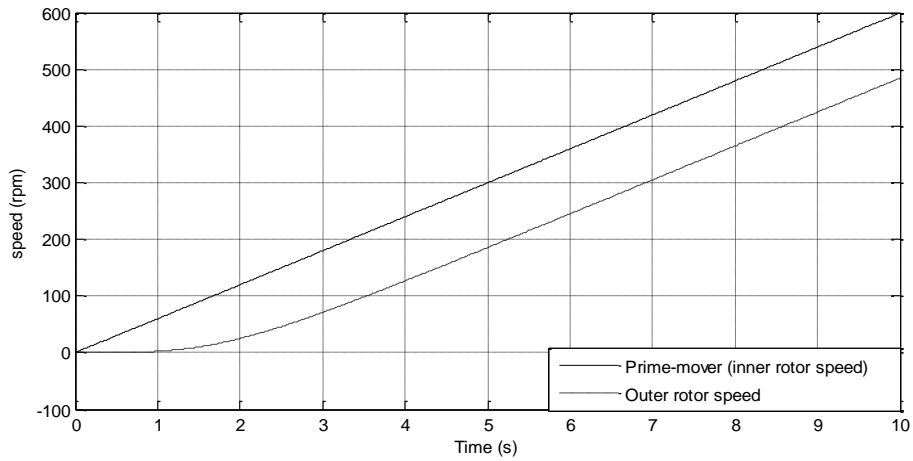


Figure 7.6: Matlab simulation results for the outer and the inner rotor speed when the inner rotor windings were connected to 6-ohm external resistance

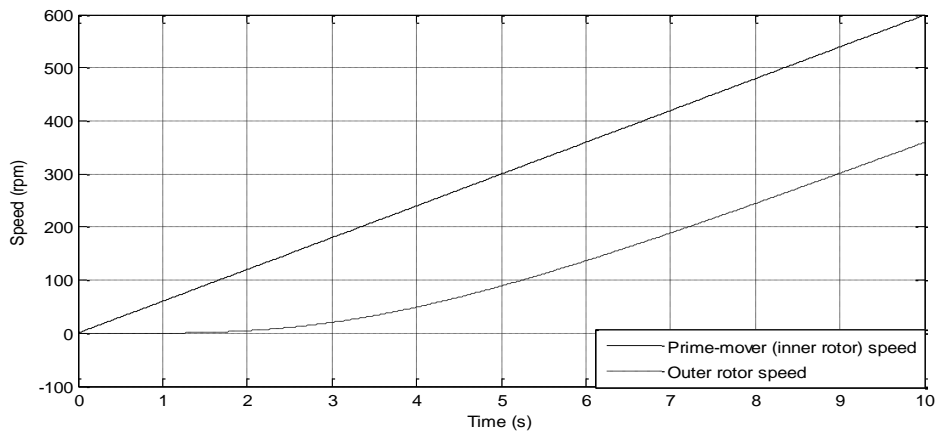


Figure 7.7: Matlab simulation results for the outer and the inner rotor speed when the inner rotor windings were connected to 58-ohm external resistance

7.4 Summary

The mathematical modelling of the DM was developed based on the brushless AC machines (BLACM) and the double rotor machine (DRM) mathematical modeling. The BLACM is a conventional permanent magnet synchronous machine, whereas the DRM is a non-conventional permanent magnet induction machine. It was developed for the Integrated Energy Transducer (IET). The IET consists of two rotors; the inner and the outer rotor. Hence, the mathematical modelling of these two machines could be used to model the DM. The mutual inductance is added to the DRM model, due to the flux links of the inner rotor and the stator of the BLDCM. On the other hand, the mathematical modelling of the VFRT machine was achieved based on the three phase transformer equations. The parameters of the DM were determined using the FEM and the analytical methods. Then, a SimPowerSystems toolbox in Matlab/Simulink was used to simulate the developed mathematical model of the EMTC system.

8 Construction of the EMTC System and the Experimental Set-Up

8.1 Introduction

In this chapter, the mechanical design and the assembly of the proposed EMTC system are introduced. The Differential Machine was designed with 10-pole 27-slot for the stator and the inner rotor. The VFRT was designed with 10-poles 24 slots for the rotor and 10-poles-27 slots for the stator. The final design of the EMTC system was undertaken according to the optimized parameters and their calculations shown in the chapters 5 and 6.

The prototype EMTC was manufactured by Alan Rice Ltd, a Company based near Nottingham, U.K. In general, the outer rotor was made by assembling twenty NdFeB, N40 grade magnets onto both surfaces of a steel cylinder with an adhesive glue to fix them. For the two layer wound components, overlap concentrated windings were utilised. The EMTC system was designed for natural air-cooling, as it would be difficult to cool the inner wound rotors.

8.1.1 The EMTC System Main Components

The main components of the EMTC system were constructed in three steps. The first step was the construction of the stators of both the Differential Machine (DM) and the Variable Frequency Rotary Transformer (VFRT). The stators were constructed identically in stack length, number of poles and slots. In the second step, the input and the output shafts of the DM and the VFRT were constructed as shown in Figure 8.1 (a, b). The input shaft was connected to a high speed-low torque electrical source, and hence, its diameter was only 25 mm. The hollow in the inner rotor shaft was used to thread the three-phase wires as shown in figure 8.2 (a).

On the other hand, the output shaft was connected to withstand the high torque loads, and thus, its diameter was designed to be 32 mm as shown in figure 8.2 (b). In the third step, both the inner rotor of the DM and the rotor of the VFRT were constructed.

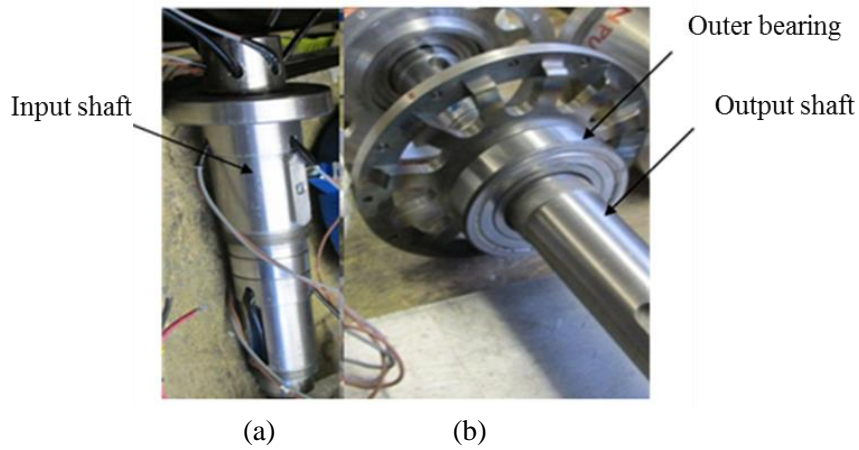


Figure 8.1: The EMTC system shafts (a) the input shaft and (b) the output shaft

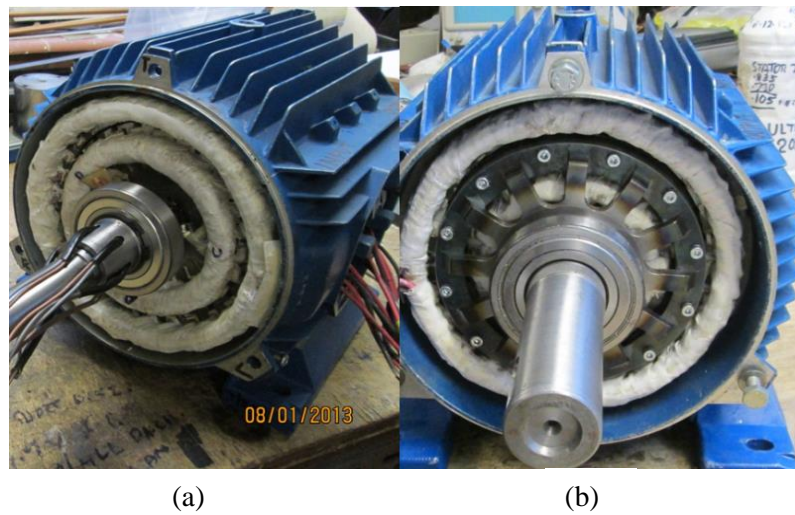


Figure 8.2: EMTC system shows input and output end drives (a) input end and (b) output end view

The EMTC system was designed to work as an electromagnetic torque converter in an automatic vehicle. The parts of the EMTC system are listed below:

- Twin stators
- the inner rotor
- the outer rotor
- slip-rings and brush holder (for measurements only)
- bearings
- VFRT rotor
- Power converter

8.1.1.1 Twin Stators

The EMTC system has a frame equipped with two stators, as shown in Figure 8.3. Each stator has a three-phase fractional slot winding. The winding ends are passed out of the frame in order to connect them either in star or in delta. 0.8 mm wire diameter was used in order to withstand a peak current of 10A.



Figure 8.3: Twin stators fabricated in a single frame

8.1.1.2 Differential Machine Inner Rotor

The inner rotor, as shown in Figure 8.4, which contains three-phase windings, is the main part of the EMTC system design. This is because it works as a motor and a generator at the same time. The generation mode is achieved as it is being driven by an external drive. On the other hand, due to its windings, which are directly connected to the VFRT machine, the current returns back to produce a flux density, and then it becomes a motor. Lamination sheets that were used in the inner rotor can be shown in figure 8.4. The main losses produced in the inner rotor are classified into copper and lamination iron losses.

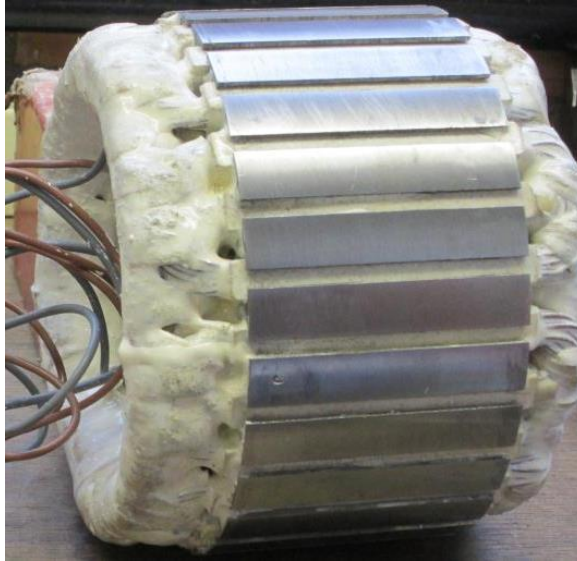


Figure 8.4: View from the inner rotor side

Both the inner and the outer air gap flux densities were analysed by the finite element modelling FEM. The results showed that the inner and the outer air gap have 0.92 T and 0.90 T respectively, at no load condition. These results imply that the teeth at the inner rotor should be wide enough to withstand their flux densities. Otherwise, the iron losses in their teeth could be high. Although the silicon steel with a thickness of 0.5 mm is used, the iron losses due to the eddy current in the inner rotor teeth might be high due to the relative motion between the permanent magnet and its conductors. The slot corners in the inner rotor, as it can be seen in Figure 8.5, are semi round shaped to protect the wires during insertion in the slots. Each slot is insulated by very thin insulation liner. Additionally, the coil separator is used in each slot to enable them for double layer utilization.



Figure 8.5: the lamination of (a) the inner rotor and the VFRT rotor

8.1.1.3 Permanent Magnet Outer Rotor

The drum of the outer rotor was fabricated by a steel cylinder as shown in figure 8.6. Hence, two sets of permanent magnet poles were glued on the inner and the outer surface of the cylinder as shown in Figure 8.6. It can be seen from Figure 8.7 that the inner and the outer sets of magnets do not have the same configuration. The magnets were coated with nickel material in order to protect them from corrosion and to withstand a high temperature as stated in [90]. The gaps between the magnets in the inner surface were filled with a non-metallic material in order to stabilise the magnets. The magnet configuration in each set was selected according to the FEM analysis of chapter 6.

The steel cylinder was designed to be only 3 mm thick. Its thickness does not affect the magnetic flux distribution, since the two sets of magnets allow the flux to flow radially. It was designed to carry the magnets in both sides with minimum weight. Furthermore, the less than 3 mm thick cylinder might bend during the rotational process. The outer rotor was fixed by both sides. The inner and the outer bearings shown in Figure 8.7 have the following specifications:

Inner bearing: Bearing reference: 6006-2z (inside diameter 30 mm, outside diameter 55 mm, rare width 13 mm).

Outer bearing: Bearing reference: 6209-2z (inside diameter 45 mm, outside diameter 85 mm, rare width 19 mm).

During the magnet setting process at the outer rotor, each set of magnets was glued individually. A simple method was used in order to set the outer set of the magnets as they were almost fully pitched. Both north and south poles of magnets were ordered with a 35° arc length. On the other hand, the inner set of magnets was gapped, and thus, the repelling and the attraction forces allowed the inner set of magnets to be firmed. A significant time was consumed to adjust the space between the magnets prior to gluing. The manufacturing of the outer rotor has another advantage because it is functions in both a squirrel cage rotor since both ends are shorted (without permanent magnet as shown in figure 8.6a) and a permanent magnet rotor as shown on in figure 8.6b. Therefore, at a certain slip speed (normally low slip speed) it works as an induction machine.



(a)

(b)

Figure 8.6: The outer rotor at (a) without permanent magnet and (b) with two sets of magnets



(a)

(b)

Figure 8.7: (a) The output end frame of the outer rotor, and (b) both end frames configuration

8.1.1.4 Slip-Rings and Brush Holders

Figure 8.8 shows the input shaft at the end-drive at the slip-ring side. These slip rings were mounted just for measurements purpose. They were mounted where the input shaft is connected to the drive DC motor.



Figure 8.8: Slip rings and rotating terminal strip

8.1.1.5 Optical Sensors

The optical sensor is used to sense the motion using an optical interrupter. Each single optical interrupter module consists of an emitter and a receiver of the energy beam separated by a slot. The interruption of the beam causes an on/off signal from the sensor to be transmitted to the drive circuit. Three optic sensors were mounted on the interrupter plate. This plate is mounted on the outer shaft as shown in Figure 8.9. It is common to divide the rotating plate into the same number as the pair poles of the machine in order to sense each pole position. The specifications of the optical position sensors are given in table 8.1.

Parameter	Rating value	Unit
Continuous Forward current	50	mA
Reverse voltage	3	V
Operating supply voltage	(Typical) 5	V
IR Emitter Forward voltage	1.6	V
IR Emitter Forward current	20	mA

Table 8.1: Optic transmission Position sensors data sheet

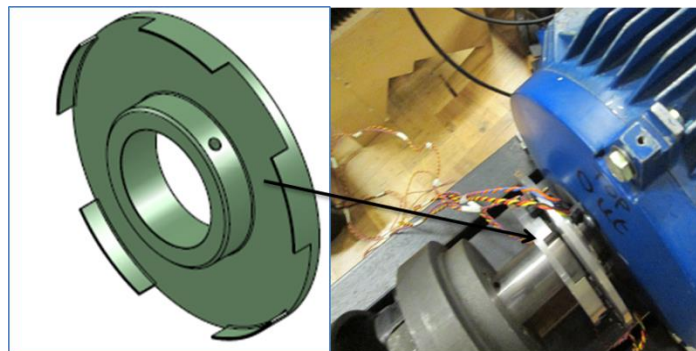


Figure 8.9: The interrupter plate and optic position sensors

8.1.1.6 Rotor of the VFRT

The electromagnetic torque converter has to have an electrical coupling between its rotors. The inner rotor cannot produce a sufficient voltage to supply its stator as the opposite back EMF may reduce the supplying voltage. Therefore, it is necessary either to use an external battery or to increase the inner rotor voltage. Using an external battery will add the cost to the system and reduce its reliability. Therefore, increasing

the voltage by built-in rotating transformer is used in this project. The VFRT, as shown in Figure 8.10, does not only increase the inner rotor voltage, but also it increases the reliability of the system. Moreover, by using the VFRT machine, the interconnection between the inner rotor and the stator is done easily. Both stators were connected via a power convertor, which gives more flexibility to the system.



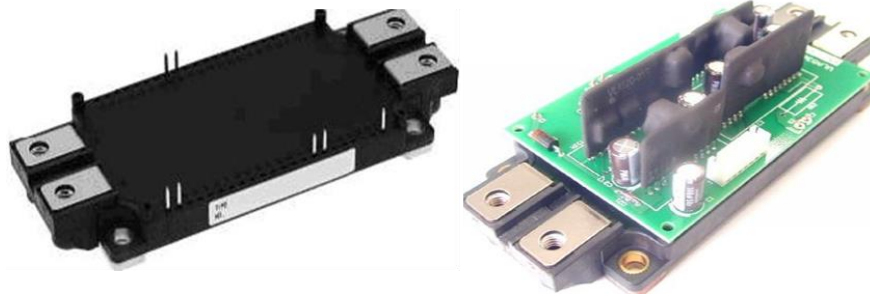
Figure 8.10: The rotor of the VFRT machine

8.1.1.7 Power Electronic Converter

The main function of the power converter is to convert one form of electric power into another as efficiently as possible. Hence, the relation between the power converters and the overall design is directly linked.

- **The Powerex Intelligent Power Module**

In this project, an Intelligent Power Module (IPM) is used, as shown in Figure 8.11. Powerex IPMs have many advantages such as high switching speed and low IGBTs power loss [91]. In addition, they are combined with protection circuitry. Hence, they can respond rapidly to short circuits and over temperature. The gate-drive unit type of the IPM is (VLA536-01R) and IGBT switches are CM200DX-24S type.

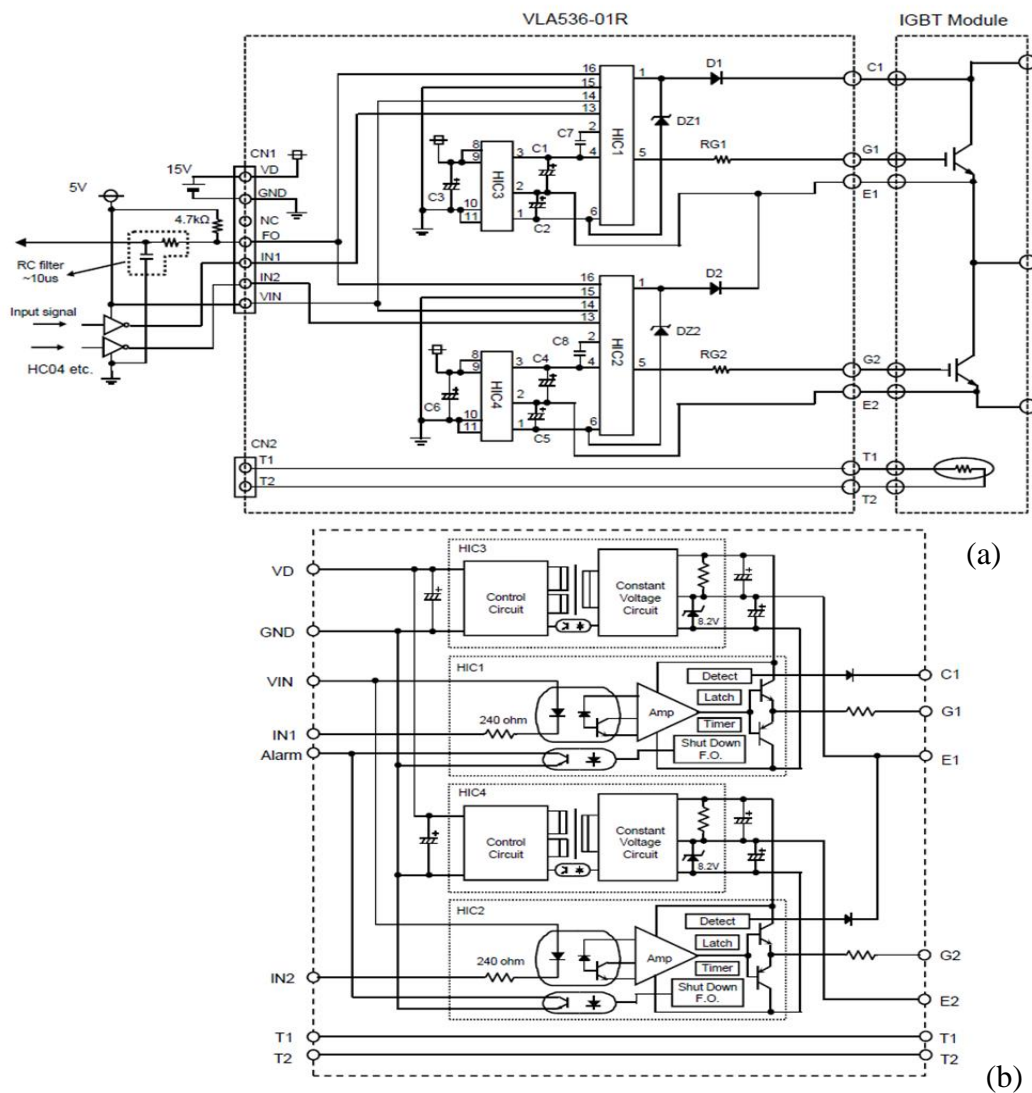


(a)

(b)

Figure 8.11: The IPM module includes (a) the Dual IGBT switching device and (b) the gate drive circuit [92]

The gate drive including the protection circuit and the voltage regulator are designed to drive the dual IGBT module as shown in Figure 8.12 (a, b).



(a)

(b)

Figure 8.12: The schematic diagram of the (a) drive circuit and (b) the protection and voltage regulator circuits [92]

- **Theoretical Calculations of the Gate Resistor**

A theoretical calculation was performed to find out the IGBTs parameters (see Appendix C4.5), such as gate resistor. These calculations are discussed in more detail in the following sections.

- **Efficiency**

The power losses at the IGBT are calculated in this section. The RMS current is needed to calculate such parameters. The demand parameters of the BLDCM such as the power and the input voltage are required to calculate the IGBT gate resistance.

$$P = 6.5 \text{ kW}, V_{Line} (Peak) = 250 \text{ Volt}$$

Assume the power factor: $\cos \theta = 0.8$, and the efficiency is 0.9. The line current can be calculated as:

$$I_L (Peak) = \frac{P}{\sqrt{3} V \cos \theta \eta} \tag{8.1}$$

Equation 8.1 gives $I_{Line} (RMS) = 14.7 \text{ A}$. From Figure 8.13, when the collector current of 14.7 A, the collector-emitter voltage can be determined to be $V_{C-E} = 1.0$ volts.

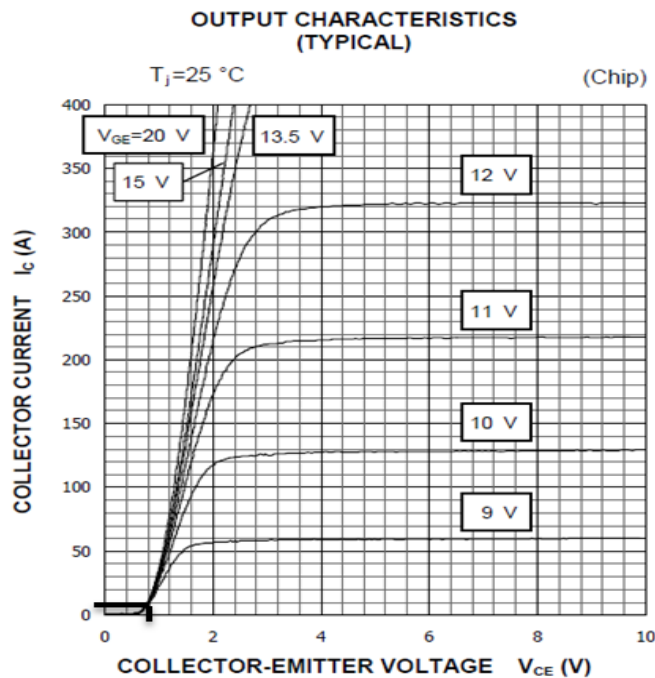


Figure 8.13: Collector-Emitter voltage versus Collector current characteristics [92]

From Figure 8.14, the determination of the free-wheel diode can be calculated as:

Rated emitter current $\approx 20 \text{ A}$ at $V_{EC} = 1 \text{ V}$.

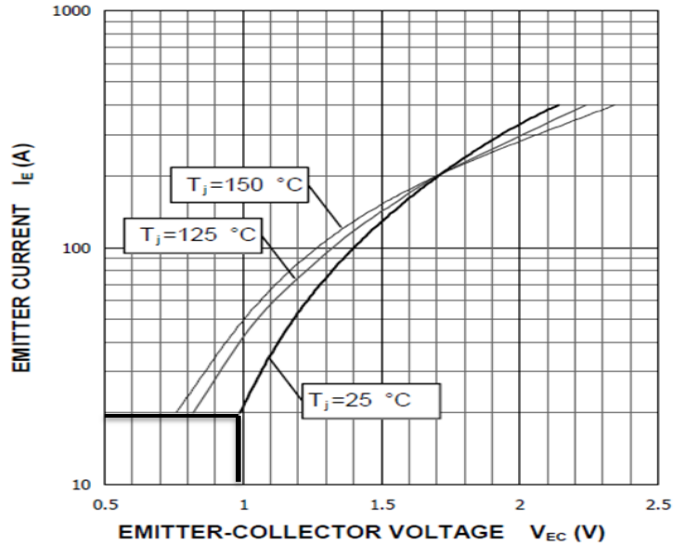


Figure 8.14: Emitter current vs. Emitter-Collector voltage characteristics [92]

From Figure 8.15, the IGBT on and off time switching can be determined as $t_{on} = 300$ ns and $t_{off} = 600$ ns. The final step is to determine the ideal value of the gate resistor that is 6.7 ohms as shown in Figure 8.16. Table 8.2 lists the other relevant specifications for this IGBT.

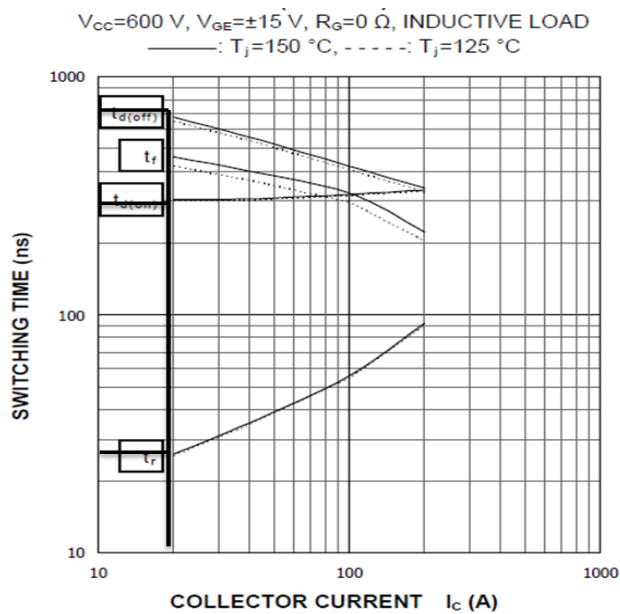


Figure 8.15: Switching time vs. Collector current characteristics [92]

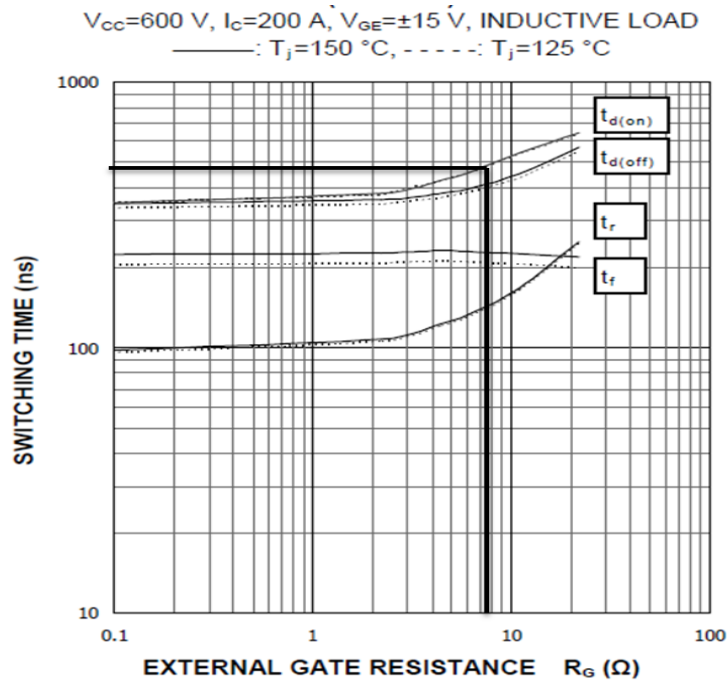


Figure 8.16: switching time vs. external gate resistor characteristics [92]

Specification	Rating	Unit
Total power dissipation	1500	W
Emitter current	200	A

Table 8.2: IPM drive IGBT specifications

Most of the dissipated energy is produced by the motor windings; however, some energy is lost in the IGBT itself during switching and in its diode as well. In case of the six-step type with square-wave current drive, the corresponding diode is conducting during the “off” status at the commutation cycle. Therefore, the diode dissipates the energy that is stored in the stator inductances during the turned off period. Since the voltage drop at the diode is 0.7 V, the estimated dissipated power is about 18 W.

In addition, since the gate drive is +15 V peak, the time constant (63% of 15V is 9.45 V), then the switching energy dissipated at turn-on or turn-off can be calculated as follows:

At one period of a signal, including the turn on and off, the IGBT switching losses can be calculated as:

$$P_T = P_{cond} + (E_{on} + E_{off}) \cdot f \quad (8.2)$$

Where P_{cond} is the conduction losses, E_{on} is the energy losses at switch-on state, E_{off} is the energy losses at switch-off state, and P_T is the total power losses, the conduction and switching losses, in the IGBT related to the switching frequency.

In addition, the maximum continued collector current can be calculated as below.

- **The Junction Temperature Rise Calculation:**

$$\Delta T = P_T \cdot R_{ThJc} \quad (8.3)$$

Where, R_{ThJc} is the thermal junction resistance.

- **The Temperature Difference between the Junction and the Case Calculation:**

$$\Delta T = T_J - T_C \quad (8.4)$$

Hence, the power dissipation can be calculated as,

$$P_T = \frac{\Delta T}{R_{ThJc}} = \frac{T_J - T_C}{R_{ThJc}} \quad (8.5)$$

Referred to the data sheet (see Appendix C4.5), where the max junction temperature T_{Jmax} is 175° C, case temperature $T_C = 25^\circ$ C and the thermal junction resistance R_{ThJc} is 0.1 K/W. The total power dissipation according to equation 8.5 is 1500 W, which is the same in the IGBT data sheet. As mentioned earlier, this power could be dissipated at the rated current 200 A. Hence, with the maximum current of the BLDCM (14.7 A) and with heat sink $\Delta T = 5^\circ$ C, the estimated power dissipated is 50 W.

8.2 Experimental Set-Up

The testing of the EMTC system followed several phases. These phases are in sequence, testing the outer part machine at the motoring mode, and then testing the PMIM machine at a generating mode. In addition, the VFRT machine was tested at the generating mode. Finally both subsystems coupled together in a closed loop.

The system hardware includes three diode bridges for power rectification, IGBT's power switches, gate drive circuit, and optic position detecting sensors with their circuits. The input torque was measured by using the torque transducer (see Appendix C4.3) and monitored by a digital AVO-meter, while the output torque was measured by

the load cell (see Appendix C4.2) and amplified with the aid of amplification circuit. The output speed was measured by the mechanical tachometer.

The proposed EMTC system was tested using two dc machines as a drive motor and a generator, two torque transducers, and two resistive loads. The input current range of this test was 0-10 A, where the power supply was 416 V Line-to-Line RMS voltage; the speed range was 0-1000 rpm for the outer rotor and 2000 rpm for the inner rotor. The resistive load NE7023, 6 kW was set as a variable load. The torque transducer DRBK type was used to measure the input torque where the input shaft speeds was measured using the generated voltage of the drive dc motor. The experimental bench view is shown in Figure 8.17. The machine bed frame of the EMTC system is built up to accommodate all the three electric machines. The details of the experimental set up in sections are shown in figures 8.18 –8.22. Figure 8.18 shows the input end view of the EMTC system includes the input torque transducer, brushes, brush holder and the rotating terminal strip. Figure 8.19 shows the output end of the EMTC system, the optic position sensor, flexible coupling between the outer rotor of the DM and the dynamic load. Figure 8.20 and figure 8.21 show the output and the input power measurement set. The output measurement set consists of the load cell to measure the output torque, and the meter to measure the output shaft speeds. The input measurement set is included to measure the slip power and the input speed. The BLDCM drive circuit is shown in figure 8.22. All of the experiments including no-load and at load modes, motoring and generating modes of the system are carried out on the same test bench as described in table 8.3.

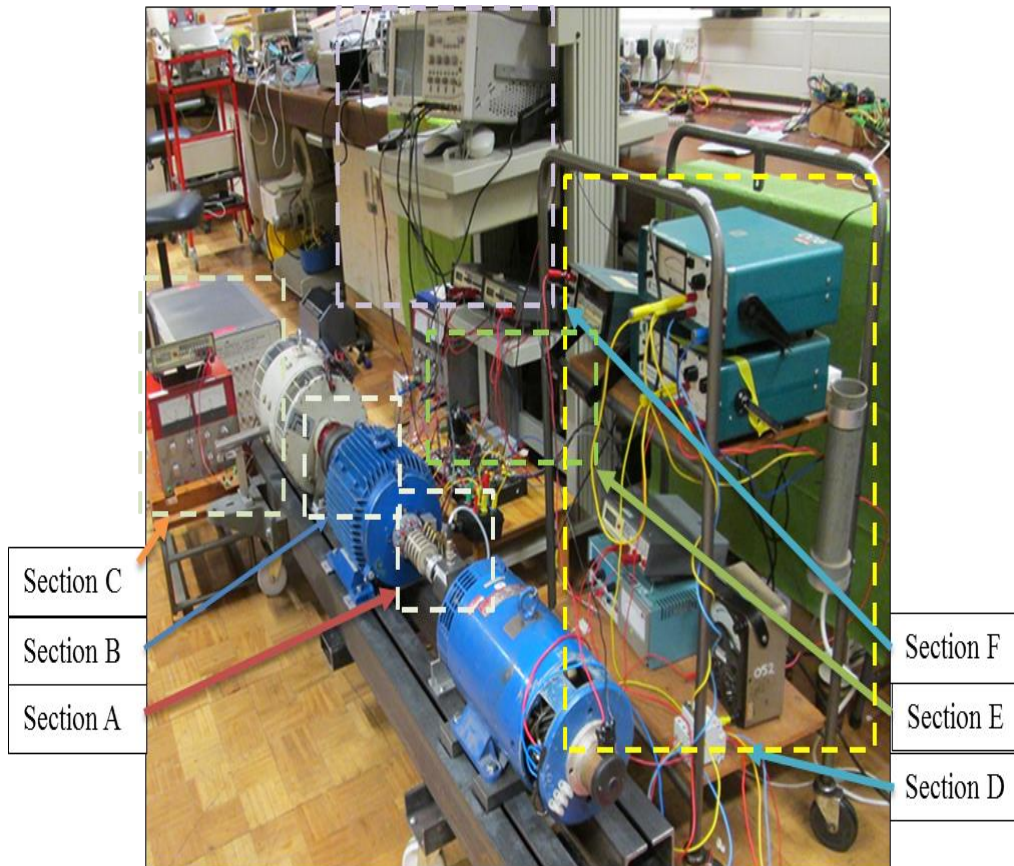


Figure 8.17: The complete Lab. bench

Drive DC motor	240 V	7.5 KW	Type: SERIES	Current: 35 A	5500 rpm
Load DC generator	220 V	3 KW	Type: SEP EX	Current: 13.6 A	2000 rpm
Input Torque Transducer	Exc. 12-28V	50 Nm	Type: DRBK	<90 mA	
Output Torque Transducer (Load cell)	Exc. 10V	5Kg	Type: 1002	Input & output Impedance: 350±50 Ω	Zero balance: ±0.4 mV/V
Output Torque Amplification circuit)	Exc. ±5V		Type: LM741 (op amp)		
Hewlett Packard Oscilloscope			HP 54825A	500 MHz	
Optic-position sensor	Ex. 5V		Type: HOA2001	Current: 20 mA	
Rectification diodes	V _{RMS} : 1200 V		Type: STTA9012TV1/2	I _{F(RMS)} : 150A	
Protection device (MCB)	400 V		Merlin Gerin Triple pole MCB D10	10 A	

Table 8.3: Types and specifications of the involved equipment in the experiment



Figure 8.18: Section-A of the complete Lab. bench components

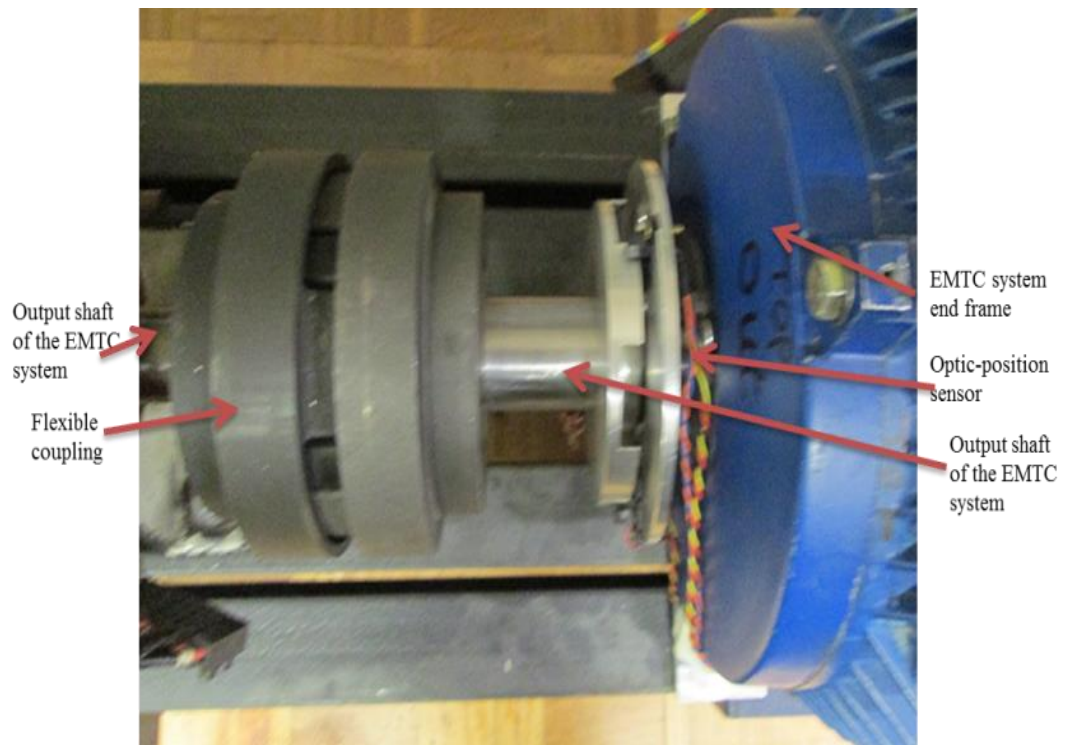


Figure 8.19: Section-B of the complete Lab. bench components

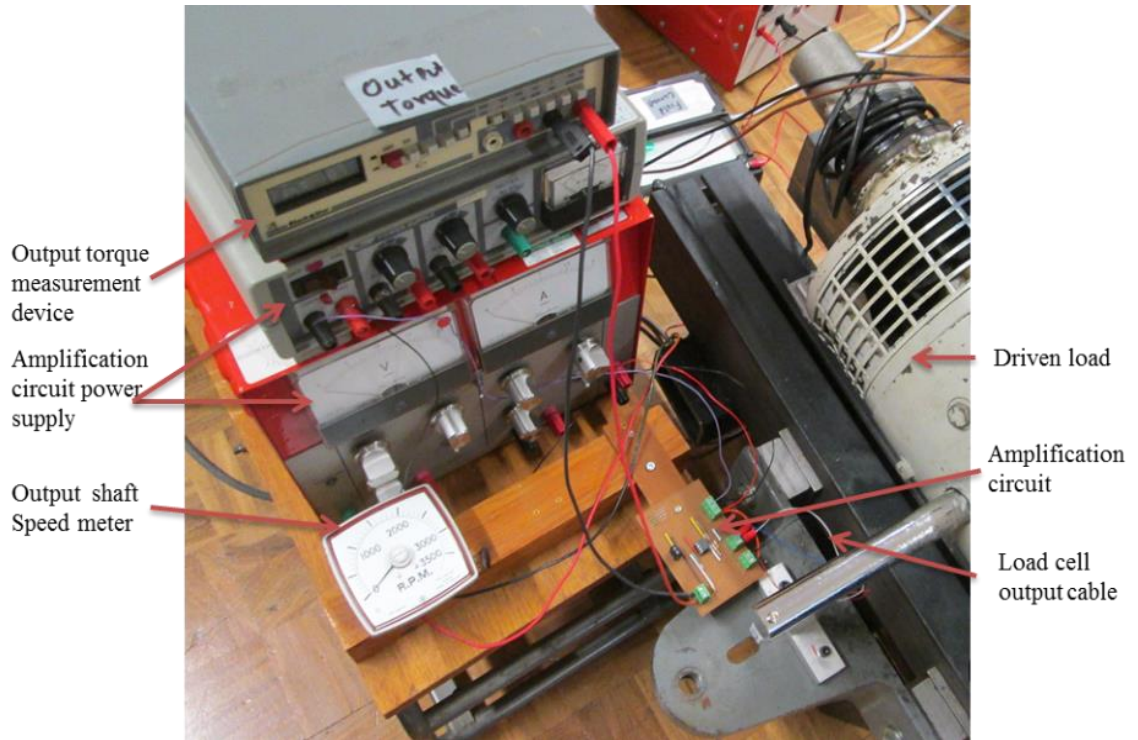


Figure 8.20: Section C of the complete Lab. bench components

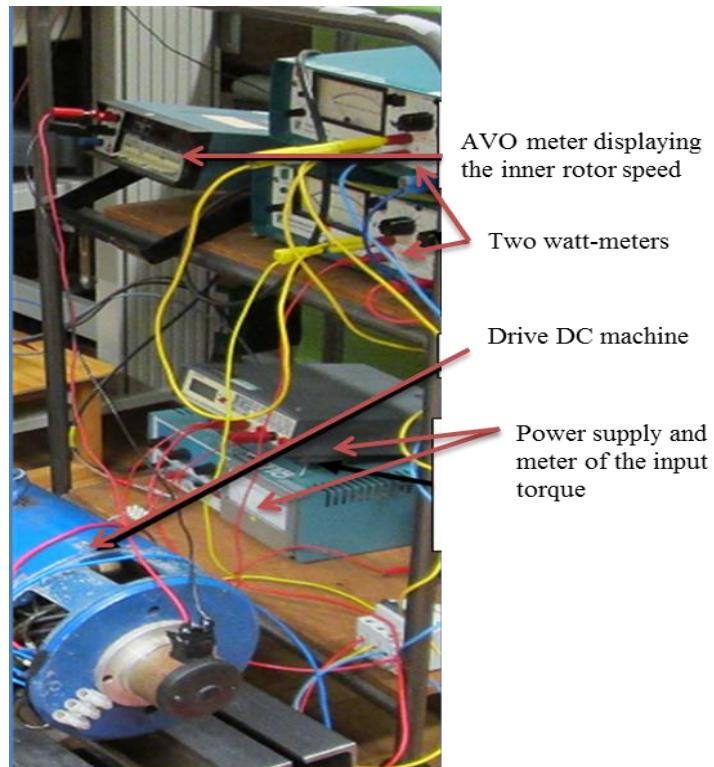


Figure 8.21: Section D of the complete Lab. bench components

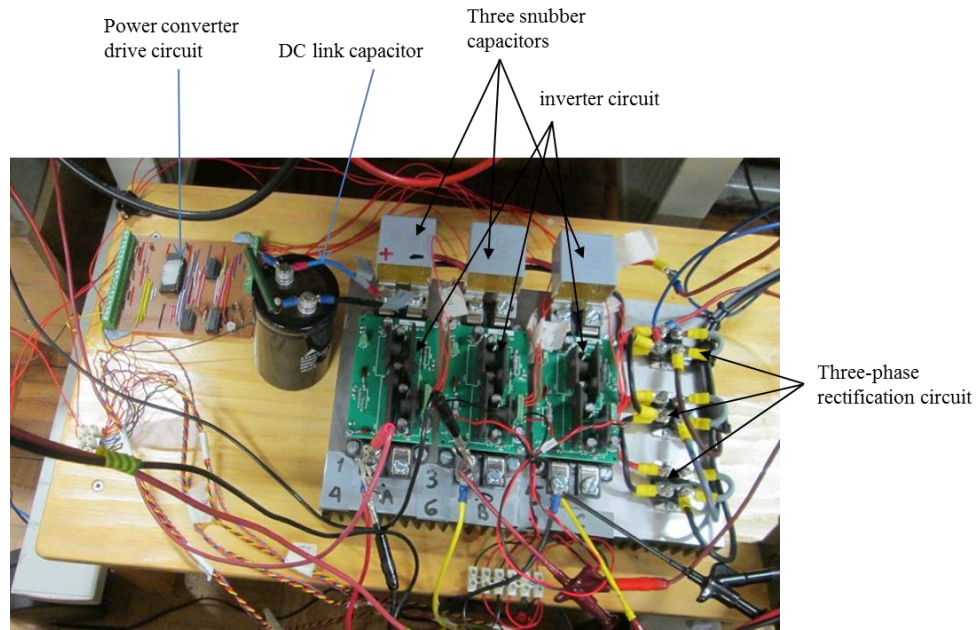


Figure 8.22: Section E of the complete Lab. bench components

- **Drive Circuit**

The drive circuit is composed of an optical sensor with its interface circuit, Pulse Width Modulation (PWM) circuit and the Erasable Programmable Read Only Memory (EPROM) circuit. The optical circuit is shown in Figure 8.23. It has two states of the sensor: first when the light beam is blocked, the leakage current of the photodiode is only allowed to flow and when the light beam is open, the sensor giving a high output voltage. An additional resistor is required to be connected in series with the light emitting diode.

Prior to testing the drive circuit, it was necessary to design a decoding circuit for the drive commutation. These signals were decoded in order to extract information of the internal phase EMFs, E_A , E_B , and E_C and their Line-Line EMFs, E_{AC} , E_{BA} , and E_{CB} . Table 8.4 shows details of the logic required to decode these signals, which comes from the optical sensors. The rotor position of the optical sensor is shown in Figure 8.23. It is supplied with 5 V and a current of 20 mA and the output signal ranges from 0 to 5 V.

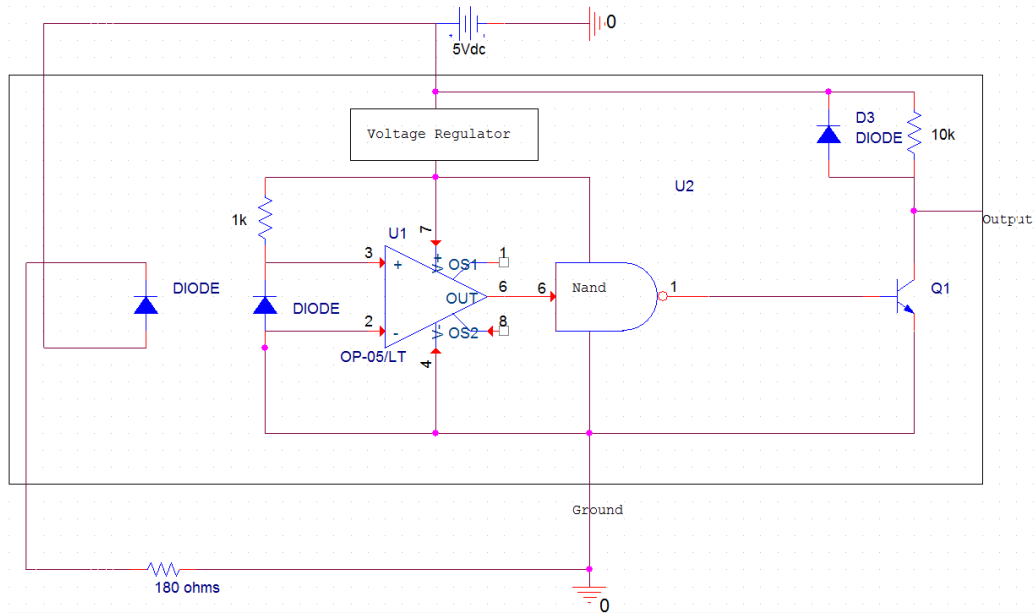


Figure 8.23: The optic-position sensor circuit

Figure 8.24 shows the drive circuit diagram of the EMTC system. The main driving circuit is made up of a bridge rectifier and an inverter. The input AC current and the voltage are rectified to produce a direct current and the voltage is then transformed by the inverter to drive the motor. The three-phase rectifier circuit is shown in Figure 8.26. The same figure shows the three-phase bridge inverter, it has six IGBT s and diodes D1-D6. These diodes return a regenerative energy from the motor to the DC link. Sometimes they are called freewheeling diodes because of their function to freewheeling the motor current. Note that the addresses A4 and A12 are set to be zero in the EPROM since there are only three logic inputs.

Figure 8.25 shows the logic diagram of the IGBT drive circuit. The NAND gates were used because the drive circuit is activated with active low inputs. The inputs of the NAND gates were produced from the PWM and the EPROM outputs. The PWM outputs are always active high. When both inputs of the NAND gates are high, the output will be low and the IGBT drive (see Appendix C4.4) can then operate the IGBT switch. Two IGBT switches in each instant will be driven. The switching sequence is listed in table 8.4.

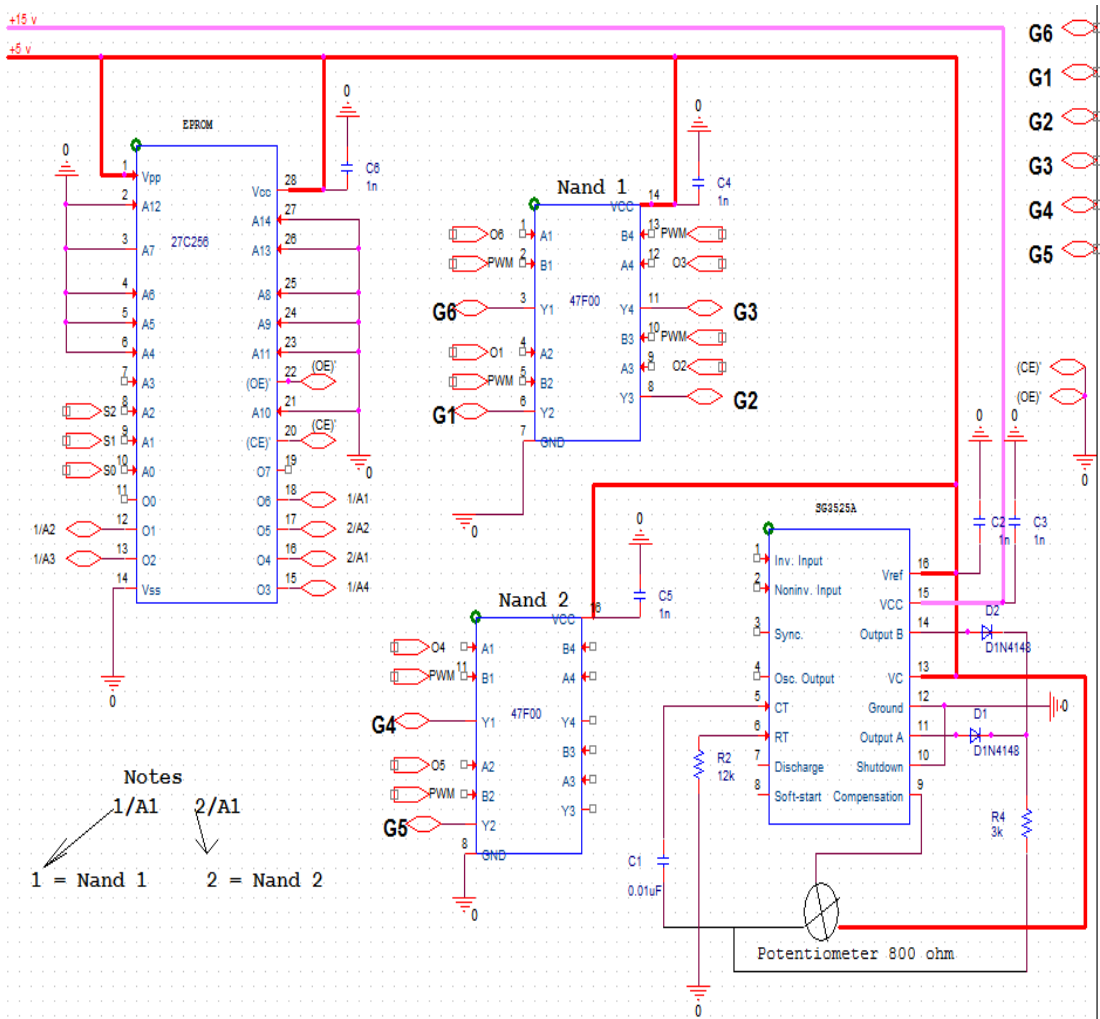


Figure 8.24: The hardware drive circuit diagram of the EMTC system.

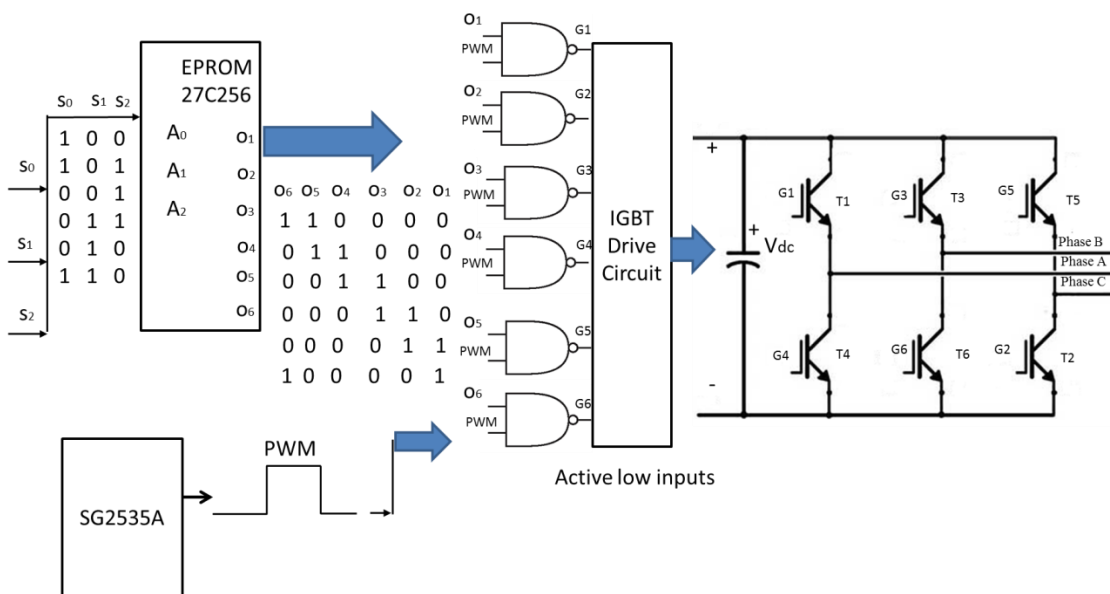


Figure 8.25: The Logic circuit diagram of the IGBT drive

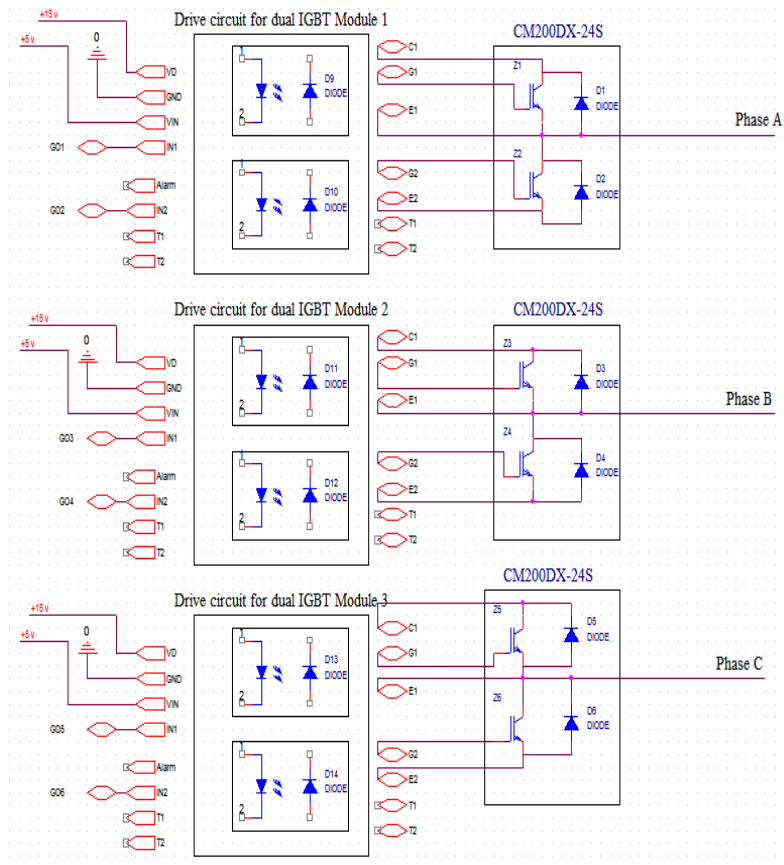


Figure 8.26: The three-phase rectifier circuit

Figure 8.27 shows the winding energizing sequence. The IGBTs were arranged as described in Table 8.4 and the ports P1-P6 correspond to the drive control signal of T1-T6.

Conduction phases	Address input			IGBT switching sequence								Address control
	S0	S1	S2	P7	P6	P5	P4	P3	P2	P1	P0	
CB	1	0	0	0	1	1	0	0	0	0	0	60H
CA	1	0	1	0	0	1	1	0	0	0	0	30H
BA	0	0	1	0	0	0	1	1	0	0	0	18H
BC	0	1	1	0	0	0	0	1	1	0	0	0CH
AC	0	1	0	0	0	0	0	0	1	1	0	06H
AB	1	1	0	0	1	0	0	0	0	1	0	42H

Table 8.4: Logical representation of the optic signals (CCW direction)

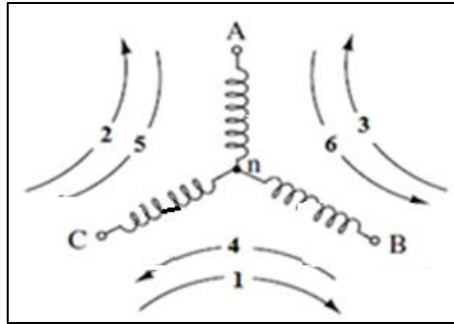


Figure 8.27: Stator of BLDCM winding diagrams

8.2.1 BLDC Machine Preparation

When testing the inverter for the first time, electrical noise was found to be present. This electrical noise appeared at the output of the amplifier as shown in Figure 8.28. These were spikes with approximately 2V in amplitude at a supply voltage of 40 V. The source of these spikes was found to be due to the lack of a DC link capacitor.



Figure 8.28: Commutation circuit noise with time switching at 20 ms/div and 1V/div

In figure 8.28, the AC current was measured with an amplifier with a gain of 20. Increasing the motor speed resulted in increasing the amplitude of the noise. The amplitude of the noise at the isolating amplifier output was found to depend on the IGBT switching at rising and falling times.

- **Ripple Current Adjustment**

The electrical noise was caused by the regenerative current spikes from the motor and the inverter. Therefore, a DC link capacitor was required to reduce these spikes or even to eliminate them altogether. A 2200 μ F electrolytic capacitor was connected to the drive

circuit board directly at the points where the snubber capacitors of $2.7\ \mu\text{F}$ are connected to the inverter IGBT as shown in Figure 8.29.

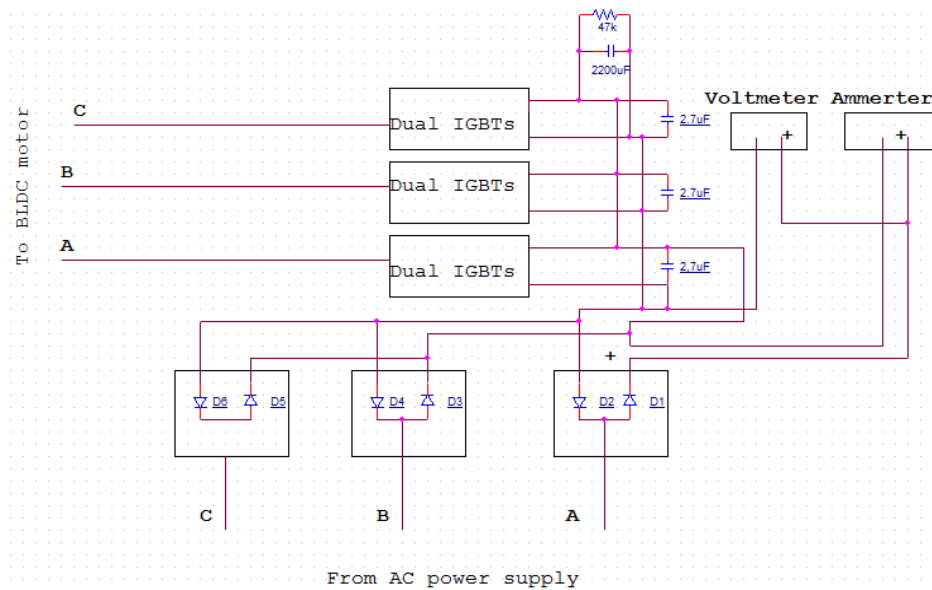


Figure 8.29: Drive circuit board with the snapper capacitors and DC link capacitor

A $47\ \text{k}\Omega$ resistance was connected in parallel to the capacitor in order to discharge the capacitor after the power off. This result the current waveform that is very smooth as can be shown in figure 8.30.

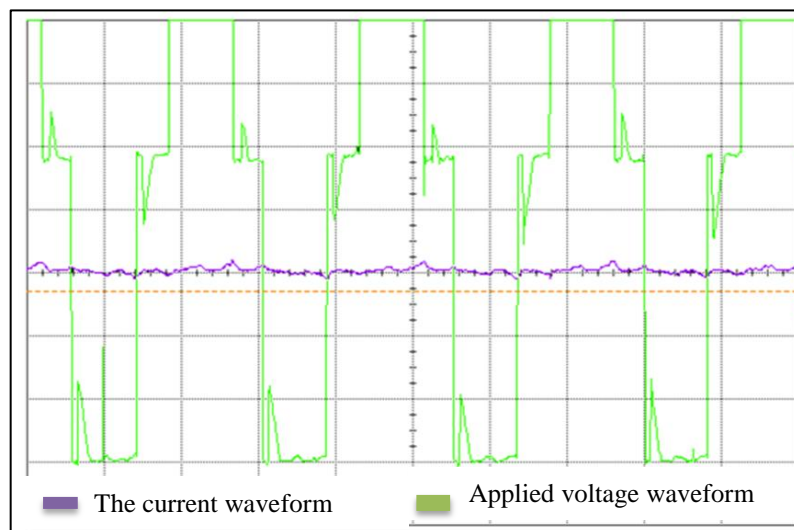


Figure 8.30: Measured phase voltage and line current with no load at 100 rpm, at supply voltage $40\text{V}_{\text{L-L rms}}$, 20 ms/div, using capacitor $2200\ \mu\text{F}$.

- **Determination of the Optimal Commutation Time**

The test bench was prepared for testing the motoring mode of the EMTC system. Several experiments were performed dynamically at no load and with a load. It is clear that the back-EMF waveforms at the outer windings are trapezoidal as shown in figures (8.31 - 8.34). These figures illustrate the voltage and the current in five states: the over-advanced, the slightly advanced, the over-retarded, the slightly retarded and the optimal commutation time. The current waveform is inclined either to the left or to the right side, which indicates that the rotor field is not matched to the stator field vectorily. Normally the commutation occurs as the two field vectors are at 90° to one another according to equation (8.6). The over-advancing or over-retarding of the commutation time leads the machine to produce a lower torque.

$$T = T_{max} \sin \theta \quad (8.6)$$

Where, θ is the angle between the rotor and stator field vectors.

Figure 8.31 shows the voltage and the current at an over-advanced state. It can be seen that the voltage has many spikes. Figure 8.32 illustrates the voltage waveforms when the commutation is slightly advanced. It is much more trapezoidal. In contrast, at the slightly retarded commutation timing as shown in Figure 8.33, the current waveform is inclined to the right side and the voltage waveforms are kept trapezoidal. The voltage waveform at the over-retarded commutation timing is shown in Figure 8.34. The current waveform is inclined at the right or the left side at the advanced and the retarded commutation timing respectively. The optimal commutation timing at several load currents is shown in figures 8.35 and 8.36, where the no load measurements at several speeds and supply voltage ranges are shown in figures 8.37 - 8.39.

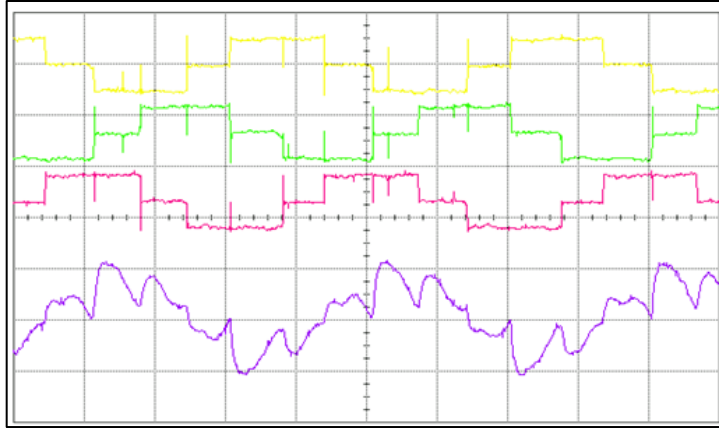


Figure 8.31: Measured line voltage (upper) and line current (lower) with no-load at 140 rpm (Phase voltage 50V, 50 ms/div), at over advanced commutation time

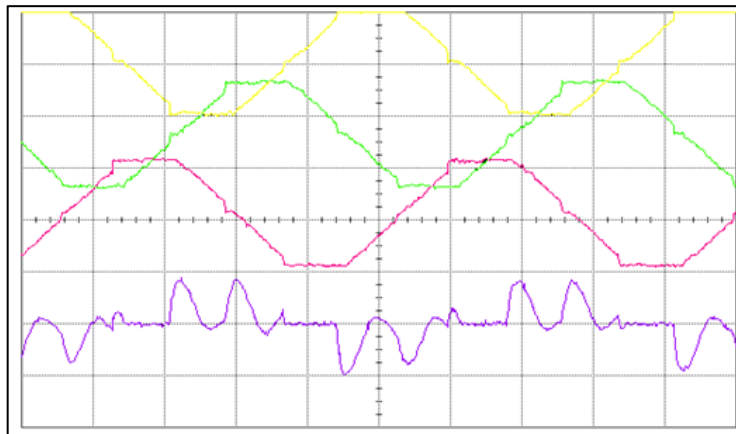


Figure 8.32: Measured line voltage (upper) and line current (lower) with no-load at 140 rpm (Phase voltage 100V, 20 ms/div), at slightly advanced commutation time

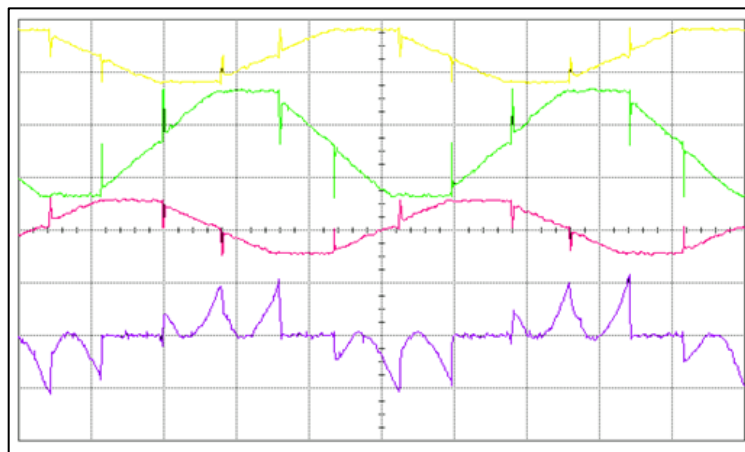


Figure 8.33: Measured line voltage (upper) and line current (lower) with no-load at 140 rpm (Phase voltage 100V, 20 ms/div), slightly retarded commutation time

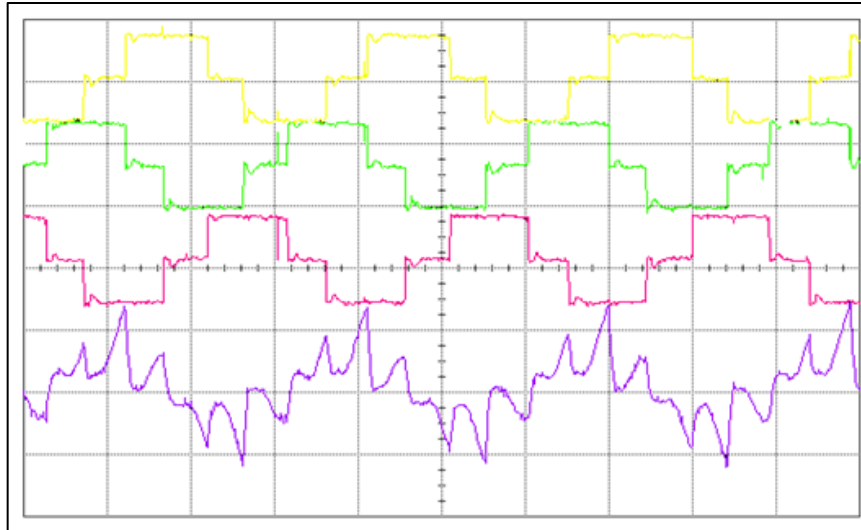


Figure 8.34: Measured line voltages (upper) and line current (lower) with no-load at 140 rpm (Phase voltage 75V and 50ms/div), at an over retarded commutation time

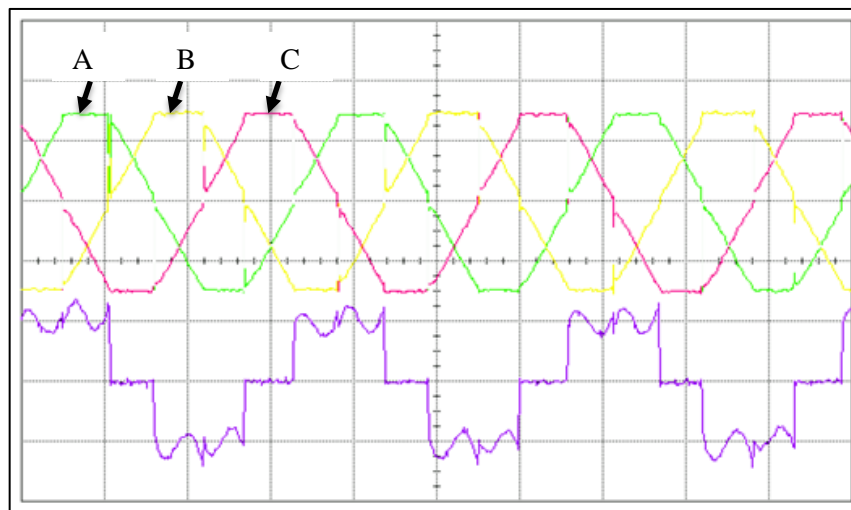


Figure 8.35: Measured line voltages (upper) and line current (lower) with $\frac{1}{4}$ full load (4Amp) at 140 rpm (Phase voltage 300V, 20mV/div, 10 ms/div), at an optimal advanced angle

The measured back EMFs in the stator windings at an optimal commutation angle is illustrated in figures 8.35 and 8.36. The waveforms were taken at $\frac{1}{4}$ and $\frac{3}{4}$ of the full load. The phase displacement between the three-phases is symmetrical of 120° degrees. The amplitude of these three-phase waveforms is identical as shown in figure 8.35. In the figure 8.36, the voltage /div of each phase is adjusted to display all the waveforms.

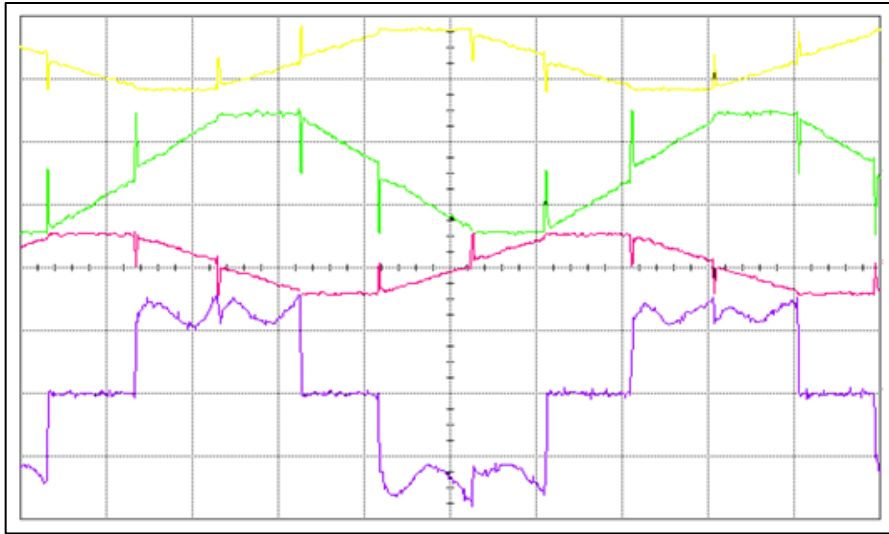


Figure 8.36: Measured line voltages (upper) and line current (lower) with $\frac{3}{4}$ full load (8Amp) at 120 rpm (Phase voltage 100V, 20 ms/div), at an optimal commutation time

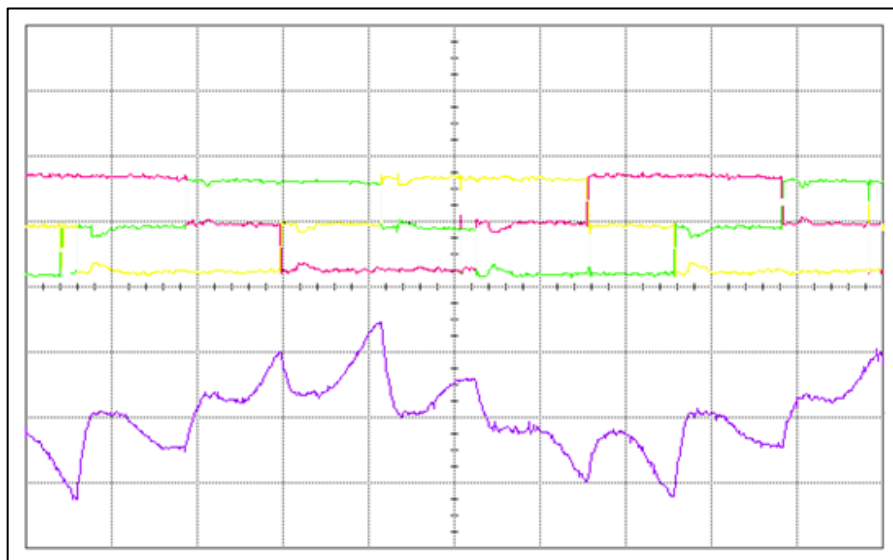


Figure 8.37: Measured line voltages (upper) and line current (lower) not connected to load at 125 rpm, (Phase voltage 30V, 5mV/div, and 20ms/div)

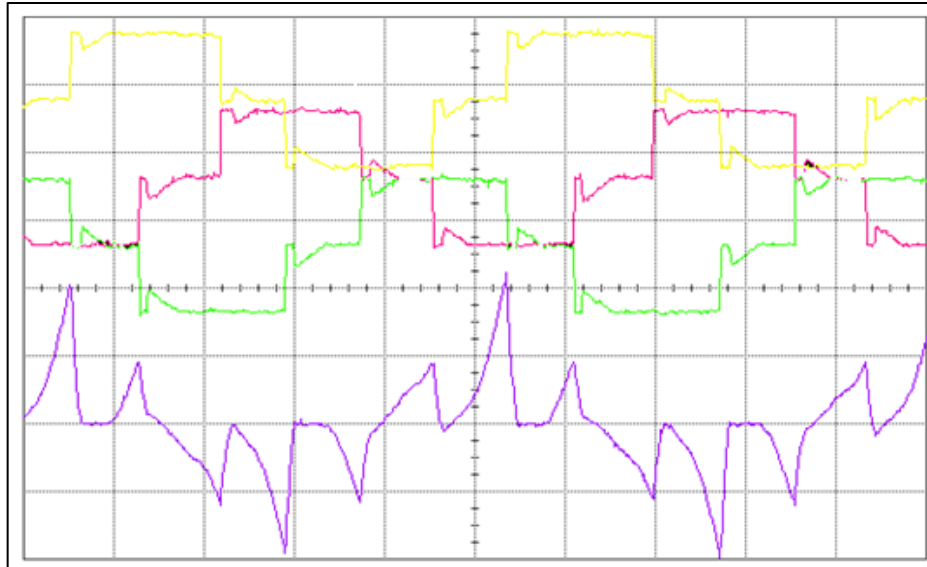


Figure 8.38: Measured line voltages (upper three waveforms) and line current (lower waveform) not connected to load at 175 rpm, (Phase voltage 100V peak, 20ms/div)

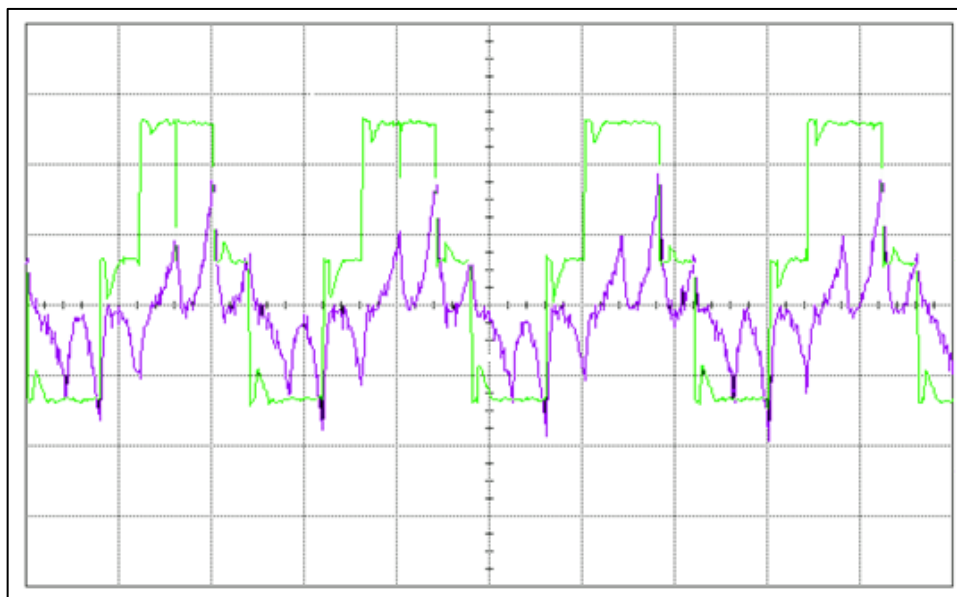


Figure 8.39: Measured phase voltage (green colour waveform) and line current (purple colour waveform) not connected to load at 400 rpm (Phase voltage 100V, 20 ms/div)

9 Experimental Results and Validation

9.1 Introduction

In this chapter, various experimental tests were carried out on the prototype EMTC system and the results are presented. Calibration of the measuring devices for the inner rotor speed, the outer rotor speed, the input torque and the output torque were carried out prior to the testing of the EMTC system. The results of these calibrations are given in Appendix E.

Figure 9.1 shows a block diagram of the sequence of experimental tests. The main objectives of the testing are to characterise each machine part in the EMTC system including the brushless DC machine (BLDCM), the permanent magnet induction machine (PMIM), and the variable frequency rotary transformer (VFRT) along with validating the FEM analysis and MATLAB simulation results of chapters 6 and 7, and to investigate the performance of the whole EMTC system

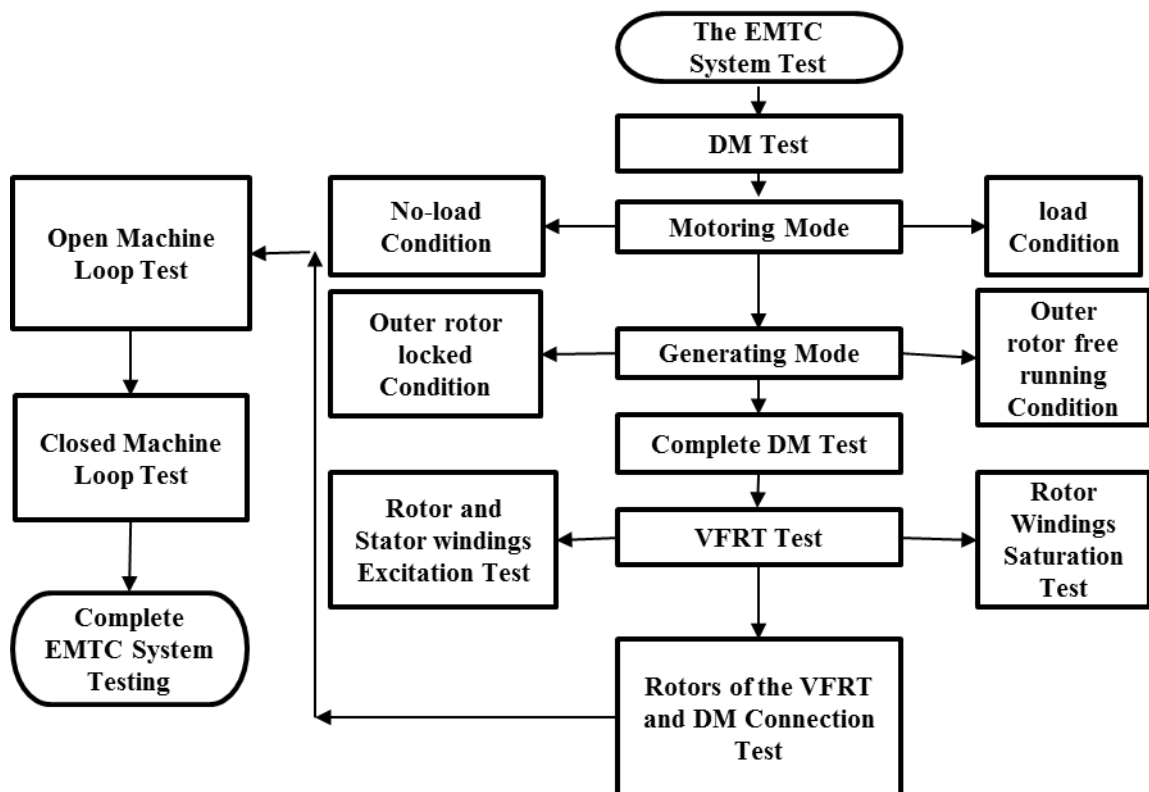


Figure 9.1: Block diagram of the EMTC system testing

9.2 Differential Machine (DM) Testing

The aim of this test is to characterise both the BLDCM and the PMIM. In addition, testing the DM will help to validate the performance of the complete EMTC system. After preparing the (BLDC) machine and adjusting its commutation time as described in chapter eight (section 8.2.1), the differential machine was then tested in two modes; motoring (the BLDCM testing) and generating (the PMIM testing) modes. The following subsections present the results of these tests.

9.2.1 The BLDCM, No-load Test with the Inner Rotor Free Running

This test was performed in the motoring mode. The outer rotor speed, the output torque, the dc-link voltage, the current, and the AC power supply were measured. The DC generator was used as a load; the power absorbed by the resistive load was then measured. The BLDC machine stator windings were connected in a star connection and supplied by an external power source. The test set-up of this mode can be shown in Figure 9.2. The outer rotor shaft was coupled with the dynamic load at the load test as shown in figure 9.2, while in the no-load test it was decoupled. The torque is measured by the amplified load cell output. The input voltage along with the speed of the outer and the inner rotors are listed in table 9.1.

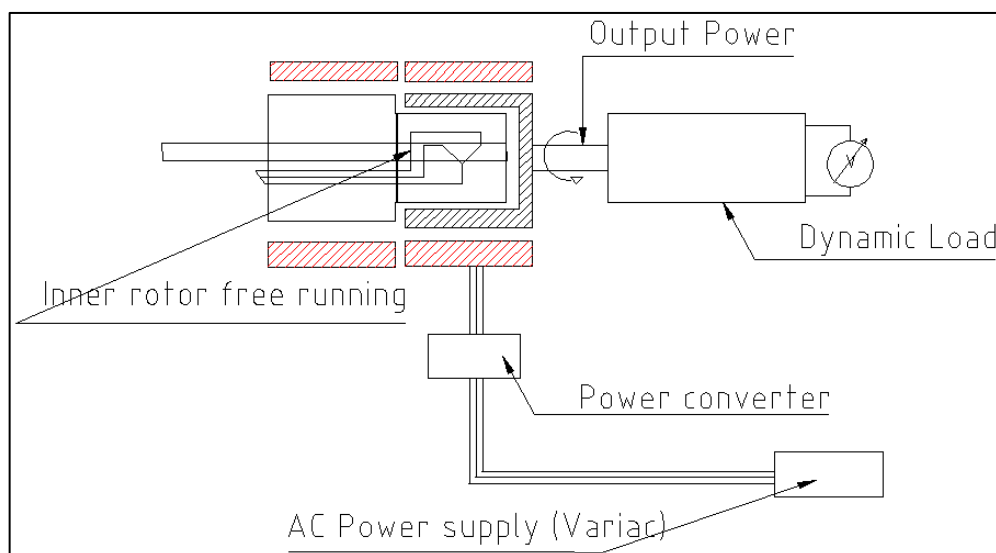


Figure 9.2: The motoring mode set-up

Input voltage (Line- Line) peak value	Inner rotor speed (rpm)	Outer rotor Speed (rpm)	Dc voltage after rectification circuit reading
0.0	0	0	0
20.0	23	30	24
40.0	50	63	53
60.0	85	93	79
80.0	93	130	106
100.0	128	155	133
120.0	176	192	160
140.0	197	222	185
160.0	232	259	215
180.0	270	296	241
200.0	305	333	268
220.0	333	370	297

Table 9.1: Speed- Voltage test of the BLDCM at the inner rotor free running

The speed-voltage characteristics of the BLDCM are shown in Figure 9.3. It can be seen that the speed of the BLDC machine responds to the change of the supply voltage and reaches its speed linearly. On the other hand, the inner rotor speed was measured and it can be noted that it tried to track the outer rotor speed as shown in figure 9.3. However, due to the phenomena of induction machine operation, there is a small slip speed between the outer speed (synchronous speed) and the inner rotor speed. This is because when the permanent magnet rotor rotates, a current is induced in the inner rotor windings, since they are shorted, by transformer action. This circulating current is reducing to zero when the inner rotor is rotating at synchronous speed. Therefore, the inner rotor is trying to catch (with slip) the rotating magnetic field that is induced by the permanent magnet. The speed of the inner and the outer rotors was simulated using FEM and the results are presented in chapter 6 in figures 6.28 and 6.29. In addition, this result can be found in chapter 7 with the Matlab simulation in figures 7.5-7.7. These three results are quite similar to each other in terms of shape and performance. This validates the precision of the simulated model in both the FEM and MATLAB when compared with the real system.

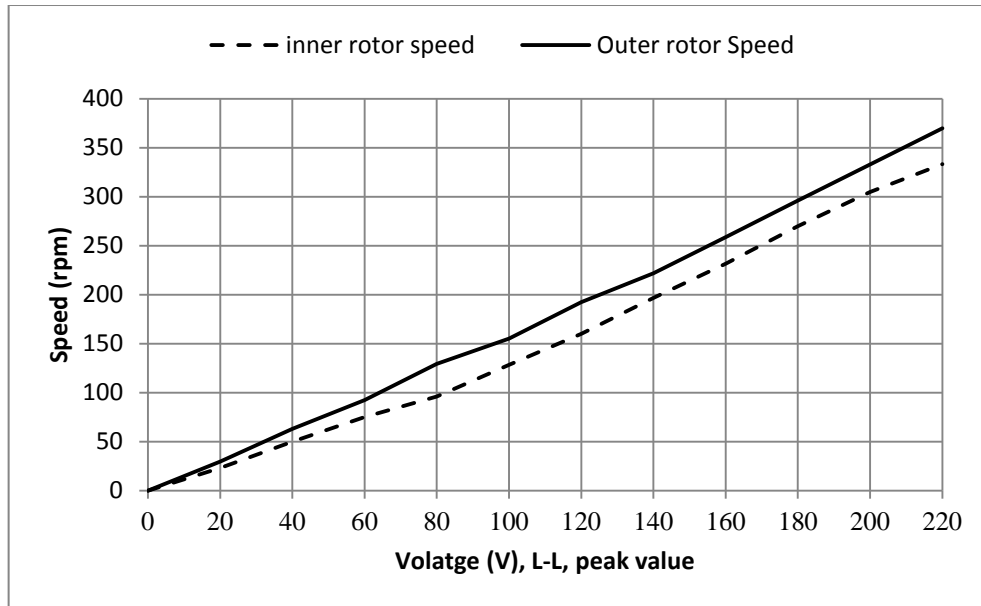


Figure 9.3: Speed-voltage characteristic at motoring mode including inner rotor speed

9.2.2 The BLDCM, Load Test with the Inner Rotor Free Running

The purpose of the test is to characterise the BLDCM on load. The absorbed current to drive the load will indicate the performance of the machine. With the test set-up shown in figure 9.2, the outer rotor was coupled to the separately excited DC machine as a dynamic load. In this test, a load torque was applied in steps while the BLDCM running at speed of 470 rpm. Figure 9.4 presents the torque-speed characteristics of the BLDCM under this load condition based on table 9.2. It can be seen that the machine can handle a torque of 19 Nm while its speed decreased by only 70 rpm. This result gives the indication that the BLDCM has a high efficiency.

Input DC parameters at the inverter		Outer rotor speed (rpm)	Output torque (mV)	Output torque (Nm)	Output power (W)	Efficiency
Voltage (DC)	Current (DC)					
372	0.42	470	85	1.95	95.84	0.61
371	0.43	470	85.6	2.05	100.93	0.63
370	0.46	465	86.6	2.22	104.76	0.62
370	0.49	430	88.2	2.5	112.52	0.62
369	0.54	430	90.4	2.88	129.59	0.65
369	0.61	430	93.4	3.4	152.87	0.68
369	0.68	420	96.4	3.91	172.05	0.69
368	0.76	410	99.6	4.47	191.63	0.69
368	0.83	410	102.8	5.02	215.31	0.70
367	0.9	410	105.8	5.53	237.5	0.72
366	0.96	410	108.8	6.05	259.7	0.74
366	1.03	410	111.6	6.53	280.42	0.74
366	1.09	410	114.3	7	300.39	0.75
365	1.34	405	125.3	8.9	377.12	0.77
364	1.47	400	130.9	9.86	412.89	0.77
363	1.6	400	135	10.82	452.9973	0.78
363	1.73	400	139.1	11.78	493.1893	0.79
363	1.86	400	143.2	12.74	533.3813	0.79
363	1.91	400	150.7	13.28	555.82	0.80
362	2.24	400	165.7	15.86	664.09	0.82
361	2.65	400	184.3	19.07	798.35	0.83

Table 9.2: The output torque versus outer rotor speed of the DM outer part (BLDCM)

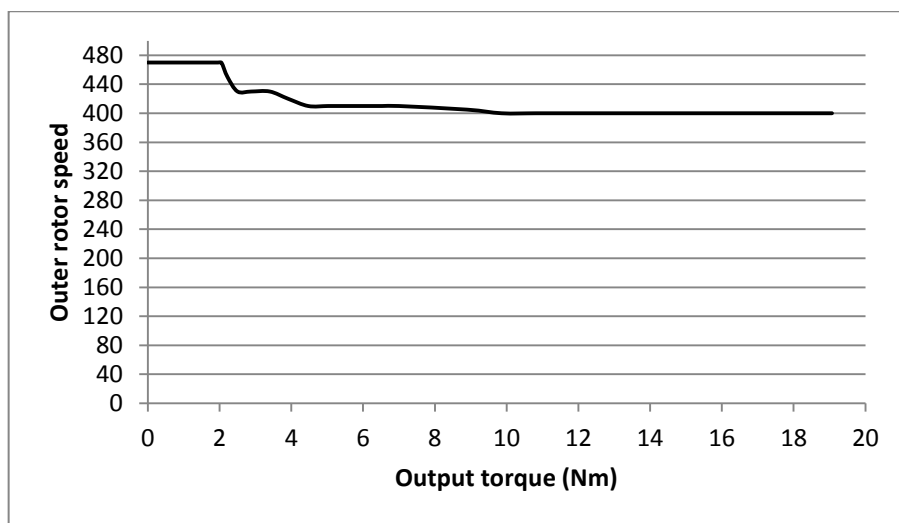


Figure 9.4: The torque-speed characteristics of the outer part (BLDCM)

9.2.3 The PMIM Test with the Outer Rotor Locked

The permanent magnet induction machine (PMIM) was tested in a generating mode. The test was carried out with the outer rotor locked. The aim of this test was to characterise the PMIM both on load and on no-load conditions. Figure 9.5, shows the test configuration to measure the slip power and the losses of the PMIM. Tables 9.3 and 9.4 list the measured speed and torque of the PMIM, and the mechanical input power to the PMIM at different resistances. The inner rotor windings were connected to the external 27-ohm and 58-ohm load bank and the rotor speed was increased gradually in 100 rpm step.

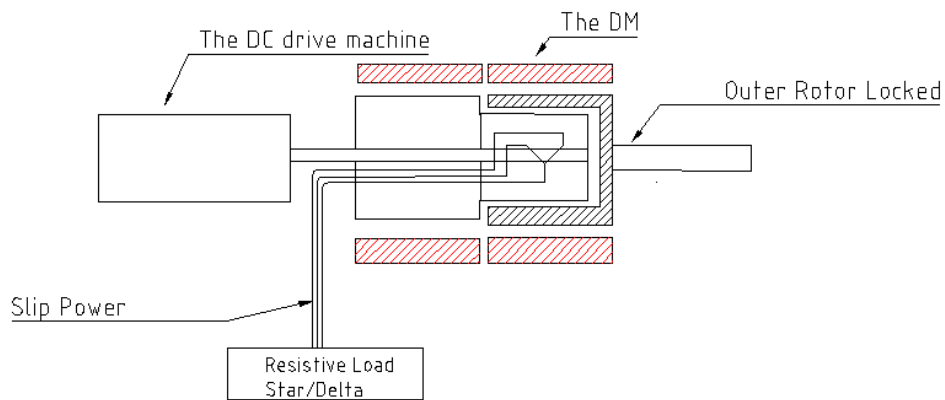


Figure 9.5: The generating mode set-up

The measured input power with locked outer rotor is listed in tables 9.3 and 9.4. In this test, the inner rotor windings were connected to the external 27-ohm and 58-ohm load bank. The inner rotor speed was increased gradually in 100-rpm steps.

Input torque (Nm)	Inner rotor (rpm)	Slip power (W)	Input power (W)	losses (W)	efficiency
0.00	0.00	0.00	0.00	0.00	0.00
1.96	100.00	15.40	20.51	5.11	0.80
3.39	200.00	55.40	70.96	15.56	0.82
4.86	300.00	125.00	152.60	27.60	0.85
6.45	400.00	230.00	270.04	40.04	0.87
7.75	500.00	342.00	405.58	63.58	0.86
9.06	600.00	489.00	568.97	79.97	0.88

Table 9.3: Generating mode of the PMIM test at locked outer rotor with an external resistance of 27 ohm

Input torque (Nm)	Inner rotor speed (rpm)	Slip power (W)	Input power (W)	Losses (W)	Efficiency
0.00	0.00	0.00	0.00	0.00	0.00
1.05	100.00	5.50	10.99	5.49	0.67
1.70	200.00	22.20	35.59	13.39	0.73
2.37	300.00	51.70	74.42	22.72	0.77
3.02	400.00	93.70	126.44	32.74	0.79
3.53	500.00	137.00	184.74	47.74	0.79
4.15	600.00	200.70	260.62	59.92	0.81
4.75	700.00	277.00	348.02	71.02	0.83
5.33	800.00	362.00	446.30	84.30	0.84
5.87	900.00	415.00	552.95	137.95	0.80
6.32	1000.00	541.00	661.49	120.49	0.85
6.96	1100.00	674.00	801.33	127.33	0.86
7.49	1200.00	796.00	940.74	144.74	0.87
8.03	1300.00	932.00	1092.62	160.62	0.87
8.62	1400.00	1090.00	1263.12	173.12	0.88

Table 9.4: Generating mode of the PMIM test at locked outer rotor with an external resistance of 58 ohm

The calculated efficiency of the PMIM can be shown in table 9.4. The efficiency with an external resistance of 27 ohms is higher than with 58 ohms by 7%. This means that the PMIM will be much more efficient when no external resistances are connected.

9.2.4 The PMIM Test with the Outer Rotor Free Running

The free running of the outer rotor with small external resistance is preferable. This will reduce the iron losses in the inner rotor. The torque-speed measurements of the PMIM in the generating mode with a free running outer rotor are shown in tables 9.5 and 9.6. Figure 9.6 shows the relationship between the speed of the inner and the outer rotors with external resistances connected to the inner rotor windings of 58 ohms. Based on measured input power and the output power of the PMIM as can be shown in table 9.5, the efficiency η is calculated according to the equation 9.1.

$$\eta = \frac{P_o}{P_i} \quad (9.1)$$

Where P_o is the output power and P_i is the input power.

The power losses P_{losses} can be calculated using the equation below:

$$P_{losses} = P_o - (P_i + P_{slip}) \quad (9.2)$$

The power losses are a function of the slip power P_{slip} , when the slip power is zero the losses are only the mechanical friction, resistive power and iron losses.

Inner rotor speed (rpm)	outer rotor speed (rpm)	Tout (Nm)	Tin (Nm)	Pslip (W)	Input power (W)	Output power (W)	Slip power (W)	Losses (W)	Efficiency
0	0	0	0	0	0.00	0.00	0.00	0.00	0.00
100	0	2.36	1	5.4	10.47	0.00	5.40	5.07	0.67
200	10	2.52	1.45	14.6	30.35	2.64	14.60	13.11	0.70
300	50	2.53	1.7	21.8	53.38	13.24	21.80	18.34	0.74
400	110	2.52	1.85	26	77.45	29.06	26.00	22.39	0.78
500	200	2.53	1.96	31.3	102.57	52.98	31.30	18.29	0.85
600	300	2.53	2.08	36.1	130.62	79.47	36.10	15.06	0.90
700	390	2.54	2.17	41.2	158.99	103.70	41.20	14.09	0.92
800	490	2.54	2.28	46.7	190.91	130.13	46.70	14.08	0.93
900	550	2.54	2.36	51.7	222.31	146.43	51.70	24.18	0.90
1000	600	2.54	2.44	55.3	255.39	159.74	55.30	40.34	0.86
1100	700	2.55	2.53	62.05	291.29	186.61	62.05	42.63	0.87
1200	800	2.54	2.56	64.1	321.54	212.72	64.10	44.71	0.88
1300	880	2.54	2.7	69	367.38	234.00	69.00	64.38	0.85
1400	990	2.55	2.76	74	404.43	263.91	74.00	66.52	0.86

Table 9.5: PMIM testing with an external resistance of 58 ohm

Figure 9.6 shows the slip speed when the external resistance is 58 ohms is getting larger as the inner rotor speed increases. In addition, at the low inner rotor speed, the outer rotor was remained at stall. This is because the PMIM behaves like the induction machine. Therefore, if the closer slip speed is required, the inner rotor windings need to be shorted.

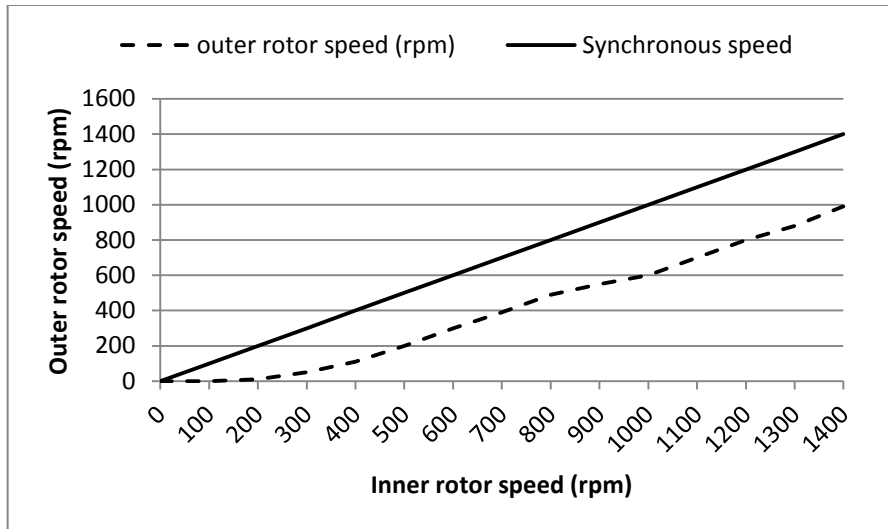


Figure 9.6: The measured inner rotor speed versus the outer rotor speed at 58-ohm external resistance

The simulated results using FEM of the DM when the inner rotor is connected to the external resistance of 58 ohms and the outer rotor is freely rotating can be shown in figure 9.7. This figure illustrates the outer rotor trying to track the inner rotor, but due to the high inertia in the simulation model, it rotated in the opposite direction at the beginning and then it follows the inner rotor direction. The aim of the simulation, which was carried out prior to the experiment, was to determine the effect of the external resistance connected to the inner rotor windings on the dynamic behaviour of the system.

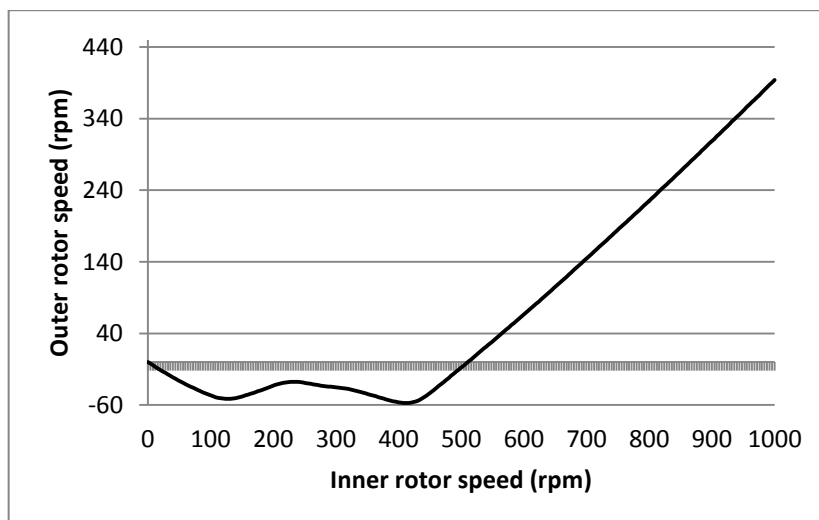


Figure 9.7: Simulated using FEM of the inner rotor speed versus the outer rotor speed at 58 - ohm external resistance

When the inner rotor windings were connected to the small external resistance of 6 ohm for example, the outer rotor tracks the inner rotor speed faster as expected due to the small slip between the synchronous and the mechanical speeds as shown in figure 9.8. Table 9.6 shows the measured the input torque, the output torque, the inner rotor speed and the outer rotor speed. The power losses are 40 W at 1000 rpm of the inner rotor speed, which is the same when the external resistance was 58 ohms. The efficiency of the PMIM when the 6 ohms external resistance was connected to the inner rotor windings is also the same when the 58 ohms resistor was connected.

Inner rotor speed (rpm)	outer rotor speed (rpm)	Tout (Nm)	Tin (Nm)	Pslip (W)	Input power (W)	Output power (W)	Losses (W)	Efficiency
0.00	0.00	0.00	0.00	0.00	0.00	0.00	0.00	0.00
100.00	40.00	2.51	1.57	0.63	16.43	10.53	5.28	0.62
200.00	120.00	2.52	1.82	1.80	38.10	31.71	4.59	0.79
300.00	215.00	2.53	1.92	3.10	60.29	56.9	3.39	0.94
400.00	310.00	2.53	2.10	2.10	87.92	82.22	3.60	0.91
500.00	420.00	2.53	2.23	3.20	116.70	111.40	2.11	0.93
600.00	510.00	2.54	2.33	4.04	146.32	135.44	6.85	0.90
700.00	600.00	2.54	2.45	3.38	179.50	159.74	16.38	0.87
800.00	700.00	2.55	2.58	4.40	216.03	186.61	25.03	0.85
900.00	810.00	2.55	2.66	4.70	250.57	215.93	29.94	0.85
1000.00	890.00	2.55	2.70	4.60	282.60	237.56	40.44	0.83

Table 9.6: PMIM testing with an external resistance of 6 ohm

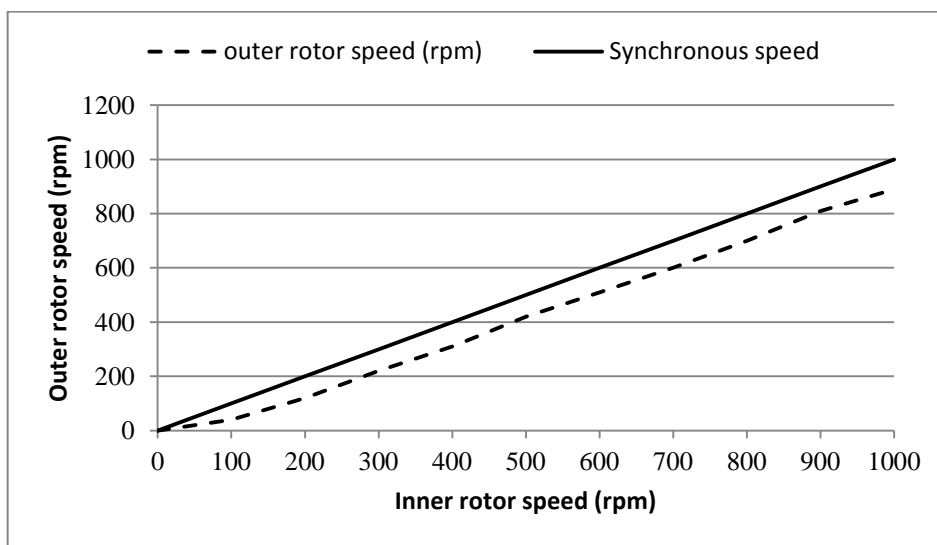


Figure 9.8: Measured inner rotor versus outer rotor speed at 6 ohm external resistance

Similar to the previous FEM simulation with 58 ohms, the FEM simulation was carried out when the inner rotor of the PMIM was connected to 6 ohms. The outer rotor tried to track the inner rotor immediately as can be shown in figure 9.9. On the other hand, the Matlab/Simulink was simulated using the mathematical model discussed in chapter 7 section 7.3. The result is shown in figure 9.10. The reason for selecting this value of resistance was that the resistive bank in the experimental setup range from 6 ohms to 58 ohms. Figure 9.11 shows the simulated model when the inner rotor windings were shorted.

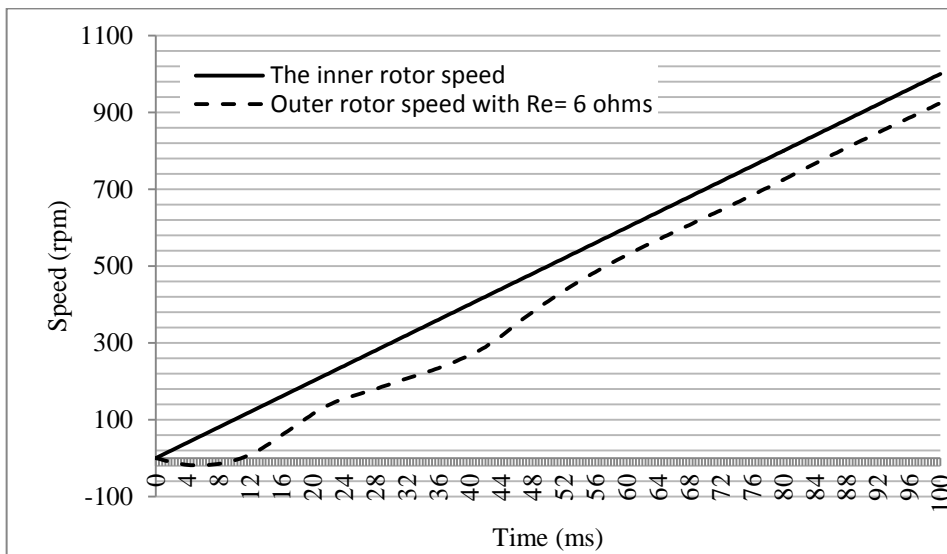


Figure 9.9: FEM simulation of the inner rotor and outer rotor speeds when 6 ohm external resistance is connected to the inner rotor windings

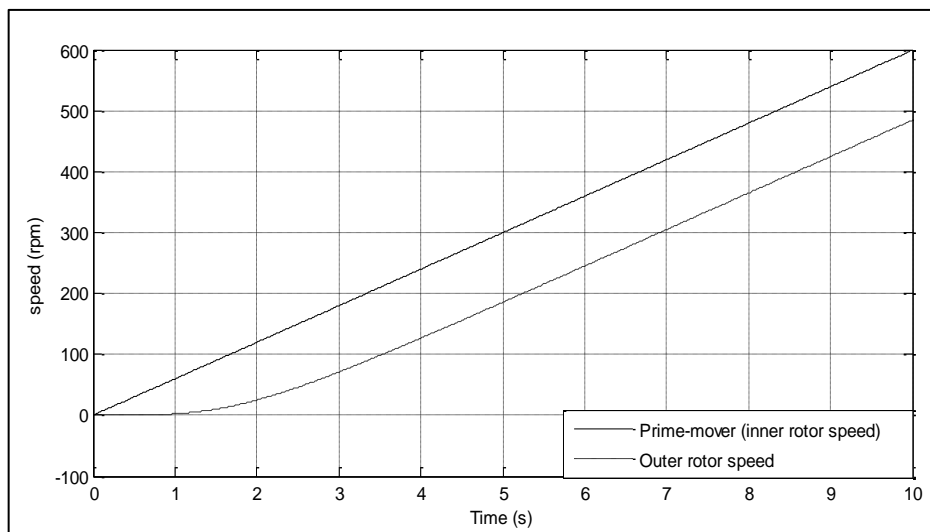


Figure 9.10: Matlab simulation results for the outer and the inner rotor speeds at 6 ohms connected to the inner rotor windings.

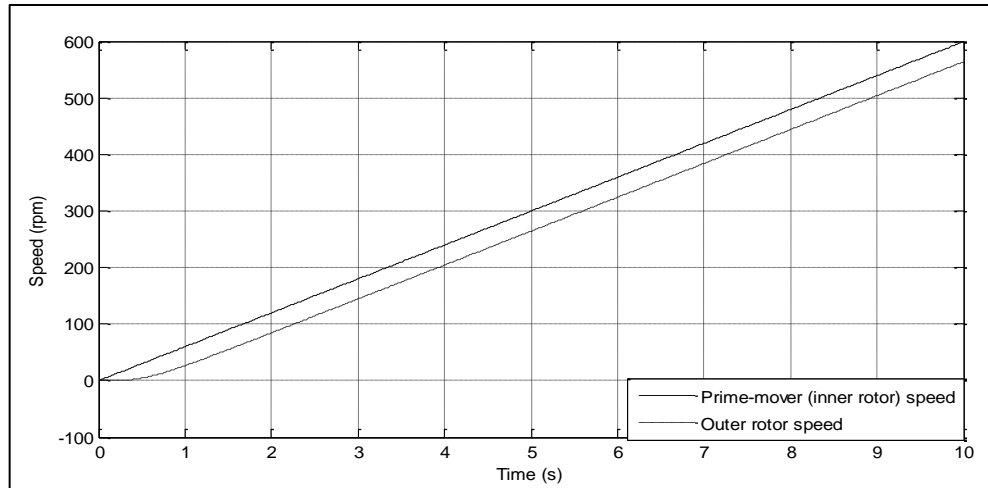


Figure 9.101: Matlab simulation results for the outer and the inner rotor speeds at inner rotor windings short-circuited

9.2.5 The PMIM Test with Locked Inner Rotor

This test was performed with the inner rotor locked and the outer rotor rotating at different speeds using the load machine as a drive motor as can be shown in figure 9.12. The aim of this test was to determine the back EMF in both the stator and the inner rotor windings of the PMIM. The measured back EMFs with respect to the outer rotor speed is shown in figure 9.13, based on the measured outer rotor speed shown in table 9.7. It is found that the relationship between the speed of the outer rotor and the back EMF is nearly the same as the DM tested in the motoring mode. This means the machine is able to operate in the both directions.

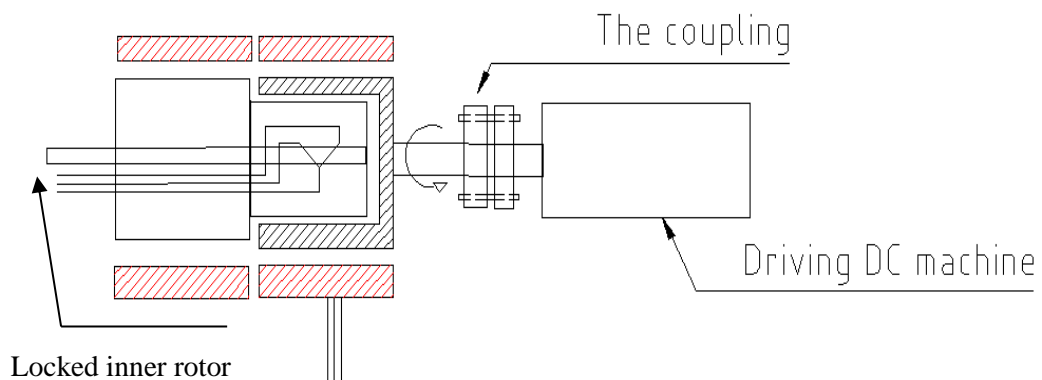


Figure 9.11: Generating mode set-up, using the driven load as a motor

speed (rpm)	stator EMF (V) phase, peak
0	0
100	68.4
200	114
300	157.6
400	210.6
500	250
600	301.6
700	348
800	398
900	446
1000	484

Table 9.7: Generating mode using the outer rotor

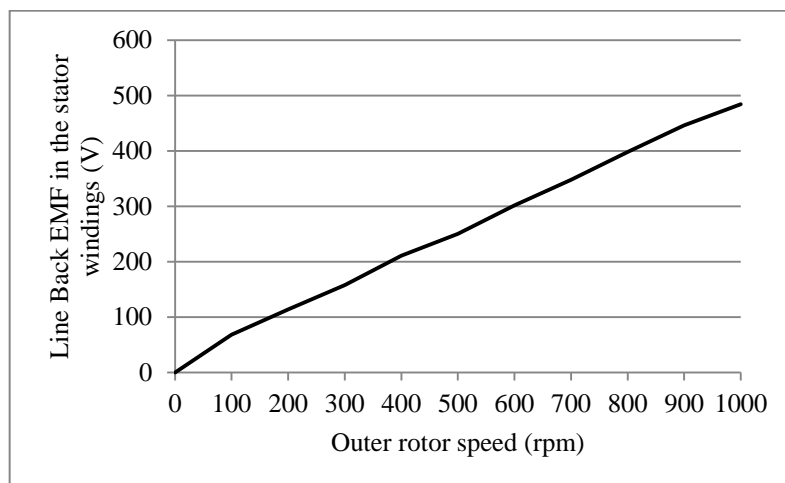


Figure 9.12: Measured back EMF in the stator windings at the inner rotor locked

Power Losses Measurement

The power losses of the slip rings may have an impact on the PMIM and the whole DM efficiency measurements. This is because the produced temperature during the slip ring rotating is considered as friction losses. In contrast, in the motoring mode only, the slip ring losses were not included in the measurements. The inner rotor windings were kept open circuited in this test. Hence, the friction losses of the slip rings and the resistive losses were not included in the total losses. The relationship between the input voltage and the inner rotor speed was measured as shown in the table 9.8.

T_{in} (Nm)	Input voltage line-to-line (V)	inner rotor speed (rpm)	Inner rotor output voltage line-to-line (V)	input power (W)
0.56	5.00	100.00	21.00	5.86
0.69	6.00	200.00	38.00	14.44
0.78	8.00	300.00	57.00	24.49
0.81	9.00	400.00	76.00	33.91
0.93	10.00	500.00	94.00	48.67
1.00	12.00	600.00	112.00	62.80
1.03	13.00	700.00	130.00	75.46
1.08	15.00	800.00	151.00	90.43
1.13	16.00	900.00	168.00	106.45
1.16	17.00	1000.00	187.00	121.41

Table 9.8: Power losses at inner rotor open circuited

The voltage- speed characteristics of the PMIM is listed in table 9.8, based on the measured induced voltage at several speeds of the inner rotor as shown in figure 9.14. In this test, the inner rotor windings of the differential machine were kept open circuited while the inner rotor was driven by the DC motor. The aim of this test was to determine the frictional losses since the resistive losses were excluded.

The losses were calculated from the measurements when both the inner rotor windings were open circuited and the external resistance was connected. Figure 9.15 illustrates the losses at open circuit inner rotor windings and external resistance was connected. The lower the resistance connected to the inner rotor windings more losses were dissipated. Higher losses were expected when the outer rotor was locked i.e. the resistive losses and the frictional losses were higher. The dissipated loss with a 28-ohm resistance is higher than the measured losses with 6-ohm resistance of 30 W at 1000 rpm as can be found in figure 9.15.

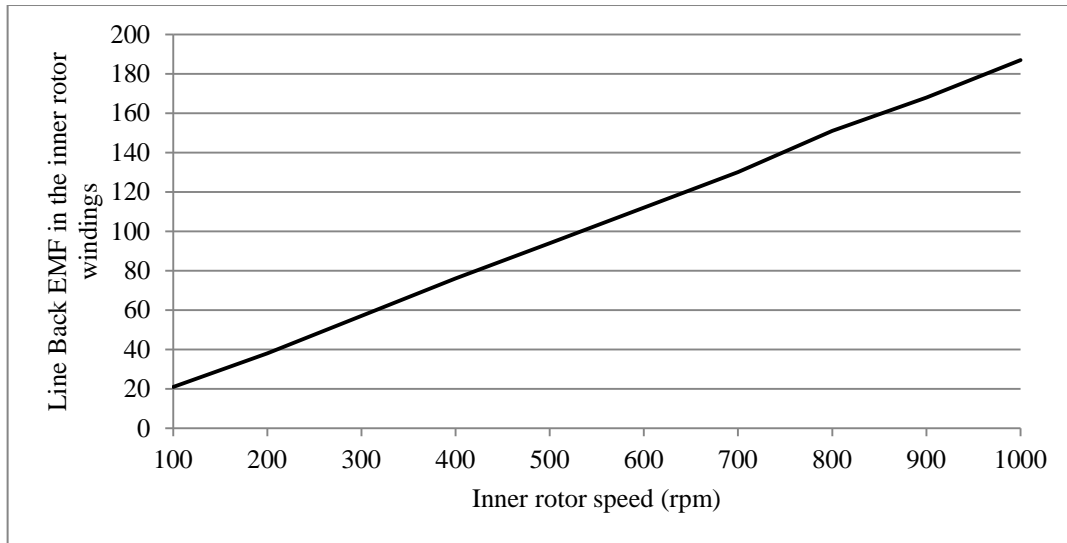


Figure 9.13: Voltage-speed characteristics of the PMIM at open circuit inner rotor windings

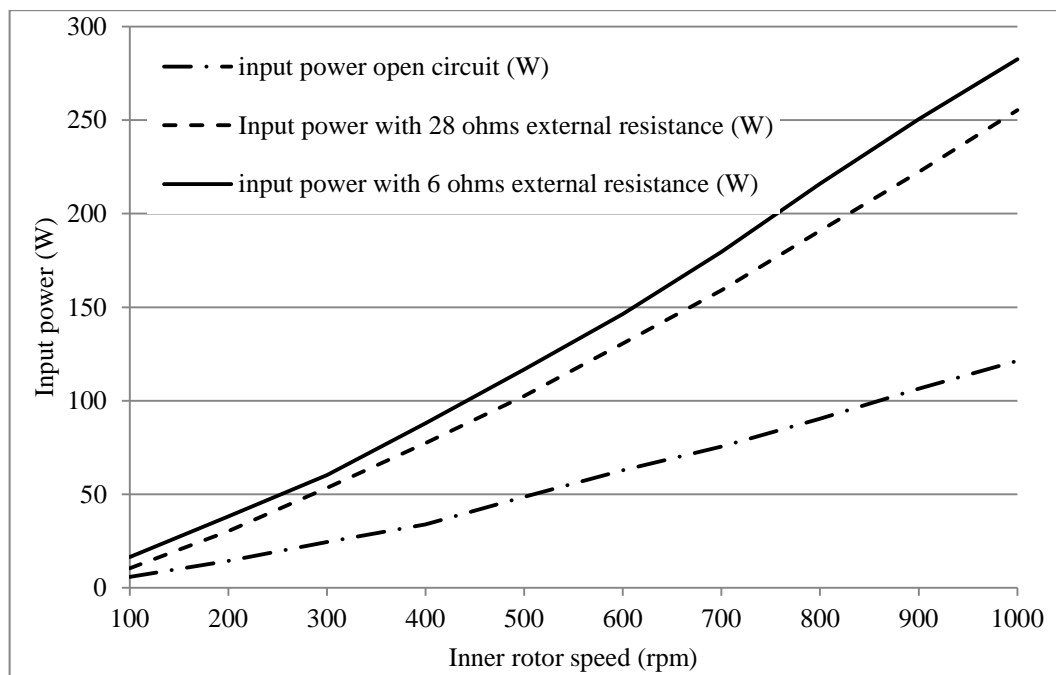


Figure 9.14: Input power difference between open slip rings and connected to the external resistance

9.2.5.1 Discussion of the PMIM (Generating Mode) Test

In the generating mode, the PMIM was investigated and characterised. At the beginning it was tested with the outer rotor locked, i.e. at the maximum slip, it was found that the machine generated an open circuit EMF validating the FEM simulation. Also, the machine was investigated with the outer rotor free running, i.e. with the minimum slip,

the outer rotor tried to track the speed of the inner rotor due to a weak induction motor effect with the inner rotor, trying to limit the slip speed between the outer rotor and the inner rotor at a light load. It was also found that the back EMF generated in the stator windings was higher than in the inner rotor windings when only the outer rotor rotates and the inner rotor locked. This is discussed in the next section.

9.2.6 Complete Differential Machine Test on no-Load Condition

The purpose of this test was to investigate and compare the back EMFs of both the inner rotor windings and the stator windings of the DM. The simulated results from the FEM showed the back EMF in the stator windings was higher than in the inner rotor windings at the slip speed less than 2.5 between the outer and the inner rotor speeds. The measured back EMF produced in both the inner rotor and the stator windings are shown in table 9.9. With the test set-up shown in figure 9.16, the voltage induced across the inner rotor windings is very low when the outer rotor of the DM is free running. The reason for that is the magnitude and frequency of the voltage induced in the inner rotor windings is directly proportional to the slip speed between the inner and outer rotors.

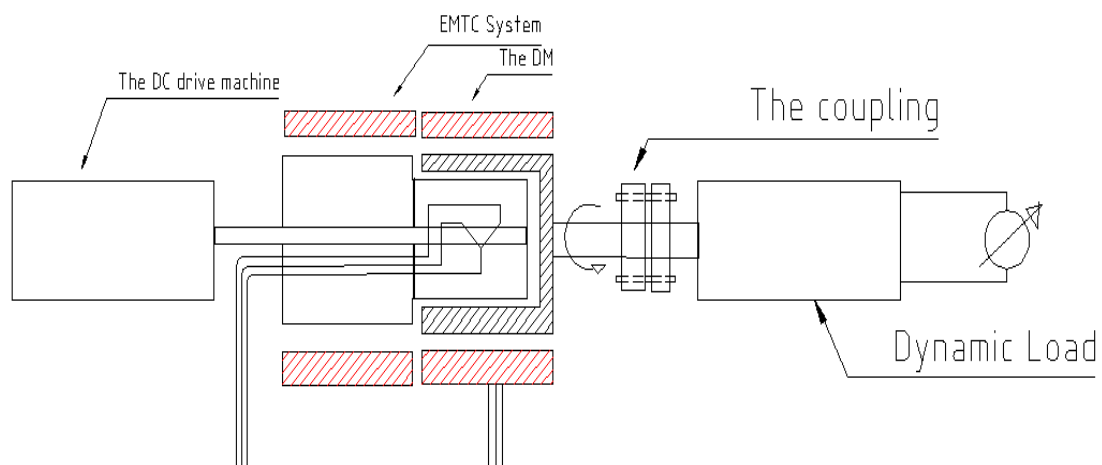


Figure 9.15: Complete open DM loop testing set-up

Table 9.9 illustrates the measured voltage induced in the inner rotor windings and the stator windings. According to table 9.9, the induced voltage in the PMIM is proportional to the slip speed, and the back EMF of the stator windings is proportional to the outer rotor speed. Figures 9.17, 9.18 and 9.19 show some of the measured back EMF waveforms for both the inner rotor and the stator windings of the Differential Machine.

DC Drive machine		Inner rotor speed (rpm)	Outer rotor speed (rpm)	Inner rotor back EMF (V) line-line (peak)	Stator back EMF (V) line-line (peak)
I(A)	V(V)				
0	0	0	0	0	0
9	8	152	122	10 (3.3 Hz)	80 (10 Hz)
11	17	600	546	26 (6.67 Hz)	400 (41.7 Hz)
12.2	26	1025	924	40 (9.5 Hz)	680 (72.7 Hz)
13	35	1467	1344	55 (10.2 Hz)	1000 (112 Hz)
13.1	44	1870	1722	65 (12.3 Hz)	1100 (90 Hz)

Table 9.9: Measured back EMF in the inner rotor windings and stator windings

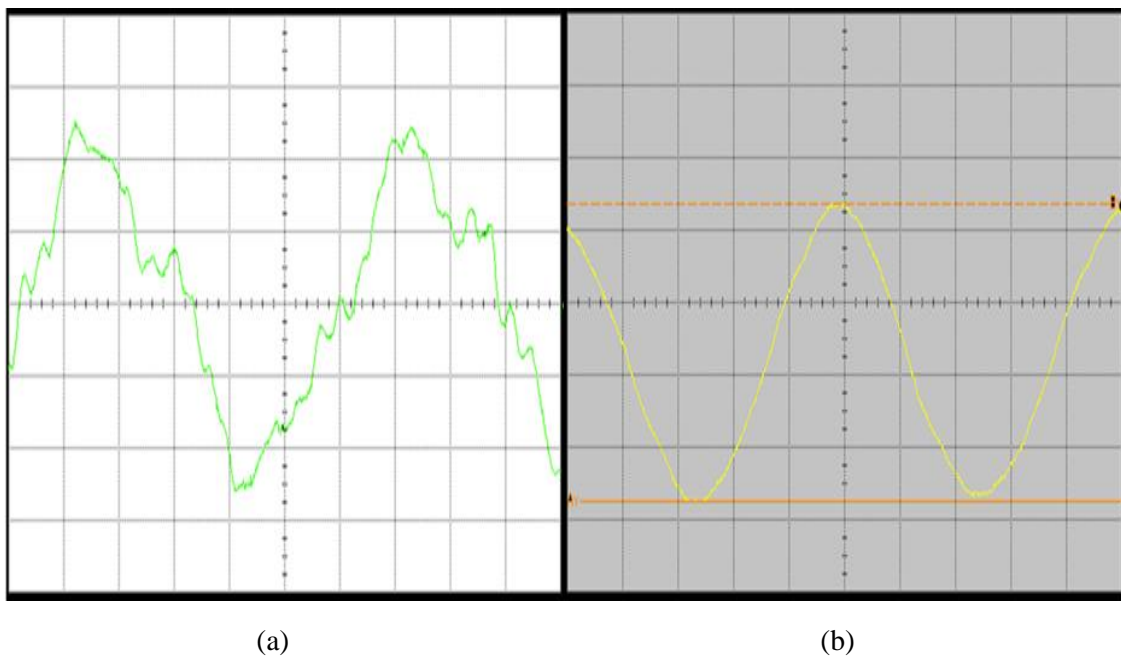


Figure 9.16: Measured line voltage of the (a) inner rotor windings (voltage 10 V, 50 ms /div) and (b) stator windings of the DM (voltage outputs is 80 V, 20 ms /div) at no-load and the inner rotor speed : outer rotor speed is 152: 122 rpm .

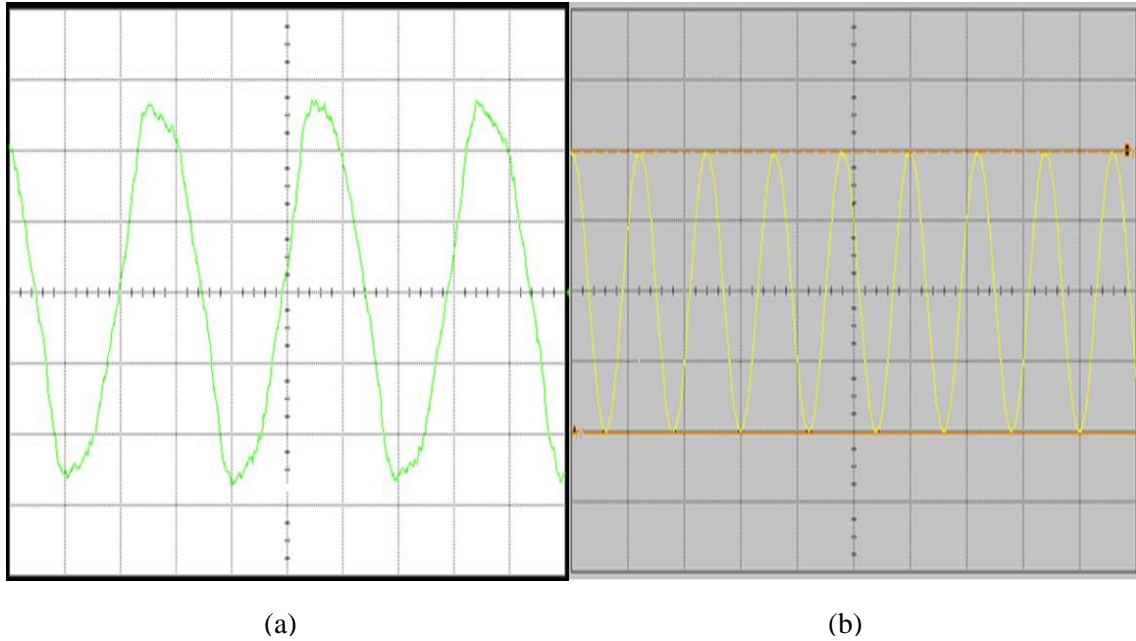


Figure 9.17: Measured line voltage of the (a) inner rotor windings (voltage outputs is 26 V, 50 ms /div) and (b) stator windings (voltage outputs is 400 V, 20 ms /div) at no-load and the inner rotor speed: outer rotor speed of 600: 546 rpm

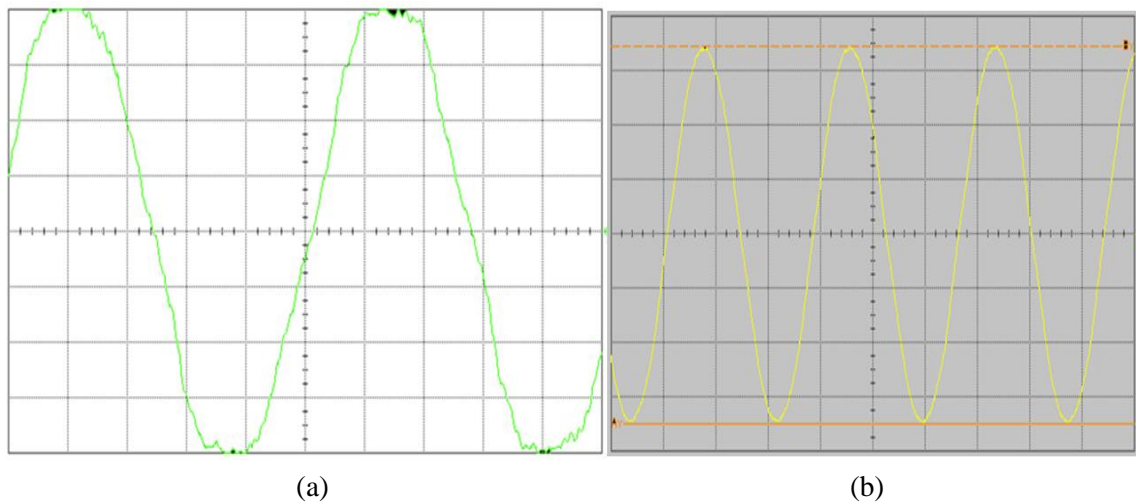


Figure 9.18: Measured line voltage of the (a) inner rotor windings (voltage outputs is 40 V, 20 ms /div) and (b) stator windings (voltage outputs is 680 V, 5 ms /div) at no-load and inner rotor: outer rotor speed of 1025: 924 rpm.

9.2.6.1 Discussion on the Complete DM Test

The complete DM was tested as a part of the EMTC system testing. It was found that the induced voltages from both stators, the DM stator and the VFRT stator, is essential to ensure that the induced voltage in the VFRT stator is higher than in the DM stator windings. If the generated voltage from the VFRT stator windings is lower than the DM

stator back EMF, the BLDCM will not work until the slip speed is great enough to allow the PMIM to generate sufficient voltage to be equal to or greater than the back EMF of the BLDCM. The next section presents the experiments carried out on the VFRT.

9.3 VFRT Testing

The purpose of this test is to investigate the characteristics of the VFRT machine when it is working as a conventional transformer. This can be done when the rotor of the VFRT is locked. In this test, the rotor windings were connected in a star connection at the rotating terminal strip. The use of rotating terminal strip allows access to the rotor winding connection. The test includes measuring the induced voltage and the absorbed current in the rotor windings and measuring the output voltage in the stator windings when the rotor is fed from an external power supply. On the other hand, when the stator is fed by an external power supply, the output voltage was measured from the rotor windings.

9.3.1 Rotor Windings Fed by an External Power Supply and Non-Rotating

Figure 9.20 shows the set-up of the VFRT testing. The purpose of this test is to determine the saturation voltage-current curve in the VFRT rotor winding, which is regarded as the input or primary winding. The saturation voltage-current curve or (B-H curve) helps to identify the limit of the Voltage/ Frequency (V/F) ratio. If the V/F limit is exceeded, then the winding could burn out. This test was carried out with the stator windings both open circuited and with a resistor bank connected.

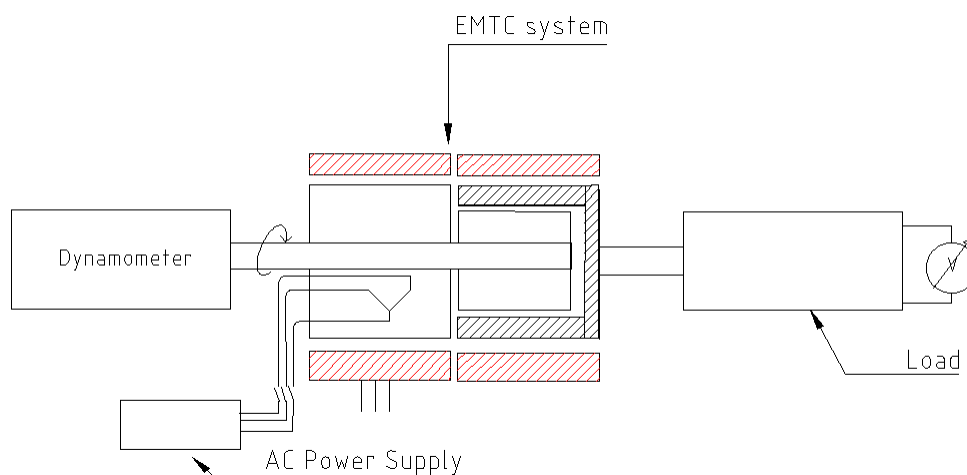


Figure 9.19: VFRT testing with star-star connection of the rotor of VFRT

1) Non-Rotating Inner Rotor with the Stator Terminals Open Circuited

The open circuit test is similar to the open circuit test of the conventional three-phase transformer. The aim of this test with a transformer is to determine the induced voltage in the secondary windings and the magnetising reactance in the primary windings. During this test, the rotor windings (primary windings) were fed by an external AC power supply while the stator windings (secondary windings) were kept open circuited as shown in figure 9.20.

Table 9.10 shows the measured voltages in the stator windings and the currents drawn by the rotor windings. The current is drawn by the machine when the rotor is locked, i.e. the VFRT machine represents a three-phase transformer. The current increases proportionally with voltage to a certain point and then becomes saturated.

Rotor side (input)					Stator side (output)			Total power
Line-line Voltage (V)	Phase Voltage (V)	Phase Current (RMS)			Phase Voltage (RMS)			
		IA (A)	IB (A)	IC (A)	VA (V)	VB (V)	VC (V)	
11.6	6.7	0.35	0.35	0.34	11	11	11	8.1
23.1	13.4	0.66	0.65	0.66	20	20	20	25.5
34.7	20.0	1	0.99	0.99	30	29	30	62
46.2	26.7	1.33	1.33	1.32	40	38	40	110.5
57.8	33.4	1.68	1.68	1.67	49	47	49	168
69.4	40.1	2.07	2.07	2.04	58	56	59	248
80.9	46.8	2.51	2.52	2.46	68	65	68	348
92.5	53.5	3.1	3.11	3.03	74	72	74	490
104.1	60.1	3.96	3.99	3.93	86	85	89	705
115.6	66.8	5.3	5.34	5.28	95	95	98	1025
127.2	73.5	7.03	7.07	7	102	103	105	1460

Table 9.10: An open circuit test measurements

For the open circuit test, the no-load current in the primary windings is small [62]. Hence, with the small resistance, the copper losses are small (I^2R) and then neglected. Therefore, the wattmeter readings represent the core losses. The turns ratio for different

input voltages of the primary (rotor) voltage (V_s), and the secondary (stator) voltage, i.e. (V^s/V_p) is can be calculated. The turn ratio is calculated from the figure 9.21, to be 1.4. However, theoretically is ($a = V^s/V_p = N^s/N_p = 1.1$). Where N_p , N_s are the number of winding turn in primary and secondary sides.

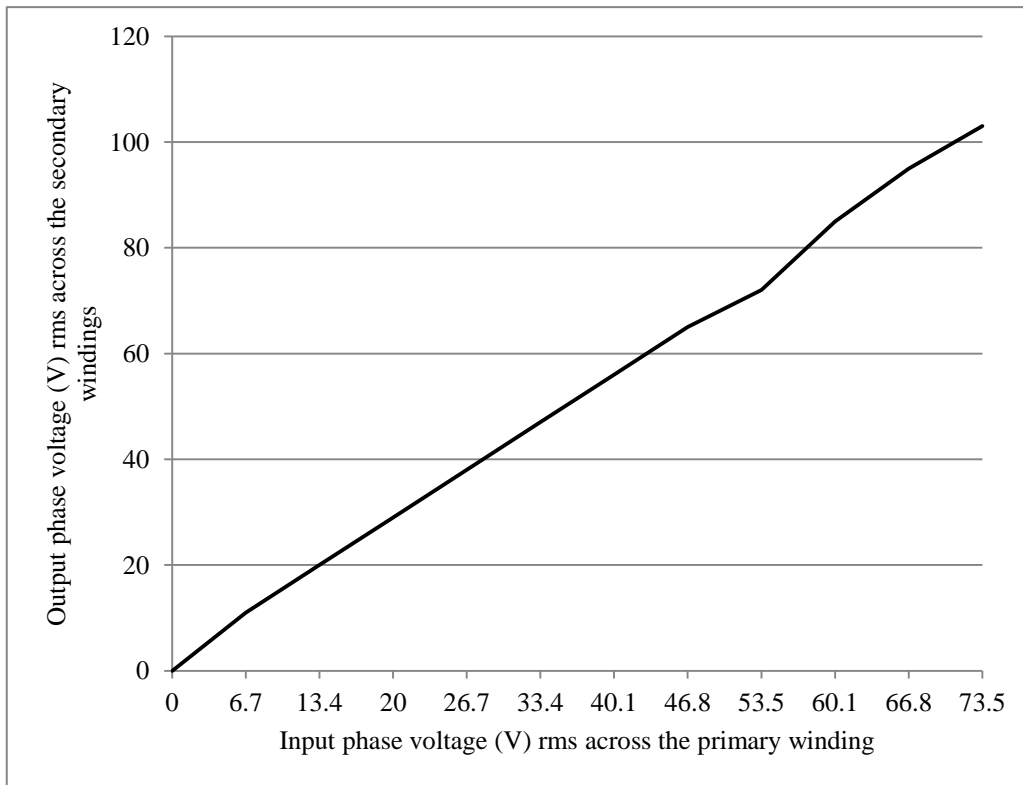


Figure 9.20: The turns-ratio validation of the VFRT machine

2) Non-Rotating Inner Rotor with Resistive Load Connected to Stator Windings

The load test was performed as can be shown in figure 9.22 for the testing set-up. The purpose of this test is to investigate the VFRT when the stator windings are connected to a load and not only the induced voltage is measured but the current, which is drawn by the load. In addition, this test aims to investigate the current that is drawn by the VFRT rotor winding when supplying them by an external power supply. The measured input, output, currents and voltages are shown in table 9.11.

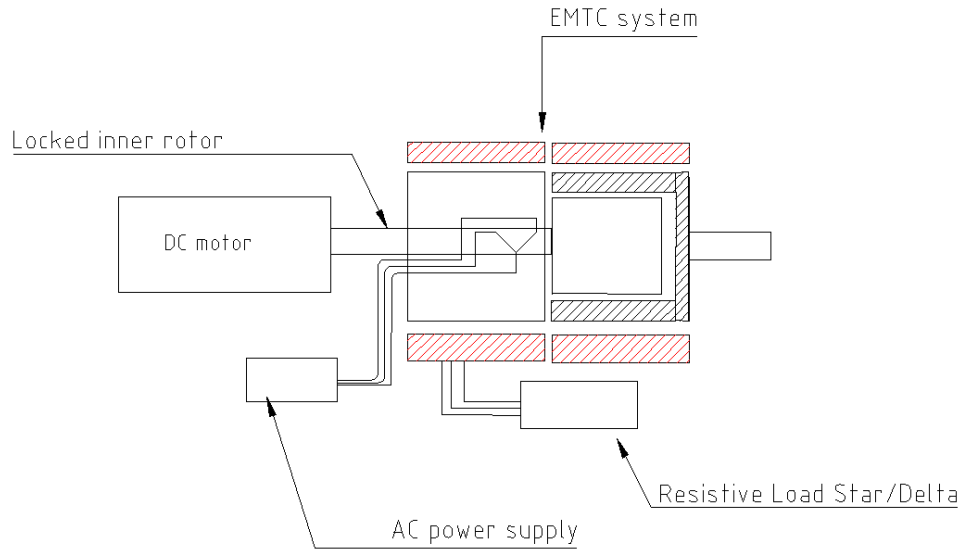


Figure 9.21: VFRT testing set-up at non-rotating its rotor and its stator is connected to the resistive load

rotor side				Stator side	Watt 1 (W)	Watt 2 (W)	Total power (W)
Phase Voltage (V)	Phase Current			Phase Current			
	IA (A)	IB (A)	IC (A)	IA (A)			
11.56	0.71	0.67	0.67	0.43	3.25	14	17.25
23.12	1.32	1.28	1.28	0.87	10	52	62
34.68	1.94	1.89	1.9	1.29	20	72	92
46.24	2.53	2.53	2.53	1.73	32	195	227
57.80	3.15	3.16	3.14	2.15	50	300	350
69.36	3.72	3.74	3.01	2.53	75	420	495
80.92	4.3	4.36	4.33	2.91	100	570	670
92.49	4.99	5.09	5.06	3.32	130	765	895
104.05	5.72	5.8	5.8	3.69	180	980	1160
115.61	6.53	6.65	6.58	4.05	250	1240	1490
127.17	7.44	7.52	7.49	4.36	340	1560	1900

Table 9.11 : Load test at feeding power into the rotor windings

9.3.2 Saturation Test

This test was performed at two conditions, the inner rotor locked and when it was free running. Figure 9.23 shows the relationship between the speed and the back EMF of the inner rotor of the differential machine based on the results in Table 9.12. The voltage supply frequency can be calculated using the following formula:

$$f = \frac{p}{2} \cdot \frac{N}{60} \quad (9.3)$$

Since the inner rotor of the differential machine feeds the rotor of the VFRT, the voltage/ frequency ratio applied to the rotor of the VFRT must be limited to avoid saturation of the VFRT.

Then using the previous test set up parameters illustrated in table 9.11 and table 9.12, the saturation test was performed. Figure 9.23 illustrates the relationship between the current and the maximum allowable voltage in the rotor windings. At 50 Hz, it can be seen from Figure 9.23 that the core starts to saturate above 110 V in. therefore, the inter-rotor connection between the PMIM and the VFRT requires the appropriate three-phase delta or star connection to avoid saturating the VFRT.

Inner rotor phase back EMF (V)		Stator line back EMF (V)	Inner rotor speed (rpm)		
locked outer rotor	Released outer rotor	Released rotor	outer rotor	Locked outer rotor	Released outer rotor
0	0	0		0	0
22	10.4	73		112	182
44	20.8	146		224	364
66	31.2	219		336	546
88	41.6	292		448	728
110	52	365		560	910

Table 9.12: Back EMF in the DM that feeds the VFRT

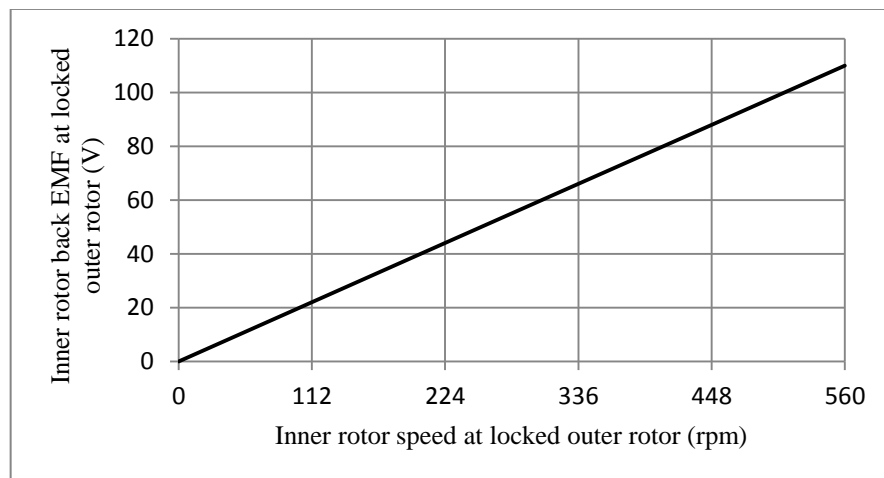


Figure 9.22: The speed versus the inner rotor back EMF

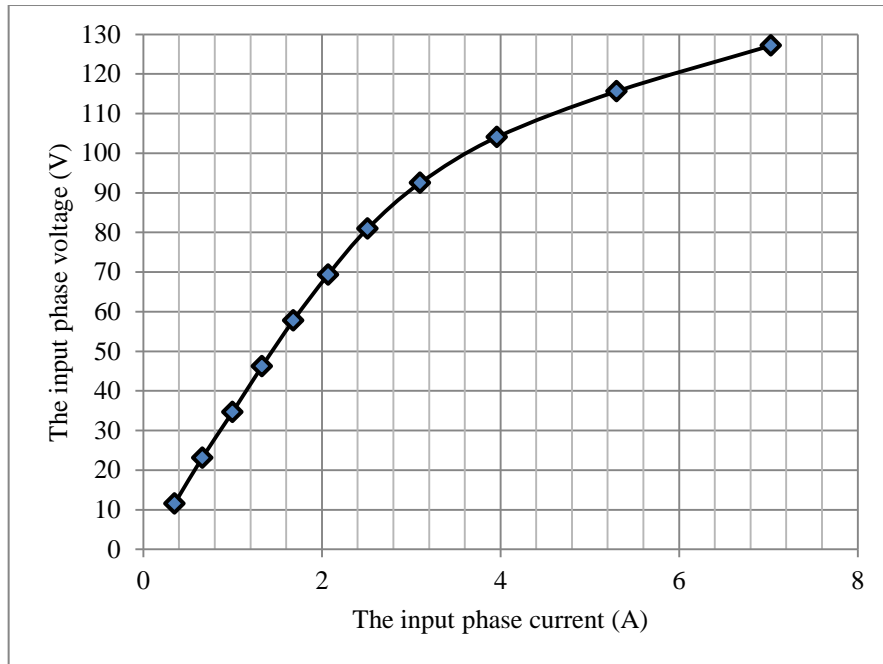


Figure 9.23: The voltage versus the current per phase of the VFRT rotor at 50 Hz voltage supply

9.3.3 VFRT Rotor and DM Inner Rotor Connection

Since the star-star connection between the inner rotor of the DM and the rotor of the VFRT machine, will exceed the V/F ratios of the input winding of the VFRT, the connection was changed to delta-star in order to prevent saturation of the rotor windings of the VFRT, and hence with a lower magnetising current. The test was carried out for two configurations, positive and negative phase sequences as shown in figure 9.25 (a, b). This is an important consideration because the phase sequence affects the operation of the VFRT.

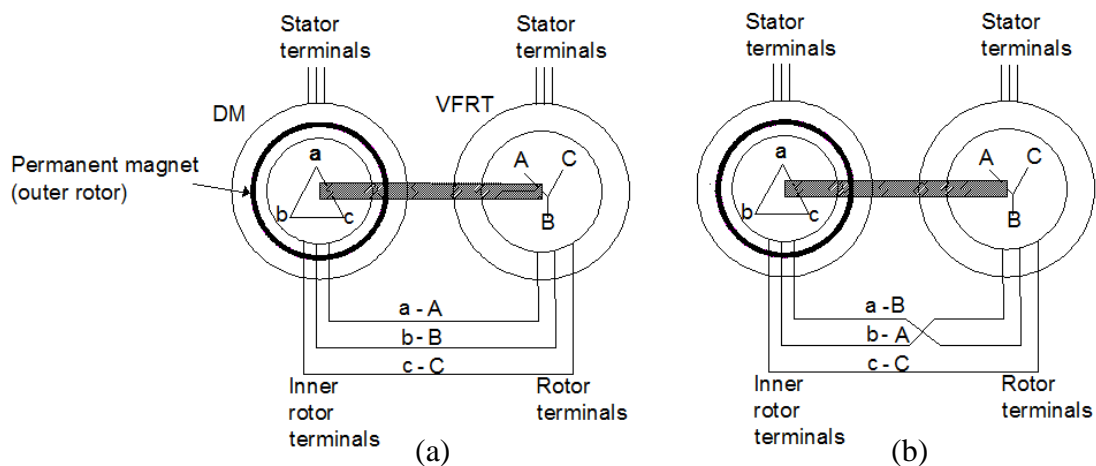


Figure 9.24: Inner rotor of the DM and rotor of VFRT connections in (a) positive sequence and (b) negative sequence

1- Positive Sequence Configuration

In this configuration, the interconnection arrangement of the three-phase wires is a-A, b-B and c-C as shown in figure 9.25 a. The magnetic rotation is in the opposite direction with the mechanical rotation speed (frequency). Therefore, the fundamental frequency was cancelled as stated in equation (7.13) in chapter 7.

a) Anticlockwise Rotation Direction

Tables 9.13 below shows the measured induced EMFs (voltages), the magnetizing current and the rotor frequency with respect to the slip speed. The stator frequency shows only harmonics where the fundamental frequency has been cancelled. The measured voltages in the rotor and the stator windings of the VFRT are shown in figures 9.26, and 9.27. It is found that the phase voltage across the stator windings is very small compared to the phase voltage in the rotor windings. Therefore, the connection between the inner rotor of DM and the rotor windings of VFRT at positive sequence is not applicable. To check the obtained results, the clockwise direction of the rotor direction is carried out. The results of the clockwise direction can be seen in the next experiment (b).

All measured voltages are per phase and peak values				
Slip speed (rpm)	VFRT Rotor voltage (V)	VFRT Stator voltage (V)	Mag. Current (A)	VFRT Rotor frequency (Hz)
0	0	0	0	0
100	14	2.1	1.48	9.8
200	35.2	5	1.71	17.1
300	47.8	6.4	1.77	25.6
400	60	8	1.8	33.3
500	85.2	11	1.82	45.4
600	104.4	13.4	1.83	54
700	115.6	15.8	1.83	58.8
800	131	15.8	1.83	74

Table 9.13: Results for anticlockwise (normal) drive direction

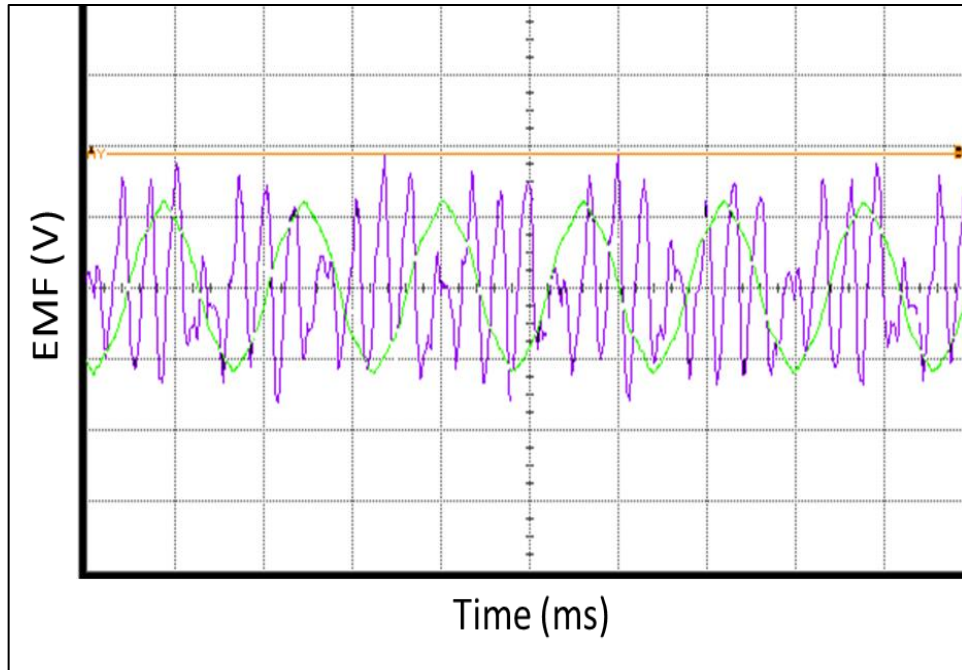


Figure 9.25: The rotor input phase voltage (green colour waveform) of the VFRT, and the stator phase voltage (purple colour waveform) with no load at 700 rpm rotor speed (rotor phase voltage is 220 V, stator phase voltage is 23 V, 5 ms/div)

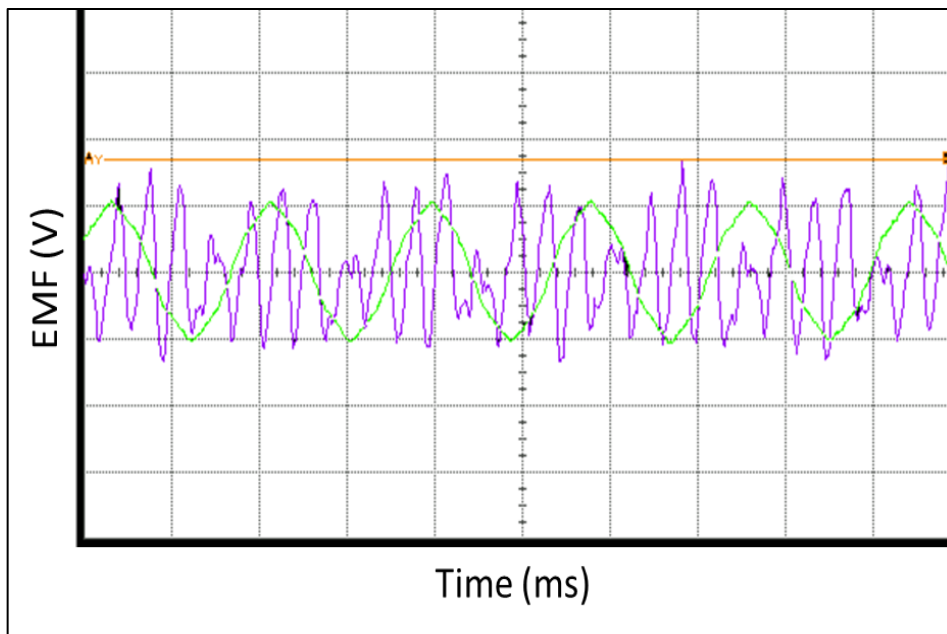


Figure 9.26: The rotor input phase voltage (green colour waveform) of the VFRT, and the stator phase voltage (purple colour waveform) with no load at 600 rpm rotor speed (rotor phase voltage is 200 V, stator phase voltage is 22 V, 5 ms/div)

Figure 9.28 shows the plotted relationship between the slip speed and the voltage in both windings the stator and the rotor of the VFRT. As stated earlier that in the positive sequence connection, the voltage in stator windings is very low compared with the

voltage in the rotor windings. The frequency in the rotor windings of the VFRT is increased when the slip speed is increases as shown in figure 9.30.

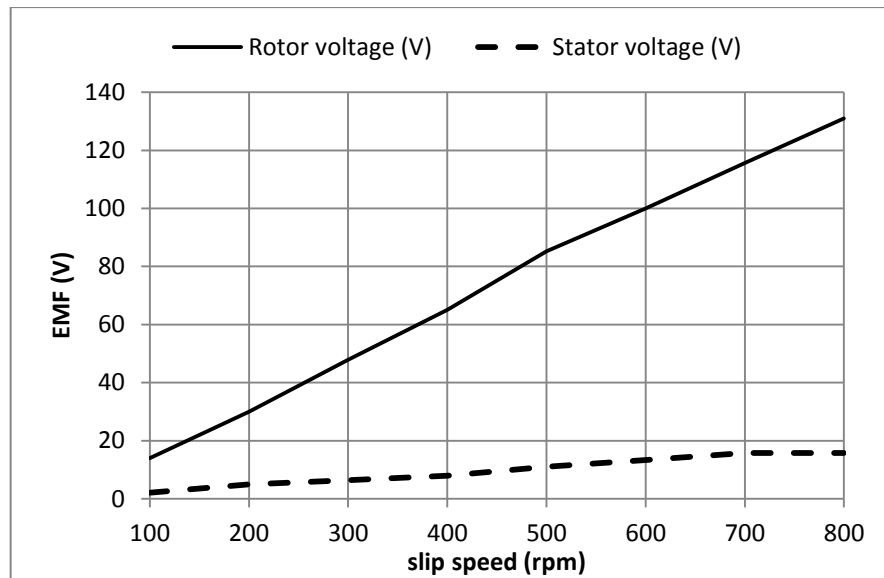


Figure 9.27: Measured phase voltages of the rotor and stator of the VFRT, the values are peak voltages.

Figure 9.29 illustrates the magnetisation current saturation in terms of speed. The relationship between the speed and the slip speed was calculated.

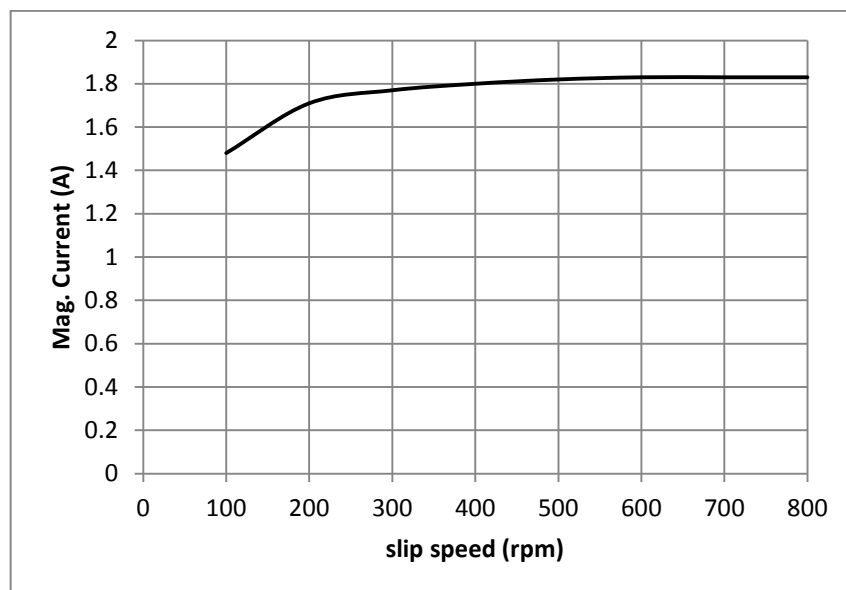


Figure 9.28: The RMS magnetizing current flowing between the two rotors with Delta-Star connection

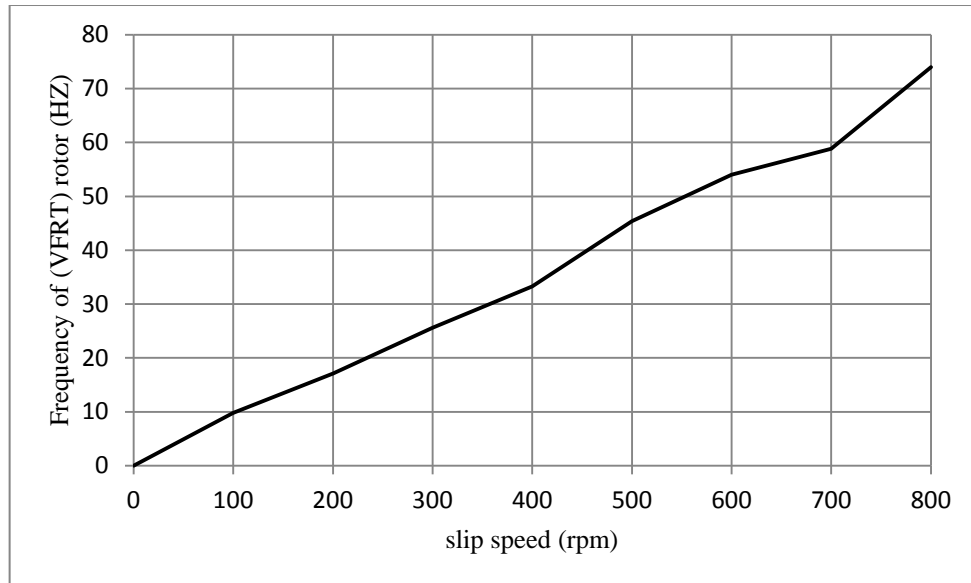


Figure 9.29: The frequency of the rotor windings of the VFRT EMF versus the slip speed

b) Clockwise Rotation Direction

In the clockwise direction test, the armature and field connections were changed of the drive DC machine to rotate in the reverse direction. The measured EMF in the rotor and stator windings at several rotor speeds are listed in table 9.14. The purpose of this test is to ensure that the positive sequence configuration stated in figure 9.25 (a), is the wrong connection between the rotor of VFRT and the inner rotor of DM as can be proved in figure 9.31. This figure shows the voltage in stator windings is very low as stated in the last test with anti-clockwise direction test. In figure 9.32, it can be seen that the magnetised current does not exceed 1.83 A. This result leads to change the configuration of the connection into figure 9.25 (b).

Slip speed (rpm)	Rotor voltage (V)	Stator voltage (V)	Current (A)	Rotor frequency (Hz)
0	0	0	0	0
100	36	4.16	1.72	20
200	73	10	1.81	44.4
300	108.4	15.8	1.83	62
400	152.4	22.5	1.83	77
500	179.2	27.8	1.83	90
600	212.2	34	1.83	100

Table 9.14: Results for Clockwise rotation of the rotor

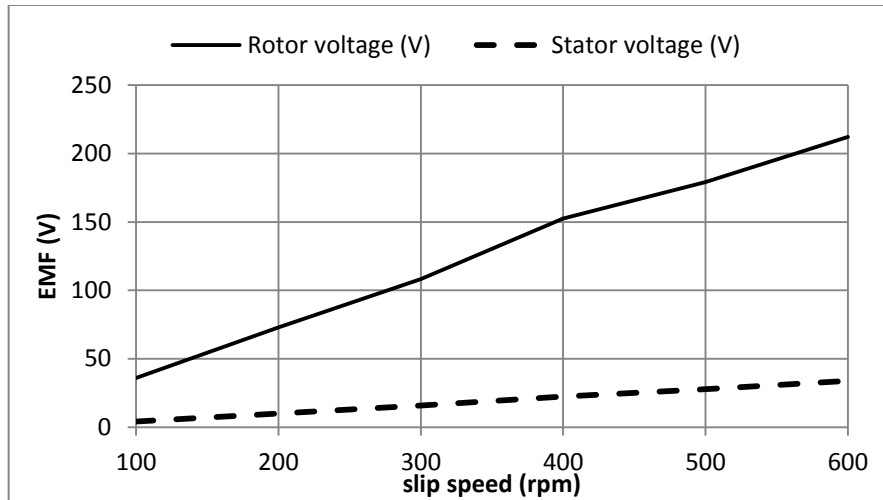


Figure 9.30: The phase voltages of the rotor and stator of VFRT

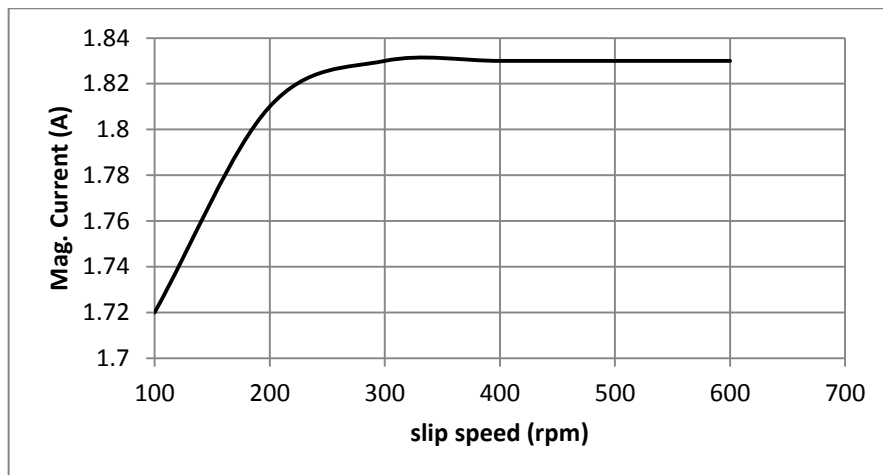


Figure 9.31: Measuring the circulating RMS magnetizing current between the two rotors

2- Negative Sequence Configuration

In the configuration shown in figure 9.25 (b), the interconnection arrangement is a-B, b-A and c-C. Hence, the frequency is doubled in the stator windings as can be seen in figures 9.33 and 9.34. These two figures show the peak phase a voltage in the stator windings is higher than in the rotor windings at several of the rotor speeds. Therefore, the negative sequence configuration is the proper connection between the inner rotor of the DM and the rotor of the VFRT windings.

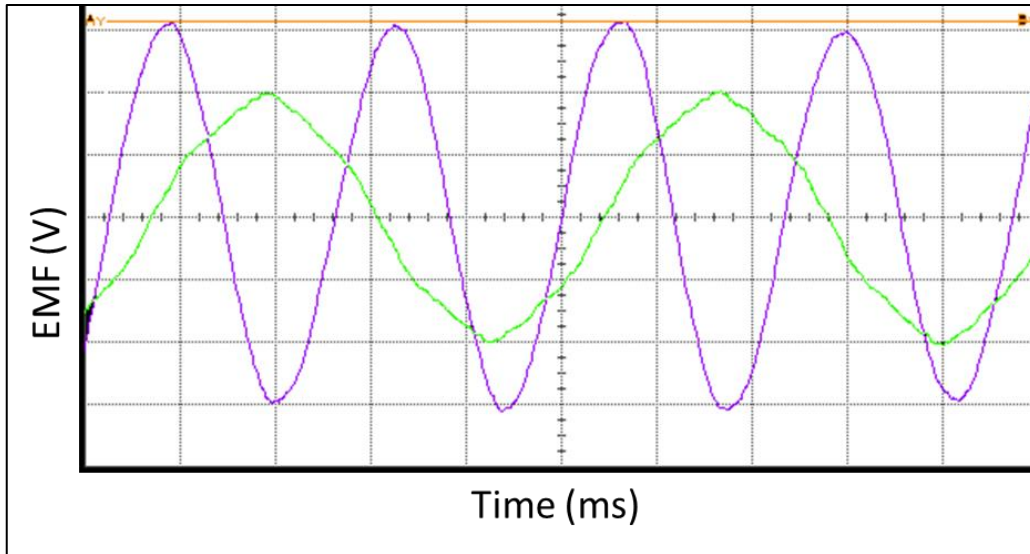


Figure 9.32: Measured rotor VFRT phase voltage (green colour waveform) and the stator VFRT phase voltage (purple colour waveform) with no load at 500 rpm rotor speed (rotor phase voltage 80 V, 124 V, 5 ms/div)

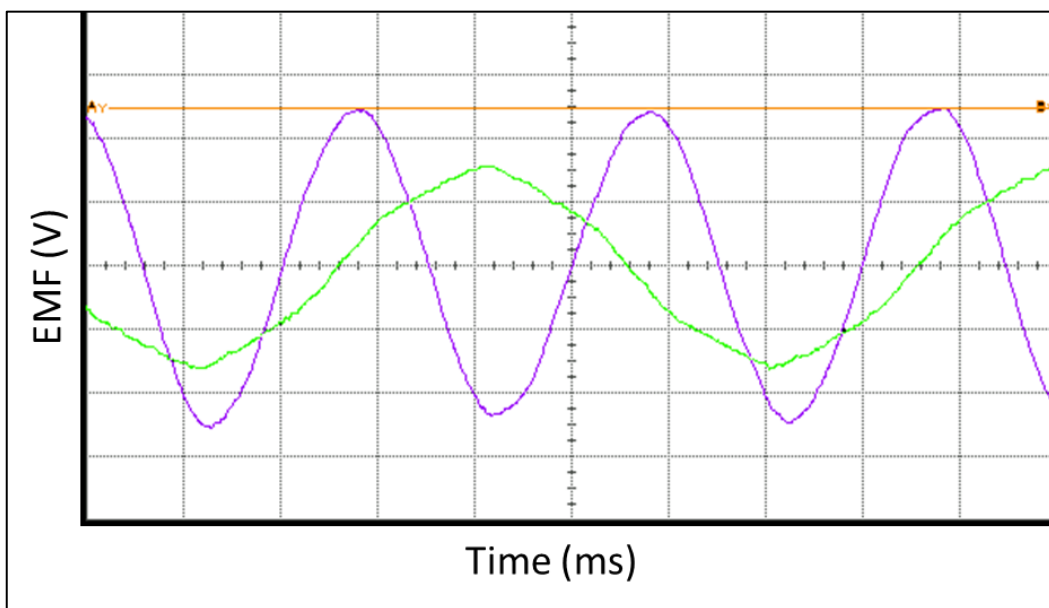


Figure 9.33: Measured rotor VFRT phase voltage (green colour waveform) and the stator VFRT phase voltage (purple colour waveform) with no load at 400 rpm rotor speed (rotor phase voltage 60V, stator phase voltage 100V, 5 ms/div)

9.3.4 VFRT Testing with the Outer Rotor Locked

This test was performed on the VFRT machine with the outer rotor locked. In this test, the back EMF from the inner rotor of the DM was transmitted to the stator of the VFRT via its rotor. The DC machine drives the inner rotor. The measured voltage of the stator

of the VFRT is listed in table 9.15. On the other hand, the voltage-speed relationship is shown in Figure 9.34. From table 9.15 and the figure 9.35, this connection is the proper connection.

Inner rotor speed (rpm)	VFRT stator per phase, peak EMF (V)	Inner rotor speed (rpm)	VFRT stator per phase, peak EMF (V)
100	21	1100	288
200	49.8	1200	314
300	79.2	1300	334
400	105	1400	362
500	144	1500	384
600	164	1600	416
700	184	1700	436
800	208	1800	460
900	238	1900	480
1000	272	2000	520

Table 9.15: Speed-voltage characteristic of the PMIM

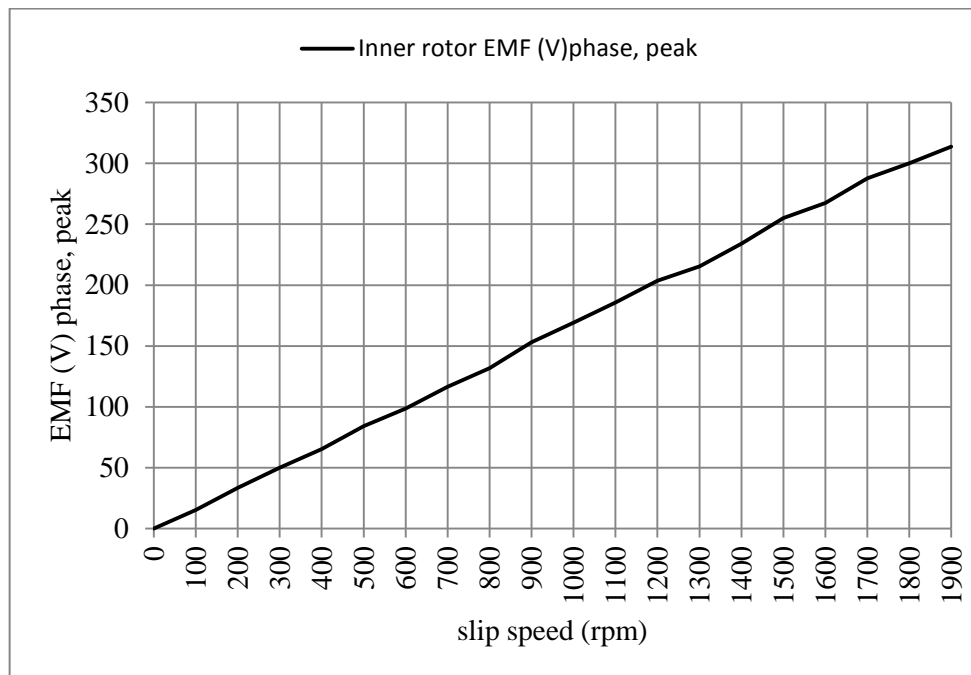


Figure 9.34: VFRT stator versus the inner rotor speed

9.3.4.1 Discussion of the VFRT Testing

The VFRT was tested under several conditions. The aim of testing was to investigate the operation of the machine. Since the VFRT role was to supply power to the BLDCM stator, the investigation was carried out using two types of inter-rotor connections. The saturation test revealed that the Star-Star connection was not appropriate, because the maximum voltage allowed at 50 Hz was about 70 V to 80 V before the onset of saturation. This investigation led to the decision to connect the inter-rotor connection in a Delta-Star configuration. The positive sequence, i.e. A-a, B-b and C-c phases led to the cancellation of the fundamental frequency in the VFRT stator windings. Therefore, the negative sequence connection was used, where the magnetic field and inner rotor rotate in the same direction.

9.4 Complete EMTC System Testing

During the PMIM testing, a fault was discovered in the inner rotor. Losses of about 1kW were measured, which was significantly higher than the expected losses caused usually by the mechanical parts. It is very likely that this fault was initiated from the circulating current at an inter-turn short circuit or a phase-to-phase short circuit. The phase-to-phase short circuit and each phase to the inner shaft short circuit tests were investigated using a Megger insulation tester. The insulation tests did not indicate any fault neither between the phases nor between each phase to the inner shaft (inner rotor laminations). Hence, the inter-turn short circuit had to be investigated. More details about the cause of this fault and the measurements carried out are discussed in appendix F1. The PMIM testing was repeated and the complete EMTC system was tested under open and closed loop test conditions.

9.4.1 Open Machine Loop Test

After re-winding the inner rotor of the DM, the complete EMTC system testing was carried out under open loop conditions. The aim of this experiment is to investigate the dynamic behaviour of the whole system at open machine loop (i.e. the inner rotor is driven by the DC motor drive while the DM stator is kept open circuited). The back EMF is monitored at the stators of the VFRT, the stator of the BLDCM and the rotor of the VFRT at several slip speeds in this experiment. The test setup of this experiment, the connection of the PMIM inner rotor winding and the VFRT rotor winding are shown

in figure 9.36. The connection was Delta-Star connection based on the saturation test of section 9.3.2. The phase back EMF of the PMIM rotor windings was taken to compare the results with the back EMF in the stator windings of the BLDCM and the VFRT.

Table 9.16 shows the measured back EMF values in the BLDCM stator, the VFRT stator and the PMIM rotor. It could be noticed that the voltage in the stator windings of the VFRT is greater than that of the stator windings of the BLDCM at high slip speed. Because when the slip speed is lower than 200 rpm the back EMF in the BLDCM stator windings and the VFRT stator windings are nearly the same. Table 9.16 shows the initial boundary conditions of the EMTC operating line. The final boundary condition of the EMTC system will be defined in the closed loop machine test. The open loop machine test measured results were initially predicted using the FEM simulations as shown in figure 9.37 and figure 9.38. However, as the simulation results were acquired from the DM only, the inner rotor of the PMIM and the stator windings of the BLDCM, were kept open circuited.

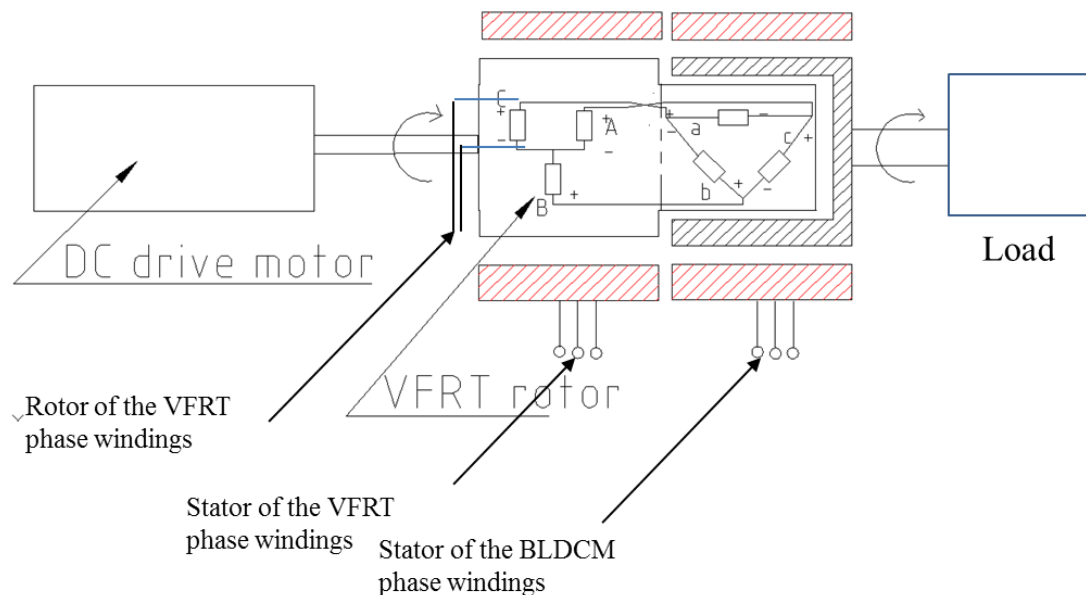


Figure 9.35: Open machine loop test set- up

Inner rotor speed (rpm)	Outer rotor speed (rpm)	BLDCM stator per phase, peak EMF (V)	PMIM rotor per phase, peak EMF (V)	VFRT stator per phase, peak EMF (V)	Slip speed (rpm)
100.0	0.0	0.0	14.0	42.5	100.0
200.0	0.0	0.0	32.0	45.0	200.0
300.0	0.0	0.0	50.0	70.0	300.0
400.0	0.0	0.0	65.0	92.0	400.0
500.0	0.0	0.0	80.0	120.0	500.0
210.0	101.8	48.0	17.5	32.0	108.3
293.3	101.8	48.0	27.5	50.0	191.6
306.7	99.9	50.0	30.0	56.0	206.8
408.3	99.9	48.0	46.0	84.0	308.4
516.7	199.8	92.0	48.0	96.0	316.9
591.7	199.8	92.0	60.0	116.0	391.9
604.2	99.9	46.0	80.0	132.0	504.3

Table 9.16: Complete EMTC system open machine loop measurements

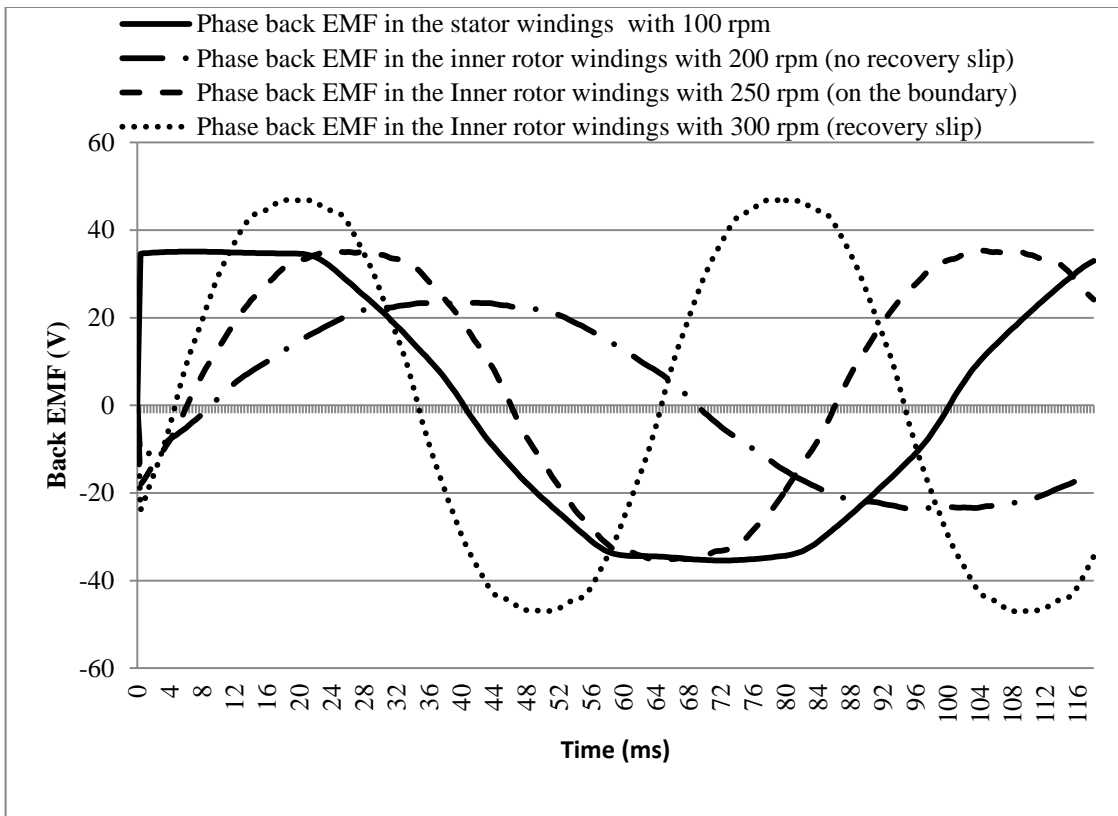


Figure 9.36: Simulated back EMF in the stator of the BLDCM and the inner rotor windings of the PMIM using FEM at inner rotor speed of 200, 250 and 300 rpm and the outer rotor speed of 100 rpm

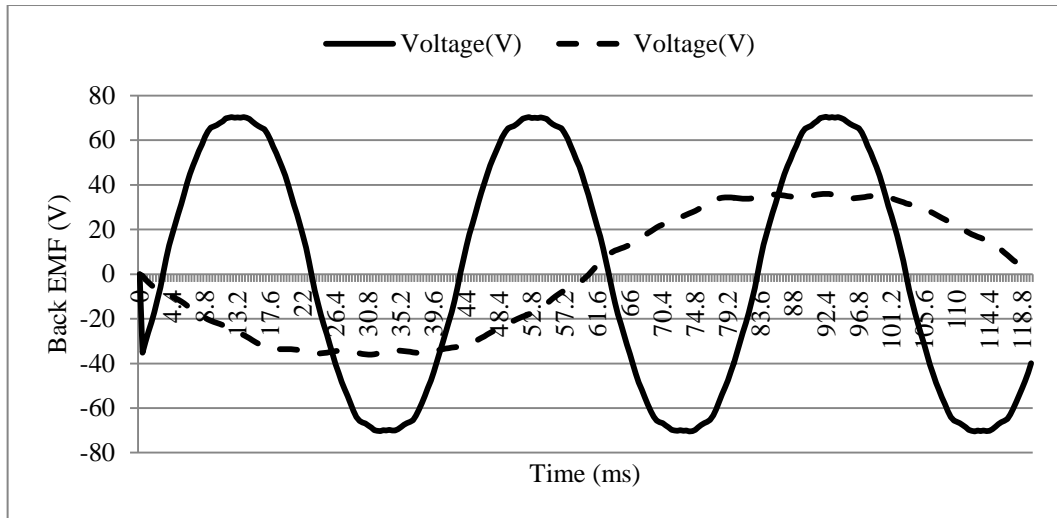


Figure 9.37: Simulated back EMF in the stator of the BLDCM and inner rotor windings of the PMIM using FEM at inner rotor speed of 400 rpm and the outer rotor speed of 100 rpm

Figure 9.39 shows the measured phase back EMF waveforms of the stator of the BLDCM, the stator of the VFRT, and the rotor of the VFRT windings at the inner rotor and outer rotor speeds of 300 rpm and 100 rpm. The difference between the measured back EMFs amplitude and frequency can be seen in the figure.

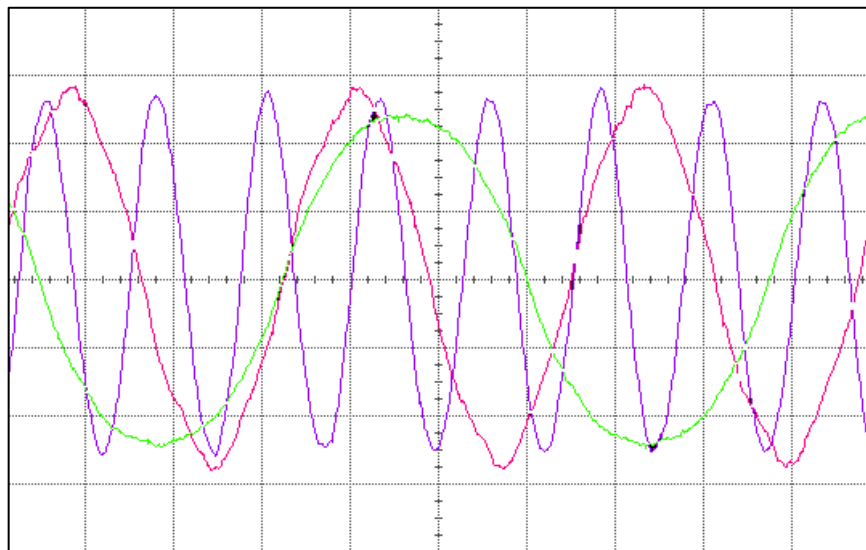


Figure 9.38: The VFRT rotor phase voltage (pink colour) (phase voltage is 27.5V, 20 ms/div). The stator phase voltage (purple colour) (phase voltage is 55V, 20 ms/div), the stator phase voltage of the BLDCM (Green colour) (phase voltage is 47V, 20 ms/div) at 300 rpm inner rotor speed and 100 rpm outer rotor speed

It can be seen that the frequency of the back EMF of the VFRT stator windings is double the frequency in its rotor windings. On the other hand, figure 9.40 illustrates the

measured back EMFs of the stator and rotor windings of the VFRT at locked outer rotor. Since the outer rotor is locked, no back EMF is generated in the BLDCM windings.

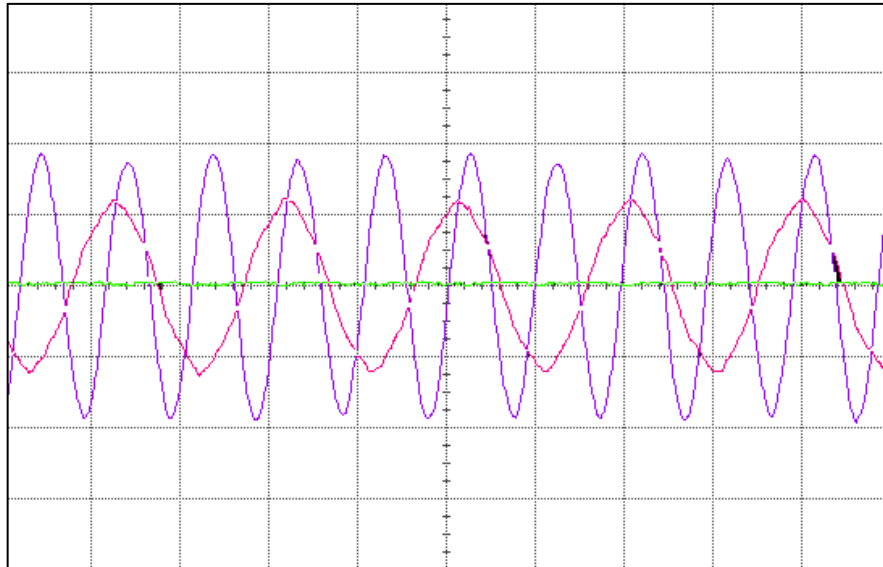


Figure 9.39: The rotor phase voltage (pink colour waveform) of the VFRT (phase voltage is 45V, 20 ms/div) and the stator phase voltage (purple colour waveform) (phase voltage is 75V, 20 ms/div) at 300 rpm inner rotor speed and the outer rotor locked.

9.4.2 Closed Machine Loop Test

The analysis of the cascaded rotors of the VFRT and the Differential Machines allows for figuring out the following conclusions: In terms of rotors inter-connection, only the negative phase-sequence rotors connection is applicable. The closed loop machine test of the EMTC system was carried out for two purposes:

9.4.2.1 Boundary Condition for Torque Amplification

The purpose of this test was to find out the boundary condition for torque amplification of the EMTC system. It is very important to determine at what minimum slip speed the VFRT can deliver power back to the DM. At this boundary condition, the amplitude of the voltage from the VFRT must be greater or equal to the back EMF of the BLDCM as shown in figures 9.41- 9.44. From these figures, the speed can be measured since the frequency of each stator is acquired. This is one of the main concepts of the EMTC system; it works at variable speed ratios. Figure 9.45 shows the measured cases at what

speed of the inner and the outer rotors, the voltages are equal of both stators of the BLDCM and VFRT; the red line is called the operational boundary line of the EMTC system.

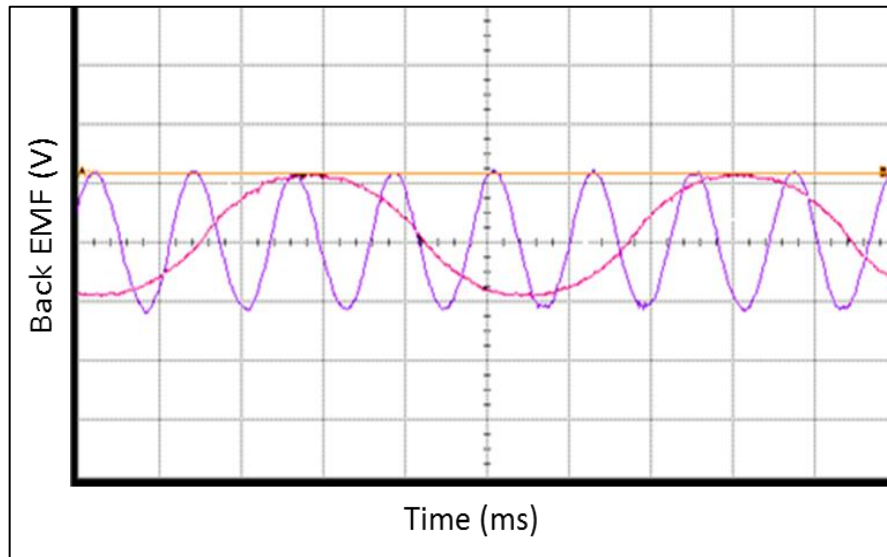


Figure 9.40: Measured stator phase voltage of the DM (pink) and stator phase voltage of the VFRT (purple) with full load at rotors speed (inner rotor :outer rotor) of 500:109 rpm. (100V, 100V, 10 ms /div)

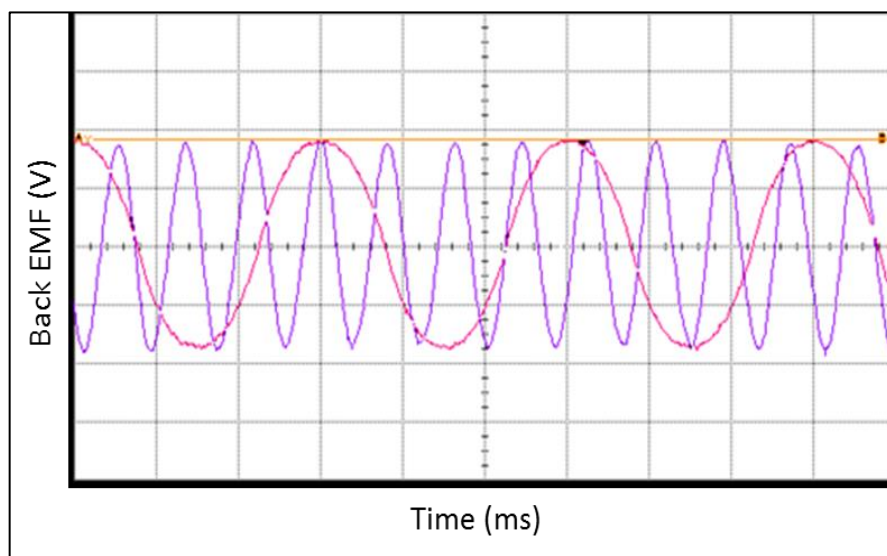


Figure 9.41: Measured stator phase voltage of the DM (pink) and stator phase voltage of the VFRT (purple) with full load at rotors speed (inner rotor :outer rotor) of 738:400 rpm. (100V, 100V, 10 ms /div)

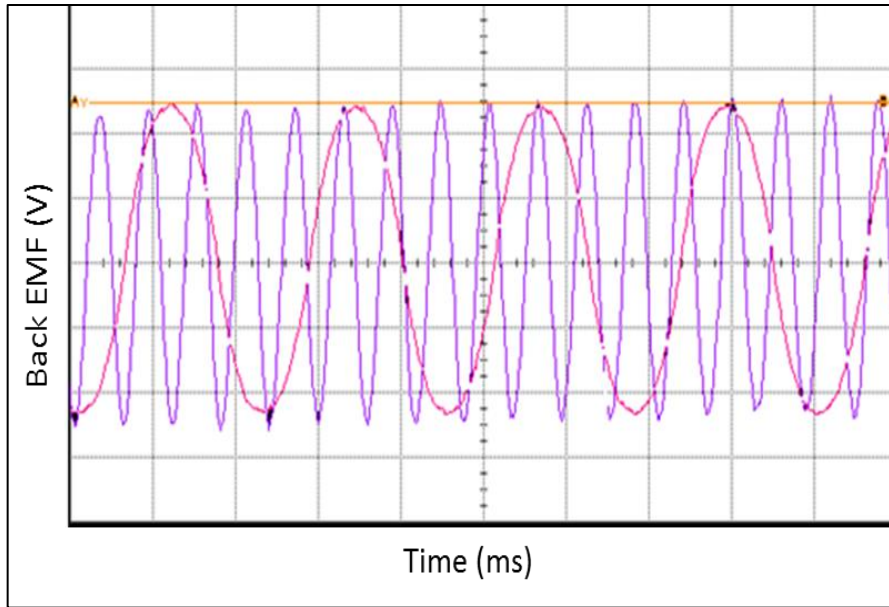


Figure 9.42: Measured stator phase voltage of the DM (pink) and stator phase voltage of the VFRT (purple) with full load at rotors speed (inner rotor :outer rotor) of 1000: 545 rpm. (250V, 250V, 10 ms /div)

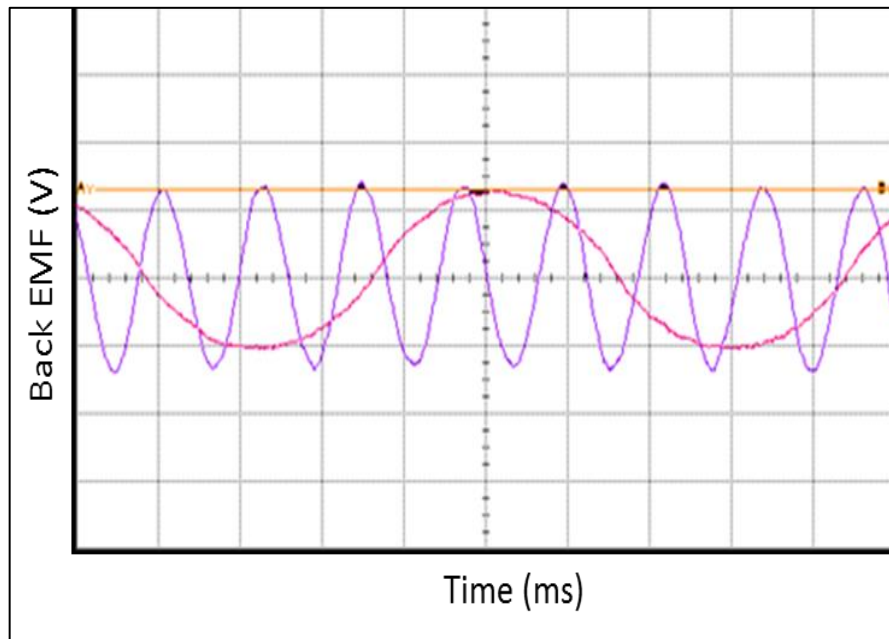


Figure 9.43: Measured stator phase voltage (peak value) of the DM (pink) and stator phase voltage (peak) of the VFRT (purple) with full load at rotors speed (inner rotor :outer rotor) of 375: 180 rpm. (50V, 50V, 10 ms /div)

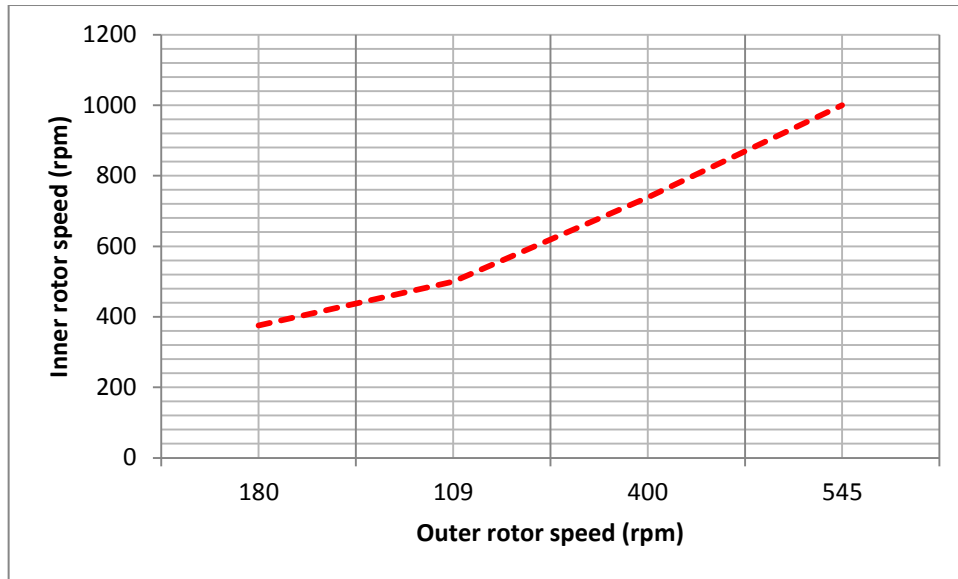


Figure 9.44: The measured speed in rpm of the inner and outer rotors is a boundary-operating line. The above red line, the inner rotor speed can make a torque multiplication.

9.4.3 Torque Amplification

The stator of the VFRT is connected to the stator of BLDCM via a DC link converter for a closed loop test. The rectification circuit changes the input alternating current to DC. Then at the DC link, the input voltage and the back EMF from the stator of the BLDCM windings are compared. At a low load torque and low slip speed, the back EMF from the BLDCM stator windings will be higher than the output voltage from the VFRT stator; no power will flow from the VFRT to the DM. In contrast, when the input voltage at the DC link is greater than the back EMF from the BLDCM, the current will flow through the inverter to excite the stator windings of the DM. In this condition, slip power is fed back to provide torque amplification. Figure 9.45 shows the boundary between these two conditions and table 9.17 lists five different cases of torque amplification. Referring to Table 9.17, stator of VFRT phase terminal voltage (peak), phase back-EMF (peak) of the BLDCM and input power are given. The DC-link voltage was measured from $105 V_{DC}$ in case (a) to $567 V_{DC}$ in case (e). The DC current had maximum value of 1 A at the load torque of 4.26 Nm, these measurements gives the electrical power demand of 576 W. Figure 9.46 illustrates the measured voltages which indicated in case (e).

Therefore, the power losses at the power converter circuit of the EMTC system can be calculated to be $576 - (567 \times 1) = 9$ W. The efficiency of the rectification system at closed machine loop is $567/576 = 0.98$ or 98%.

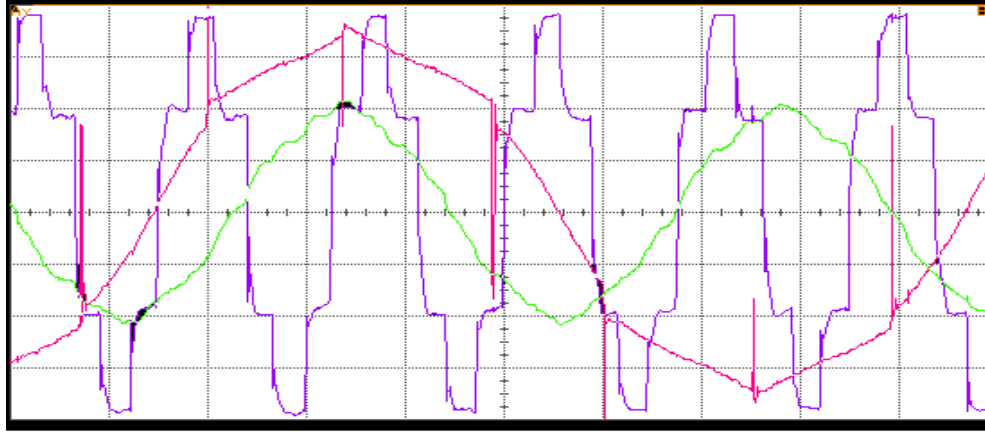


Figure 9.45: Measured stator phase voltage (peak value) of the DM (red), stator phase voltage (peak) of the VFRT (blue) and phase voltage (peak) across the rotor of VFRT, with full load at case (e), (350V, 375V, and the time is 2ms/ div).

Operational points	T _{in} (Nm)	T _{out} (Nm)	Outer rotor Speed (rpm)	Dc Link Voltage (V)	Dc Link current (A)	Inner rotor speed (rpm)	Input power (W)	output power (W)	Efficiency
(a)	3	3.03	100	105	0.08	358	112.4	31.7	0.3
(b)	3.5	4.22	200	181	0.25	615	225.3	88.3	0.4
(c)	4.5	7.03	400	360	0.6	1258	592.5	294.3	0.5
(d)	5.6	9.79	600	547	0.95	1977	1158.8	614.8	0.5
(e)	5.7	10.13	650	567	1	2067	1233.2	689.2	0.6

Table 9.17: the measured cases of the torque amplification

9.5 Summary

A series of tests have been carried out to verify the value and the advantages of the proposed EMTC system. In addition, the construction and testing set-up have been described, the hardware drive and auxiliary circuits were presented. The measurements back-EMF, waveform of the outer part (BLDCM) of the DM was a trapezoidal waveform, which validates the FEM simulation waveform. Therefore, the measured and the simulated results agree well with each other.

10 Conclusion and Future Work

In this thesis, the modelling, design and the operation of an Electromagnetic Torque Converter (EMTC) system has been presented. The EMTC system aims to replace the conventional hydraulic torque converter including the gearbox in order to overcome most of its drawbacks by the use of powerful permanent magnet machine. The system consists of two parts, namely the Differential Machine (DM) and the Variable Frequency Rotary Transformer (VFRT). The DM part is composed of two electrical machines; the Brushless DC Machine (BLDCM) with rated torque of 63 Nm at 1000 rpm and the Permanent Magnet Induction Machine (PMIM) with rated torque of 40 Nm at speed 3000 rpm. The inner rotor of the DM is connected to the prime mover while the outer rotor is connected to the load. The VFRT comprises of a primary side (rotor) and a secondary side (stator). The primary windings are connected to the inner rotor of the DM. The output power from the secondary windings is fed to the stator windings of the DM via a power electronic converter. Torque amplification is achieved by returning this slip power to the output shaft as additional low speed torque, in addition to the directly coupled torque between the input and output shafts.

The main contributions of this thesis are:

- The design of a novel EMTC system that is applicable to transmit mechanical power between any prime mover and a driven load.
- The brushes and slip rings used in the previous electromagnetic torque converter schemes are eliminated in the new design of the EMTC system by the use of the VFRT.
- The proposed EMTC system provides a high torque density compared to other electromagnetic torque converter schemes.
- The proposed EMTC system is designed with the minimum cogging torque by employing non-integer pole-slot ratios in the design.
- The output load torque is based on slip power recovery with frequency changer rather than using an external power supply.

10.1 A Summary of the Key Research Output in the Modelling, Design and Operation of the EMTC System

The DM was modelled using Finite Element Modelling (FEM) in order to select a pole slot combination that has the minimum cogging torque and the high electromagnetic torque with low ripple torque. Once the DM model was selected, the pole slot combination of the VFRT was then selected.

- **Selection of the Pole Slot Combination of DM**

34 permanent magnet (PM) models were selected for comparison. 17 models were simulated with fully pitched magnet arc length and 17 models were simulated with gapped magnet structures for each machine: the BLDCM and the PMIM. The comparisons were done using FEM computation. A minimum cogging torque of less than 0.2 Nm was firstly used to nominate the suitable pole slot combinations. Then, the high electromagnetic torque and low ripple torque criteria were used to select the best pole-slot combination model. The FEM simulations show that the 10 poles-27 slot is the optimum combination for both the BLDCM and the PMIM machines. This combination was verified also by using the optimal arc length technique. This technique was applied according to the Least Common Multiple (LCM) method. Several calculations were carried out to the selected models to obtain the optimum arc length.

- **Selection of the Pole Slot Combination for the VFRT Machine**

The selection of the VFRT machine configuration was carried out according to three conditions; (1) the number of turns was selected in order to have a unity ratio between its stator and the DM stator windings; (2) the minimum cogging torque was considered using different number of slots in its primary (rotor) and secondary (stator) sides; (3) the stator pole-slot configuration was selected to have the same bore size as the stator of the DM. The reason for this condition was to provide an easier way to remove the rotors in case of maintenance.

- **Design Process of the EMTC Machine**

Two techniques were used to design the EMTC machine: analytical and FEM modelling. The analytical method was used first to determine the basic parameters of

the machine design and then FEM was used to optimise the analytical design. The FEM included both static and dynamic modelling to determine the flux distribution, the magnet saturation, and the electromotive force (EMF) induced in each part of the EMTC machine.

In addition to the FEM modelling, a mathematical model was derived for each part of the EMTC machine. The mathematical modelling was carried out using MATLAB / Simulink toolboxes. The derived dynamic equations of the DM show that the speed between the two rotors of the DM has a slip with and without an external resistance connected to the inner rotor windings. This was validated in the experimental results.

- **The Construction of the EMTC System**

A prototype EMTC machine was designed according to the proposed full specification. Also, the prototype had shorter lamination stack lengths so that the complete machine could be fitted into a standard IEC 132 size frame and the power rated for natural air-cooling. If liquid cooling was to be used, then the machine could be used at full power. The most powerful permanent magnet material NdFeB type was chosen to be in the outer rotor of the DM, for high torque density and efficiency. The high torque and low cogging torque used in the proposed EMTC system makes it suitable for a small hybrid car.

10.2 Experimental Validation of the FEM Modelling

10.2.1 The BLDCM and PMIM Characterisation Test

Prior to the start of the experimental work, the commutation time of the BLDCM was adjusted for maximum output torque and smooth operation. This was achieved by adjusting the optical interrupter on the output shaft. If the commutation timing was too advanced or too retarded, there was a noticeable roughness in sound from the machine. It was important also to place a suitable capacitor in the DC link of the inverter to absorb sufficient inductance energy produced during commutation of the phases of the BLDCM. The BLDCM and PMIM were characterised so that the speed-voltage and speed-torque relationships were determined for both machines. The experiments show that the speed and voltage in both machines have a linear relationship. The tests on the BLDCM at load condition showed that its efficiency is 93%. This efficiency proved to handle the high load torque. The PMIM test results showed that the relationship

between the input speed and the output back EMF was linear up to 110 V and thereafter the laminations were saturated. These test results led to the motivation to conduct an investigation to the V/F characteristics of the PMIM inner rotor.

10.2.2 The VFRT Machine Test

The VFRT was tested to determine the magnetic saturation point of the entire steel core (both stator and rotor laminations stacks). This is so that the maximum V/F characteristic could be determined to ensure efficient operation of the VFRT. It is the inner rotor of the DM, the PMIM, that feeds the primary winding of the VFRT, and so, the correct three phase inter-rotor connection should be made. Hence, after a series of experiments on the connection of the two rotors of the EMTC system, the three-phase star connected windings of the VFRT rotor were cascaded with the delta connected inner rotor windings of the DM. Having determined the correct connection between these two rotors, the open machine loop test was carried out.

10.2.3 Open Machine Loop Test

One of the concepts of the EMTC system is to utilise the slip power to drive the BLDCM. This can be achieved only when the amplitude of the slip voltage is higher than the back EMF in the BLDCM stator windings. Therefore, experiments were carried out to ensure this concept and being able to close the slip recovery loop can be achieved. After performing this test, the initial boundary condition of the EMTC operating line was defined. It was defined according to the slip speed between the inner and the outer rotors. Based on the initial boundary condition line, the closed loop test was carried out. The calculated results of the back EMF using FEM showed good agreement with the experimentally measured results even though the FEM simulations were obtained only for the DM.

10.2.4 Closed Machine Loop Test

The results acquired by the open machine loop experiments showed that the back EMF in the stator windings of the VFRT was higher than that of its inner rotor windings. This means that the expected function of the VFRT was achieved. The VFRT was found to be a rotating transformer which operates with any input frequency, unlike the conventional transformer, which works with a specific frequency. Moreover, the obtained results from the open machine loop indicate that the back EMF in the stator of

the VFRT was higher than the back EMF in the stator of the BLDCM at different slip speeds between the inner rotor and the outer rotor. Prior to conducting the closed machine loop test, it is necessary to ensure that the back EMF in the VFRT stator windings is higher than the back EMF in the stator windings of the BLDCM, which was confirmed by the open machine loop results.

The closed loop test was performed and the system was operated as a self-excited system when the slip power is recovered. The slip power can be recovered in the condition of the power produced from the VFRT is higher than that in the BLDCM stator. From the test, the ratio between the input and the output torques with respect to the obtained slip speed are as follows: When the slip speed was 250 rpm, the obtained output torque was 101% of the input torque. As the slip speed increases, the percentage of the output torque increases. Thus, the output torque reached 177.7% of the input torque when the slip speed was 1417 rpm. The torque and speed relation showed that their relation was nonlinear unlike the gearing system operation. Therefore, the theory of the torque converter was proved experimentally.

10.3 Future Work

There are still many features remaining to investigate in the EMTC system, since it is not limited to automobile applications only. The controllability and the observability of the system's dynamics is a challenging and interesting research topic. Once the dynamic system is determined, a suitable control system could be implemented.

Finally, the EMTC system could be used to run a vehicle purely on electric propulsion, if a suitable battery was connected to the DC link. Furthermore, regenerative braking can also be utilised to recharge that battery via the BLDCM. This feature would be a new type of hybrid electric transmission that is neither a conventional series nor a conventional parallel hybrid transmission system, but has elements of both systems.

References

- [1] C. David and M. Behrooz, *Vehicle Powertrain Systems*. West Sussex, United Kingdom: John Wiley & Sons 2012
- [2] J. Gordon and K. M. G. Maher, *Chilton's Automatic Transmission/Transaxle Diagnosis and Repair*, W.G. Nichols, 1998.
- [3] A. Kuchle, H. Naunheimer, B. Bertsche, J. Ryborz, W. Novak and P. Fietkau, *Automotive Transmissions: Fundamentals, Selection, Design and Application*, Springer, 2010.
- [4] I. V. Middelmann and U. Wagner, "The torque converter as a system," 6th Luk Symposium in Comfort and Economy, Bühl /Baden, Germany, pp. 123-156, 1998.
- [5] A. N. D'Arcy, "Hydro-Kinetic Drives, Hydraulic torque converters and hydraulic couplings," vol. 8, pp. 10-16, 1945.
- [6] Y. L. Zhou, "Modelling and simulation of hybrid electric vehicles," MSc, Mechanical Engineering, University of Victoria, 2007.
- [7] E. G. D. Pritchard, R. D. Gould, and R. R. Johnson, "Torque converter interactions in a parallel post transmission hybrid driveline," IEEE in Vehicle Power and Propulsion Conference, pp. 1-5, 2011.
- [8] J. Happian-Smith, *An introduction to Modern Vehicle Design*. Oxford: Butterworth-Heiemann, 2002.
- [9] H. A. Asl, N. L. Azad, and J. McPhee, "Modelling torque converter characteristics in automatic drivelines: lock-up clutch and engine braking simulation," SAE International, 2012.
- [10] K. Kawashima, "Torque converter using magnetic viscous fluid as working fluid," U.S. Patent No. 8,640,840. 4 Feb. 2014.
- [11] A. E. Ayman Abdel-Khalik, Ahmed Massoud and Shehab Ahmed, "Brushless doubly-fed induction machine as a variable frequency transformer," *Journal of Energy and Power Engineering*, vol. 7, pp. 110-117, 2013.
- [12] D. A. Kelly, "Magnetic torque converter," U.S. Patent No. 4,082,969. 4 Apr. 1978.
- [13] E. C. Ellis, "Torque converter," U.S. Patent No. 2,490,789. 13 Dec. 1949.
- [14] Trofimov, Lev A. "Electric torque-converter." U.S. Patent No. 2,654,849. 6 Oct. 1953.
- [15] Trofimov, Lev A. "Electric torque-converter transmissions." U.S. Patent No. 2,790,917. 30 Apr. 1957.

- [16] F. Masato, Y. Sumi, and N. Shizuoka. "Electric torque converter mounted on parallel hybrid vehicle." U.S. Patent No. 6,474,428. 5 Nov. 2002.
- [17] D. O. Bishop and G. S. Brosan, "An Electromagnetic variable-ratio torque convertor," Proceedings of the IEE - Part A: Power Engineering, vol. 106, pp. 485-490, 1959.
- [18] S. Christopher "Continuously variable torque converter." U.S. Patent No. 4,644,206. 17 Feb. 1987.
- [19] Amara, Yacine, et al. "Hybrid excitation synchronous machines: energy-efficient solution for vehicles propulsion." Vehicular Technology, IEEE Transactions on 58.5 (2009): 2137-2149.
- [20] T. Backstrom, C. Sadarangani, and S. Ostlund, "Integrated energy transducer for hybrid electric vehicles," 8th International Conference on Electrical Machines and Drives, London, UK, pp. 239-43, 1997.
- [21] D. H. Kelly, "Double-rotor induction motor," IEEE Transactions on Power apparatus and systems, pp. 1086-1092, 1969.
- [22] Z. Fengge, N. Neuberger, E. Nolle, P. Gruenberger, and W. Fengxiang, "A New type of induction machine with inner and outer double rotors," The 4th International Conference in Power Electronics and Motion Control, pp. 286-289, 2004.
- [23] Y. Yoshikawa, H. Li, and H. Murakami, "Design of ultra-low acoustic noise and high power density direct drive machines with double rotor and Toroidally wound structure," IEEE, 41st IAS Annual Meeting Conference Record in Industrial Applications, pp. 1949-1954, 2006.
- [24] S. Cui, Y. Yuan, and T. Wang, "Research on switched reluctance double-rotor motor used for hybrid electric vehicle," ICEMS International Conference in Electrical Machines and Systems, pp. 3393-3396, 2008.
- [25] P. Pišek, B. Štumberger, T. Marcic, and P. Vrtič, "Design and FE analysis of a double rotor synchronous PM machine," IEEE, 14th Conference in Electromagnetic Field Computation (CEFC), Biennial, pp. 1-1, 2010.
- [26] C. Tong, P. Zheng, Q. Wu, J. Bai, and Q. Zhao, "A Brushless claw-pole double-rotor machine for power-split hybrid electric vehicles," IEEE Transactions on Industrial Electronics, pp. 4295-4305, 2014.
- [27] J. M. Hendershot, T. J. *Design of Brushless Permanent-Magnet Motors*, Magna Physics, 1994.
- [28] J. M. Wing. *Permanent Magnet Motor Technology Design and Applications*, New York: Marcel Dekker, 2002.
- [29] R. H. Park, "Two-reaction theory of synchronous machine: Part II," Electrical Engineering, vol. 52, pp. 44-45, 1933.

- [30] P. C. Krause. Analysis of Electric Machinery and Drive Systems, 2nd Edition ed.: New York, Wiley, 2002.
- [31] C.-M. Ong. Dynamic Simulation of Electric Machinery Using MATLAB/ SIMULINK, Prentice Hall PTR Upper Saddle River, NJ, 1998.
- [32] J. Gao and J. Kang, "Modeling and Simulation of Permanent Magnet Synchronous Motor Vector Control," Information Technology Journal, vol. 13, 2014.
- [33] T. D. Nguyen, V. Lanfranchi, C. Doc, and J. P. Vilain, "Comparison of optimization algorithms for the design of a brushless DC machine with travel-time minimization," 8th International Symposium on Advanced Electromechanical Motion Systems & Electric Drives Joint Symposium, Piscataway, NJ, USA, pp.1- 6 , 2009
- [34] P. Pillay and R. Krishnan, "Application characteristics of permanent magnet synchronous and brushless DC motors for servo drives," IEEE Transactions on Industry Applications, vol. 27, pp. 986-996, 1991.
- [35] M. V. Cistelecan, M. Popescu, and M. Popescu, "Study of the number of slots/pole combinations for low speed permanent magnet synchronous generators," IEEE, International Electric Machines and Drives Conference, IEMDC 2007, Antalya, Turkey, pp. 1616-1620, 2007.
- [36] Zhu, Li, S. Z. Jiang, and C. C. Chan. "Comparison of alternate analytical models for predicting cogging torque in surface-mounted permanent magnet machines," IEEE, Conference on Vehicle Power and Propulsion, pp. 1-6, 2008.
- [37] L. Dosiek and P. Pillay, "Cogging torque reduction in permanent magnet machines," IEEE Transactions on Industry Applications, vol. 43, pp. 1565-1571, 11/ 2007.
- [38] P. Zheng, P. Thelin, E. Nordlund, S. Eriksson, and C. Sadarangani, "Consideration of skewed slots in the performance calculations of a four-quadrant transducer," IEEE, Published in Proceedings of the Vehicular Power and Propulsion Symposium, VPP04, Paris, France, pp. 6-8, 2004.
- [39] M. Aydin, Z. Q. Zhu, T. A. Lipo, and D. Howe, "Minimization of cogging torque in axial-flux permanent-magnet machines: design concepts," IEEE Transactions on Magnetics, vol. 43, pp. 3614-3622, 2007.
- [40] D. Min, A. Keyhani, and T. Sebastian, "Torque ripple analysis of a PM brushless DC motor using finite element method," IEEE Transactions on Energy Conversion, vol. 19, pp. 40-45, 2004.
- [41] Z. Q. Zhu and D. Howe, "Influence of design parameters on cogging torque in permanent magnet machines," IEEE Transactions on Energy Conversion, vol. 15, pp. 407-412, 2000.
- [42] C. C. Hwang, M. H. Wu, and S. P. Cheng, "Influence of pole and slot combinations on cogging torque in fractional slot PM motors," Journal of Magnetism and Magnetic Materials, vol. 304, pp. e430-e432, 2006.

- [43] Z. Q. Z. K. Wang, G. Ombach, M. Koch, S. Zhang and J. Xu, "Design and experimental verification of an 18-slot/10-pole fractional-slot surface- mounted permanent-magnet machine," IEEE International Electric Machines and Drives Conference, IEMDC 2013, pp. 287-294, 2013.
- [44] H. Zhu, X. Xiao, and Y. Li, "Torque ripple reduction of the torque predictive control scheme for permanent-magnet synchronous motors," IEEE Transactions on Industrial Electronics, vol. 59, pp. 871-877, 2012.
- [45] D. M. Ionel, M. Popescu, M. I. McGilp, T. J. E. Miller, and S. J. Dellinger, "Assessment of torque components in brushless permanent-magnet machines through numerical analysis of the electromagnetic field," IEEE Transactions on Industry Applications, vol. 41, pp. 1149-1158, 2005.
- [46] N. Bianchi and S. Bolognani, "Design techniques for reducing the cogging torque in surface-mounted PM motors," IEEE Transactions on Industry Applications, vol. 38, pp. 1259-65, 2002.
- [47] H. Zeroug, B. Boukais, and H. Sahraoui, "Analysis of torque ripple in a BDCM," IEEE Transactions on Magnetics, vol. 38, pp. 1293-1296, 2002.
- [48] J. F. Gieras, "Analytical approach to cogging torque calculation of PM brushless motors," IEEE Transactions on Industry Applications, vol. 40, pp. 1310-1316, 2004.
- [49] T. Ishikawa and G. R. Slemon, "A method of reducing ripple torque in permanent magnet motors without skewing," IEEE Transactions on Magnetics, vol. 29, pp. 2028-2031, 1993.
- [50] P. G. Cummings, "Comparison of IEC and NEMA/IEEE motor standards. II," IEEE Transactions on Industry Applications, vol. IA-20, pp. 67-73, 01/ 1984.
- [51] A. M. El-Refaie and M. R. Shah, "Comparison of induction machine performance with distributed and fractional-slot concentrated windings," IEEE in Industry Applications Society Annual Meeting, IAS'08, October 5, 2008 - October 9, 2008, Edmonton, AB, Canada, pp. 1-8, 2008.
- [52] P. Salminen, M. Niemela, J. Pyrhonen, and J. Mantere, "High-torque low-torque-ripple fractional-slot PM-motors," International Conference in Electric Machines and Drives, Piscataway, NJ, USA, pp. 144-148, 2005.
- [53] F. Magnussen and C. Sadarangani, "Winding factors and Joule losses of permanent magnet machines with concentrated windings," International Conference in Electric Machines & Drives, Piscataway, NJ, USA, 2003, pp. 333-339, 2003.
- [54] P. B. Reddy, T. M. Jahns, and A. M. El-Refaie, "Impact of winding layer number and slot/pole combination on AC armature losses of synchronous surface PM machines designed for wide constant-power speed range operation," IEEE, Industry Applications Society Annual Meeting, Edmonton, AB, Canada, pp. 1-8, 2008.

- [55] A.K. Theraja. *AC & DC Machines in S.I. System of Units*, S. Chand Limited, 2005.
- [56] J. A. Guemes, A. M. Iraolagoitia, P. Fernandez, and M. P. Donsion, "Comparative study of PMSM with integer-slot and fractional-slot windings," 19th International Conference on Electrical Machines, ICEM 2010, Rome, Italy, 2010.
- [57] Kenjío, Takashi, and S. Nagamori. *Permanent Magnet and Brushless DC Motors*, Clarendon Press, Oxford and New York, 1985.
- [58] A. M. El-Refaie and T. M. Jahns, "Optimal flux weakening in surface PM machines using fractional-slot concentrated windings," IEEE Transactions on Industry Applications, vol. 41, pp. 790-800, 2005.
- [59] J. Cros and P. Viarouge, "Synthesis of high performance PM motors with concentrated windings," IEEE Transactions on Energy Conversion, vol. 17, pp. 248-253, 2002.
- [60] A. M. El-Refaie, "Fractional-slot concentrated-windings synchronous permanent magnet machines: opportunities and challenges," IEEE Transactions on Industrial Electronics, vol. 57, pp. 107-121, 2010.
- [61] L. Chong, R. Dutta, and M. F. Rahman, "Application of concentrated windings in interior permanent magnet machine," Australasian Universities Power Engineering, AUPEC, Perth, WA, Australia, pp. 1-5, 2007.
- [62] M. S. Sarma. *Electric Machines: Steady-State Theory and Dynamic Performance*, Cengage, 1985.
- [63] J.J. Cathey. *Electric Machines: Analysis and Design Applying Matlab*, McGraw-Hill Education, 2001.
- [64] K. G. Upadhyay, *Design of Electrical Machines*, New Age International, 2008.
- [65] Jacek F., Gieras, Rong-Jie Wang, and J. Kamper Maarten, *Axial Flux Permanent Magnet Brushless Machines*, vol. 1. New York, NY: Springer, 2008.
- [66] Z. Q. Zhu and D. Howe, "Influence of design parameters on cogging torque in permanent magnet machines," IEEE Transactions on Energy Conversion, vol. 15, pp. 407-412, 12/ 2000.
- [67] Singh, Bhim, and Devendra Goyal, "Computer aided design of permanent magnet brushless DC motor for hybrid electric vehicle application." IEEE, International Conference on Power Electronics, Drives and Energy Systems, pp. 1-6, 2006.
- [68] C. Marchland and A. Razek, "Optimal torque operation of digitally controlled permanent magnet synchronous motor drives," Electric Power Applications, IEE Proceedings B, vol. 140, pp. 232-240, 1993.

- [69] A. Michaelides and C. Pollock, "Modelling and design of switched reluctance motors with two phases simultaneously excited," *Electric Power Applications, IEE Proceedings*, vol. 143, No. 5, pp. 361-370, 1996.
- [70] A. Tenhunen and A. Arkkio, "Modelling of induction machines with skewed rotor slots," *Electric Power Applications, IEE Proceedings*, vol. 148, No.1, pp. 45-50, 2001.
- [71] A. Parviainen, M. Niemela, and J. Pyrhonen, "Modeling of axial flux permanent-magnet machines," *IEEE Transactions on Industry Applications*, vol. 40, pp. 1333-1340, 2004.
- [72] P.P. Silvester, R.L. Ferrari. *Finite Elements for Electrical Engineers*, Cambridge University Press, Cambridge, 1990.
- [73] E. G. Strangas and T. Ray, "Combining field and circuit equations for the analysis of permanent magnet AC motor drives," *Conference Record of the 1988 Industry in Applications Society Annual Meeting New York, NY, USA*, pp. 7-10, 1988.
- [74] G. Kovács and M. Kuczmann, "Simulation of a PMS motor by the help of two different design software tools," *Bulletin of the Transilvania University of Braşov Series I: Engineering Sciences*, vol. 6, pp. 59-66, 2013.
- [75] N. Bianchi and S. Bolognani, "Design techniques for reducing the cogging torque in surface-mounted PM motors," *IEEE Transactions on Industry Applications*, vol. 38, pp. 1259-1265, 2002.
- [76] Z. Q. Zhu, S. Ruangsinchaiwanich, N. Schofield, and D. Howe, "Reduction of cogging torque in interior-magnet brushless machines," *Conference in International Magnetism, USA*, pp. 3238-3240, 2003.
- [77] E. Diryak, P. Lefley, L. Petkovska, and G. Cvetkovski, "Design optimization of a double stator cup- rotor machine," *World Academy of Science, Engineering and Technology*, vol. 6, pp. 1516-1522, 2012.
- [78] E. Diryak, P. Lefley, "Cogging torque minimization of the double stator cup-rotor machine," in *4th Symposium on Applied Electromagnetics SAEM'12, Sopron Hungary*, pp. 72-75, 2012.
- [79] J. J. Germishuizen and M. J. Kamper, "IPM traction machine with single layer non-overlapping concentrated windings," *IEEE Transactions on Industry Applications*, vol. 45, pp. 1387-1394, 2009.
- [80] A. M. El-Refaie, "Fractional-slot concentrated-windings synchronous permanent magnet machines: Opportunities and challenges," *IEEE Transactions on Industrial Electronics*, vol. 57, pp. 107-121, 2010.
- [81] E. M. Tsampouris, M. E. Beniakar, and A. G. Kladas, "Geometry optimization of PMSMs comparing full and fractional pitch winding configurations for aerospace actuation applications," *IEEE Transactions on Magnetism*, vol. 48, pp. 943-946, 2012.

- [82] F. Meier and J. Soulard, "PMSMs with non-overlapping concentrated windings: design guidelines and model references," in International Conference and Exhibition on Ecologic Vehicles and Renewable Energies (EVER), pp. 4-6, 2009.
- [83] F. Meier and J. Soulard, "Analysis of flux measurements on a PMSM with non-overlapping concentrated windings," IEEE in Industry Applications Society Annual Meeting, IAS'08, pp. 1-8, 2008.
- [84] O. Bottauscio, M. Chiampi, P. Guglielmi, G. Pellegrino, and A. Vagati, "Rotor loss estimation in permanent magnet machines with concentrated windings," IEEE, International Conference in Magnetics. Digests of the, pp. 97-98, 2005.
- [85] C. Magnet, "package: User manual," Infolytica Corporation Ltd., Montreal, Canada, 2006.
- [86] B. Farhad Ilahi, S. Islam, and M. Khursheed, "Modeling, analysis and simulation of VFT for power flow control through asynchronous power systems," ACEEE on Electrical and Power Engineering, vol. Vol. 02, pp. 4-8, 2011.
- [87] B. Hopfensperger, D. Atkinson, and R. Lakin, "Steady state of the cascaded doubly-fed induction machine," European transactions on electrical power, vol. 12, pp. 427-437, 2002.
- [88] T. J. Eastham Miller. *Brushless Permanent Magnet and Reluctance Motor Drives*, 1989.
- [89] N. Bianchi, *Electrical Machine Analysis Using Finite Elements*: CRC press, 2005.
- [90] T. Minowa, M. Yoshikawa, and M. Honshima, "Improvement of the corrosion resistance on Nd-Fe-B magnet with nickel plating," IEEE Transactions on Magnetics, vol. 25, pp. 3776-3778, 1989.
- [91] Iwamoto, Hideo, et al. "New intelligent power modules for appliance motor control." IEEE, Conference and Exposition in Applied Power Electronics, Vol. 2. 2001.
- [92] CM200DX-24S Datasheet, Mitsubishi Electric CM200DX-24S IGBT Modules - High Power Switching Use Insulated Type [pdf]
Available at:< www.ineltron.de/english/mitsubishi-data/IGBT/CM200DX-4S.pdf >,[Accessed 22 April 2012].
- [93] N. Bianchi and S. Bolognani, "Design techniques for reducing the cogging torque in surface-mounted PM motors," IEEE-IAS Annual Meeting in Proceedings of World Congress on Industrial Applications of Electrical Energy and 35th, 8-12 Oct. 2000, Piscataway, NJ, USA , pp. 179-185, 2000.
- [94] J. L. Coulomb, "A methodology for the determination of global electromechanical quantities for a finite element analysis and its application to the evaluation of magnetic forces, torques and stiffness," Conference on the Computation of Electromagnetic Fields, USA, pp. 2514-2519, 1983.

APPENDICES

Appendix A

A1. Differential Machine Design

A.1.1 Design of the BLDCM

```
*****
% Calculate the slot pitch
*****

D1=input ('please insert the stator diameter by mm=')
S1= input (' please insert the stator slot number=')
L1= (pi*D1)/S1% L1 is the lambda 1 in mm
L1_in = L1/25.4% L1 is the lambda 1 in In
*****

% calculate the winding factor
*****

N_ph= input ('Please Enter the number of phases=')
N_m= input ('Please Enter the pole number=')
q=S1/(N_ph*N_m) % stator slots per pole per phase
Gamma=180/(3*q)
K_ds=1/ (2*q*sin(180/(6*q)*pi/180)) % Pitch factor
K_ps=cos ((pi/180)*(180-Gamma)/2) % coil pitch factor
K_w1= K_ds*K_ps
*****

% calculate the conductor per slot
*****

L= input ('Please Enter the stack length by mm=')
L_in = L/25.4;
n= input ('Please Enter the rotor speed by rpm=')
f = n*N_m/120 % frequency
B_rho = input ('Please Enter the assumed air gap flux density=')
V_ph = input('Please Enter the phase voltage=')
Ns = V_ph/(sqrt(2)*pi*L/1000*D1/1000*f*B_rho)
% 8 poles with validated slots

if N_m ==8 & S1==9
    Nc=3
elseif N_m==8 & S1==12
    Nc=4
```

```

elseif N_m= =8 & S1= =18
    Nc=6
elseif N_m= =8 & S1= =21
    Nc=7
elseif N_m= =8 & S1= =24
    Nc=8
elseif N_m= =8 & S1= =27
    Nc=9
elseif N_m = =8 & S1= =30
    Nc=10
elseif N_m = =8 & S1= =33
    Nc=11
end
    % 10 poles with validated slots

if N_m= =10 & S1= =12
    Nc=4
elseif N_m= =10 & S1= =15
    Nc=5
elseif N_m= =10 & S1= =24
    Nc=8
elseif N_m= =10 & S1= =27
    Nc=9
elseif N_m = =10 & S1= =30
    Nc=10
elseif N_m = =10 & S1= =33
    Nc=11
end
    % 12 poles with validated slots
if N_m = =12 & S2 = = 9
    Nc=3
elseif N_m = =12 & S2 = =18
    Nc=6
elseif N_m = =12 & S2= =27
    Nc=9
end
Nt= Ns/Nc
Nt= round (Nt) % Number of turns
*****

% Calculate the maximum current loading

*****

P=input ('Please Enter the machine electrical power= ')
I_ph=P/ (3*V_ph)
Delta_C = (Ns*I_ph) / (L1*25.4)*10 % maximum current loading, 10 is to convert from
mm to cmm
% Slot design
Ws1=0.55*L1;
ds1=0.7*L1

```

```

*****

% Calculate the stator flux density

*****

t_s1=L1-Ws1
SF= input (' Please Enter the sticking factor between 0.95 and 0.97 =')
if N_m == 8
    C=1.9
elseif N_m == 10
    C=1.8
elseif N_m == 12
    C=1.7
end
phi_m = C*1E5 * (sqrt (P/745)*(60/f))
B_stm = ((pi/2)*phi_m) / ((S1)*t_s1*L*SF)
*****

% Calculate the core flux density B_scm

*****

Do= input (' Please Enter the machine outer diameter=')
B_scm = (phi_m/2) / (((Do-D1/25.4)/2)-ds1)*L*SF)
*****

% Calculate the outer magnet thickness

*****

Br_o= input (' Enter the magnet remanance Br =')
Be_o= input (' Enter the air gap flux density Be =')
la_o= input (' Enter the air gap length la =')
M_ao=la_o*((Be_o/ Br_o) / (1-(Be_o/ Br_o)))
M_ao= round (M_ao)
*****

% Calculate the inner magnet thickness

*****

Br_i = input (' Enter the magnet remanance Br_i =')
Be_i = input (' Enter the airgap flux density Be_i =')
la_i = input (' Enter the air gap length la =')
M_ai = la_i*((Be_i/Br_i) / (1-(Be_i/Br_i)))
M_ai= round (M_ai)

```

A.1.2 Design of the PMIM

```

*****

% Calculate the inner rotor diameter
*****
SH=3.0 % ring sheet = 3 mm thickness
rho = 1.0 % the air gap length for both sides
Dr=D1-2*M_ao-2*M_ai-2*SH-4*rho
*****

% Calculate the inner rotor slot pitch
*****

D2= input ('insert the stator diameter by mm=')
S2= input ('insert the stator slot number=')
L2 = (pi*D2) / S2% L1 is the lambda 2 in mm
L2_in = L2/25.4% L1 is the lambda 2 in In
*****

% calculate the winding factor
*****

q = S2 / (N_ph*N_m) % stator slots per pole per phase
Gamma=180/(3*q)
K_ds =1/ (2*q*sin(180/(6*q)*pi/180)) % Pitch factor
K_ps = cos ((pi/180)*(180-Gamma)/2) % coil pitch factor
K_w2=K_ds*K_ps
*****

% calculate the conductor per slot
*****

L_2= input ('Enter the PMIM stack length by mm=')
L_2in = L_2/25.4
n2= input ('Enter the rotor speed by rpm=')
f = n2*N_m / 120 % frequency
B_e = input ('Enter the assumed air gap flux density=')
V_ph = input ('Enter the phase voltage=')
Ns2 = V_ph / (sqrt(2)*pi*L/1000*D1/1000*f*B_rho)
% 8 poles with validated slots

if N_m= =8 & S2= =9
    Nc2=3
elseif N_m= = 8 & S2 = = 12
    Nc2=4
elseif N_m = = 8 & S2 = = 18
    Nc2=6
elseif N_m = = 8 & S2 = = 21
    Nc2=7

```

```

elseif N_m == 8 & S2 == 24
    Nc2=8
elseif N_m == 8 & S2 == 27
    Nc2=9
elseif N_m == 8 & S2 == 30
    Nc2=10
elseif N_m == 8 & S2 == 33
    Nc2=11
end
% 10 poles with validated slots

if N_m == 10 & S2 == 12
    Nc2=4
elseif N_m == 10 & S2 == 15
    Nc2=5
elseif N_m == 10 & S2 == 24
    Nc2=8
elseif N_m == 10 & S2 == 27
    Nc2=9
elseif N_m == 10 & S2 == 30
    Nc2=10
elseif N_m == 10 & S2 == 33
    Nc2=11
end
% 12 poles with validated slots
if N_m == 12 & S2 == 9
    Nc=3
elseif N_m == 12 & S2 == 18
    Nc=6
elseif N_m == 12 & S2 == 27
    Nc=9
end

```

A2. MATLAB Simulink

The Specification of both Induction Machines for the Simulink propose

```

% clc

% Differential machine parameters

% BLDCM parameters

f=50;           %synchronous frequency (Hz)

w=2*pi*f;      % angular speed (rps)
V_ph = 250;     % phase voltage (Vrms)
J=0.01;        % BLDCM inertia (kg.m2)
p=10;          % number of poles
Lls=18e-3;     % stator windings self- inductance (hennergy)
Lm=0.5e-3;     % mutual inductance (hennergy)

```

$R_s=0.6;$ % stator resistance (ohms)
 $L_s=L_{ls}+L_m;$ % stator inductance including self- inductance and mutual inductance
 $F_m=0.17;$ % magnet flux linkage (tesla)
% PMIM parameters
 $R_r=0.32;$ % rotor resistance (ohms)
 $L_{sr}=15e-3;$ % rotor windings self- inductance (henry)
 $L_r=L_{lr}+L_m;$ % rotor inductance including self- inductance and mutual

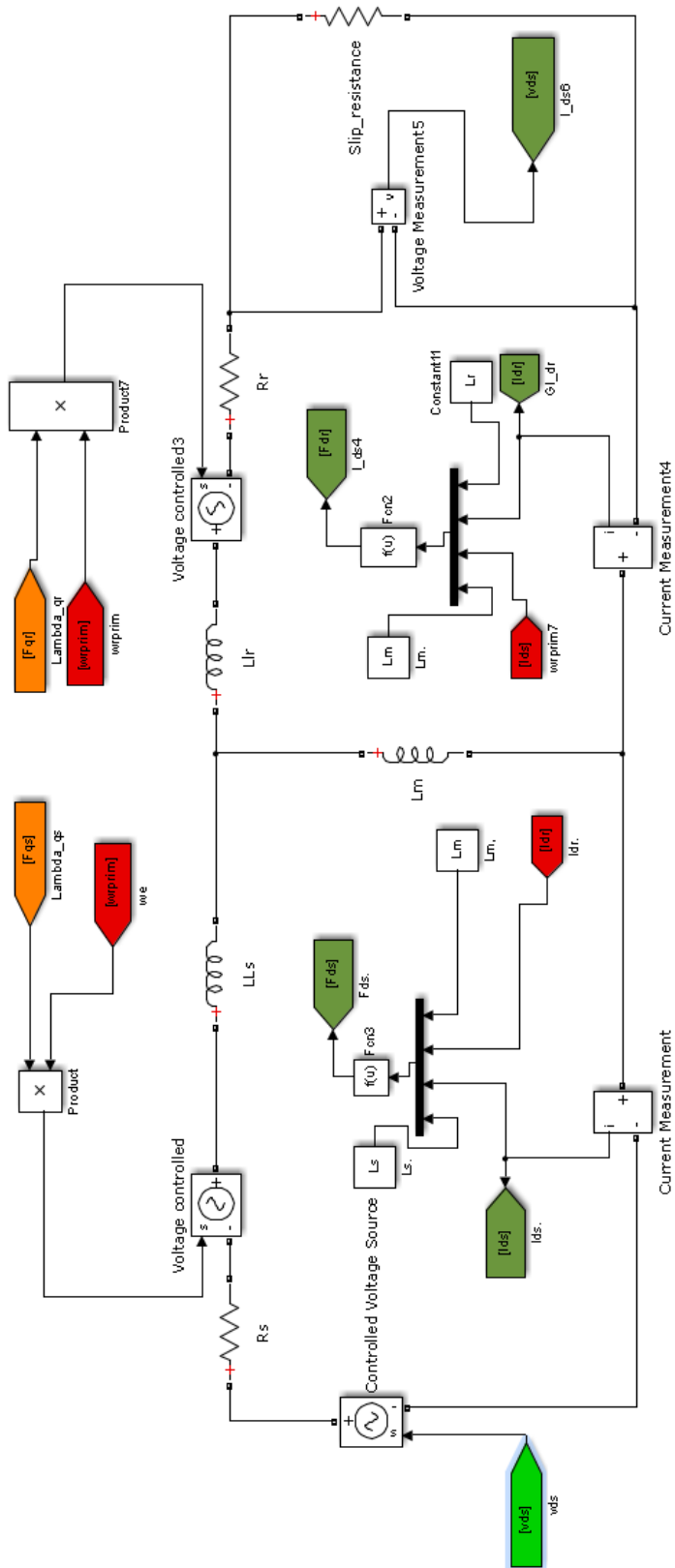


Figure A.1: d-axis equivalent

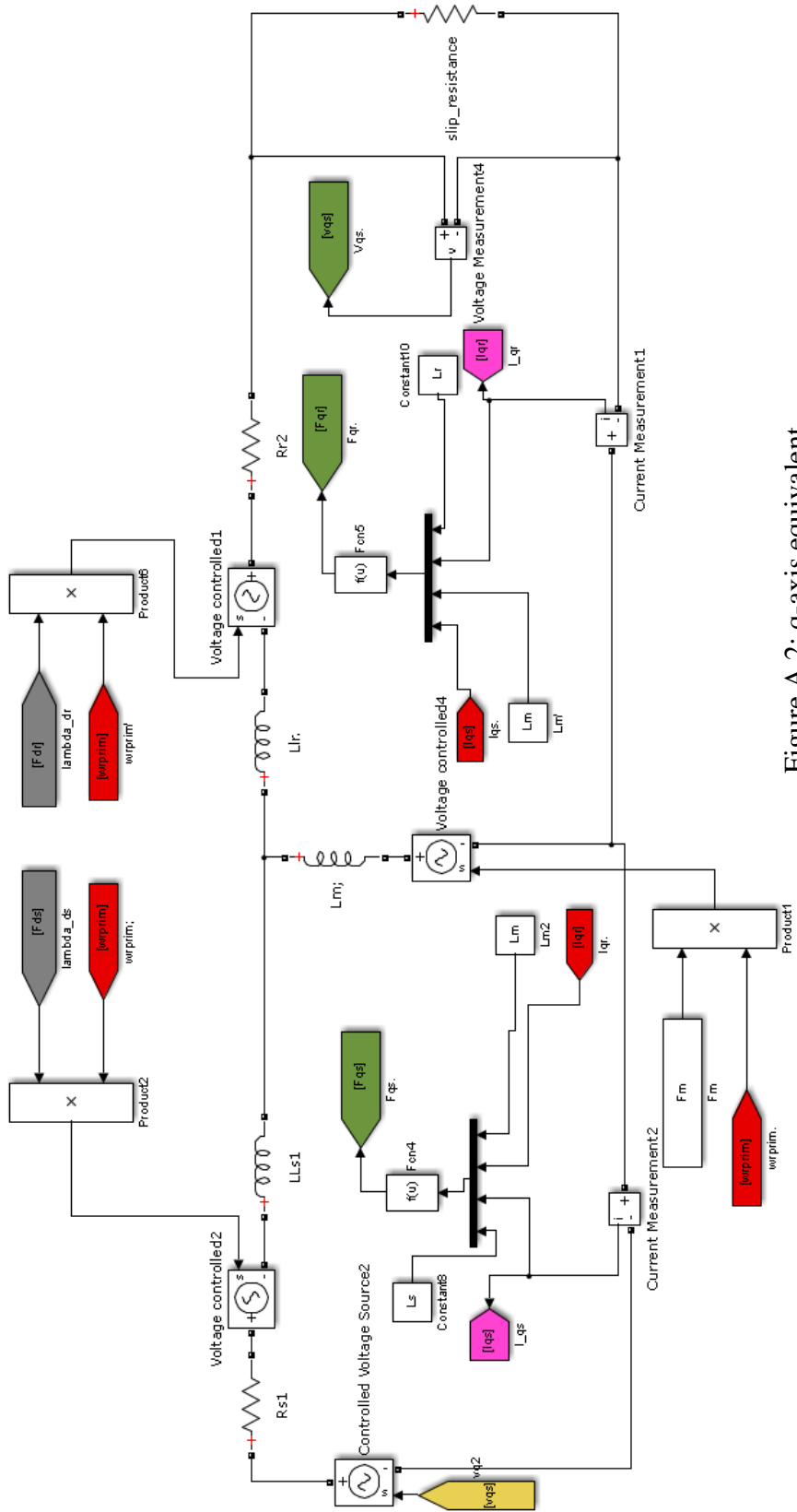


Figure A.2: q-axis equivalent

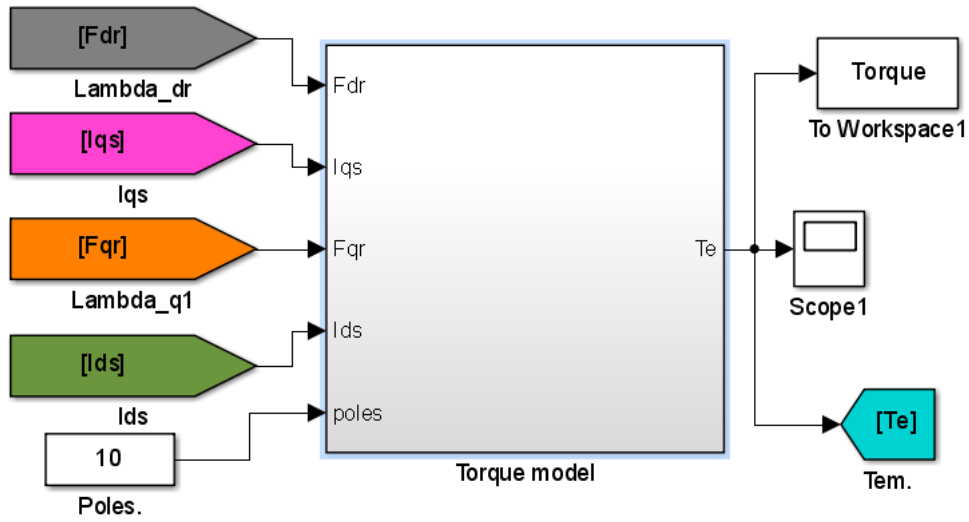


Figure A.3: The torque model

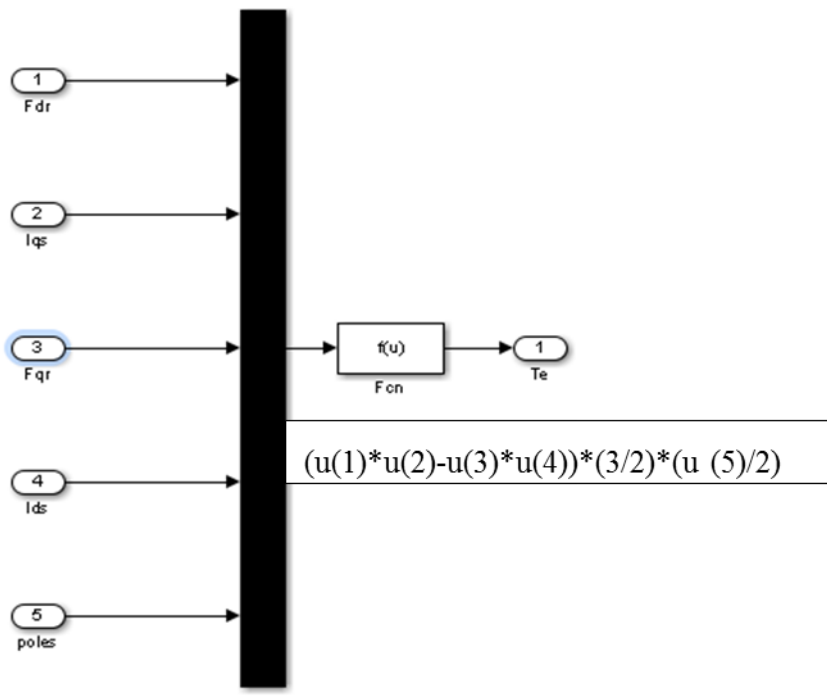


Figure A.4: The torque model equation

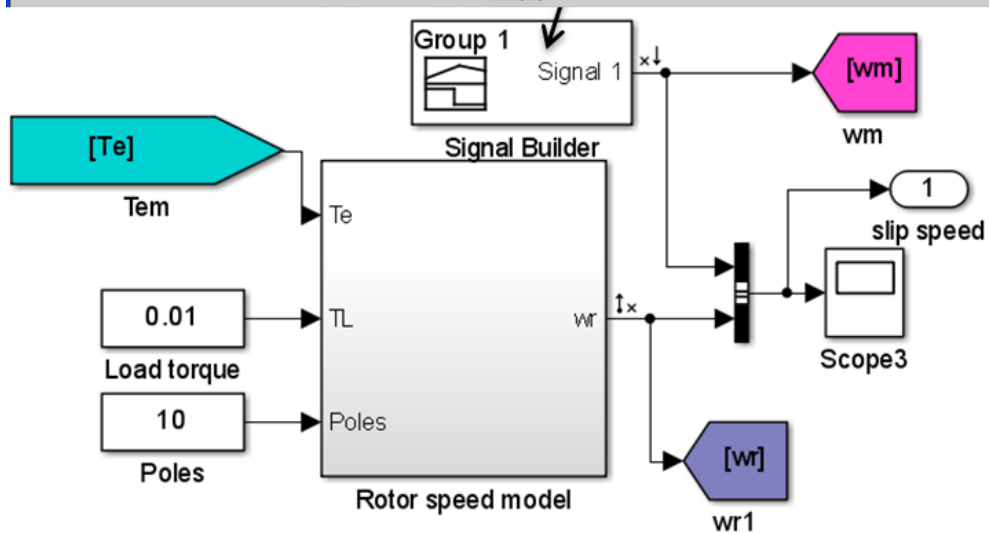
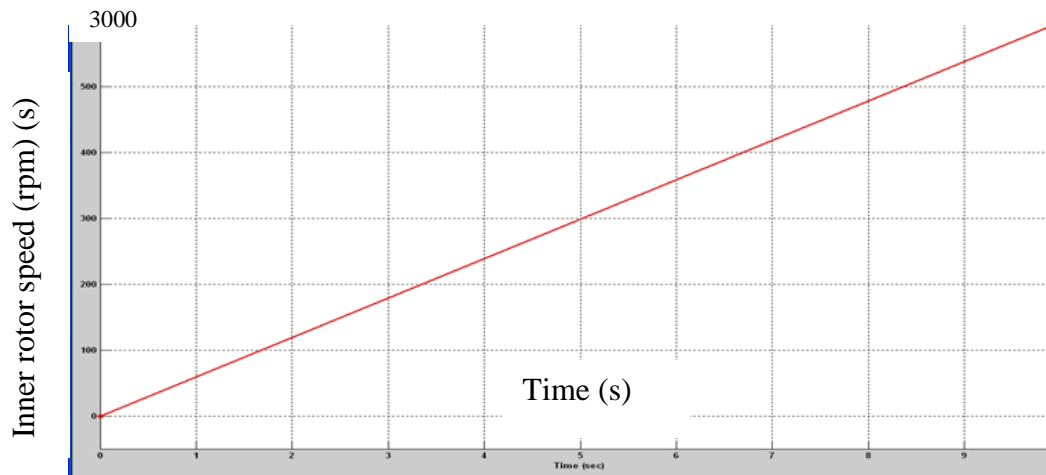


Figure A.5: The speed model

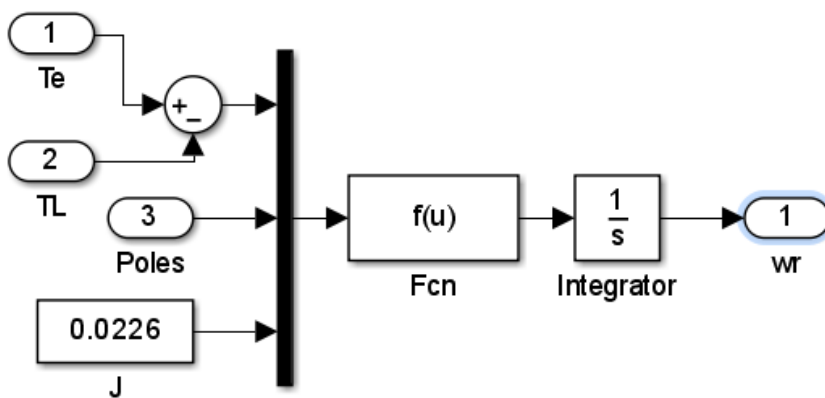


Figure A.6: The speed equation model

Appendix B

B1. MagNet Software Package

The open circuited induced voltage can be determined by finite element modelling (FEM) as the derivative of the flux linkage in the stator coils. The 2-D FEM analysis is applied and the flux linkage is converted to a scalar value. Therefore, the induced voltage in one coil is deduced by

$$e = -N \frac{d\phi}{dx} \cdot \frac{dx}{dt} \quad (\text{B.1})$$

Where, N is the number of turns of the coil.

The same technique is applied for the inner rotor. As the generated voltage of one coil is obtained, the voltage of one phase can be determined by vectorily summing the voltage of each coil of that phase.

▪ Flux Distribution

The flux distribution in the yoke and the teeth can be determined using FEM for a complete 360 ° rotation. The flux that does not link with the permanent magnet (PM) and the iron core is considered as a flux leakage at the conditions of load and no-load. Usually, the result at no load gives better indications than those acquired at on-load. At various load conditions there are differences in the flux lines at the stator teeth depending upon the reluctance in the air-gap. An additional reason is to do with the coils contributing to the flux flow in the tooth, which is controlled by Magneto-motive-force (MMF).

The flux distribution issue of the PM motors can be expressed by a set of Maxwell Equations. The flux density B equations are written in differential forms as below:

$$B_x = \frac{\partial A_z}{\partial y} \quad (\text{B.2})$$

$$B_y = \frac{\partial A_z}{\partial x} \quad (\text{B.3})$$

$$\frac{\partial}{\partial x} \left(v \frac{\partial A_z}{\partial x} \right) + \frac{\partial}{\partial y} \left(v \frac{\partial A_z}{\partial y} \right) = -J_z \quad (\text{B.4})$$

Where A is the magnetic vector potential, v is the material reluctivity and J is the current density.

In electrical machines, the 2-dimensional field calculation method is usually used to analyse the field distribution inside the motors. Equations (B.5 and B.6) describe the non-linear magneto-static field of the electric machines where Figure B1 shows the permanent magnet material characteristics and their parameters such as the remanance flux density (B_r) and the Co-ercitivity (H_c).

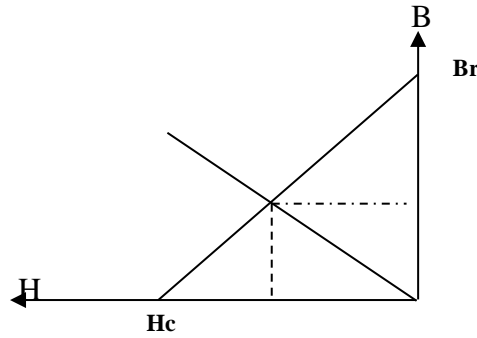


Figure B1: B-H curve for atypical permanent magnet material

Equation (B5) implies the relationship between the magnetic flux density (B) and the magnetic field intensity (H) as stated in [27]:

$$B = \mu H \quad (\text{B5})$$

$$M = X_m H \quad (\text{B6})$$

Where, $\mu = \mu_r \mu_o$. The permeability of a vacuum (μ_o) typically has a value of 10^{-6} henry/m, μ_r is a relative permeability and X_m is the susceptibility with less variable units.

- **Cogging Torque**

As any other parameter, FEM analyses the cogging torque at each time step of time and angular position. The Maxwell stress tensor is integrated in order to cover the rotor surface with no stator currents [93]. Assuming that the magnet leakage is ignored, the 2-D FEM can be utilised to predict the cogging torque more accurately. The FEM prediction involves the integration of the stress tensor along with the air gap circumference. The acquired result is then multiplied by the stack length (l_s). The equation of the stress tension across the air-gap volume S_{l_a} can be stated as [93]:

$$T_{cog} = \frac{l_s}{l_a \mu_o} \int_{S_{l_a}} r B_n B_t dS \quad (B7)$$

Where l_a is the air gap length, r is the rotor radius, B_n and B_t are the normal and tangential flux density in the air-gap.

- **Inductance Calculation**

By using the flux linkage value, the phase inductance can be calculated. With the presence of PM excitation, the total flux linkage of the coil will add the flux linkage produced by current with and without using PMs. The inductance of one coil is determined by:

$$L = \frac{\psi_i}{i} = \frac{\psi_{tot} - \psi_{PM}}{dx} \quad (B8)$$

Where, ψ_i and ψ_{PM} are the flux linkages produced by the current i and the PMs respectively, and ψ_{tot} is the sum of the two items.

When the flux density in the iron core goes in to saturation, the winding inductance is different from that calculation by (B8). The actual inductance is calculated by the incremental inductance:

$$L = \frac{\Delta\psi_i}{\Delta i} \quad (B9)$$

- **Torque Response**

The dynamic solve is applied to display the shape of the torque result. On the other hand, the static torque can be determined by discretely rotating the rotor mesh around the z-axis. This is done using the script method. The change of torque is virtually determined by stepping the time between any two positions. The new position of the rotor is determined at the beginning of each time step and the new mesh is shaped in the air gap. The predicted electromagnetic torque is calculated using the following equation (B10).

$$T_e = \frac{\partial}{\partial \theta} \int_A \left(\int_0^H B \cdot dH \right) dA \quad (\text{B10})$$

Where, A is the air gap area. The derivation of the above equation and its implementation in FEM is presented in [94].

- **Torque Ripple of the Current Driven Model**

The permeance variation at the air gap causes a pulsation in the torque waveform. The interaction of the air gap flux with the voltage harmonics could increase this ripple. The effect of the magnet width and the slot opening width on the torque ripple of the fractional slot PM motor is studied. The torque ripple peak-to-peak value is computed using the FEA (Motor-Solve software) with a current driven model at the same number of turns of the windings and phase current. There are other parameters such as the magnet mass (about 10 kg for 20 pieces of magnets), the inner and outer diameter of all machine parts, whereas the slot numbers and their area are variable. The typical modelled motors have a 120 mm stator inner diameter of the inner machine part. In the outer machine part, the modelled motors have 150 mm.

B.2 MotorSolve software package details

The MotorSolve software package (Montréal, Canada) is dealing with a default models. The existing models need to be modified. There are only radial flux motor models that can be analysed. The model size is determined by the required torque (T); the following formula can be used:

$$T = k D_r^2 L \quad (\text{B11})$$

Where k is a constant, D_r is the outer diameter of the rotor, and L is the stack length.

These variables are calculated as:

$$L = r D_s \quad (\text{B12})$$

$$D_s = \frac{D_r}{f} \quad (\text{B13})$$

Where D_s the outer diameter of the stator, (B14) can be rewritten as:

$$T = k \frac{r}{f} D_r^3 \quad (\text{B14})$$

Where r is the motor aspect ratio, f is the rotor-stator ratio.

Appendix C

C1: The FEM simulation results of the cogging torque

The cogging torque simulations at both the GM and FP models can be shown in figures C1.1-C1.12.

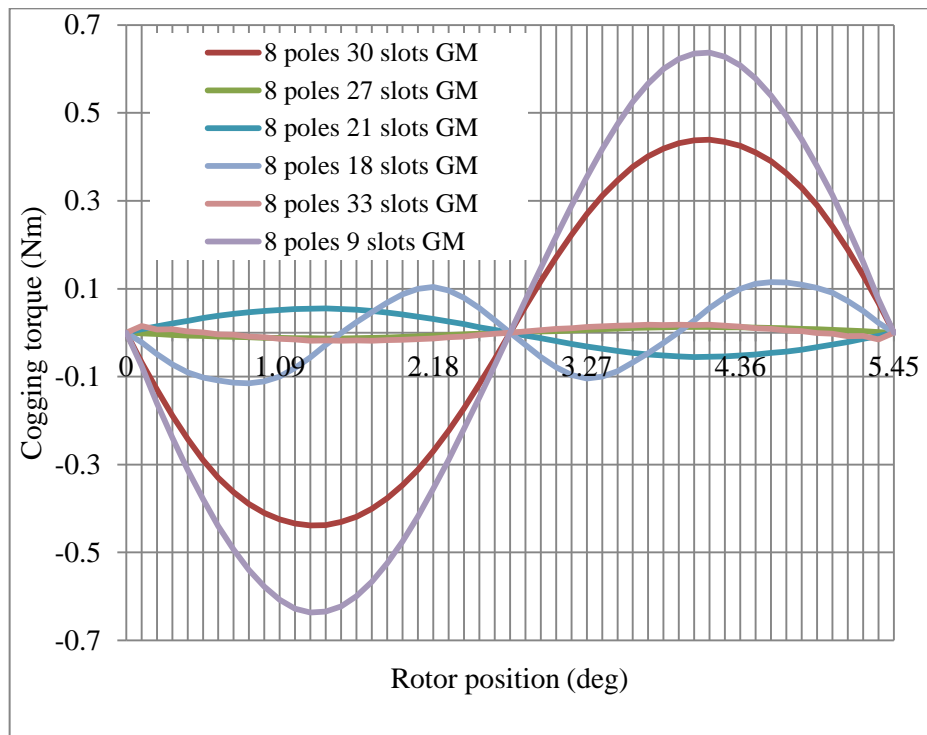


Figure C1.1: The cogging torque of the 8 poles GM models of the fractional windings

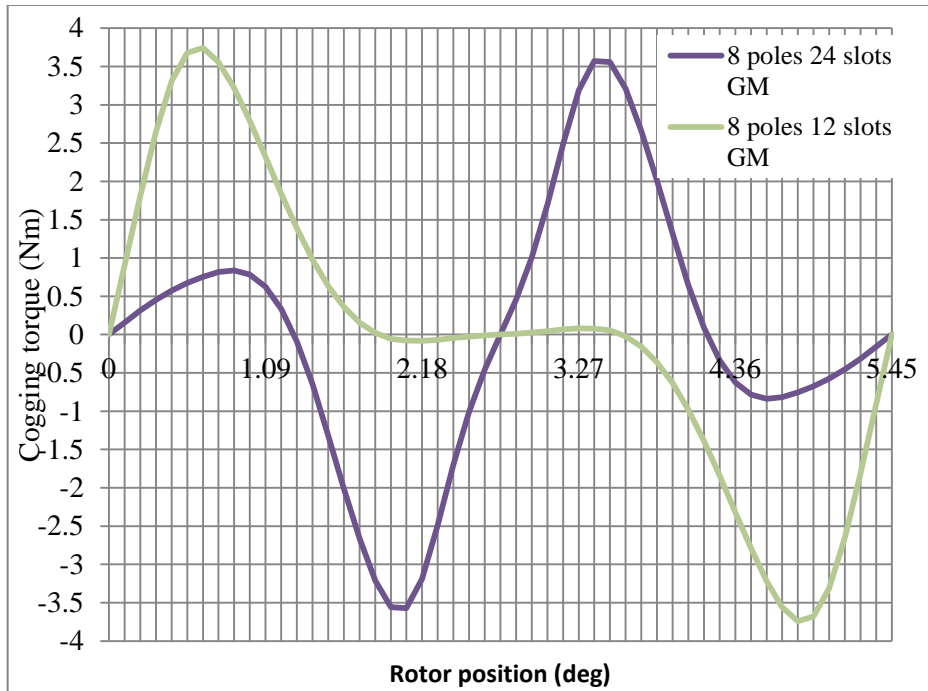


Figure C1.2: The cogging torque of the 8 poles GM models of the integral windings

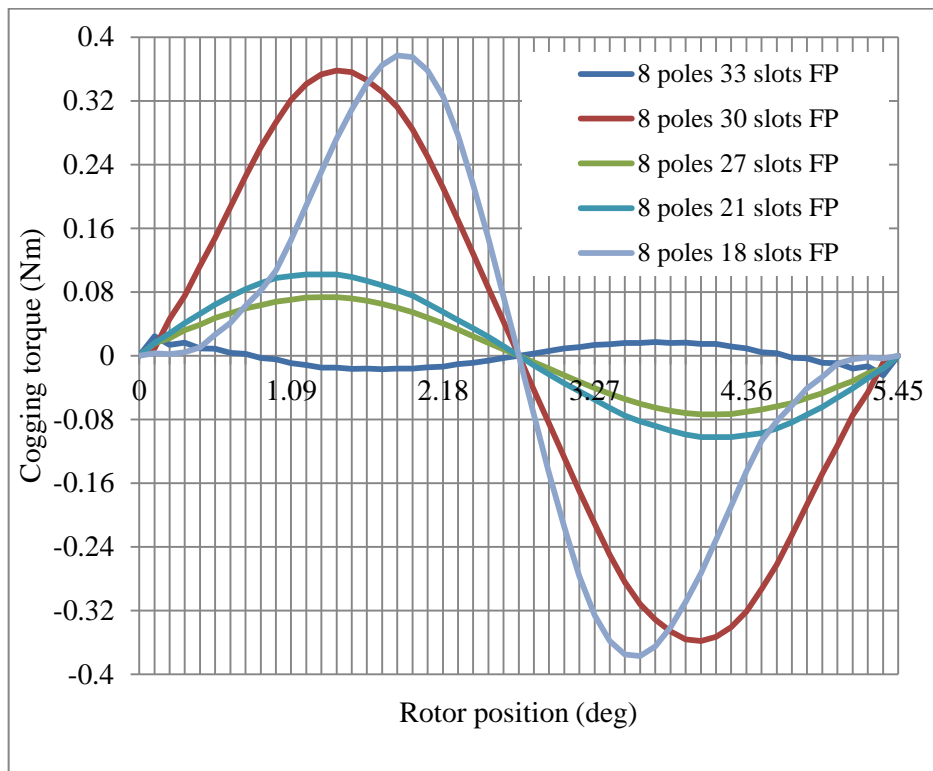


Figure C1.3: The cogging torque of the 8 poles FP models of the fractional windings

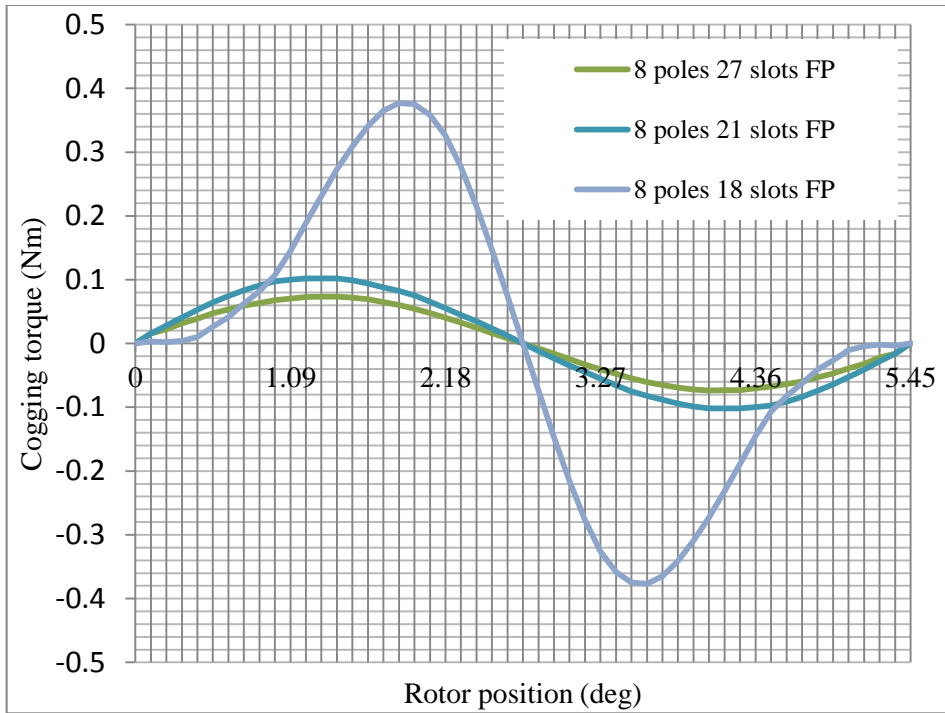


Figure C1.4: The cogging torque of the 8 poles FP models of the fractional windings

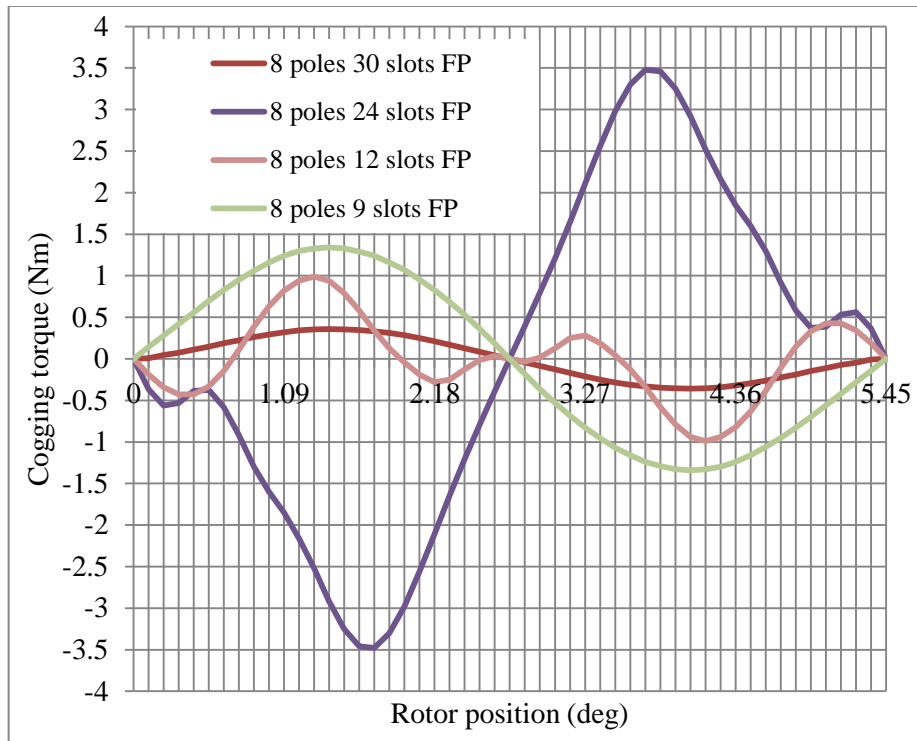


Figure C1.5: The cogging torque of the 8 poles FP models of the integral windings

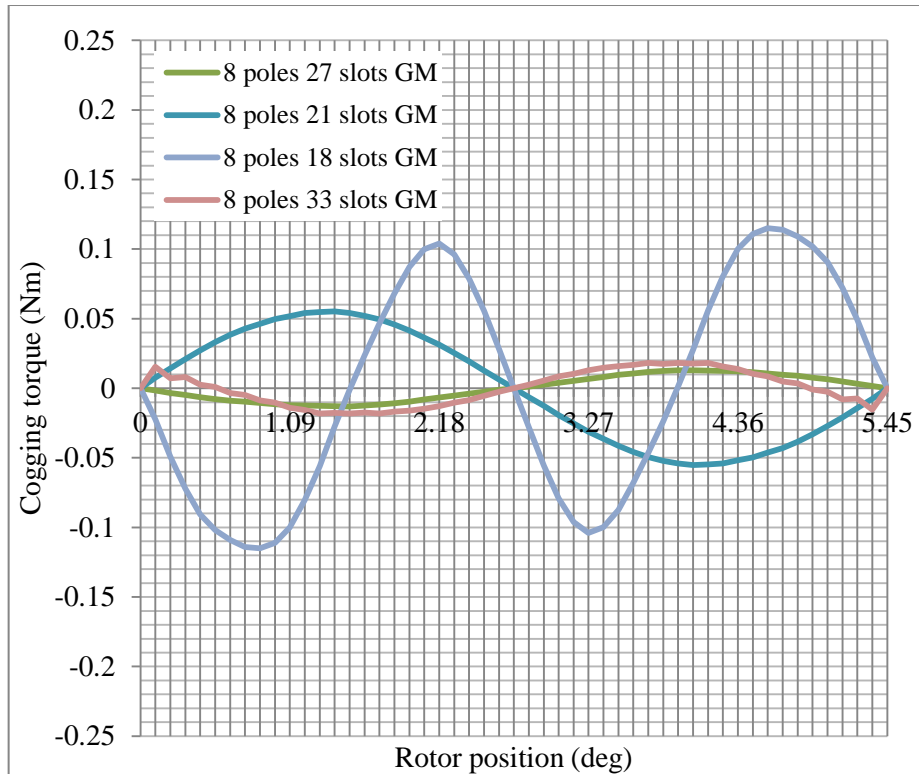


Figure C1.6: The cogging torque of the 8 poles GM models of the fractional windings

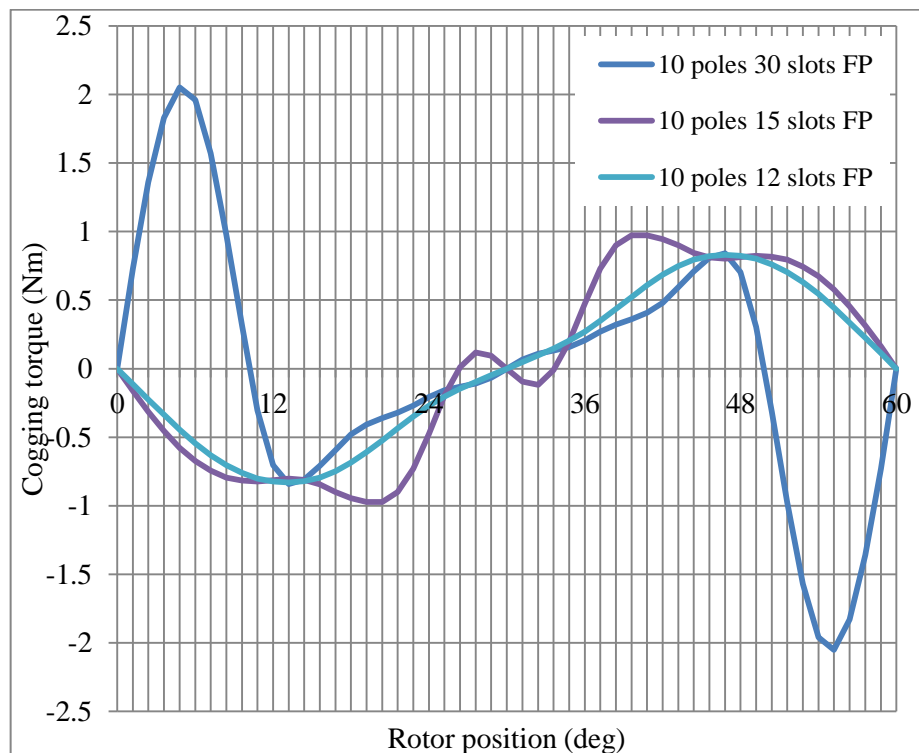


Figure C1.7: The cogging torque of the 10 poles FP models of the integral windings

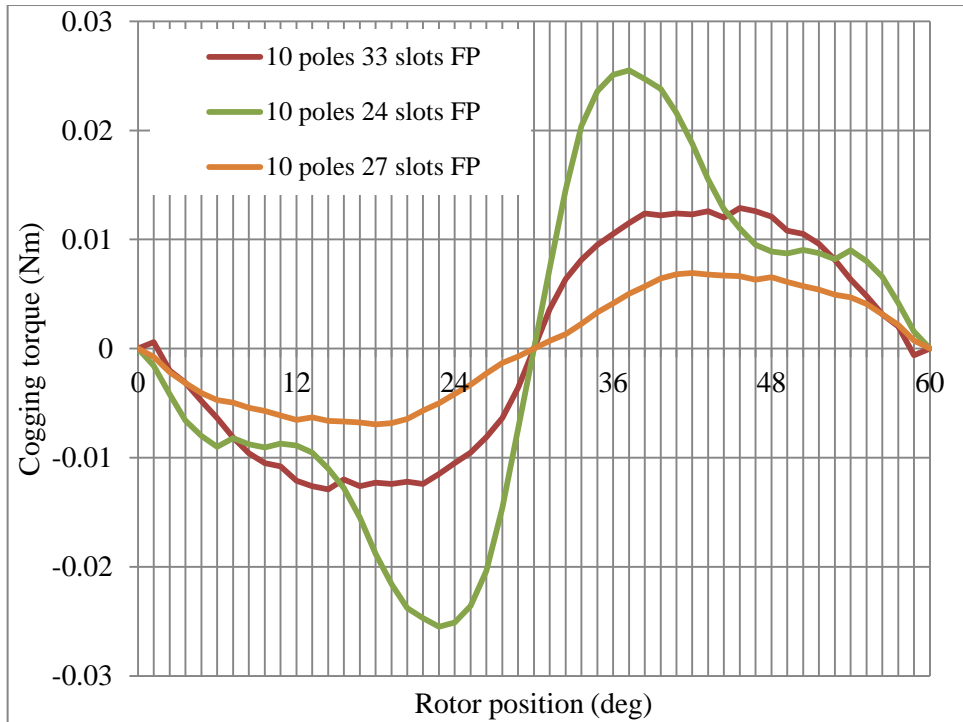


Figure C1.8: The cogging torque of the 10 poles FP models of the fractional windings

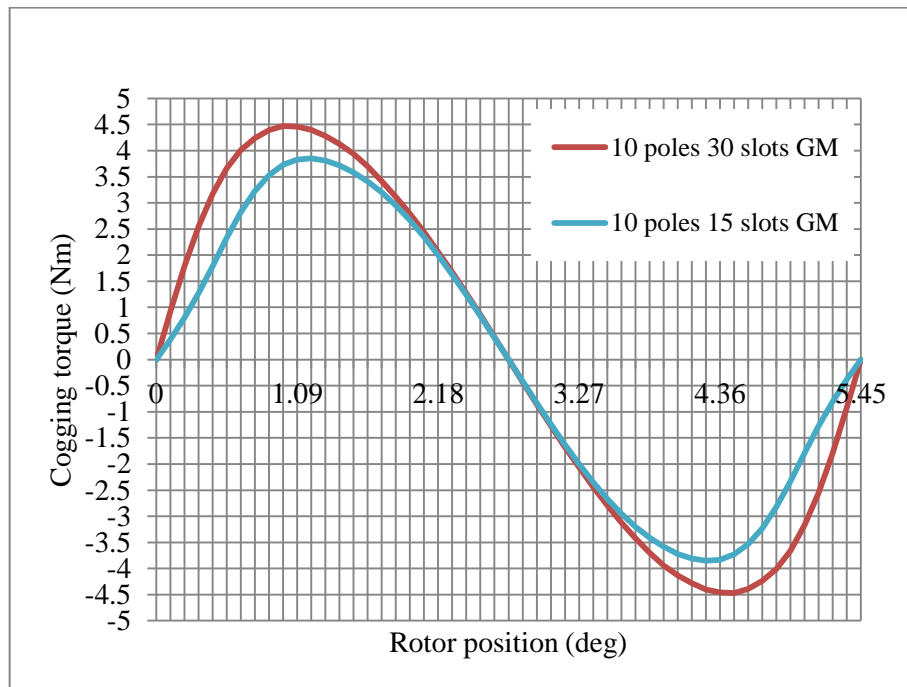


Figure C1.9: The cogging torque of the 10 poles GM models of the integral windings

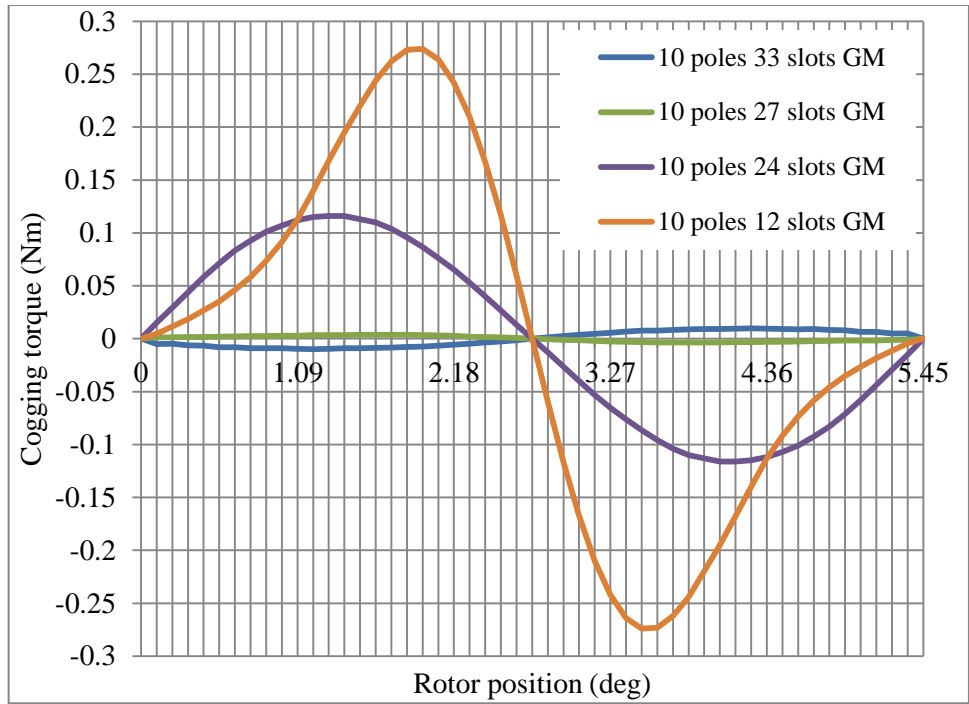


Figure C1.10: The cogging torque of the 10 poles GM models of the fractional windings

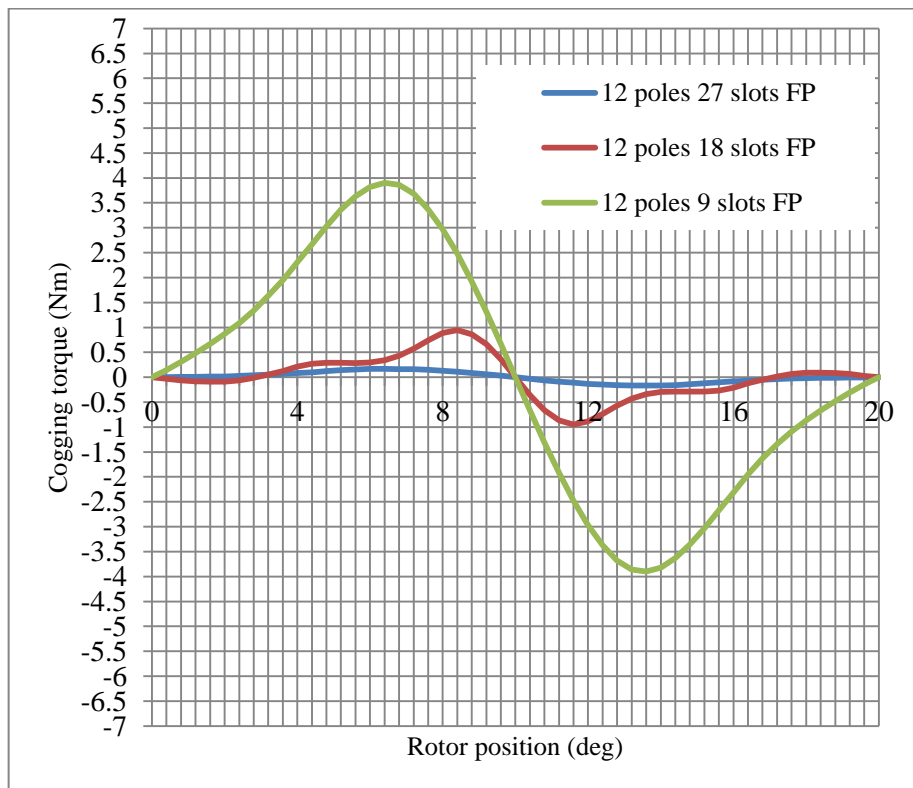


Figure C1.11: The 12 poles FP models simulations for the cogging torque

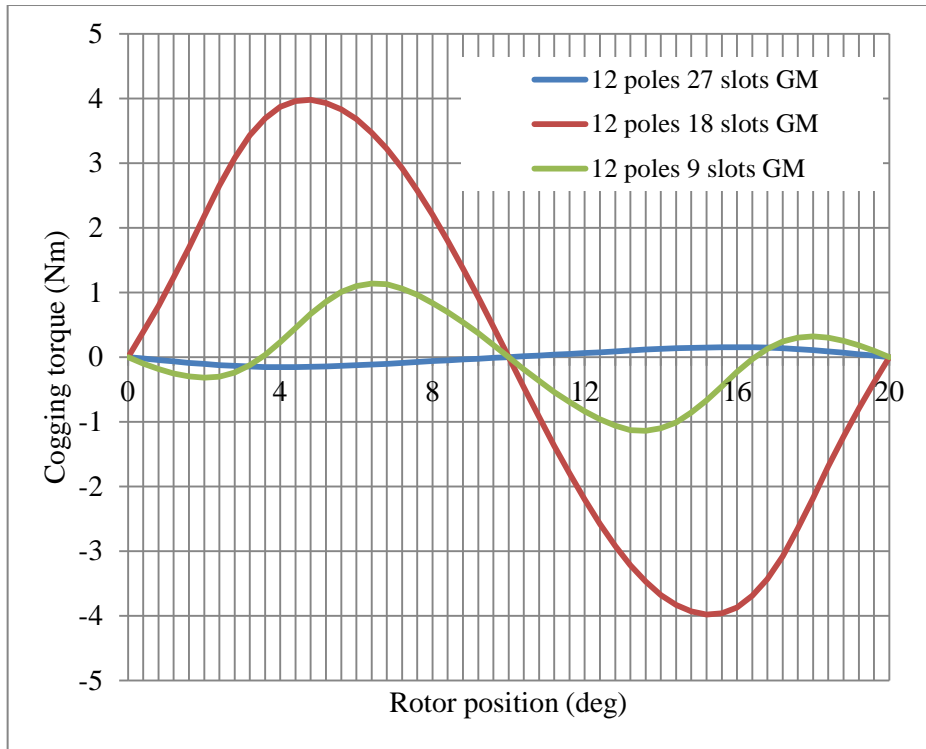


Figure C1.12: The 12 poles GM models simulations for the cogging torque

C2: The air gap flux at the inner and outer parts of the DM

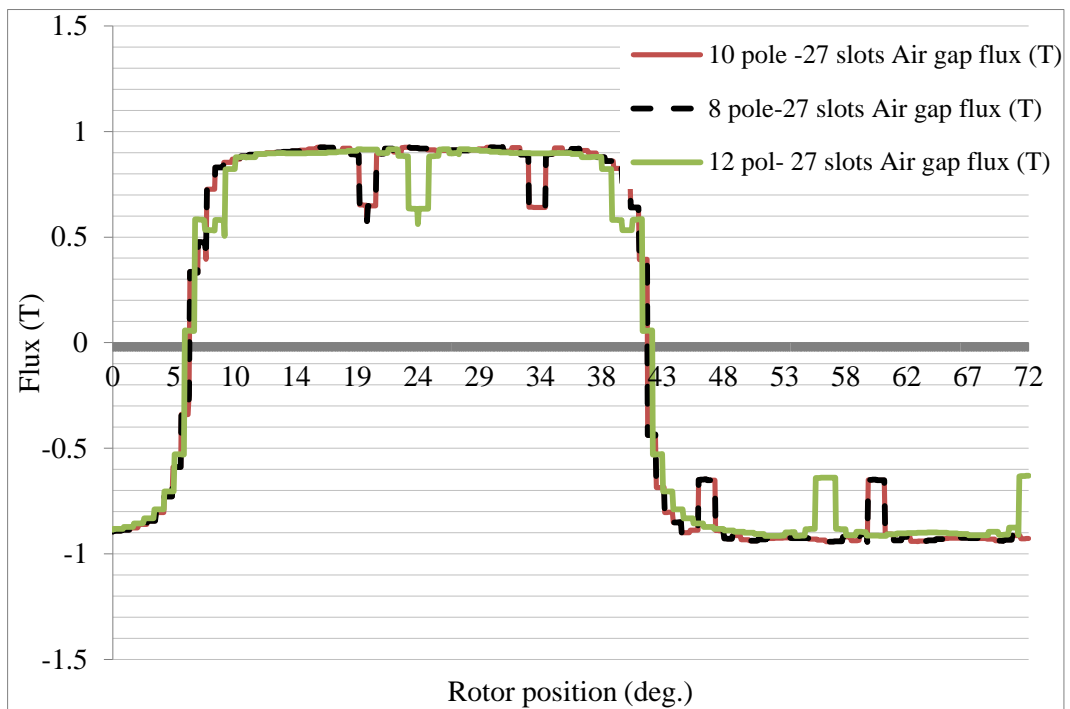


Figure C2.1: The air gap flux of the differential machine outer part (BLDCM)

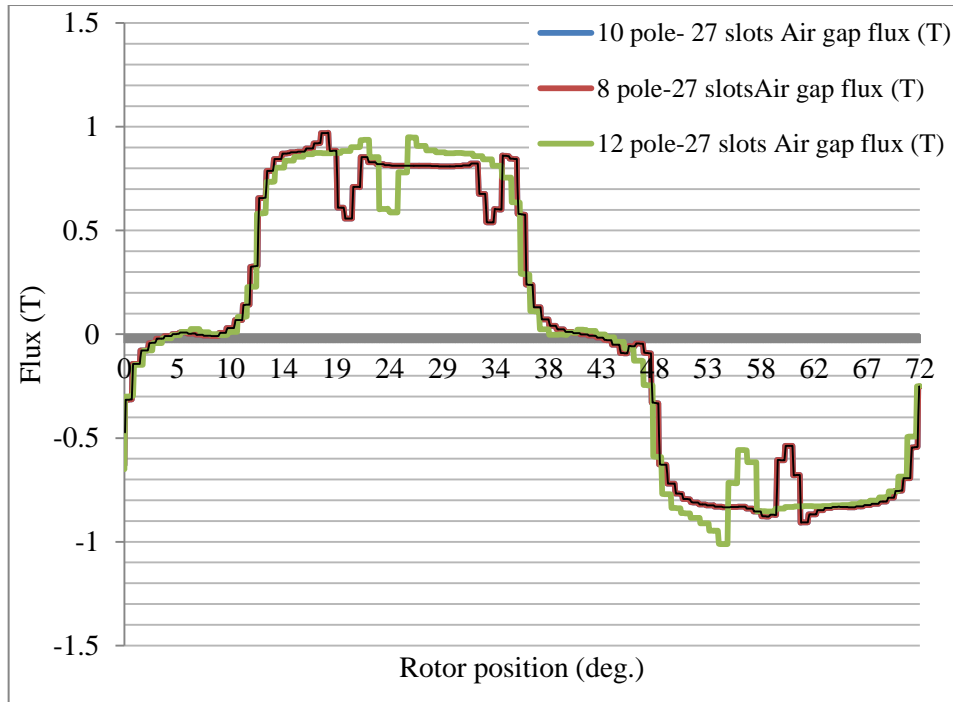


Figure C2.2: The air gap flux of the differential machine outer part (BLDCM)

C3: Closed Differential Machine Loop Simulation

This simulation was carried out in order to investigate the operation of the DM when it was operated in a closed loop. The inner rotor was rotated with different speeds. The back EMF in the inner rotor windings was then induced. By using the full wave rectification circuit, the induced back EMF was rectified. The output of the rectification circuit was then fed the stator of the DM using the inverter circuit. The following step was carried out to obtain the voltage result in the stator windings.

Step 1: define the back EMF in the stator windings

The aim of the defining the back EMF in the stator windings is to determine the switching sequence of the six-step inverter circuit. The six-step inverter circuit uses six transistors turned on/off frequently to control the commutation. In order to define the on/off switching sequence, the positive and negative peaks of the back EMF waveform per phase have to be determined from figure C3.1. The positive peak represents the switching of the upper switches of the six-step inverter circuit. Similarly, the negative peak in each phase represents the switching of the lower switches. In order to simulate the system in a load driven, i.e. the windings are excited by six-step inverter circuit; the switching degrees are identified to each switch as listed in table C3.1. Once the

switching degrees are defined, the windings are excited properly and then the machine is operated.

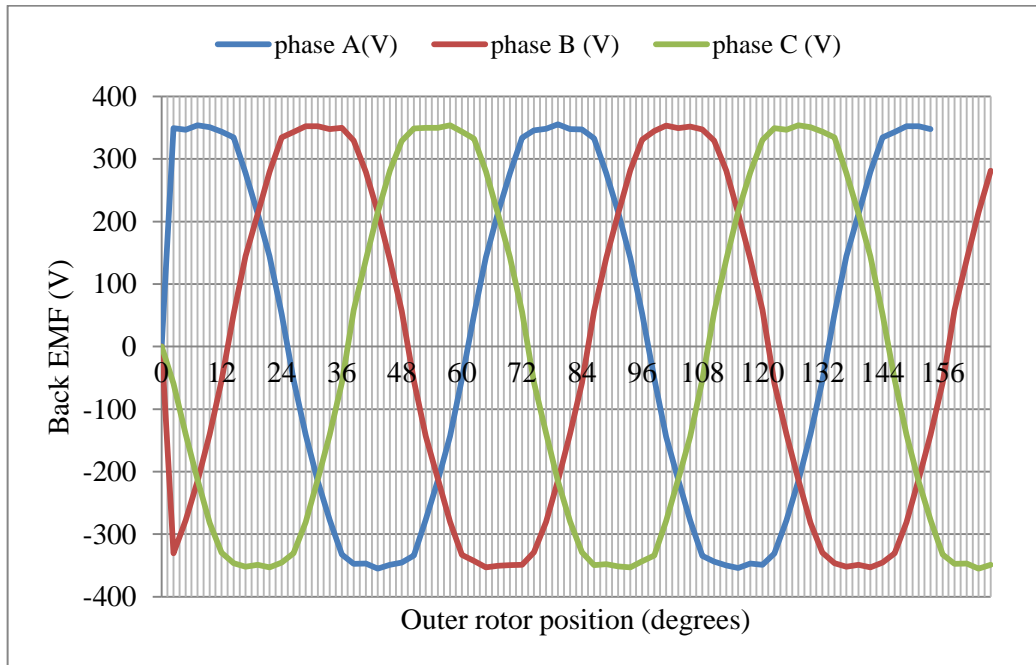


Figure C3.1: Stator back EMF versus outer rotor position at speed 1000 rpm

Phase	Turn on switch	Turn off switch	Turn on switch
A (upper switch)	60°	96°	132°
A (lower switch)	24°	60°	96°
B (upper switch)	84°	120°	156°
B (lower switch)	48°	84°	120°
C (upper switch)	36°	72°	108°
C (lower switch)	72°	108°	144°

Table C3.1: the switches on/off according to the back EMF in the stator windings

Step 2: Examine the output voltage of the full bridge rectifier

This aim of this step is to examine the output voltage of the full bridge rectification circuit. The capacitor is used to identify the voltage across its plates. The output DC voltage can be then used to supply the inverter circuit. The speed of the inner rotor is chosen to 1000 rpm stepped up to 2000 rpm and back to 1000 rpm. It can be seen from figure C3.2 that the output voltage is tracking the inner rotor speed as shown in figure C3.4.

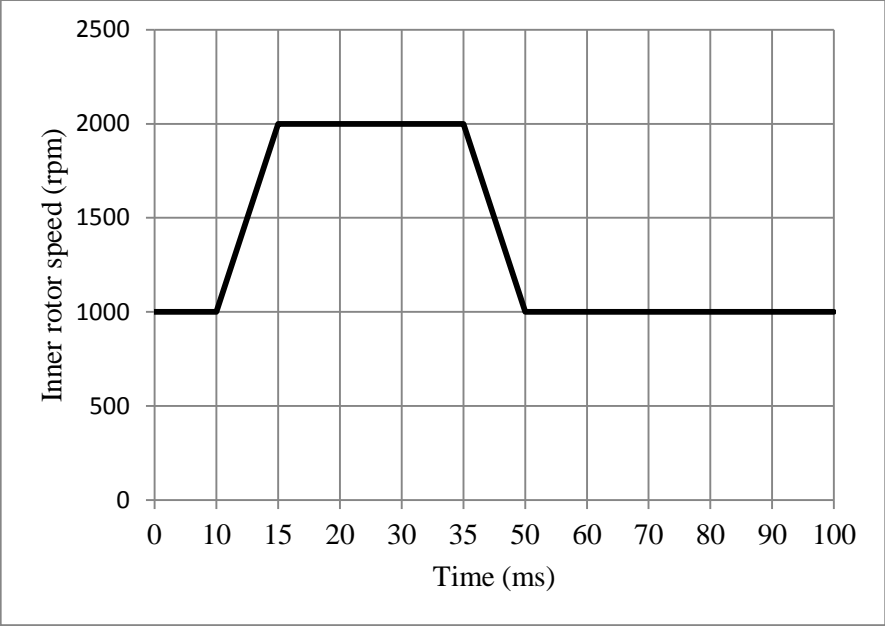


Figure C3.2: the inner rotor speed

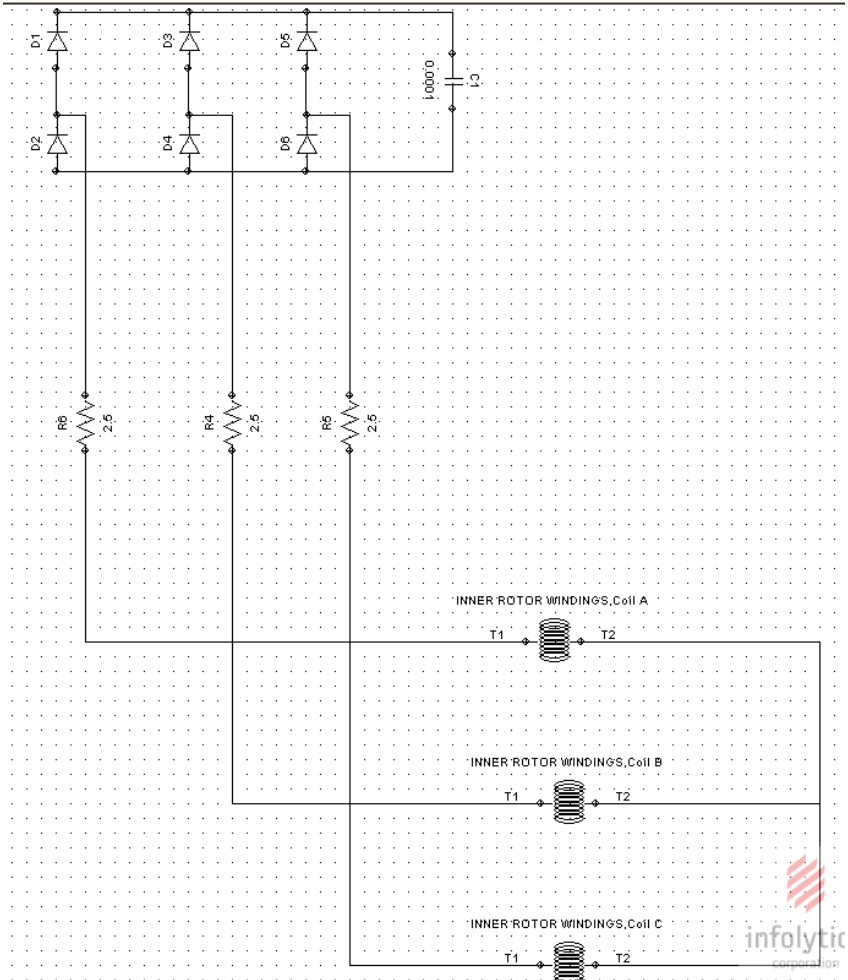


Figure C3.3: Circuit connection in the FEM simulation

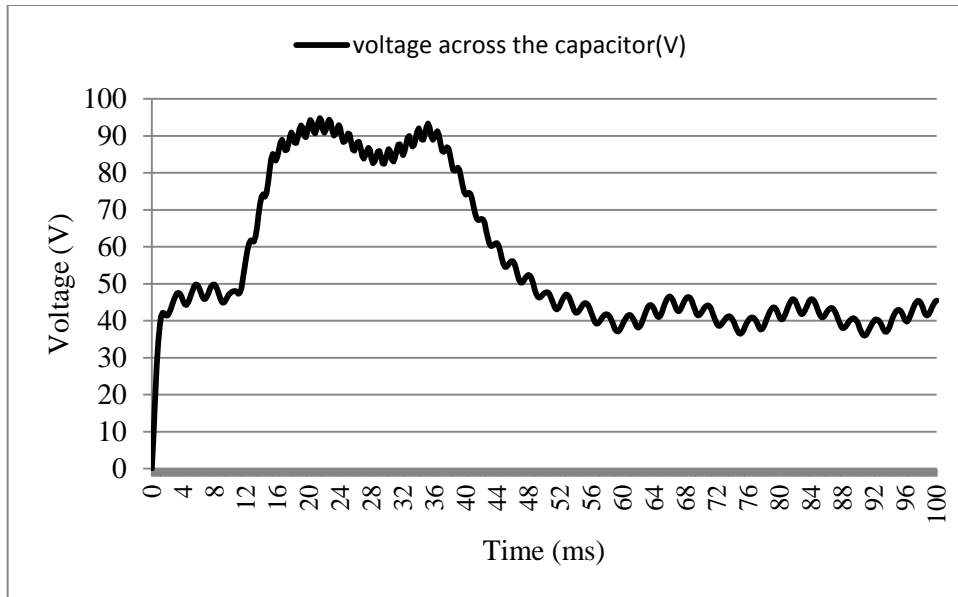
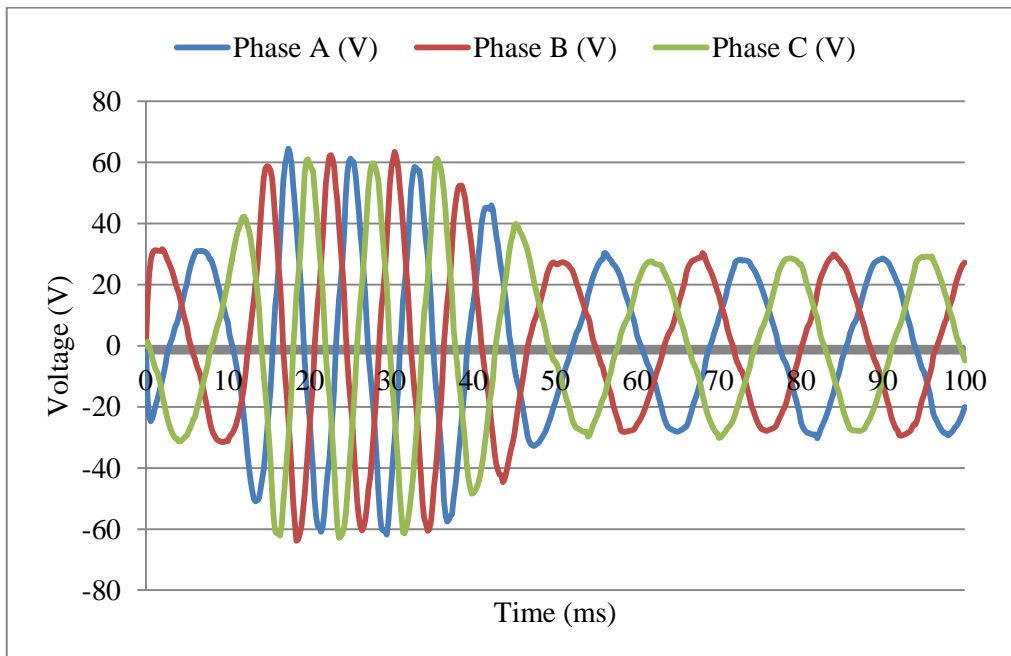


Figure C3.4: the voltage across the capacitor C1

Step 3: connect the full bridge rectification circuit with the capacitor to the inverter circuit to supply the stator windings. The connection can be seen in figure C3.3. Once the inner rotor rotates, the voltage supplies the rectification circuit and then the stator windings commutated. The voltage waveform across the stator windings is shown in figure C3.5.



C3.5: The voltage waveform in the stator windings

C4: The Data Sheet Parameters of the Used Devices in the EMTC System Measurements



C4.1: Permanent magnet specifications

Datasheet

3133 - Micro Load Cell (0-5kg) - CZL635

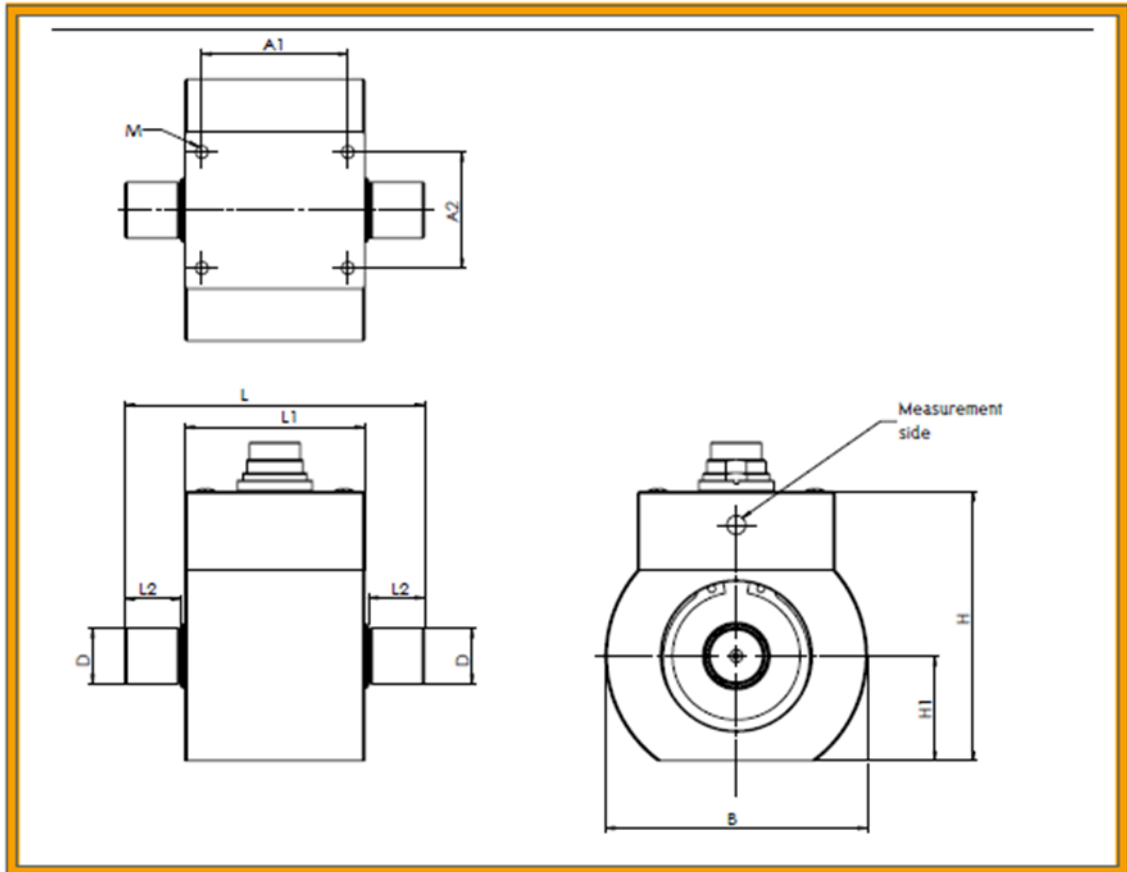


Product Specifications

Mechanical	
Housing Material	Aluminum Alloy
Load Cell Type	Strain Gauge
Capacity	5kg
Dimensions	55.25x12.7x12.7mm
Mounting Holes	M5 (Screw Size)
Cable Length	550mm
Cable Size	30 AWG (0.2mm)
Cable - no. of leads	4
Electrical	
Precision	0.05%
Rated Output	1.0±0.15 mv/V
Non-Linearity	0.05% FS
Hysteresis	0.05% FS
Non-Repeatability	0.05% FS
Creep (per 30 minutes)	0.1% FS
Temperature Effect on Zero (per 10°C)	0.05% FS
Temperature Effect on Span (per 10°C)	0.05% FS
Zero Balance	±1.5% FS
Input Impedance	1130±10 Ohm
Output Impedance	1000±10 Ohm
Insulation Resistance (Under 50VDC)	≥5000 MOhm
Excitation Voltage	5 VDC
Compensated Temperature Range	-10 to ~+40°C
Operating Temperature Range	-20 to ~+55°C
Safe Overload	120% Capacity
Ultimate Overload	150% Capacity

3133_0_Datasheet - May 4, 2012

C4.2: The data sheet of the load cell (The output torque measurement-device)



Size	I	II	III
Measurement range: [Nm]	5/10/20	50/100/200	500/1000
Dimensions:			
L [mm]	80	90	120
Ø B [mm]	70	75	105
H [mm]	72	77.5	97.5
H ₁ ± 0,05 [mm]	28	30	40
Ø D g6 [mm]	15	24	40
L ₁	48	52	65
L ₂	15	18	26
A ₁	39	42	50
A ₂	31	35	55
M	M4 x 6	M4 x 6	M5 x 10
	General tolerances DIN 2768 - m		
Weight ca.: [g]	550	850	2400
Max. speed [1/min]	22000	16000	9000

C4.3: The data sheet of the inner shaft torque transducer

(PRELIMINARY)

MAXIMUM RATINGS (unless otherwise noted, Ta=25°C)

Symbol	Parameter	Conditions	Ratings	Unit
VD	Supply voltage	DC	18	V
VI	Input signal voltage	Applied between VIN - IN1,2 50% Duty cycle, Pulse width 1ms	-1 ~ +7	V
IOHP	Gate peak current	Pulse width 2us	-5	A
IOLP			5	A
Viso	Isolation voltage	Sine wave voltage 60Hz, for 1min	2500	Vrms
Topr	Operating temperature	No condensation allowable	-20 ~ 70	deg C
Tstg	Storage temperature	No condensation allowable	-25 ~ 85	deg C
Ialm	Alarm output current	-	10	mA
Valm	Alarm pin voltage	-	50	V
Idrive	Gate drive current	Gate average current (Per one circuit)	TBD	mA

ELECTRICAL CHARACTERISTICS (unless otherwise noted, Ta=25°C, VD=15V)

Symbol	Parameter	Conditions	Limits			Unit
			Min	Typ	Max	
VD	Supply voltage	Recommended range	12	15	18	V
VIN	Pull-up voltage on input side	Recommended range	4.75	5	5.25	V
IiH	Input signal current	Recommended range	10	13	16	mA
f	Switching frequency	Recommended range	-	-	20	kHz
RG	Gate resistance	Recommended range	2	-	-	Ω
Ialm	Alarm output current	Recommended range	-	-	5	mA
VOH	Plus bias voltage	-	TBD	TBD	TBD	V
VOL	Minus bias voltage	-	TBD	TBD	TBD	V
tPLH	"L-H" propagation time	IiH = 13mA	0.2	0.45	0.8	us
tPHL	"H-L" propagation time	IiH = 13mA	0.2	0.4	0.7	us
tL_timer	Timer	Between start and clear (under input signal "OFF")	1	1.4	2	ms
talarm	Alarm delay time	Ialm=2.5mA	-	6.5	10	us
VSC	SC detect threshold voltage	IGBT collector voltage	TBD	TBD	TBD	V

**ISAHAYA ELECTRONICS CORPORATION**<http://www.idc-com.co.jp>

C4.4: The data sheet of the IGBT drive

MITSUBISHI IGBT MODULES
CM200DX-24S
HIGH POWER SWITCHING USE
INSULATED TYPE

ABSOLUTE MAXIMUM RATINGS ($T_J=25\text{ }^\circ\text{C}$, unless otherwise specified)

INVERTER PART IGBT/FWDi

Symbol	Item	Conditions	Rating	Unit
V_{CES}	Collector-emitter voltage	G-E short-circuited	1200	V
V_{GES}	Gate-emitter voltage	C-E short-circuited	± 20	V
I_C	Collector current	DC, $T_C=119\text{ }^\circ\text{C}$ (Note 2)	200	A
I_{CM}		Pulse, Repetitive (Note 3)	400	
P_{TOT}	Total power dissipation	$T_C=25\text{ }^\circ\text{C}$ (Note 2, 4)	1500	W
I_E (Note 1)	Emitter current	$T_C=25\text{ }^\circ\text{C}$ (Note 2, 4)	200	A
I_{EM} (Note 1)		Pulse, Repetitive (Note 3)	400	

MODULE

Symbol	Item	Conditions	Rating	Unit
T_{Jmax}	Maximum junction temperature	-	175	$^\circ\text{C}$
T_{Cmax}	Maximum case temperature	(Note 2)	125	
T_{Jop}	Operating junction temperature	-	-40 ~ +150	$^\circ\text{C}$
T_{stg}	Storage temperature	-	-40 ~ +125	
V_{ISO}	Isolation voltage	Terminals to base plate, RMS, f=60 Hz, AC 1 min	2500	V

ELECTRICAL CHARACTERISTICS ($T_J=25\text{ }^\circ\text{C}$, unless otherwise specified)

INVERTER PART IGBT/FWDi

Symbol	Item	Conditions	Limits			Unit	
			Min.	Typ.	Max.		
I_{CES}	Collector-emitter cut-off current	$V_{CE}=V_{CES}$, G-E short-circuited	-	-	1	mA	
I_{GES}	Gate-emitter leakage current	$V_{GE}=V_{GES}$, C-E short-circuited	-	-	0.5	μA	
$V_{GE(th)}$	Gate-emitter threshold voltage	$I_C=20\text{ mA}$, $V_{CE}=10\text{ V}$	5.4	6.0	6.6	V	
V_{CEsat} (Terminal)	Collector-emitter saturation voltage	$I_C=200\text{ A}$ (Note 5), $V_{GE}=15\text{ V}$	$T_J=25\text{ }^\circ\text{C}$	-	1.80	2.25	V
			$T_J=125\text{ }^\circ\text{C}$	-	2.00	-	
			$T_J=150\text{ }^\circ\text{C}$	-	2.05	-	
V_{CEsat} (Chip)	Collector-emitter saturation voltage	$I_C=200\text{ A}$ (Note 5), $V_{GE}=15\text{ V}$	$T_J=25\text{ }^\circ\text{C}$	-	1.70	2.15	V
			$T_J=125\text{ }^\circ\text{C}$	-	1.90	-	
			$T_J=150\text{ }^\circ\text{C}$	-	1.95	-	
C_{iss}	Input capacitance	$V_{CE}=10\text{ V}$, G-E short-circuited	-	-	20	nF	
C_{oss}	Output capacitance		-	-	4.0		
C_{res}	Reverse transfer capacitance		-	-	0.33		
Q_G	Gate charge	$V_{CC}=600\text{ V}$, $I_C=200\text{ A}$, $V_{GE}=15\text{ V}$	-	468	-	nC	
$t_{d(on)}$	Turn-on delay time	$V_{CC}=600\text{ V}$, $I_C=200\text{ A}$, $V_{GE}=\pm 15\text{ V}$, $R_G=0\text{ }\Omega$, Inductive load	-	-	800	ns	
t_r	Rise time		-	-	200		
$t_{d(off)}$	Turn-off delay time		-	-	600		
t_f	Fall time		-	-	300		
V_{EC} (Note 1) (Terminal)	Emitter-collector voltage	$I_E=200\text{ A}$ (Note 5), G-E short-circuited	$T_J=25\text{ }^\circ\text{C}$	-	1.8	2.25	V
			$T_J=125\text{ }^\circ\text{C}$	-	1.8	-	
			$T_J=150\text{ }^\circ\text{C}$	-	1.8	-	
V_{EC} (Note 1) (Chip)	Emitter-collector voltage	$I_E=200\text{ A}$ (Note 5), G-E short-circuited	$T_J=25\text{ }^\circ\text{C}$	-	1.7	2.15	V
			$T_J=125\text{ }^\circ\text{C}$	-	1.7	-	
			$T_J=150\text{ }^\circ\text{C}$	-	1.7	-	
t_{rr} (Note 1)	Reverse recovery time	$V_{CC}=600\text{ V}$, $I_E=200\text{ A}$, $V_{GE}=\pm 15\text{ V}$,	-	-	300	ns	
Q_{rr} (Note 1)	Reverse recovery charge	$R_G=0\text{ }\Omega$, Inductive load	-	10.7	-	μC	
E_{on}	Turn-on switching energy per pulse	$V_{CC}=600\text{ V}$, $I_C=I_E=200\text{ A}$,	-	30.7	-	mJ	
E_{off}	Turn-off switching energy per pulse	$V_{GE}=\pm 15\text{ V}$, $R_G=0\text{ }\Omega$, $T_J=150\text{ }^\circ\text{C}$,	-	21.5	-	mJ	
E_{rr} (Note 1)	Reverse recovery energy per pulse	Inductive load	-	14.2	-	mJ	
$R_{\theta(C-E)}$	Internal lead resistance	Main terminals-chip, per switch, $T_C=25\text{ }^\circ\text{C}$ (Note 2)	-	-	1.1	m Ω	
r_g	Internal gate resistance	Per switch	-	9.8	-	Ω	

C4.5: The data sheet of the IGBTs switches

Appendix D

D1: Stator Windings Fed by an External Power Supply

This test is similar to the test in chapter 9 section 9.3.1, but it was carried out in a different way. The purpose of the test is to investigate the dynamic behaviour of the VFRT machine when its stator windings are supplied an external power. This can happen if the BLDCM stator windings and the VFRT stator windings are fed by an external power supply but the inner rotor is locked.

1) VFRT Test at Open Circuit Rotor Windings Condition

The stator windings were fed by an external power while the rotor windings were open circuited in this test. Figure D1.1 shows the testing set-up in this condition. The induced voltage in the rotor windings is according to Faraday's law. Table D1.1 illustrated the measurement results of the input and the output voltages along with the measured input power. The input current was plotted against the input voltage per phase as can be shown in Figure D1.2. The figure illustrated the relationship between these two variables while the rotor was locked, i.e. the characteristics of the VFRT machine.

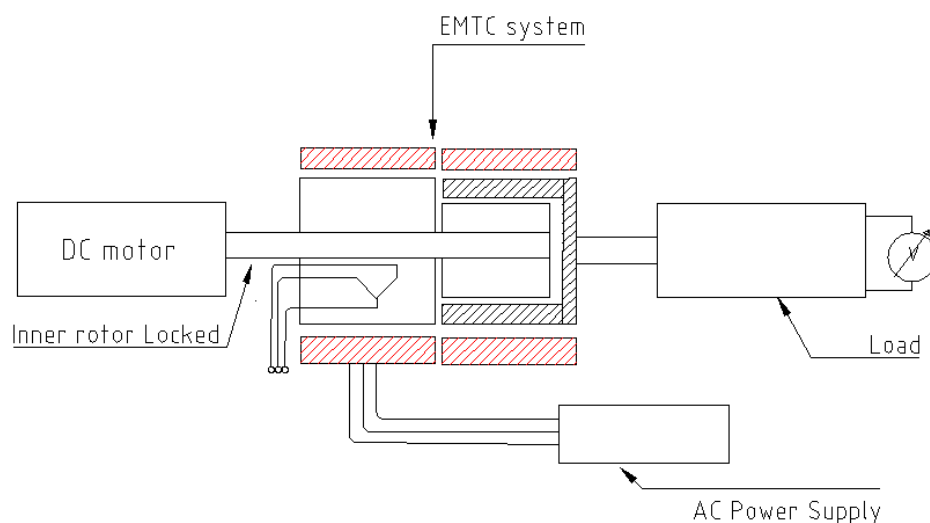


Figure D1.1: VFRT testing set-up with its rotor open circuited

Stator side				Rotor side			Watt 1 (W)	Watt 2 (W)	Total power (W)
Line Voltage (V)	Current			Voltage					
	I _A (A)	I _B (A)	I _C (A)	V _A (V)	V _B (V)	V _C (V)			
11.56	0.31	0.3	0.29	8.528	8.8	8.5	1	4.5	5.5
23.12	0.59	0.88	0.57	16.328	16.8	16.2	3	16	19
34.68	0.88	0.87	0.85	24.232	24.9	24.8	18	35	53
46.24	1.16	1.17	1.14	31.616	32.7	32.5	32	60	92
57.80	1.45	1.49	1.43	39	40.4	40.2	48	88	136
69.36	1.77	1.78	1.74	46.904	48.5	48.5	70	128	198
80.92	2.07	2.11	2.05	54.288	55.8	55.7	96	176	272
92.49	2.39	2.45	2.39	61.568	63.4	64	128	232	360
104.05	2.79	2.86	2.8	69.472	71.4	72.5	168	312	480
115.61	3.23	3.3	3.24	76.752	78.8	80	200	415	615

Table D1.1: open circuit test measurements

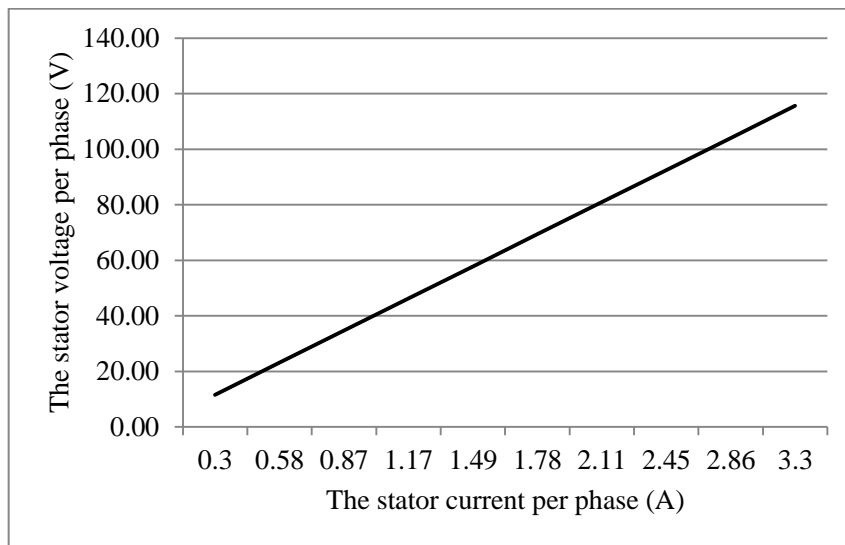


Figure D1.2: Rotor current versus the stator voltage at open circuit test

2) VFRT Test at Load Connected with its Rotor Windings

The load test was also performed of the VFRT machine by connecting the rotor windings in series to the resistive bank. The purpose of this test is to do more investigations the performance of the VFRT when its stator windings are fed by the external AC power supply instead of its rotor windings. Table D1.2 shows the input and

the output power flow, while the relationship between the input (stator) and the output (rotor) currents is shown in figure D1.3.

Stator side				Rotor side			Watt 1 (W)	Watt 2 (W)	Total power (W)
Voltage L-L (V)	Current			Voltage		Current			
	I _A (A)	I _B (A)	I _C (A)	V _A (V)	V _B (V)	I _C (A)			
20	0.6	0.58	0.58	3.8	4.5	0.44	12.5	2.5	15
40	1.12	1.11	1.09	7.3	8.56	0.84	8	44	52
60	1.57	1.56	1.52	10.5	10.7	1.11	12	87	99
80	2	2.02	1.97	13.4	13.42	1.42	12	146	158
100	2.49	2.53	2.47	16.7	16.78	1.79	18	300	318
120	2.98	3.05	2.97	20	20.23	2.16	30	320	350
140	3.52	3.6	3.53	23.6	24.2	2.57	40	450	490
160	4.03	4.14	4.07	26.9	27.8	2.96	60	580	640
180	4.69	4.83	4.8	31	32.7	3.42	60	780	840

Table D1.2: The measured input and output power on load

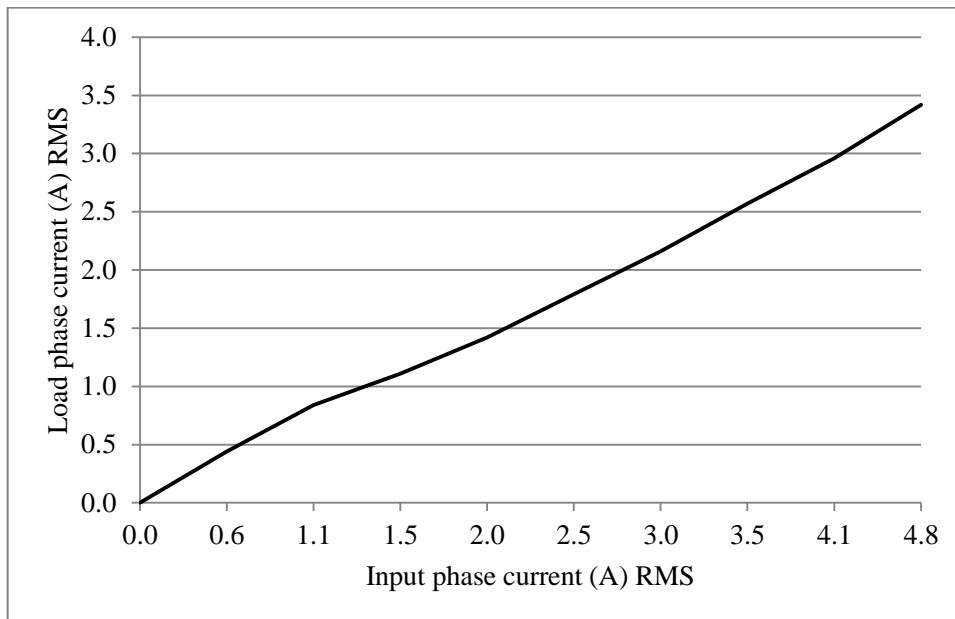


Figure D1.3: the relationship between the load and input currents

Appendix E

E1. Measurement Calibration

The measurement devices are calibrated to get accurate results out of the electromagnetic torque converter (EMTC) system. The inner rotor speed, the outer rotor speed and the load-cell output signal with its amplification circuit are calibrated as:

1- The EMTC Inner Rotor Speed Calibration

Since the inner rotor of the EMTC system is coupled to the driving DC machine, the speed of the DC machine is similar to that of the inner rotor. The DC machine speed is monitored by the induced voltage at armature windings. Table E1 shows the relation between the mechanical tachometer and the induced voltage. This voltage values are used for all the testing experiment of the EMTC system. Figure E1 illustrates the linearity of the relationship between the obtained voltage and the speed of the DC machine.

Tachometer (rpm)	Induced voltage (V)
0	0
100	6
200	12
300	18
400	24
500	30
600	36
700	42
800	48
900	54
1000	60

Table E1: The relation between the tachometer and the induced voltage

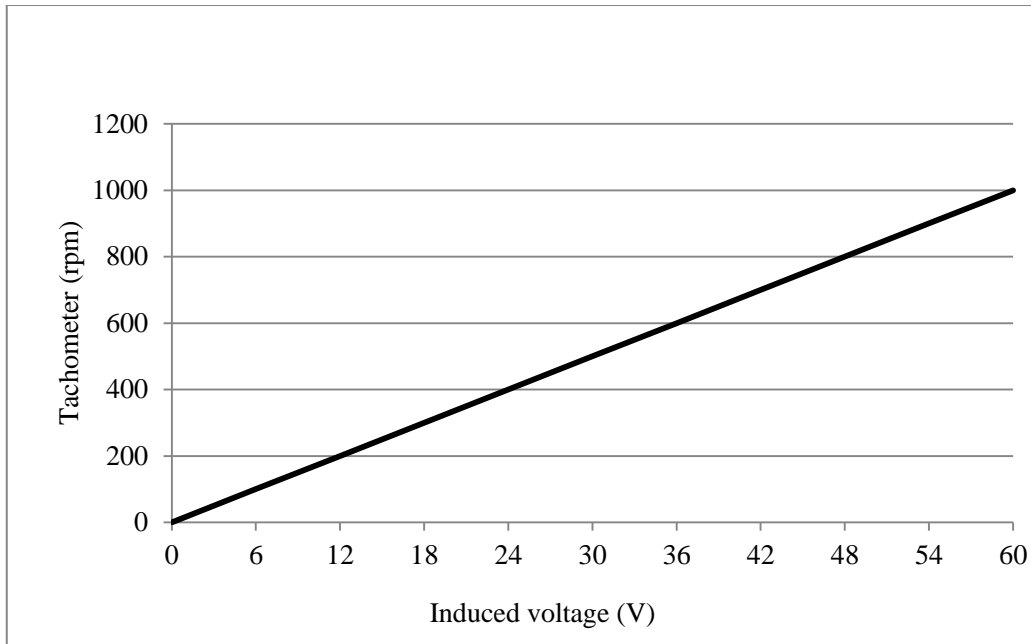


Figure E1: The relationship between the tachometer and induced voltage

2- Load Cell with its Amplification Circuit

The outer rotor of the EMTC system is coupled to the DC generator (Load). The DC generator is used to measure the output torque. The load cell is used with the amplification circuit to measure the output torque. Table E2 shows the calibration test of the load cell using the weights and the distance between the machine centre and the measuring point, which was measured as 30.2 cm. based on the readings in table E2, the relationship between the load (Kg) and the output voltage (mV) of the load cell can be shown in figure E2.

Load (Kg)	output voltage (mV)
0	73.2
1	91.3
2	109.1
3	124.8

Table E2: The measured load and the output voltage of the load cell

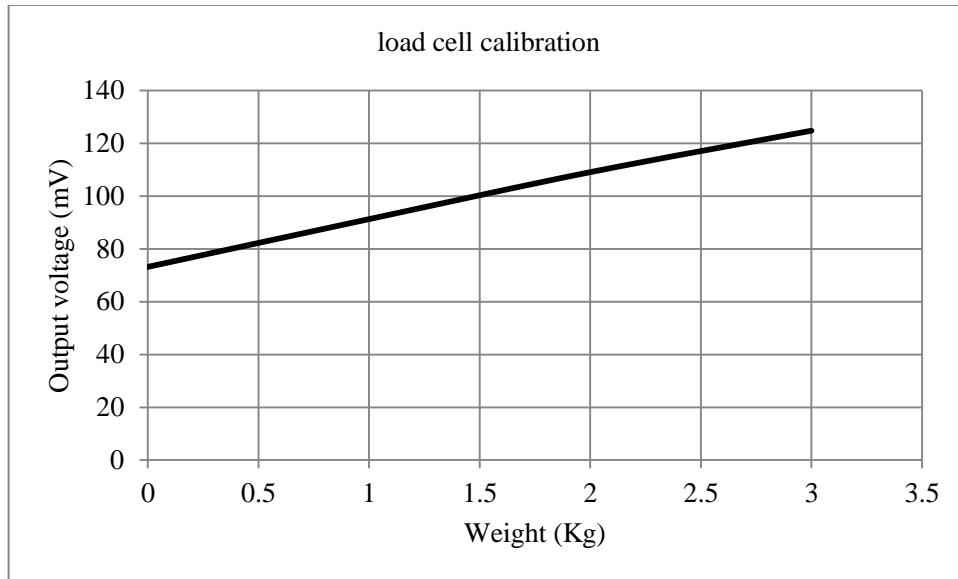


Figure E2: The relationship between the load and the output voltage

3- Outer Rotor of the EMTC Speed Calibration

The outer rotor speed is calibrated using the mechanical tachometer. The obtained measurements are then multiplied by the conversion factor (0.37). Table E3 shows the speed measured the tachometer readings and the machine speed. The relationship between these data can be shown in figure E3. It can be seen that the induced voltage is more linearly related to the speed meter than the tachometer readings.

Tachometer speed reading (rpm)	speed using conversion factor (rpm)	Voltage (V)	Speed meter (rpm)
360	133.2	5	100
480	177.6	10	210
1050	388.5	15	360
1460	540.2	20	500
1730	640.1	25	600
2000	740	30	710
2300	851	35	810
2800	1036	40	1000

Table E3: Outer rotor speed calibration

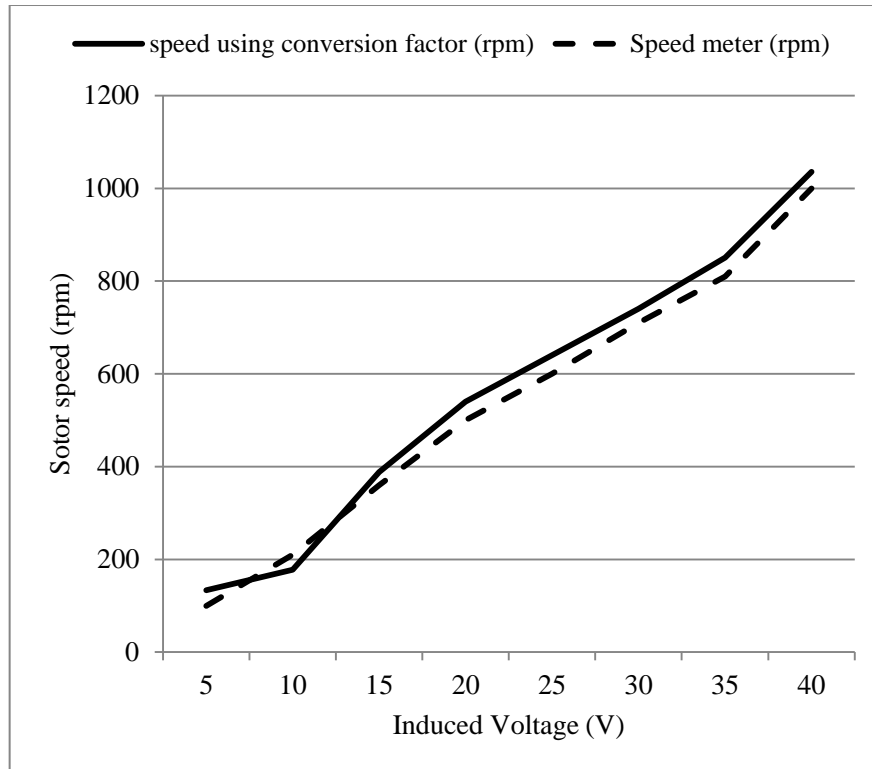


Figure E3: The relationship between the tachometer speed meter and the DC machine induced voltage using the conversion factor

E2. Analytical Calculations

- **The Back EMF Calculations of the BLDCM Using the Analytical Method**

The back EMF is calculated analytically from equation (E1) [27].

$$\text{Back EMF} = B_g D_r l_r N_{ph} \omega \quad (\text{E1})$$

Where:

B_g : Air gap flux density (T)

D_r : Outer rotor diameter (m)

l_r : Stack length (m)

N_{ph} : Number of turns per phase (value)

ω : Rotation speed (rad/s)

With B_g is equal to 0.9 T, D_r is 0.136 m, l_r is 0.059m, N_{ph} is 450 turns and ω is 104.67 rad/s, equation (E1) gives the back EMF at the outer part to be 378 V.

- **The Back EMF Calculations of the PMIM Using the Analytical Method**

Similarly for the permanent magnet induction machine (PMIM) with B_g is equal to 0.8T, D_r is 0.122 m, l_r is 0.059m, N_{ph} is 450 turns and ω is 314 rad/s, equation (5.49) gives the back EMF at the outer part to be 814 V

Appendix F

F1: Faults on the EMTC System during the Research

F1.1: The Inner Rotor Fault

The measured values of the inner rotor speed, the input torque and the input power were presented in table F1.1.

The testing of the inner rotor at a locked outer rotor status was performed by increasing the inner rotor speed. According to table F1.1, the power loss are quite high which gives an indication that there is a circulating current which could occur due to the extensive testing and weak manufacturing insulation at some points.

Speed (V)	speed (rpm)	Tin (Nm)	input power (W)
3	50	0.8	4.19
6	100	1	10.47
9	150	1.3	20.41
12	200	1.6	33.49
24	400	2.6	108.85
36	600	3.5	219.80
48	800	4.1	343.31
60	1000	4.5	471.00
72	1200	4.8	602.88
84	1400	4.8	703.36
96	1600	4.9	820.59
108	1800	4.9	923.16
120	2000	4.9	1025.73

Table F1.1: the measured power of the PMIM machine with locked outer rotor

The voltage across each phase at open circuit and the machine is rotate with 500 and 1000 rpm was measured. The phase voltage results are shown in table F1.2.

Analysis of the measured voltages and resistance at the inner rotor windings showed that the voltage across the phase C is lower than the other phases by about 10%.

Phases	Voltage at 500 rpm	Voltage at 1000 rpm
Phase A	98 V	199 V
Phase B	99 V	201 V
Phase C	88 V	179 V

Table F1.2: The Back EMF measurements

Since the measured phase voltages at different speeds are unequal, the possibility of the inter-turn short circuit at phase C is large. Measuring phase resistance is further investigation; the resistance of phase C is lower than the other phases as can be shown in table F1.3.

Phases	Applied DC voltage (V)	Measured current (A)	Resistance (Ω)
Phase (A)	10	2.8	3.57
Phase (B)	10	2.8	3.57
Phase (C)	10	3.2	3.125

Table F1.3: The resistance measurements

After the outer rotor was pulled off, it was revealed that inter-turn short circuit in the inner rotor winding at the phase C had occurred as expected as shown in figure F1.1a. The inner rotor windings were re-winded as shown in figure F1.1b to resume the experiments in order to evaluate the EMTC system performance.



Figure F1.1: The inner rotor windings at (a) inter-turn short circuit and (b) after re-winded